THE UNIVERSITY *of* EDINBURGH

Examining Ground-Based In Situ Monitoring Capability To Improve Understanding Of The Atmospheric Methane Budget

Alice Drinkwater

Doctor of Philosophy

THE UNIVERSITY OF EDINBURGH

2022

Abstract

Methane (CH_4) is the second most abundant anthropogenic greenhouse gas. Amount fractions have been rising in recent years, but we still do not have a complete understanding of the driving forces behind these changes. It is of great importance to understand what has been driving CH_4 increases in recent years so we can focus efforts on emissions reduction and therefore mitigate the harmful impacts of climate change. Stable isotope ratios of CH_4 (specifically δ^{13}C and δD) may be the key to providing this understanding, as atmospheric isotope ratios are sensitive to changes in CH_4 sources and sinks. To address the gaps in our understanding, this thesis aims to assess ground-based *in situ* monitoring capability, to understand how CH_4 fluxes have varied over a recent 17 year period; develop the protocols for examining measurements from a new type of *in situ* instrument to study methane isotopes; and assess where new *in situ* instruments could be deployed in the future to aid in budget quantification. First, variations in large-scale regional CH_4 fluxes and δ^{13}C emissions signatures are examined, 2004-2020. The GEOS-Chem 3D Chemical Transport Model is used to simulate CH_4 and δ^{13}C. Ground-based *in situ* data from the NOAA global greenhouse gas monitoring database provides a constraint in an inversion to solve for regional fluxes and δ^{13}C source signatures. Results show that there has been a latitudinal shift from mid-latitudinal Northern Hemisphere emissions to tropical emissions. Coevally, δ^{13}C emissions source signatures have become lighter, with the greatest lightening occurring around the tropics. As such, increasing emissions are attributed to tropical wetland emissions. Second, data analysis protocol for a new CH_4 measuring instrument 'Boreas' is outlined. Boreas is a preconcentration system, attached to a laser spectrometer, which has the capability to measure CH_4 isotopologues ($^{12}CH_4$, $^{13}CH_4$ and CH_3D) continuously to a high precision. The data analysis consists of a calibration on each isotopologue amount fraction; a drift correction to account for noise; and an internal calibration adjustment to ensure Boreas measurements are comparable with measurements of external laboratories. Real-world data from when Boreas was located at the National Physical Laboratory (Teddington, UK) is shown, demonstrating the capability of Boreas to differentiate between source types. Third, the thesis considers where to deploy continuous monitoring instruments around the world, to best capture variations in CH_4 isotope ratios. To examine this, δ^{13}C and δD are simulated using GEOS-Chem over the period 2016-2020, and compared with typical precision on continuous monitoring instruments. The analysis covers current network site locations and a potential new location for instrument deployment. The results show such instruments would effectively capture isotope ratio variations on both a daily and monthly scale, especially in areas with active sources present. This potential future deployment would be useful to constrain the drivers behind global CH_4 variations, to prepare future emission reduction scenarios.

Lay Summary

This thesis is concerned with the greenhouse gas methane (CH_4). It is a powerful and prevalent greenhouse gas, 28 $\times$ more powerful than carbon dioxide on a gram/gram basis over 100 years. Due to its short atmospheric lifetime (approximately 10 years), CH_4 is becoming the focus of emissions reduction strategies. In recent years (2000-2007), the amount fraction of CH_4 has plateaued, increasing again more recently (post-2007). We do not have full understanding of what caused these variations and therefore what is driving increases in greenhouse gas amount fractions worldwide.

The thesis consists of three separate studies examining variations in CH_4 and its primary stable isotope ratios. Isotope ratios are conventionally represented by 'delta' values, which represent the abundance of a rare to more common isotope in a sample, compared to a reference standard (for CH_4, these are δ^{13}C for carbon-13 vs carbon-12, and δD for deuterium vs hydrogen). These values vary depending upon what emissions contribute to a sample, and so may provide insights into the changing balance of CH_4 sources and sinks. Major sources of CH_4 include wetlands, oil and gas, agriculture and waste; the major sink is the reaction with the OH molecule in the troposphere.

The first chapter examines how CH_4 and δ^{13}C varied over the period 2004-2020. CH_4 and δ^{13}C are simulated in a 3D Chemical Transport Model, and inversions are performed to solve for large-scale regional CH_4 emissions and δ^{13}C emissions source signatures, using real-world data as a constraint to understand the changes. The results show that tropical wetland emissions have been strongly increasing in recent years, at the same time as a decrease of mid-latitudinal Northern Hemisphere emissions.

Next, the data processing approach is established for a new CH_4 measurement instrument (known as 'Boreas'), which is capable of making continuous, high-precision isotope ratio measurements. The correct approach for data processing is detailed and assessed. This processing includes calibration on isotopologue amount fractions, a drift correction, and adjustment to align the measured values with those measured by international laboratories. The sensitivities that Boreas can achieve on measured data are shown, being able to pinpoint specific sources in an area.

Finally, the thesis assesses where to deploy continuous monitoring instruments around the world, to best capture isotope ratio variations. The increased sampling frequency from a continuous monitoring instrument means isotope ratio variations are finely monitored and understood. Results show find that central tropical oceanic regions would be a good location

to position a Boreas instrument in order to capture monthly-scale isotope ratio variations without the influence of pollution events; that an east Asia location would capture daily-scale variations; and locations in eastern Canada could capture both daily and monthly-scale variations.

Future work in this field could concern the modelling of rarer isotope ratios, such as multiply-substituted ‘clumped’ isotope ratios. Also there will be opportunity for future field campaigns using a Boreas instrument, to measure isotope ratios around the world.

Acknowledgements

I would like to thank my funding bodies, the NERC E3 DTP, and my CASE partner, the National Physical Laboratory, for making this project possible. Thank you to my primary supervisor Tim Arnold for his support, and to Paul Palmer for going above and beyond second supervisor duty. All of the E3 DTP, Edinburgh School of GeoSciences and NPL PGI staff, especially Stephanie Robin, Sophie Ramette and Linden Fradet, have been wonderfully supportive throughout this time.

This work would have been impossible without the staff at NOAA-ESRL, CU-INSTAAR, NIES and GOSAT for providing their data and giving me feedback on my studies when needed. Thanks also to the GEOS-Chem team at Harvard University for the use of their model, which was essential to this work.

Thank you to all my friends in the NPL atmospheric composition group, especially Caroline, Dafina and Emmal, for being endlessly helpful, kind, and open. Emmal, you have been invaluable, and I owe you so much. Likewise, to Palmer Group Edinburgh (especially Caterina, Doug, and Maggie) for providing resolute support in Edinburgh, both academically and socially.

There are not enough words to describe my gratitude to my family: you all continue to inspire me, providing everything from phone calls and letters to catering and a place to stay. To friends around the world, from New Zealand to Calgary via Warrington, London, and York, who have all brought with them so much light over this time: you are all so loved.

Finally, to my friends in Edinburgh: especially Hannah, Helen, Polly, Nadia, and Sam — you are all the best thing to come from these four years, and I could not have done this without you.

Declaration

I declare that this thesis was composed by myself, that the work contained herein is my own except where explicitly stated otherwise in the text, and that this work has not been submitted for any other degree or professional qualification except as specified.

Alice Drinkwater

Contents

Figures and Tables

Figures

Tables

Chapter 1

Introduction

Global greenhouse gas (GHG) amount fractions are continuing to rise in response to increased anthropogenic emissions, creating a climate emergency, with increased global temperatures causing multiple crises, such as rising sea levels, changing weather patterns, species loss and food shortages (IPCC, 2021). Methane (CH_4) is the second most abundant anthropogenic greenhouse gas and has more than doubled in the last 150 years. It is both powerful and prevalent, with a global warming potential (GWP_{100}) of 28, meaning that on a gram/gram basis, it is 28 $\times$ more effective than carbon dioxide (CO_2) at capturing heat in the atmosphere, over a 100 year period (IPCC, 2021).

As greenhouse gas amount fractions (an equivalent descriptor to 'mole fractions' or 'volume mole fractions' in the ideal gas limit, measured in ppb or nmol/mol) continue to increase worldwide, the question of source and sink assignation (calculating how greenhouse gas emissions and sinks are varying) becomes more and more pressing. Understanding changes in CH_4 fluxes on a global scale is crucial to assess the impact of changes in human activity on the Earth's atmosphere as a whole, as well as to deduce changes taking place in the atmosphere (such as sinks changing in magnitude). A better understanding of atmospheric CH_4 sources would allow us to focus on specific sectors for emissions reduction pathways in order to achieve emissions reduction targets, such as those set out by the Paris Agreement (UNFCCC, 2015). Emissions reductions protocols can limit the full impact of global warming, protect ecosystems and save lives.

The correlation between increasing atmospheric carbon levels (primarily CO_2) and rising global temperature has been considered since the work of Eunice Newton Foote in the 1850s, who first proposed a connection between greater concentration of carbon gases resulting in increased temperature (Foote, 1856). She was followed by John Tyndall, whose lectures brought public awareness to the relationship between greenhouse gases and global temperature for the first time, establishing the term 'greenhouse effect' to represent the trapping of solar radiation in the lower atmosphere, at a greater rate than it escapes (Tyndall, 1861). Further evidence of a relationship between carbon gas amount fraction and global temperature was added at the turn of the century with the work of Svante Arrhenius, who calculated the impact of rising CO_2 levels on temperature. His work indicated that human activity may bring about

global warming (Arrhenius, 1896). Such work was mostly rejected and ignored at the time; with the scientific community assuming that oceans would absorb any additional human-caused emissions. Greater understanding has been established since the 1950s; driven by ground-based *in situ* CO_2 observations such as those from Mauna Loa (the oldest continuous CO_2 monitoring station). This station has recorded rapidly rising CO_2 levels since its establishment in 1958; the results of which are demonstrated by the Keeling Curve. This plot showed how CO_2 levels (in parts per million) have changed over time, demonstrating consistent increases of CO_2 since the establishment of the Mauna Loa site in 1958 (Keeling, 1960). The Keeling Curve drew worldwide popular attention to rising levels of carbon gases.

Ground-based measurements of carbon gases have therefore long been key in highlighting and comprehending anthropogenic climate change. The global greenhouse gas measurement network has continuously expanded since 1958, to the point where there are now over 100 monitoring sites located around the world, some of which have been operating for decades. The most widespread and oldest measurement network is the National Oceanic and Atmospheric Administration Earth System Research Laboratory (NOAA-ESRL) Global Greenhouse Gas Reference Network, with over 100 CH_4 flask sampling sites currently operating (Lan et al., 2021). Other networks include the Advanced Global Atmospheric Gases Experiment (AGAGE) network which comprises 17 active global network sites (Prinn et al., 2018) and the Japan-Russia Siberia Tall Tower Inland Observation Network (JR-STATION), with 9 active sites (Sasakawa et al., 2010). The sites often measure multiple greenhouse gases, including CH_4, CO_2, nitrous oxide (N_2O), and other important gases such as carbon monoxide (CO) and molecular hydrogen (H_2). The sites measure greenhouse gases for understanding both longer term changes in the well-mixed atmosphere and for pollution monitoring for regional scale emissions estimation studies. Altogether the recorded data give us insight on how global greenhouse gas levels (and their emissions) are changing.

Stable isotope ratios of atmospheric CH_4, specifically, δ^{13}C and δD (sometimes written as δ^{2}H) values are less frequently measured than amuont fractions. However, they have been proven to be a useful tool in delineating between emissions types, as the δ value of a sample is related source of the CH_4. These values are therefore able to differentiate between biogenic, pyrogenic and thermogenic sources (Bréas et al., 2001), and may therefore provide additional constraint upon our understanding of how atmospheric CH_4 emissions are changing.

1.1 Aims of the Thesis

The overall aim of this thesis is to examine ground-based *in situ* monitoring capability of atmospheric CH_4 amount fractions and isotopic composition, to understand the global CH_4 budget. In particular, CH_4 amount fractions and isotope ratios are studied in three contexts: how they have varied in the period 2004-2020; in terms of how to process CH_4 isotope ratio data using a new measurement system that has potential for improved deployment capabilities; and where instruments would be best positioned in order to capture CH_4 variations effectively.

1.1.1 Overarching Research Questions

The thesis comprises three research chapters, each assessing a major overarching research question. The principle research questions addressed by this thesis are:

—How have CH_4 amount fractions and isotope ratios varied over a recent 17 year period, and what regions/sources are responsible?

—How should data from a newly developed laser-based measurement system be processed to produce high-precision data for analysis?

—Where should new ground-based *in situ* continuous monitoring instruments be located, in order to measure CH_4 isotope ratios most effectively?

1.2 Structure of Thesis

1.2.1 Chapter 1 - Introduction

This first chapter outlines the main plan of the thesis, and assesses current knowledge of CH_4, its major sources and sinks, and how isotope ratios are used as a tool in source and sink assignation. Specifically, this chapter focuses on ground-based monitoring as a tool in greenhouse gas modelling and metrology. The content of the chapter assesses current knowledge of CH_4 sources and sinks, and in doing so determines knowledge gaps (in terms of CH_4 emissions and specific measurement approaches) that will be targeted throughout the thesis. The knowledge gaps pursued cover the overarching research questions as outlined in Section 1.1, to improve understanding of the CH_4 budget, through the use of ground-based *in situ* data.

1.2.2 Chapter 2 - Large-Scale Regional Inversions for CH_4 emissions and δ^{13}C signature, 2004-2020

The GEOS-Chem 3D chemical transport model (Bey et al., 2001) is used to simulate atmospheric CH_4 amount fractions and δ^{13}C values. The chapter consists of an inversion to understand the driving forces behind increasing CH_4 amount fractions in recent years. The inversion solves for large-scale regional emissions and source signatures separately, using a Maximum *A Posteriori* inversion approach, with ground-based *in situ* data of CH_4 amount fractions and δ^{13}C as a constraint. The chapter presents a unique approach for both the length of time the inversion is solved over (2004-2020) and the approach of solving for both regional CH_4 fluxes and regional δ^{13}C emissions source signatures. The results of the CH_4 emissions inversion are considered alongside results obtained from an inversion which used satellite data to solve for regional CH_4 fluxes, over the same regions as in the ground-based *in situ* inversion. The comparison of these approaches is used to both bolster findings and assess the limitations of each approach.

1.2.3 Chapter 3 - Data Processing for Analysis of δ^{13}C and δD Methane Using a Laser Spectrometer Based System

This chapter concerns a continuous laser spectrometer system for creating accurate and precise measurements of δ^{13}C and δD. We use an instrument that was recently constructed at the National Physical Laboratory in Teddington, Greater London (NPL); this work has involved collaborating with colleagues there (Rennick et al., 2021). This chapter is unique in that the instrument is newly established — the instrument ('Boreas') is capable of making continuous, independent measurements using laser spectroscopy, achieving a precision similar to that of flask sampling using isotope ratio mass spectrometry. The work in this chapter covers data processing of the raw isotopologue amount fractions, in order to obtain accurate, high precision results on δ data. The approach includes calibration on isotopologue amount fractions, a drift correction, and an offset adjustment. The offset adjustment ensures the data are on the same scale as other international laboratories, meaning that the data can be employed in regional isotope ratio modelling studies (Umezawa et al., 2018). The chapter also presents some isotope ratio data measured by Boreas while it was sampling air from the roof of NPL in spring 2021. This is to demonstrate the instruments capability to distinguish between biogenic, thermogenic and pyrogenic sources of CH_4.

1.2.4 Chapter 4 - Potential Improved Monitoring of δ^{13}C and δD Methane Through Deployment of Continuous Monitoring Systems

This chapter considers where to deploy a continuous monitoring instrument around the world, in order to effectively capture variations in CH_4 amount fractions and isotope ratios. To achieve this, *a posteriori* regional δ^{13}C source signatures from Chapter 2 are employed, as well as simulated δD values using the same modelling methodology as in Chapter 2. These data are compared with typical precision from a continuous monitoring instrument (using Boreas as a basis) to establish what percentage of daily and monthly scale variations in CH_4 and its isotope ratios it would be able to measure. The chapter therefore considers the detectability of atmospheric isotope ratio signals at the current locations of isotope ratio measurement sites. Potential new site locations are also examined, as is the sensitivity of different locations to changing background source signatures and sinks. Potential site locations are also considered qualitatively, in terms of ease of access for scientists and equipment. The result is a series of recommended locations for continuous monitoring instrument deployment. This chapter is unique in that it considers a new measurement site and the establishment of a new measurement system. It also constitutes performing detectability analysis over a longer time period and greater geographical area than has previously been assessed (Rigby et al., 2012; Thonat et al., 2019).

1.2.5 Chapter 5 - Conclusions and Future Work

This final chapter summarises the work completed in this thesis, for each individual chapter. It considers the success of each of the individual studies in the context of the research aims as outlined in Chapter 1. It also details possible future projects, relevant to this thesis, which would continue to expand knowledge in this topic for future studies.

1.3 Methane Problem

A 'Greenhouse Gas' refers to an atmospheric gas which captures outgoing longwave radiation in the atmosphere. These occur naturally in the atmosphere, however, increased anthropogenic activity (including fossil fuel extraction and use, increased agriculture and waste emissions from a growing population) has caused increasing levels of these gases, resulting in increased global temperature. CH_4 is the second most abundant greenhouse gas with significant anthropogenic origin, after CO_2, and as mentioned has a GWP_{100} value of 28. These GWP values represent the amount of energy one ton of a gas would capture over a given time period, relative to one ton of CO_2 over the same time period. This makes it easy to compare between different the relative impacts of various GHGs, considering both their ability to absorb energy and their atmospheric lifetime. CH_4 is therefore 28 $\times$ more powerful than CO_2 at capturing heat on a gram/gram basis over 100 years.

The amount fraction burden of CH_4 has more than doubled since the industrial revolution, increasing by 156% from 722 ppb to 1850 ppb between the years 1750 to 2021 (IPCC, 2021). This trend is due to increased anthropogenic activity since the industrial revolution, leading to changing population levels and agricultural practices. With these trends continuing, CH_4 poses a real and significant threat to climate change. CH_4 has become a focus of climate change mitigation policy in recent years (United Nations Environment Programme and Climate and Clean Air Coalition, 2021). It has an atmospheric lifetime of approximately 10 years, as opposed to up to several hundreds of years for CO_2. This means that CH_4 is a useful gas to focus on for limiting climate change effects, as reduction attempts will be realised on a shorter timescale.

The growth rate of atmospheric CH_4 has not been consistent over the past 30 years. Between 1999 and 2007, the global growth rate of CH_4 flattened off almost entirely (Figure 1.1). This was followed by an uptick post-2007 (Lan et al., 2021, IPCC, 2021). We still do not fully understand the driving forces behind these events: understanding the drivers behind growth rate changes can inform emissions reduction strategies.

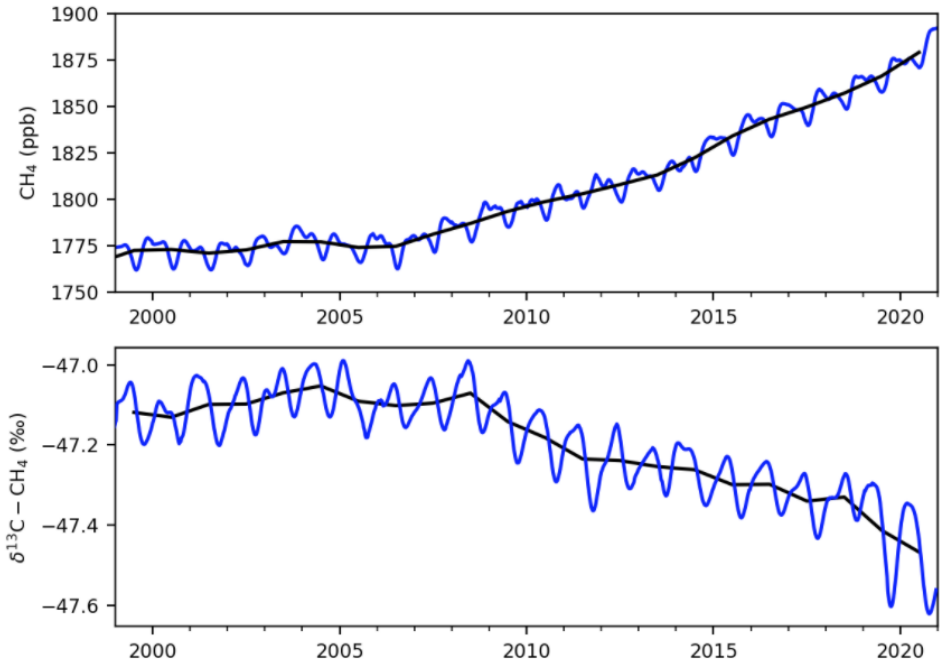

Figure 1.1: Global monthly mean CH_4 amount fraction (ppb) and $\delta^{13}C$ signature (‰) as published by NOAA-ESRL. The blue lines are globally-averaged weekly data, the black lines are annual means. (Lan et al., 2021)

1.4 Methane Sources

Sources of CH_4 are both natural and anthropogenic in origin. The magnitudes of various sources are listed in Table 1.1. Natural sources of CH_4 include wetlands, wild ruminants, geological seepage, termites, oceans and wildfires. Wetlands are the greatest natural source (Saunois et al., 2020); methanogenic micro-organisms that live in the soil and plants within wetlands produce CH_4 under anaerobic conditions. Wetland emissions depend on temperature, carbon availability and water table height; therefore, different forms of wetland environment produce different amounts of CH_4 (Ganesan et al., 2018). In wild animals, fermentation takes place in the stomachs of ruminants, as food is digested (Crutzen et al., 1986). Likewise for termites; CH_4 is produced in their digestive tracts (Fung et al., 1991). Geological seepage occurs mostly from hydrocarbons degassing, along with a small amount of abiotic production (such as CO_2 hydrogenation) (Etiope et al., 2019). Ocean sources are mainly from gas hydrates in near-shore settings. Wildfires contribute from incomplete combustion occurring in low-oxygen environments; this source is responsible for 10% of all CH_4 emissions (Crutzen & Andreae, 1990; Crutzen et al., 1979; Seiler & Crutzen, 1980). This source can be considered both natural and anthropogenic due to biomass burning being used a technique in agriculture, for fast crop production for clearing field space.

Anthropogenic sources are estimated to comprise 60% of all CH_4 emissions (Saunois et al., 2020). Major anthropogenic sources are fossil fuel emissions from oil, gas and coal. The emissions are produced along the processing and transportation stages of fossil fuel production. Leaks from oil and gas pipes are important for this source, and have been suggested as a sensible approach for reducing emissions, as an easy target. Waste management (both from household waste and manure) is another anthropogenic emission type; microbes breaking down organic waste emit CH_4 (Saunois et al., 2020). Agriculture is another large emission source of CH_4; these are produced from ruminant stomachs and from rice fields. The diet the animals are fed has an impact upon the amount of CH_4 produced (certain foods can inhibit methanogens in cattle's stomachs), and therefore may present a sensible emissions reduction approach (Archimède et al., 2011; Crutzen et al., 1986; Moss et al., 2000).

1.5 Methane Sinks

The major sink of CH_4 in the troposphere is oxidation with the OH molecule to form formaldehyde (CH_2O). This pathway comprises approximately 80% of CH_4 sinks (Badr et al., 1992; Kirschke et al., 2013). The chemical pathway of this reaction is shown in Equations 1.1 to 1.7.

$$\mathrm{CH_4 + OH \rightarrow CH_3 + H_2O}, \tag{1.1}$$

$$\mathrm{CH_3 + O_2 \rightarrow CH_3O_2}. \tag{1.2}$$

Table 1.1: Magnitudes of different CH_4 source types and stable isotope ratios that correspond to them (Sherwood et al., 2017, 2021). Magnitudes are from bottom-up inventories (detailed in Saunois et al., 2020), with uncertainties as max-min values in square brackets.

Source Type	Annual Mean Emission 2008–2017 (Tg/CH_4)	Isotope Ratio δ^{13}C	Isotope Ratio δD
Gas and Oil	80 [68-92]	-44.0 [±10.7]	-194 [±47]
Coal	42 [29-61]	-49.5 [±11.2]	-232 [±52]
Livestock	111 [106-116]	-65.4 [± 6.7]	-316 [±29]
Waste	65 [60-69]	-56.0 [± 7.6]	-298 [±11]
Biomass Burning	17 [14-26]	-26.2 [± 4.8]	211 [±15]
Termites	9 [3-15]	-63.4 [± 6.4]	-343 [± n/a]
Wetlands	149 [102-182]	-61.5 [± 5.4] (Tropical) -71.5 [± 5.4] (Arctic)	-322 [±42]
Rice	30 [25-38]	-62.2 [± 3.9]	-323 [±16]

The next step then depends on the abundance of nitrogen oxides (NO_x) present in the environment. If sufficient amounts of NO are present, the oxidation follows the following pathway (Badr et al., 1992):

$$\mathrm{CH_3O_2 + NO \rightarrow NO_2 + CH_3O}, \tag{1.3}$$

$$\mathrm{CH_3O + O_2 \rightarrow CH_2O + HO_2}, \tag{1.4}$$

$$\mathrm{HO_2 + O_2 \rightarrow OH + NO_2}. \tag{1.5}$$

However, if low amount fractions of NO are present, the pathway will be as follows:

$$\mathrm{CH_3O_2 + HO_2 \rightarrow CH_3O_2H + O_2}, \tag{1.6}$$

$$\mathrm{CH_3O_2H + OH \rightarrow CH_2O + H_2O + OH}. \tag{1.7}$$

A smaller sink (less than 5% of the sink overall, (Badr et al., 1992; Kirschke et al., 2013)) is the reaction with chlorine in the troposphere, which takes place in the marine boundary layer (Equation 1.8):

$$\mathrm{CH_4 + Cl \rightarrow HCl + CH_3}. \tag{1.8}$$

Other important (yet less significant, in terms of magnitude) are the stratospheric reaction with $O(^1D)$ and Cl (approximately 10% of all sinks), and uptake by bacteria in soil (approximately 5% of total sink) at the surface, especially under somewhat dry conditions (Badr et al., 1992; Keller et al., 1983).

1.6 Isotope Ratio Measurements

1.6.1 Sources

Isotope ratios may provide an insight into the driving forces behind CH_4 emissions variation. For CH_4, the most common isotopologues are $^{12}CH_4$ (98.80%), $^{13}CH_4$ (1.11%) and CH_3D (0.062%) (Table 1.2).

Table 1.2: Masses and abundances of all stable CH_4 isotopologues, following Stolper et al. (2014).

Isotopologue	Relative Abundance	Mass (amu)
$^{12}CH_4$	0.988	16.031
$^{13}CH_4$	1.11×10^{-2}	17.035
$^{12}CH_3D$	6.16×10^{-4}	17.038
$^{13}CH_3D$	6.92×10^{-6}	18.041
$^{12}CH_2D_2$	1.44×10^{-7}	18.044
$^{13}CH_2D_2$	1.62×10^{-9}	19.047
$^{12}CHD_3$	1.49×10^{-11}	19.05
$^{13}CHD_3$	1.68×10^{-13}	20.053
$^{12}CD_4$	5.82×10^{-16}	20.056
$^{13}CD_4$	6.54×10^{-18}	21.06

Different isotopes of both carbon and hydrogen behave differently in response to atmospheric chemical reactions (Bréas et al., 2001). The heavier isotopes react more slowly than the lighter, as heavier isotopes form stronger chemical bonds, therefore more energy is needed to break the bonds and create a reaction. This leads to a greater abundance of heavy isotopes in the product of more energetic reaction sequences, such as the formation of CH_4 in fossil fuel reservoirs (Bréas et al., 2001; Douglas et al., 2017; Sherwood et al., 2017). Conversely, lower-energy formation settings (such as biogenic settings) lead to lower abundance of heavy isotopes, due to the reaction of the lighter isotope being energetically easier in the reaction pathway. As such, isotope ratio measurements can distinguish between biogenic and pyrogenic emissions, and even the nature of a particular source, such as different forms of coal mines (Zazzeri et al., 2016) and different forms of wetland (Ganesan et al., 2018). The difference in signatures for wetlands arises from different mechanisms for which CH_4 is produced. In polar settings, wetlands are from bogs and fens, whereas in tropical settings wetlands are dominated by marshes. The difference in water table height and vegetation type

in these settings results in different signatures, as the CH_4 is slowly fractionated as it moves towards the water surface (Ganesan et al., 2018). The vegetation type also has an impact upon the isotopic composition; C4 vegetation produces relatively more ^{13}C than C3 vegetation (Archimède et al., 2011). This has a subsequent impact upon the isotope ratio signature of ruminant and biomass burning signatures, depending on the vegetation type consumed or burnt.

These isotope abundances are typically described in ratio form, with the abundance of the least common isotope being compared with the more common isotope in the sample:

$$\delta = (\frac{R_{sample}}{R_{ref}} - 1), \tag{1.9}$$

where R_{sample} is the ratio of the rare isotope to the most abundant isotope in the sample, and R_{ref} is the isotope ratio for a given standard (for carbon, this is the Vienna Pee Dee Belemnite). The greater abundance of heavy isotopes from thermogenic emissions results in a higher value of δ (typically -40 to -50‰ for $\delta^{13}C$ or -150 to -250 for δD), whereas biogenic emissions are generally less enriched in heavy isotopes (due to lower energy formation setting) and so will display lower δ values (typically -60 to -70‰ for $\delta^{13}C$ or -280 to -360 δD, Sherwood et al., 2017).

Isotope measurements are presented in ratio space because ratios are calculated more precisely than the abundance of individual isotopologues, due to extreme low abundances of rare isotopologues. Furthermore, parameters such as sectoral source signatures and sink variations are understood more accurately for ratios rather than absolute reaction rates for different isotopologues, due to the convention of recording values in δ space (as originally established by Urey (1948) and McKinney et al. (1950)). For the stable isotopes of CH_4, δ values are $\delta^{13}C$ (representing the relative abundance of carbon-13 compared with carbon-12) and δD (representing the relative abundance of deuterium compared with hydrogen).

Therefore, by measuring isotope ratios, we can determine the source of the CH_4 in a given sample (Bréas et al., 2001). Expanding this to a global perspective can indicate how sources of CH_4 are changing over time by measuring changing global CH_4 δ values, indicating how the balance of various sources has shifted over time. Alongside the increasing amount fractions of CH_4, there has been recorded an ongoing decrease of mean global $\delta^{13}C$ since 2007 (Figure 1.1; Michel et al., 2021), which will be examined in this work.

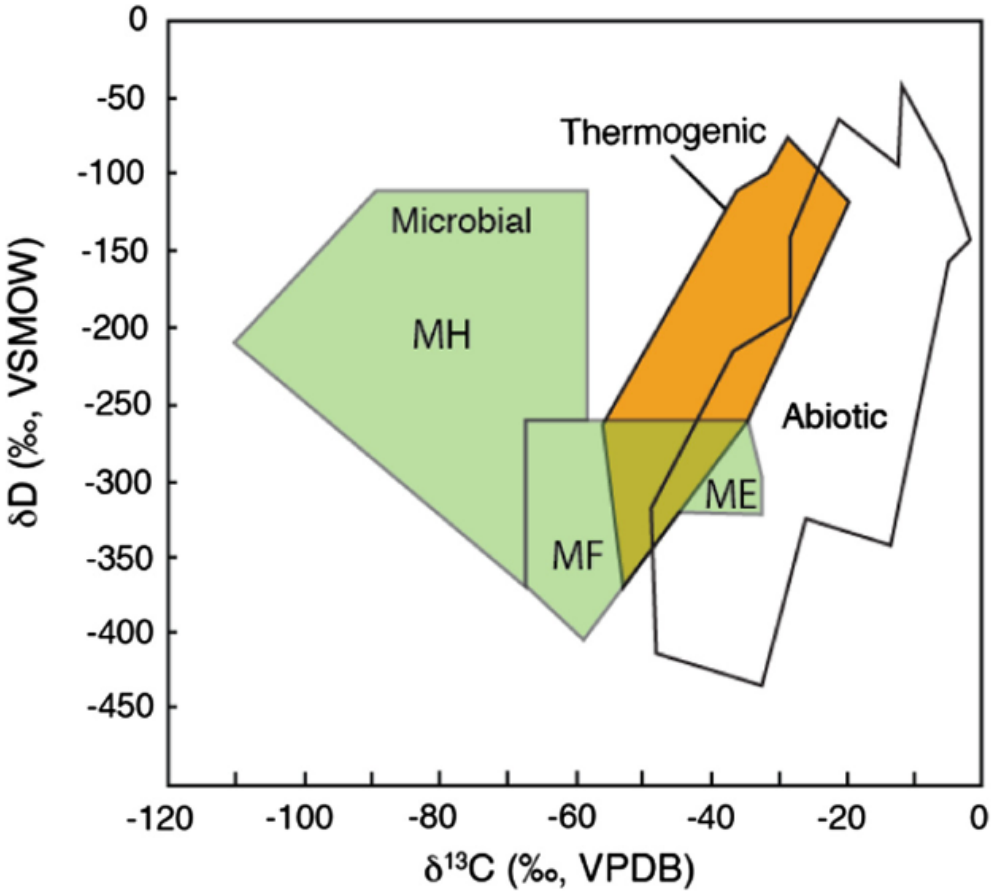

Figure 1.2: Indicating typical sectoral source signatures for δ^{13}C and δD (‰), from Douglas et al. (2017). MH – microbial hydrogenotrophic; MF – microbial fermentation; ME – microbial evaporitic environment. Hydrogenotrophic and fermentation pathways depend upon the nature of the environment (hydrogenotrophic is more common in rain-fuelled bogs, for example), wheras evaporitic seetings indicates CH_4 trapped in seafloor sediments. Abiotic CH_4 is not produced involving organic matter, such as in geological settings.

1.6.2 Sinks

Atmospheric sinks of CH_4 (such as oxidation with OH, the Cl reaction and uptake by soils) are also subject to isotopic fractionation. This is because heavy isotopes react more slowly than lighter (Laidler, 1987), with reactions requiring more energy to break apart heavier isotope bonds. Because of this, lighter isotopes are preferentially reacted away, leading to the atmosphere having a heavier isotope ratio signal (approximately -47‰ for δ^{13}C) than it would based upon source signatures alone (which would lead to a background value of -52‰, without the influence of the sink's fractionation).

Table 1.3: Kinetic Isotope Effects for different isotopologues reacting with the three main sinks of CH_4 (OH, Cl, soil) at 298K. KIE indicates relative reaction rate compared with $^{12}CH_4$; Reaction Rate is the resulting reaction rate constant, in the modelling in Chapter 2 these are applied to the OH and Cl sinks, and are dependent upon temperature (T); SF is a scaling factor applied in Chapter 2 modelling to the soil sink, at each time step (this sink is handled as a negative emission in GEOS-Chem)

Isotopologue	Sink	KIE	Reaction Rate	SF	Literature Source
$^{12}CH_4$	OH	1	$2.45 \times 10^{-12} \times e^{\frac{-1775}{T}}$	n/a	Burkholder et al. (2020)
$^{12}CH_4$	Cl	1	$9.600 \times 10^{-12} \times e^{\frac{-1360}{T}}$	n/a	Feilberg et al. (2005)
$^{12}CH_4$	soil	n/a	n/a	1	Snover and Quay (2000)
$^{13}CH_4$	OH	1.0039 $\pm$0.0015	$2.44 \times 10^{-12} \times e^{\frac{-1775}{T}}$	n/a	Burkholder et al. (2020)
$^{13}CH_4$	Cl	1.06 $\pm$0.01	$9.057 \times 10^{-12} \times e^{\frac{-1360}{T}}$	n/a	Feilberg et al. (2005)
$^{13}CH_4$	soil	n/a	n/a	1.0670 $\pm$0.001	Snover and Quay (2000)
CH_3D	OH	1.3208 $\pm$0.02	$3.5 \times 10^{-12} \times e^{\frac{-1950}{T}}$	n/a	Burkholder et al. (2020)
CH_3D	Cl	1.47 $\pm$0.03	$6.53 \times 10^{-12} \times e^{\frac{-1360}{T}}$	n/a	Feilberg et al. (2005)
CH_3D	soil	n/a	n/a	1.099 $\pm$0.03	Snover and Quay (2000)

The extent of isotopic fractionation due to sinks are designated by a Kinetic Isotope Effect (KIE):

$$\mathrm{KIE} = \frac{k_a}{k_b}, \tag{1.10}$$

where k_a is the reaction rate of the more common isotope, k_b is the reaction rate of the rarer isotope. KIE values for CH_4 are therefore represented relative to the most common isotopologue ($^{12}CH_4$). A higher KIE value of an isotopologue, the less reactive the isotoplogue is to a particular sink process, compared with $^{12}CH_4$. Table 1.3 indicates typical KIE values for CH_4 isotopologues. The KIEs for CH_3D are more significant than for $^{13}CH_4$ due to greater relative mass change for this replacement; mass increases 100% for replacing hydrogen with deuterium, but increases by 8% replacing carbon-12 with carbon-13 (Table 1.2; Laidler, 1987).

1.7 Modelling Approaches

Computer-based modelling of CH_4 is an effective and well-established method of simulating atmospheric amount fractions and isotope ratios, to represent and understand how greenhouse gases are changing. The modelling can take place on a variety of scales and framings (from box models to 3D Chemical Transport Models). This thesis concerns 3D global modelling of CH_4, $\delta^{13}C$ and δD, using an inversion approach for CH_4 and $\delta^{13}C$. Inversions are a common approach to improve understanding of CH_4 fluxes. The inversion approach takes current estimates of fluxes and real-world data combined in an atmospheric model, to produce improved estimates of emissions and isotope ratios.

Modelling of CH_4 isotope ratios has primarily taken place using box models (Rigby et al., 2017; Schaefer et al., 2016; Schwietzke et al., 2016; Turner et al., 2017). Box models are primarily used as most studies are focused on long term trends, and so are easier than three-dimensional (3D) models to produce an average of, due to the more simple representation of the atmosphere. Furthermore, they are more computationally efficient than 3D transport models (again due their relative simplicity), and so save computational power when ran over a long period of time. Box models perform well as they can include more chemistry processes due to the simpler implementation (i.e. represent more sophisticated chemistry). However, the box model representation is less comprehensive than 3D representation for simulating geographic distribution of emissions sources and transport (Naus et al., 2018). As such, for representing the same processes over the same time period, 3D models are more accurate.

The use of 3D models in simulating both CH_4 amount fractions and isotope ratios is similarly well established. For example, McNorton et al. (2018) and Fujita et al. (2020) perform inversions by using amount fraction data to calculate estimates of global scale CH_4 emissions, with isotope data as an additional constraint. Concurrent studies have used 3D models to represent CH_4 isotope ratios singularly for detailed event-source attribution (Rice et al., 2016); for exploring small-scale δ^{13}C variations (Feinberg et al., 2018) and for characterising CH_4 wetlands emissions (Ganesan et al., 2018). However, something which has not been examined is how δ^{13}C emissions signatures from geographic regions are broadly changing, the signature representing a combination of all the contributing sources in a region. This analysis indicates what source types are dominant in different regions (i.e biogenic, thermogenic or pyrogenic emissions) and how the balance of sources in a region is changing over time (whether becoming lighter or heavier; moving towards biogenic or pyrogenic emissions source). No study has solved for regional isotope emissions signatures over an extended period. This would indicate the regions and sectors that are increasing recently, indicating which are best to focus on in order to limit climate change impacts.

The events over the period 2004-2020, specifically the levelling off and later uptick of global mean CH_4 amount fractions in 2007, have been attributed to multiple pathways (Turner et al., 2019), without overall consensus. As such, there remains a need for a study to understand how sources of CH_4 have varied during and since the recorded levelling off of global CH_4 amount fractions. Chapter 2 concerns an inversion in a 3D chemical transport model (CTM), in order to understand how regional emissions of CH_4 and regional isotope ratios of δ^{13}C have changed in recent years. The approach in this chapter is unique in two ways: the extended time series solved over (simulating 17 years of CH_4 and isotope ratios) and the fact that the inversion solves for regional isotope emissions signatures, rather than using isotope data as a constraint for CH_4 emissions inversion. The *a posteriori* regional emissions and δ^{13}C source signatures from Chapter 2 are then used to simulate CH_4 and δ^{13}C for the detectability studies in Chapter 4, alongside a simulation for δD.

1.8 Ground-Based *In Situ* Measurements

The thesis will primarily focus on ground-based *in situ* measurement systems, both CH_4 amount fractions and isotope ratios. Considering the capabilities of *in situ* data informs the development and deployment of a new instrumentation (Chapters 3 and 4), and used as a constraint in modelling for an inversion on CH_4 emissions and isotope ratios (Chapter 2).

The NOAA network (Lan et al., 2021; Michel et al., 2021) measures amount fraction CH_4 (reported as nmol/mol, abbrieviated as ppb) using flask samples — discrete samples of air filled at each measurement site. They are then sent to Boulder, Colorado to be analysed by either ESRL (for amount fractions) or the Institute of Arctic and Alpine Research (CU-INSTAAR, for isotope ratios). To measure amount fractions, the NOAA network previously used gas chromatography with flame ionisation (Dlugokencky et al., 2005; Steele et al., 1987). This approach measures molecules by separating the analyte from other gases in a packed column; the CH_4 is then combusted by a hydrogen flame to ionise it, producing a current at electrodes which is measured. Since August 2019, cavity ring-down spectroscopy (the measurement of different molecules by the extent to which they absorb and scatter light at different wavelengths) has been used by the NOAA network to measure CH_4 amount fractions (Lan et al., 2021).

Due to the monetary expense, time and effort involved in producing isotope data values, there are less than 20 laboratories worldwide that currently measure isotopes regularly, be it from labs or in the field (Umezawa et al., 2018). The most common method of measuring gaseous isotope ratios is isotope ratio mass spectrometry (IRMS) (Bock et al., 2014, 2010; Brass & Röckmann, 2010; Fisher et al., 2006; Sapart et al., 2011; Schmitt et al., 2014). This technique is used by the NOAA network (performed at CU-INSTAAR) for measuring isotope ratios (Michel et al., 2021). An isotope ratio mass spectrometer ionises and accelerates the sample of interest on a track, separating the sample according to the mass/charge ratio of each ion. Heavier ions bend on a greater radius than lighter, leading to separation of different ions by mass. Specifically for CH_4 carbon isotope ratio analysis, the sample passes through a series of traps to remove water and CO_2, before the CH_4 is oxidised into CO_2 and passed into the spectrometer (Fisher et al., 2006). The NOAA network, the most widespread isotope ratio and amount fraction network, relies primarily on flask sampling on an approximately weekly scale, which may lead to amount fraction and isotope ratio variations on a finer scale being missed due to the sparseness of sampling.

Fourier transform infrared and/or laser absorption spectrometers, in which a laser is trained on a sample and the absorption response of the sample is recorded (Bergamaschi et al., 1994; Santoni et al., 2012), have proven to be able to provide high-frequency measurements with lower maintenance requirements than IRMS. However, these instruments are not able to match precision from typical IRMS methods due to poor signal-to-noise ratio caused by the low abundance of CH_4 isotopologues in ambient air (Bergamaschi et al., 1994; Miles et al.,

2018; Rella et al., 2015). For this reason, laser spectrometers are paired with preconcentrator instruments to concentrate the CH_4 in air before analysis. This approach involves passing the sample through a series of traps in order to increase the relative concentration of the analyte you are interested in (in this case an isotopologue of CH_4). The relative concentration is increased to the point at which the sample can be passed into a laser spectrometer and measured. However, contamination of samples can be introduced through preconcentration if not performed rigorously (Eyer et al., 2016). There is therefore need for a preconcentration system which is able to effectively sample sufficient amounts of ambient air in a manner which does not introduce contamination.

Chapter 3 introduces the 'Boreas' instrument, designed and developed at NPL (Rennick et al., 2021). This system uses a custom-built preconcentration system that is capable of coupling to a laser spectrometer. This instrument can obtain precision on isotope ratio values that are comparable with traditional IRMS (Bock et al., 2014, 2010; Brass & Röckmann, 2010; Fisher et al., 2006; Sapart et al., 2011; Schmitt et al., 2014), while operating continuously without intervention, making it possible to measure in remote settings and at regular time intervals.

In setting up a new system, the correct procedure for data calibration and processing has to be established. Approaches for calibrating isotope ratio values from optical instruments have been discussed in several studies (Bowling et al., 2003; Braden-Behrens et al., 2017; Esler et al., 2000; Flores et al., 2017; Griffis et al., 2005; Griffith, 2018; Griffith et al., 2012; Miles et al., 2018; Pang et al., 2016; Rella et al., 2015; Steur et al., 2021; Tans et al., 2017; Tuzson et al., 2011; Vardag et al., 2015; Wehr et al., 2013; Wen et al., 2013). Chapter 3 follows Griffith (2018) and Steur et al. (2021) in examining two methods of calibration: on individual isotopologue concentrations and on isotope ratio values. These approaches are rigorously assessed, along with approaches for drift correction and offset adjustment to align values with the scale of external laboratories. Data from the instrument is also presented, demonstrating this instrument's capability to delineate between different source types.

Furthermore, with the establishment of a new measurement system, it is important to consider where such an instrument should be located in order to obtain most useful data towards future modelling efforts; this is assessed in Chapter 4. By assessing potential instrument deployment, the work contributes to solving the problem identified in Chapter 2; that more numerous and widespread data are important to understand changing CH_4 emissions and isotope ratio signatures.

1.9 Satellite Data

Satellite data are becoming more and more frequently used in GHG measurement, as a constraint in modelling studies. Satellite data by nature provides greater worldwide coverage than ground-based *in situ* stations, providing data where ground-based measurements do not exist. Furthermore, whole-column measurements are useful for monitoring pollution plumes, as well as providing the capability of measuring multiple greenhouse gases simultaneously, by using downward facing instruments with a broad coverage in terms of wavelengths of light detected.

While it is not the main focus of this thesis, the results of an inversion using satellite data as a constraint is considered in Chapter 2. This is to quality check ground-based *in situ* inversion results. Specifically, the data employed is from the Greenhouse gases Observing SATellite (GOSAT; Parker et al., 2020). GOSAT has been running since 2009 at a height of 666 km on a sun-synchronous orbit, with a repeat time (time between two identical orbits) of three days. Satellite data has been employed in global (Fraser et al., 2014; McNorton et al., 2016) and regional studies (Lunt et al., 2021), to understand how CH_4 amount fractions are changing. Satellite data can be limited by weather conditions, such as cloud coverage, and may require 'ground-truthing' from ground-based *in situ* observations.

Overall, the thesis will establish how large-scale regional emissions and source signatures have varied in recent years; introduce a new measurement instrument and examine appropriate data processing approaches; and consider locations for instrument deployment. In doing so, the work contributes to understanding of the effect of climate change upon global greenhouse gas levels, by determining (through both modelling and metrology) the driving forces behind increasing CH_4 amount fractions worldwide.

Chapter 2

Large-Scale Regional Inversions for CH_4 emissions and δ^{13}C Signature, 2004-2020

A paper based upon the work in this chapter is in review under the title 'Atmospheric data support a multi-decadal shift in the global methane budget towards natural tropical emissions' to Atmospheric Chemistry and Physics Discussions.

2.1 Introduction

The overall aim of the thesis is to examine ground-based *in situ* CH_4 isotope ratio monitoring capability, to understand the CH_4 budget and how it is changing. Data from the current network is therefore examined for both its capability and limitations. This chapter focuses upon the first major research question from Chapter 1: How have CH_4 amount fractions and isotope ratios varied over recent a 17 year period, and what regions/sources are responsible?

As described in Chapter 1, there are gaps in our understanding of how CH_4 emissions have varied in the past 20 years. This is especially true following the observed levelling-off and subsequent uptick of CH_4 global growth rate post-2007 (as detailed in Figure 1.1), which occurred alongside the global atmospheric δ^{13}C signature becoming progressively more light. There are multiple overlapping explanations of how both emissions and sinks have varied, without overall consensus (Turner et al., 2019). This chapter aims to address these knowledge gaps, by calculating changes in large-scale regional emissions and isotope ratio source signatures (which bring source apportionment information) over the period 2004-2020.

Changes in atmospheric CH_4 over the last decades have unfolded without clear explanation, exposing inadequacies in our measurement coverage and our ability to definitively attribute those changes to individual emissions and losses. The climatic importance of atmospheric CH_4 lies in its ability to absorb and emit infrared radiation, at wavelengths that are relevant

to outgoing terrestrial radiation. Consequently, atmospheric CH_4 contributes to maintaining Earth's radiative balance and surface and atmospheric temperatures. Concentrations of atmospheric CH_4 are determined by a large range of thermogenic, pyrogenic, and biogenic emissions and losses from the hydroxyl radical (OH), reaction with chlorine, uptake from soils, and a small stratospheric loss. These are all accounted for in the modelling.

The global CH_4 growth rate was close to zero from 2000 to 2006 (Lan et al., 2021) but has since accelerated to unprecedented values in 2020 and 2021. Concurrently, we are witnessing progressively lighter CH_4 (more negative $\delta^{13}C$), indicative of a higher proportion of biogenic emissions. A growing body of work have proposed a range of hypotheses to explain short periods of observed global and regional variations in atmospheric CH_4 (Turner et al., 2019). In this study, a step back is taken to look at observed CH_4 variations from 2004 to 2020 and argue that short-term variations are part of a large-scale shift of predominately anthropogenic emissions from high northern latitudes to natural emissions from the tropics, driven by North African and Tropical South American wetlands. As the global atmospheric mass balance of CH_4 shifts further from anthropogenic to natural sources, our ability to mitigate emissions becomes more of a challenge.

The post-2007 increase in atmospheric CH_4 has been the focus of many studies and has been attributed to different plausible hypotheses associated with changes in fossil fuel, biomass burning, agriculture and wetland emissions, and the OH sink (Turner et al., 2019). These studies have reached their conclusions using *in situ* amount fraction observations alone or in combination with other observations as additional constraints, e.g. *in situ* $\delta^{13}C$ (Basu et al., 2022; Fujita et al., 2020; Lan et al., 2021; Nisbet et al., 2016; Rice et al., 2016; Schaefer et al., 2016), satellite observations (Feng et al., 2022; McNorton et al., 2018; Worden et al., 2017; Yin et al., 2021), or other trace gases, using a variety of analysis methods and computational models.

The use of ground-based data in assessing CH_4 changes is well established. For example, Kirschke et al. (2013) aggregate both top-down and bottom up approaches to examine regional CH_4 budgets, suggesting that increases in wetland and fossil fuel emissions are responsible for the uptick following 2007. They acknowledge that the relative importance of these sources remains uncertain. Saunois et al. (2016) build on this by accumulating top-down and bottom-up approaches to produce regional and global CH_4 budgets from 2000-2012. The post-2007 emissions increase is the focus of many studies; Rice et al. (2016) employ isotope ratio data from a measurement site to solve for CH_4 fluxes, finding an increase in energy emissions to be the reason for the CH_4 increase after 2007. Nisbet et al. (2016) use ground-based data to examine 2007-2013; they acknowledge that fossil fuel emissions may have grown, however tropical biogenic emissions were the dominant driving force post-2007 by comparing ground-based $\delta^{13}C$ data from multiple measurement campaigns. McNorton et al. (2018) use ground-based data in a 3D inversion from 2003-2015, with $\delta^{13}C$ as an

additional constraint, and found that a decrease in OH along with increases from both energy and wetland emissions, explained the CH_4 increase post-2007. Similarly, Fujita et al. (2020) use ground-based CH_4 and $\delta^{13}C$ data in 3D inversions from 1995-2006, to solve for regional CH_4 fluxes, and use the inverse simulation for forward runs of global isotope ratio values. They found an increase in biogenic emissions and a decrease in biomass burning in the tropics to be responsible for the observed uptick of global CH_4 amount fraction and lighter trend of global $\delta^{13}C$ signature from 2007. The work in this chapter builds upon these previous studies by solving over a longer time period (2004-2020) and in the way that $\delta^{13}C$ data are used; rather than being used as a constraint (e.g. McNorton et al., 2018; Warwick et al., 2016; Yin et al., 2021) or solving for sectoral signatures (e.g. Lan et al., 2021), the inversion here solves for regional emissions signatures.

Satellite data has been frequently employed in CH_4 modelling; at a global scale (e.g. Fraser et al., 2014); to discern the impact of specific regions upon the global CH_4 budget (e.g. Lunt et al., 2021) and to validate inversion results (McNorton et al., 2018). Satellite data by nature provides greater worldwide coverage than ground-based stations, providing data where ground-based measurements do not exist. Furthermore, whole-column measurements are useful for monitoring pollution plumes, as well as providing the capability of measuring multiple greenhouse gases simultaneously. However, satellite data are limited by being reliant on weather (for example, cloud coverage leads to data being lost), and may have less frequent measurements than ground-based data depending on orbital period. Ground-based data can be employed alongside satellite data; for example Yin et al. (2021) solve for CH_4 emissions 2010-2017 using satellite data with ground-based as an extra constraint, finding that increases are centred upon the tropics and eastern Asia.

Changes in the OH sink have been suggested to play some role in recent changes in atmospheric CH_4 (Rigby et al., 2017; Turner et al., 2017) but they are probably not a dominant factor in the budget. However, Lan et al. (2021) simulated CH_4 and $\delta^{13}C$ in a 3D CTM from 1984-2016, and found that a proposed decreasing trend in OH (Turner et al., 2017) does not align with the increasingly light trend in $\delta^{13}C$ observed in the atmospheric record. In this analysis, the impact of trend in reducing OH upon CH_4 emissions is examined in a sensitivity study. The first COVID-19 lockdown in 2020 corresponded to an unexpected large increase in atmospheric CH_4. Studies have suggested this could be partly explained by a 3–5% reduction in global OH (Laughner et al., 2021; Miyazaki et al., 2021) resulting from a large-scale reduced emissions of nitrogen oxides associated with industry. This has yet to be corroborated by satellite data that provide complementary constraints on the key emitting regions over the tropics (Feng et al., 2022), or by $\delta^{13}C$ data.

Both ground-based *in situ* amount fraction CH_4 and $\delta^{13}C$ data are used as constraints to perform an inversion for regional CH_4 emissions and emissions source signatures. In this chapter 'ground-based *in situ*' refers to data collected at measurement sites and measured separately (flask sampling data). Although the thesis as a whole covers both major stable isotope ratios of CH_4 (specifically $\delta^{13}C$ and δD), this chapter only considers $\delta^{13}C$ as a constraint in the inversion. This is because of a paucity of data available for δD, which is measured much less frequently and less widely than $\delta^{13}C$.

Alongside the work of this chapter in performing inversions using ground-based *in situ*/flask data, results are presented from an inversion for CH_4 emissions performed using satellite data as a constraint. This inversion was performed by a co-author on the published work, and is presented within this thesis to demonstrate the full effect that was intended from the paper in which this research is published. The approach and results of this inversion are detailed alongside the ground-based *in situ* inversion results.

In the next section, data and methods are described, including the NOAA and NIES ground-based data, the GOSAT satellite data, the GEOS-Chem global 3-D atmospheric chemistry transport model, and the employed inversion methods. Results are reported in section 3 and the work is concluded in section 4.

2.2 Data and Methods

2.2.1 *In Situ* and Satellite Remote Measurements of Atmospheric Methane

Ground-based *in situ* flask data are used as constraints on both total CH_4 emissions and $\delta^{13}C$ regional emissions signatures. These data are taken from 31 National Oceanic and Atmospheric Administration -Earth System Research Laboratories (NOAA-ESRL) sites around the world (Figure 2.1), version 2020-07 (Dlugokencky et al., 2020). The data are monthly mean values, averaged from discrete data as collected at each site, analysed at NOAA-ESRL in Boulder, Colorado, and recorded to the NOAA 2004A standard scale (Dlugokencky et al., 2005). Up to August 2019, the analysis was performed using gas chromatography (Steele et al., 1987, Dlugokencky et al., 2005, 1994) and since August 2019, cavity ringdown spectroscopy has been used (Dlugokencky et al., 2020). Also included is data from a site in Siberia, Karasevoe (KRS), which is monitored by the National Institute for Environment Studies (NIES). This site was included to maximise geographical coverage of *in situ* data. The CH_4 measurements from this site are continuous, measuring from 65 m height, covering the period 2004-2020 (Sasakawa et al., 2010). A scale factor of 0.997 is applied to the NIES data in order to align it with the NOAA 2004A scale (Zhou et al., 2009). The site constitutes part of the Japan-Russia Siberia Tall Tower Inland Observation Network (JR-STATION).

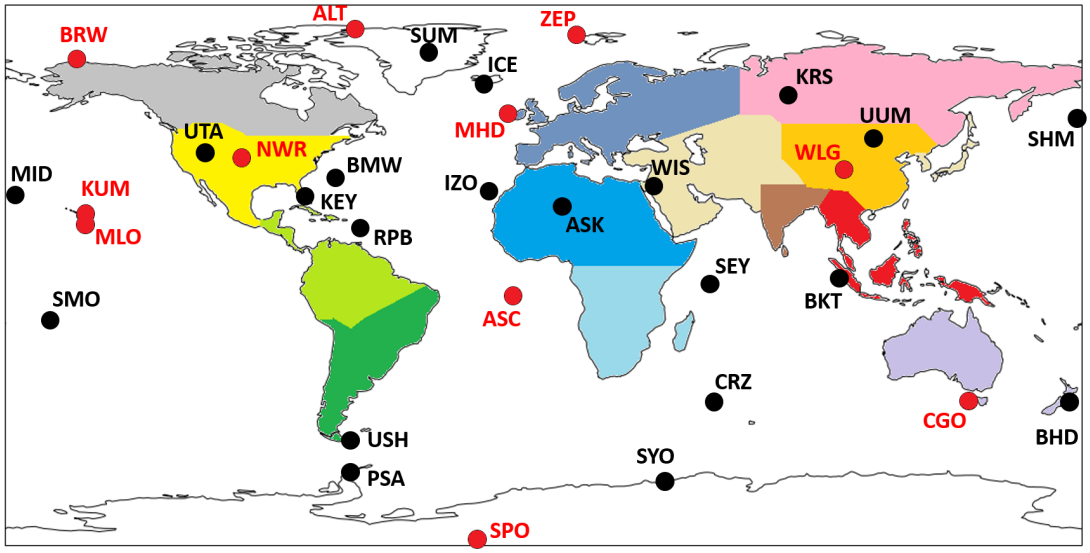

Figure 2.1: Map showing regions that are optimised in the CH_4 and $\delta^{13}C$ inversions, in different colours. Black dots and labels show the location of ground-based *in situ* measuring sites that measure CH_4 amount fraction. Red dots and labels indicate both total CH_4 and $\delta^{13}C$ measuring sites. Regions are named as follows: Grey -North American Boreal; Yellow -North American Temperate; Light Green -South American Tropical; Dark Green -South American Temperate; Purple -Europe; Blue -North Africa; Light Blue -Southern Africa; Pink -Boreal Eurasia; Orange -China; Brown -India; Peach -Temperate Eurasia; Red -Tropical SE Asia; Lilac -Oceania; White -Oceans. Site identifiers are detailed in Table A1.

$\delta^{13}C$ data are likewise monthly average values, calculated from discrete flask samples at NOAA network sites. Isotopic analysis of $\delta^{13}C$ was performed at the University of Colorado Institute of Arctic and Alpine Research Stable Isotope Laboratory (CU-INSTAAR). They follow an isotope ratio mass spectrometry approach (Miller, 2002; Vaughn et al., 2004). The geographical locations of ground-based *in situ* data used are shown in Figure 2.1 and represent a subset of those used to collect total CH_4 (10 of 32). The sites included in the inversion, both for CH_4 and $\delta^{13}C$ are those that cover the entire period of the inversion (2004–2020) without significant period of measurement breaks so as to ensure a consistent interpretation of trends without consideration of possible biases introduced through the inclusion or exclusion of specific sites.

Also estimated are CH_4 fluxes for 2010–2020 from the Japanese Greenhouse gases Observing SATellite (GOSAT) that was launched in 2009. GOSAT is in a sun-synchronous orbit with an equatorial overpass time of 13:30. Since launch, continuous global observations of dry-air atmospheric column-averaged CO_2 (XCO_2) and CH_4 (XCH_4) have been recorded, retrieved from shortwave infrared wavelengths that are most sensitive to changes in CH_4 and CO_2 in the lower troposphere (Parker et al., 2020). The latest (v9) proxy XCH_4:XCO_2

retrievals that use spectral absorption features around the wavelength of 1.6 μm (Palmer et al., 2021; Parker et al., 2020), are used as a constraint. Because of the smaller bias and better global coverage than those provided by the full physics retrievals, the precision of single proxy retrieval is about 0.72%, with a global bias of 0.2% (Parker et al., 2015, 2011, 2020).

In the calculations, a higher observation uncertainty of 1.2% is assumed for the satellite observations, and a globally uniform bias of 0.3% is deducted to obtain better *a posteriori* agreement with the independent ground-based XCH_4 data by the Total Carbon Column Observing Network (TCCON). To anchor the constraints from the proxy XCH_4:XCO_2 ratio (Fraser et al., 2014), GLOBALVIEW CH_4 and CO_2 data (Schuldt et al., 2021) is also assimilated. The GLOBALVIEW data has assumed uncertainties of 0.5 ppm and 8 ppb for *in situ* measurements of CO_2 and CH_4, respectively. Locations of the assimilated GLOBALVIEW CH_4 data (sub-)set are shown in Feng et al. (2022).

2.2.2 GEOS-Chem Atmospheric Chemistry and Transport Model

To relate CH_4 emissions to atmospheric CH_4 concentrations, v12.1 of the GEOS-Chem 3-D global transport model (Bey et al., 2001) is used at a horizontal resolution of 2° (latitude) by 2.5° (longitude) with 47 vertical levels from the surface to 80 km height, driven by the MERRA-2 meteorological reanalyses (Gelaro et al., 2017) from the NASA Global Modeling and Assimilation Office (GMAO). The specific model setup is the GEOS-Chem tagged CH_4 model, meaning that the emissions types are treated separately in the model and can be extracted individually.

A priori emissions include: 1) monthly EDGAR v4.3.2 anthropogenic emissions (Janssens-Maenhout et al., 2019) that accounts for emissions from oil and gas, coal, livestock, landfills, wastewater, rice, and other anthropogenic sources; 2) monthly GFED-4 biomass burning emissions (version 4.1; Randerson et al., 2017); and 3) monthly v1.0 WetCHARTs wetland emissions (Bloom et al., 2017). The Harvard-NASA Emissions Component (HEMCO) software within GEOS-Chem converts the emission inventories at their native horizontal resolution to the GEOS-Chem $2^\circ \times 2.5^\circ$ resolution. The HEMCO configuration file handles sectoral emissions separately, with the possibility to apply scale factors to different emissions types. The emissions magnitudes that are produced by these *a priori* inventories are indicated by Figure 2.2. The emissions are repeated yearly after their final available year (i.e. EDGAR repeats yearly post-2012, WetCHARTs and GFED-4 repeat after 2014).

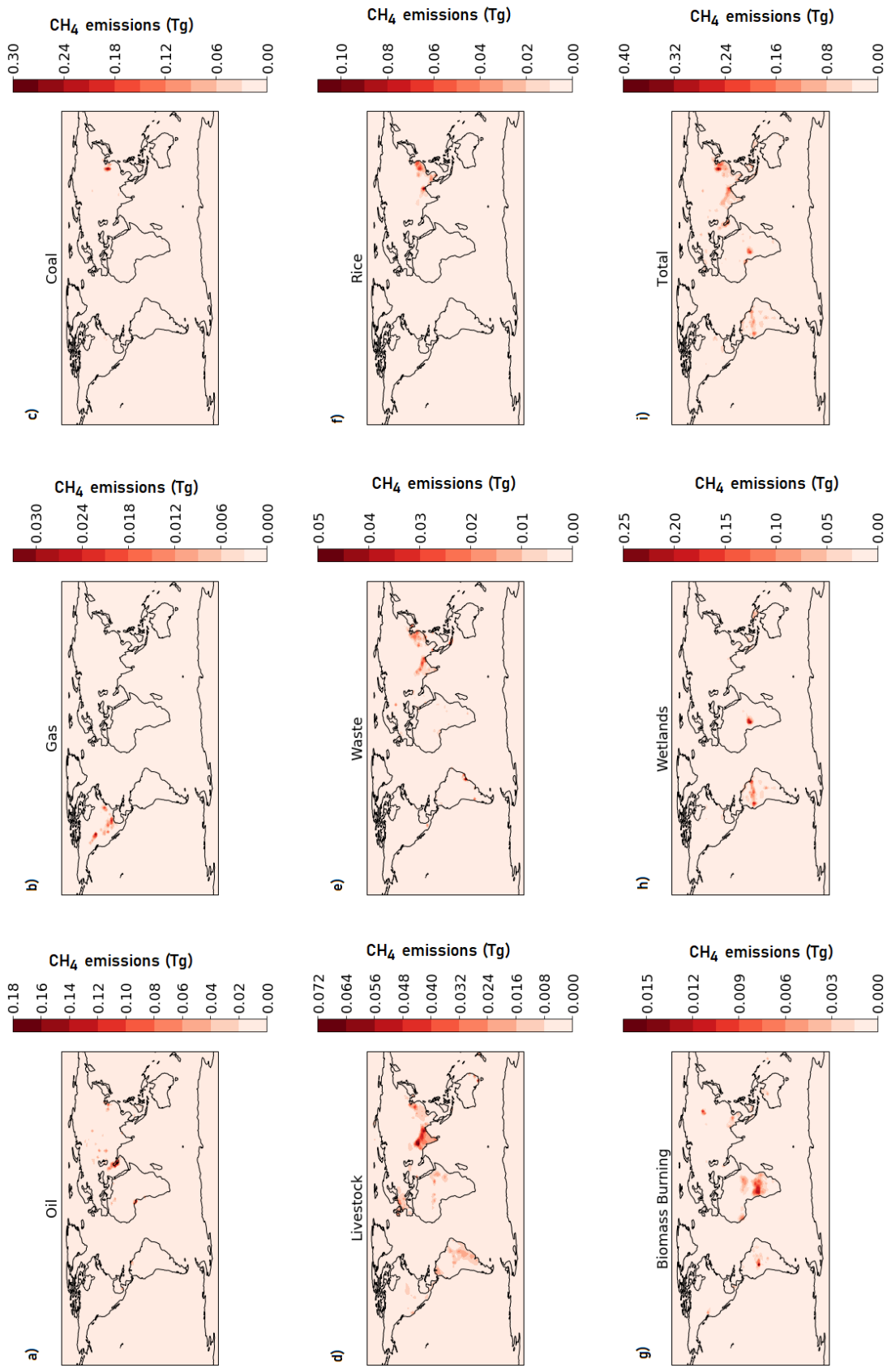

Figure 2.2: Maps of *a priori* sectoral CH_4 emissions (Tg/yr), broken down into major sectors, with source type indicated by subplot title. The emissions inventories used to obtain these emissions are listed in Table 2.1. The shown values are averaged for monthly emissions over the time period 2004-2020.

Table 2.1: Overview of emissions data sets used in the GEOS-Chem CH_4 and $\delta^{13}C$ simulations.

Emissions Type	Data Set
Anthropogenic (Oil and Gas, Coal, Livestock, Waste)	EDGAR v4.3.2 Janssens-Maenhout et al. (2019)
Termites	Fung et al. (1991)
Biomass Burning	GFED-4 Randerson et al. (2017)
Wetlands, Rice	WetCHARTs Bloom et al. (2017)

Table 1.1 shows the $\delta^{13}C$ signatures for the source types included in the simulations. These are extracted as mean global values from Sherwood et al. (2017), which provides a database of global source signatures, broken down into the same sectors as in the simulations. However, individual source types show a wide range of source signatures (e.g., coal mines, as detailed by Zazzeri et al. (2016)), and this uncertainty is reflected in the assigned uncertainty given to the *a priori* source signatures in inversion (Section 2.3). The simulations attempt to differentiate, however, between Arctic and tropical wetlands by applying a 10‰ lighter signature to the Arctic source (Table 1.1), following Ganesan et al. (2018), who produced a global wetland source signature map based upon published $\delta^{13}C$ data from Keeling plots.

Sinks included are the loss of atmospheric CH_4 from reaction with chlorine, soil uptake, and from oxidation by OH. To simulate sinks, monthly 3-D fields of OH, calculated using the full-chemistry version of GEOS-Chem, and monthly 3-D field of atomic chlorine (Sherwen et al., 2016) are part of the model setup. Stratospheric loss frequency fields are determined using the NASA GMI stratospheric model (Duncan et al., 2007). Estimates of the biogenic consumption of CH_4 in soils is determined from Fung et al. (1991). The resulting atmospheric lifetime in the model of CH_4 against OH is 9.73 years, consistent with the modelled methyl chloroform lifetime of 5.39 years. This compares well with multi-model simulations such as Voulgarakis et al. (2013) and Morgenstern et al. (2017), who listed the global mean lifetime of CH_4 as 9.6 ± 1.8 years and 7.2-10.1 years, respectively. The atmospheric lifetime of methyl chloroform has been calculated to be 6 $\pm$ 1.5 years (Khalil & Rasmussen, 1984); the modelled lifetimes compares well. In the default model configuration, none of these loss processes include interannual variations.

For the isotope simulations, published relative kinetic isotope effect values (KIEs; Table 1.3) are applied to the reaction rates for the reaction with OH and Cl used in the GEOS-Chem model output. These reaction rates are used to calculate loss of CH_4 at each model time step, using the 3D sink fields and the current state of the atmosphere. The soil sink is handled differently from OH and Cl, as a negative emission in the model. In this case, the KIE is directly applied as a scale factor in the HEMCO configuration file (Gierczak et al., 1997; Snover & Quay, 2000; Whitehill et al., 2017).

The regions that have emissions and δ^{13}C emissions signature solved for are shown in Figure 2.1. These regions are based upon those constructed for the Atmospheric Tracer Transport Model Intercomparison Project (TransCom) experiments (Gurney et al., 2002), which compared CO_2 inversion results from multiple atmospheric models using the same data, to examine model performance. The regions were based primarily upon separating different biomes, and are large-scale, meaning that subtleties within these large scale regions (that are not already built into the prior) may be missed.

For all of the calculations, GEOS-Chem is sampled at the nearest location and local time that corresponds to the ground-based *in situ* and satellite remote sensing data. For the satellite data, scene-dependent averaging kernels are applied. This approach allows us to directly compare the model with the data.

2.2.3 Isotopologue Emissions

In simulating δ^{13}C, isotopologues $^{13}CH_4$ and $^{12}CH_4$ are simulated separately in GEOS-Chem. To calculate the specific sectoral isotopologue emissions, Equation 1.9 is rearranged to find the ratio of rare to most common isotope (^{13}C/^{12}C), using typical δ^{13}C values from Sherwood et al. (2017).

The isotope ^{13}C considered relative to all isotopes in the sample (designated thereafter as $13x$), is calculated by:

$$13x = \frac{^{13}\mathrm{C}}{^{12}\mathrm{C} + ^{13}\mathrm{C}} = \frac{^{13}\mathrm{C}/^{12}\mathrm{C}}{1 + (^{13}\mathrm{C}/^{12}\mathrm{C})}. \tag{2.1}$$

This is the proportional molar abundance of the isotopologue $^{13}CH_4$. This value has to be adjusted before being applied in GEOS-Chem, to account for the fact that the calculated ratio is in moles and the emissions inventories (Table 2.1) are in kg:

$$SF13 = 13x \times \frac{M13}{Mtot}, \tag{2.2}$$

where $SF13$ is the scale factor applied to each emissions type for the $^{13}CH_4$ simulation, $M13$ is the molecular weight of $^{13}CH_4$ (17.035 g/mol; Stolper et al., 2014) and $Mtot$ is the molecular weight of CH_4 (16.04 g/mol; Stolper et al., 2014).

For the $^{12}CH_4$ counterpart to $^{13}CH_4$, a similar approach is applied. The ratio of ^{12}C compared with all isotopes in the sample (designated as $12x$) is:

$$12x = \frac{^{12}\mathrm{C}}{^{13}\mathrm{C} + ^{12}\mathrm{C}}. \tag{2.3}$$

This has to similarly be adjusted from molar to mass ratio; $SF12$ is the scale factor for each emissions type in the $^{12}CH_4$ simulations:

$$SF12 = 12x \times \frac{M12}{Mtot}, \tag{2.4}$$

where $M12$ is the molecular weight of $^{12}CH_4$ (16.03 g/mol; Stolper et al., 2014).

As $^{13}CH_4$ and $^{12}CH_4$ are the only stable carbon isotopologues of CH_4, $13x$ and $12x$ should sum to 1.

Likewise, once the simulation has been run, values of emissions of $^{12}CH_4$ and $^{13}CH_4$ have to be processed to produce the $\delta^{13}C$ emissions source signatures from each region. The $13x$ value is calculated for the emissions is calculated using Equation 2.1, assuming that $^{12}CH_4$ comprises all ^{12}C isotopologues and $^{13}CH_4$ comprises all ^{13}C isotopologues. This is then adjusted from kg to mol using Equation 2.2. The values of $^{13}C/^{12}C$ are then calculated from $13x$ (again using equation 2.1) and from this, the $\delta^{13}C$ emissions signature is determined.

2.2.4 Model Spin-Up

'Spinning-up' the model is an important aspect of setting up the forward model simulations; this initialises global mixing ratios for the different isotopologues to January 2004 amount fractions.

The model is spun up by first scaling a CH_4 restart file downloaded from GEOS-Chem online servers. An initial 1.11% relative abundance of $^{13}CH_4$ to total CH_4 is assumed as a starting point for spin up, with emissions scaled as detailed in Section 2.2.3. The model is then ran over the year 2004 60 times using the 2004 MERRA2 meteorology and and emissions, corresponding to approximately six times the chemical lifetime of CH_4. This is sufficient to allow mixing ratios to equilibrate, as demonstrated by Figure 2.3. A similar process is followed for $^{12}CH_4$, using this isotopologue's expected relative abundance and source signatures.

A single-year inversion is run for 2004 to optimise the δ^{13}C and total CH_4 values relative to NOAA observations, following inverse method detailed below, under the same uncertainties. The output of this short inversion is improved estimates of δ^{13}C and total CH_4, which serve as a starting point for the *a priori* simulation. The simulation is then ran forwards up to and through 2020 using scaled *a priori* emissions fields (as listed in Table 2.1).

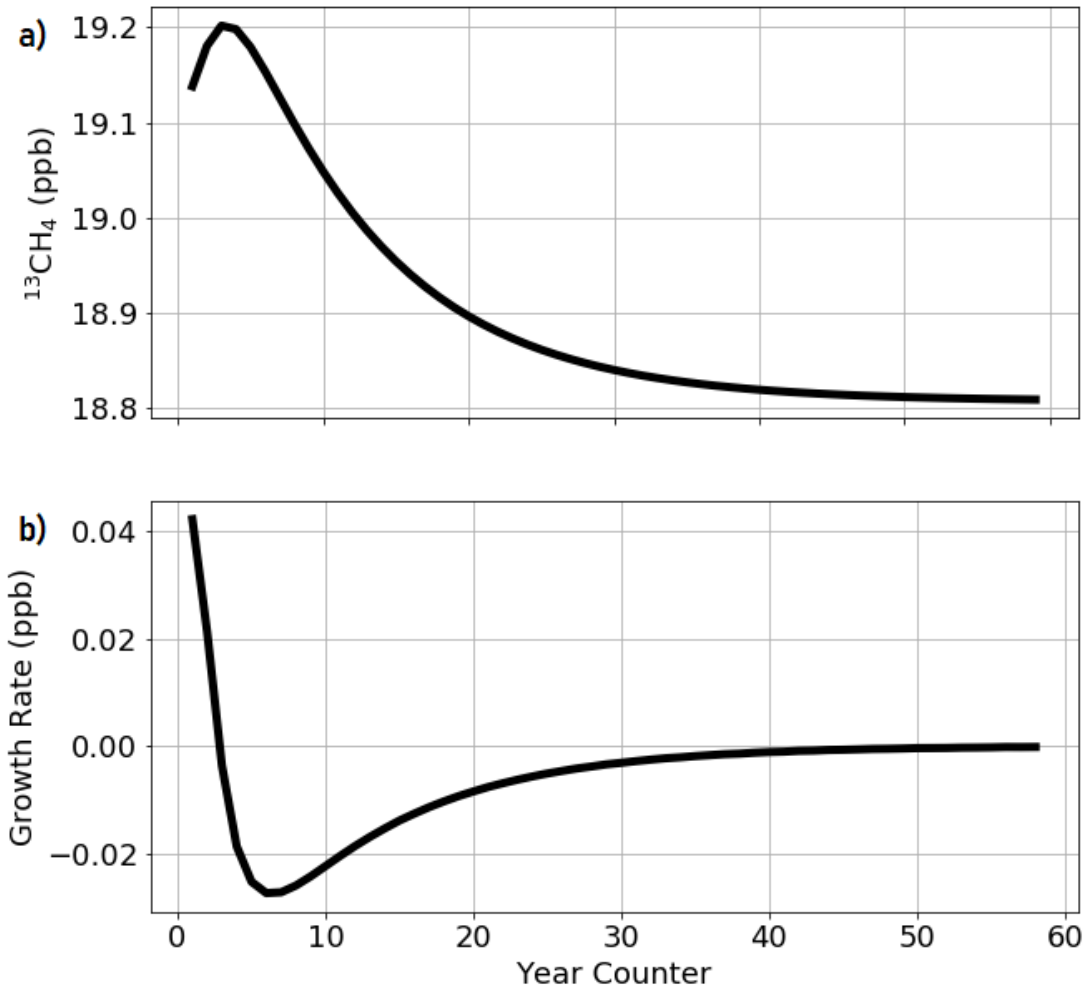

Figure 2.3: Demonstrating the spin up of the model, over a sixty year period, at the grid square in the model which corresponds with the Alert measurement site (details of the site location are in Table A1). a) $^{13}CH_4$ amount fraction value (ppb) corresponding to January of each year of spin up. b) Growth year-on-year, calculated by subtracting amount fraction one year from the previous year.

2.2.5 Inverse Methods

In performing atmospheric inversions, the aim is to improve the model's simulation of regional CH_4 fluxes and $\delta^{13}C$ emissions signatures by fitting the model to the data, considering uncertainties in the model and chosen data sets. Two separate inverse methods are used, that reflect the volume and simplicity of the data being used. For ground-based *in situ* flask data, the Maximum *A Posteriori* (MAP) inverse method is employed, and for the more voluminous satellite data an ensemble Kalman filter was used.

Maximum A Posteriori

To infer regional *a posteriori* CH_4 fluxes and $\delta^{13}C$ emissions signatures from the atmospheric measurements of CH_4, the Maximum A Posteriori solution (MAP) inverse method is employed (Rodgers, 2000). This method combines *a priori* knowledge and its uncertainty with the measurements and their uncertainties, and has been used in a number of studies (e.g. Fraser et al., 2014; McNorton et al., 2018).

The MAP solution and the associated *a posteriori* uncertainty is described as, using the conventional that lower-case and upper-case variables denote vectors and matrices, respectively:

$$\mathbf{x}^a = \mathbf{x}^b + (\mathbf{H}^T\mathbf{B}^{-1}\mathbf{H} + \mathbf{R}^{-1})^{-1}\mathbf{H}^T\mathbf{B}^{-1}(\mathbf{y} - \mathbf{H}\mathbf{x}^b), \tag{2.5}$$

$$\mathbf{A} = (\mathbf{H}^T\mathbf{B}^{-1}\mathbf{H} + \mathbf{R}^{-1})^{-1}, \tag{2.6}$$

where $\mathbf{x}$ denotes the state vector that describes the estimated quantities, which in this chapter includes monthly CH_4 fluxes and $\delta^{13}C$ signatures from regions across the world (Figure 2.1). Subscripts a and b denote *a posteriori* and *a priori* fluxes, respectively, and superscripts -1 and T denote matrix inverse and transpose operations, respectively.

The measurement vector $\mathbf{y}$ includes either NOAA/NIES amount fraction data or the $\delta^{13}C$ data.

The matrices $\mathbf{B}$, $\mathbf{A}$, and $\mathbf{R}$ denote the error covariances matrices for the *a priori*, *a posteriori*, and measurements, respectively. $\mathbf{B}$ and $\mathbf{R}$ are diagonal matrices. For $\mathbf{B}$ assumed uncertainties of 50% of the regional CH_4 fluxes and 20‰ for the $\delta^{13}C$ values are applied, and for $\mathbf{R}$ an assumed 10 ppb uncertainty for the amount fraction data and 0.1‰ for the isotope data are applied. An assumed model transport error of 2 ppb is also taken into account.

The Jacobian matrix $\mathbf{H}$ describes the sensitivity of the measurements to changes in the state vector, i.e. $\partial\mathbf{y}/\partial\mathbf{x}$. For the total CH_4 inversion, the Jacobian matrix describes the sensitivity of mixing ratios in the model to changes in regional CH_4 emissions. The matrix is constructed using a series of GEOS-Chem model runs. Systematically, each individual emitting region (described by the state vector) emits for one month while all other regions are emitting as normal (following spin up of the model). The individual regional source is then switched off (emissions become zero), and the resulting 3-D atmospheric distribution of CH_4 amount

fractions is recorded over four months. The effect of the emissions changes upon CH_4 amount fractions are recorded at the grid squares which correspond with the measurement sites. This therefore describes the sensitivity of a particular measurement site to changes in a specific regional source up to three months after emission. This is repeated for every month within the inversion timescale, for every region described in the state vector.

For the δ^{13}C inversions, the *a priori* simulation uses *a posteriori* regional emissions from the CH_4 inversion as a starting point. The Jacobian matrix in this case describes the sensitivity of modelled δ^{13}C to changes in the regional source signatures. The Jacobian comprises the difference between a control model calculation (using the CH_4 *a posteriori* regional emissions) and perturbed source signature model calculation for the whole study period (2004–2020). For the perturbed model calculation, systematically, each region's source signature (all of the sectors that are containing geographically within a region) is perturbed to be heavier by 20% for the period 2004-2020. The difference between the control and perturbed run in δ^{13}C value at the location of each measurement site is then divided by the (‰) value of δ^{13}C perturbation for the region source signature, to understand the effect of changing a regions source signature upon the δ^{13}C value recorded at each measurement site location. Each individual region's model calculation is spun up separately from the control model calculation in order to account for lagging in the model.

The output from the inversion are improved estimates of regional fluxes and δ^{13}C source signatures. The model simulates the global atmosphere on a $2^\circ \times 2.5^\circ$ grid. The *a posteriori* regional fluxes and signatures are applied to the grid squares in the model which correspond with a given region in an *a posteriori* simulation.

Ensemble Kalman Filter

The inversion using GOSAT was performed by a colleague, and used to compare with the ground-based *in situ* inversion results. The GOSAT results are included because they form an important part of context for the ground-based *in situ* results. The approach for the inversion performed is detailed here, so as to give clarity to the results.

For the satellite data based inversion, an Ensemble Kalman Filter (EnKF) approach is used (Evensen, 1994, 2003; Feng et al., 2009), because it is more straightforward than evaluating the matrix operations for an inversion, considering the higher volume of satellite data. A collection of flux perturbation pulses (from each sub-region) is used to represent uncertainty in the *a priori* estimates for regional monthly fluxes. GEOS-Chem is then used to track the transport and chemistry processes upon the tagged emission pulses, to project their spreads over the modelled atmosphere. With the ensemble of *a priori* flux perturbations, and the simulated observation impacts, Ensemble Transform Kalman Filter (ETKF) algorithm is used to estimate *a posteriori* fluxes and the associated uncertainties, by comparing the model simulation with observations; this same approach is followed by Feng et al. (2017). To reduce

the computational costs, mainly from tracking the tagged emission pulses, a 4-month moving lag window for each assimilation step was employed, because any observation has limited ability to distinguish between the signals emitted and the background from more than 4 months onwards (Feng et al., 2017). As a result of the high data volume, a larger state vector (than the MAP approach) is used, consisting of monthly scaling factors for 487 (476 land regions and 11 oceanic regions) regional CH_4 (and CO_2) emissions pulses (Table S1 in Feng et al., 2022). These land sub-regions are constructed by dividing each of the TransCom (Gurney et al., 2002) land regions into 42 nearly equal sub-regions (Temperate Eurasia is divided in 56 regions due its large landmass), with 11 oceanic regions. Because of the small sizes of each region, a higher uncertainty percentage (60%) for *a priori* emissions than the MAP approach described above is applied. Also included is spatial correlation, with a correlation length of 500 km between the sub-regions.

2.3 Results

Figure 2.4 compares growth rates calculated from a range of sources: from the values published by NOAA, from ground-based *in situ* data and from the results of both the ground-based *in situ* and GOSAT inversion results. These are global growth rates year-on-year. This plot shows that *a posteriori* CH_4 emissions inferred from ground-based and GOSAT data are consistent (typically within 3 ppb) with global atmospheric growth rates inferred directly by the atmospheric data (Dlugokencky et al., 2005) and the values as reported by NOAA. This result provides confidence in the ground-based *in situ* estimates on the global scale.

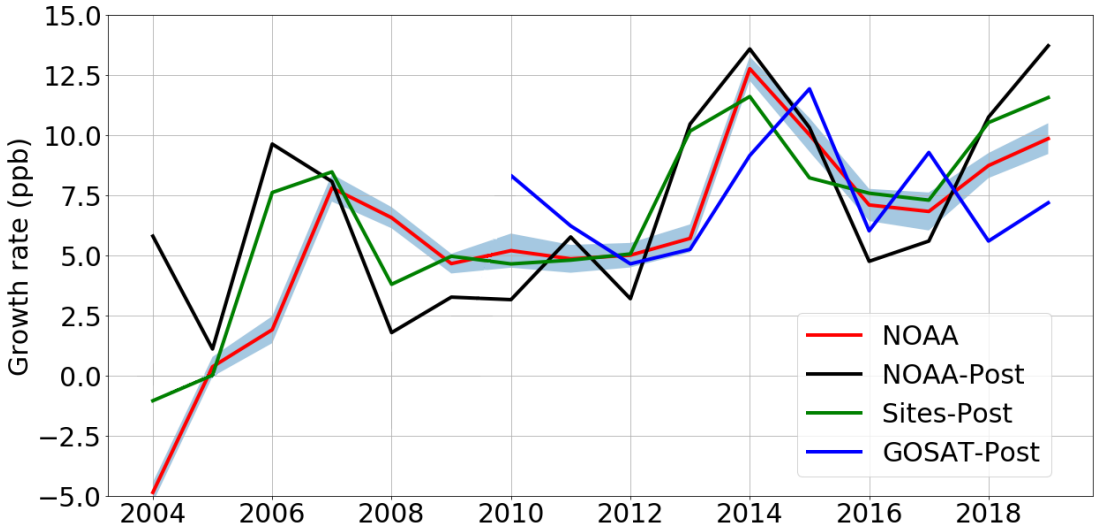

Figure 2.4: *A posteriori* amount fraction yearly increase (ppb), compared with the equivalent data as published by NOAA (Dlugokencky et al., 2020). Indicating the NOAA published growth rate values ('NOAA', with uncertainty as a blue band) and growth rate calculated using ground-based *in situ* amount fraction data from the sites included in the inversion ('Sites-Post'), alongside growth rate values calculated from *a posteriori* amount fractions; from the ground-based *in situ* inversion ('NOAA-Post') and GOSAT inversion ('GOSAT-Post'), which commences in 2010. To calculate the growth rates from simulations (NOAA-Post and GOSAT-post), the average global CH_4 amount fraction in one year (the mean amount fraction of every grid square in every month of a year), is compared with the mean of the following year. The calculation is January-January, in order to remove the effects of the seasonal cycle. This follows the same approach as the NOAA calculated values (Lan et al., 2021).

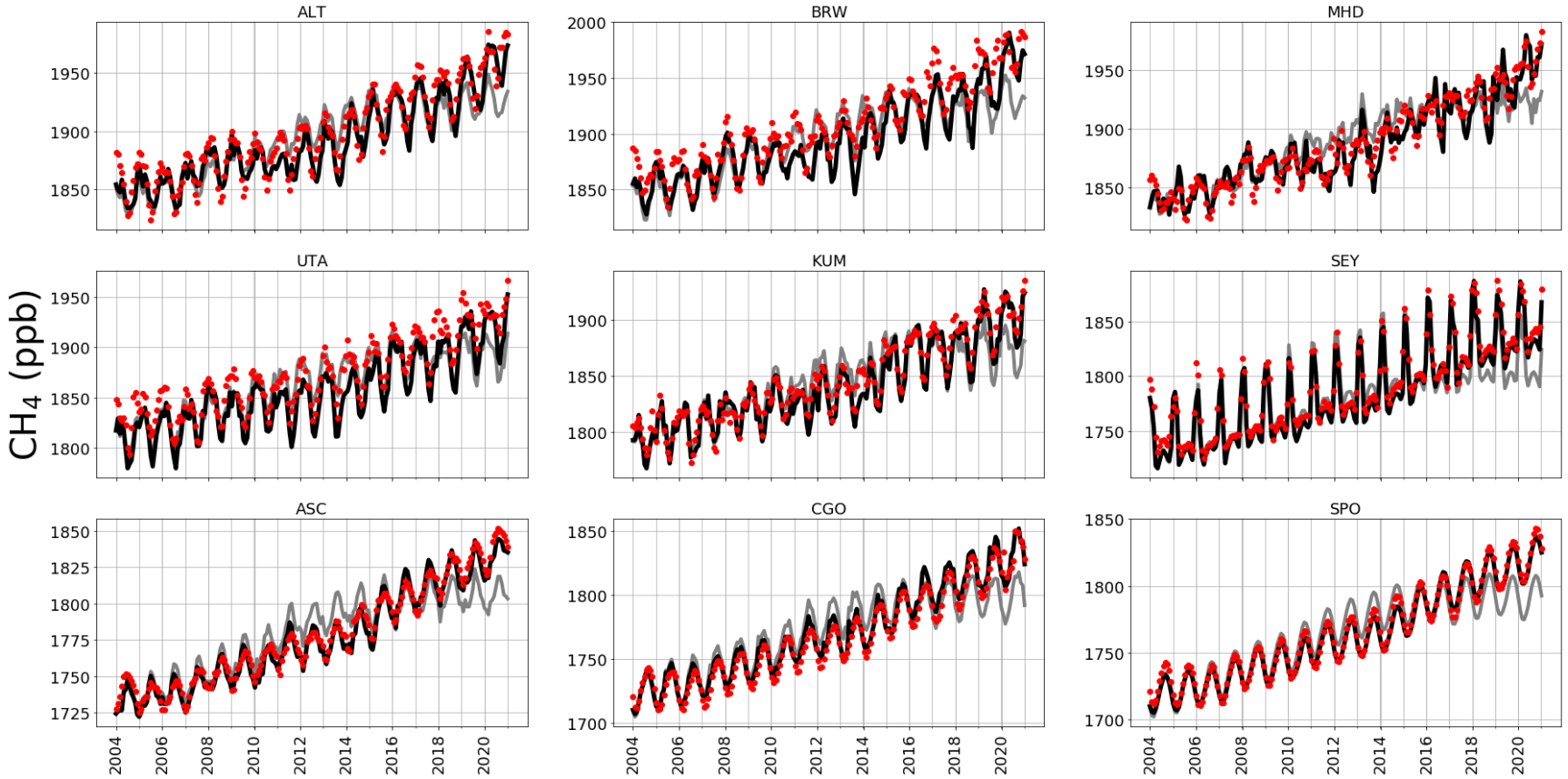

Figure 2.5: *A priori* (grey) and *a posteriori* (black) simulated amount fraction estimates (ppb) at a series of NOAA sites (subplot titles indicate site represented, detailed in Table A1), covering a range of latitudes. Red dots indicate NOAA monthly-averaged amount fraction measurement data from the given site.

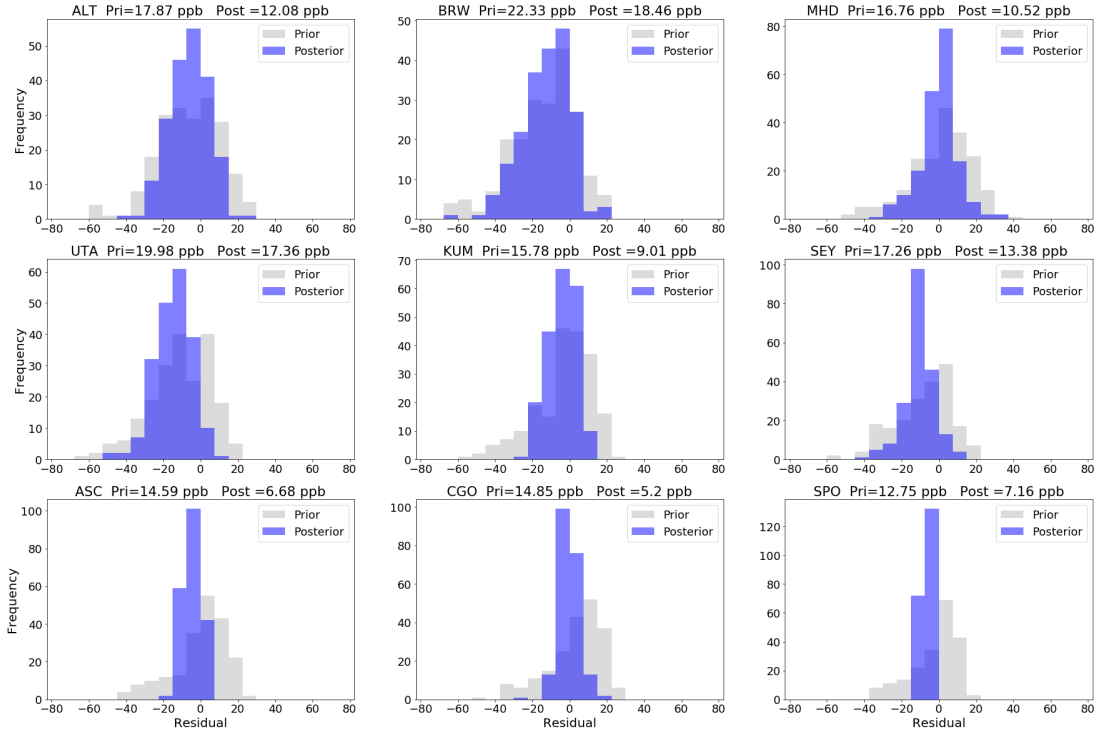

Figure 2.6: *A priori* (grey) and *a posteriori* (blue) histograms representing residuals between modelled values of CH_4 and those measured at sites (model -measurement, ppb). Model values are sampled at the grid square which corresponds with each site location. *A priori* and *a posteriori* root-mean-square error is indicated for each site.

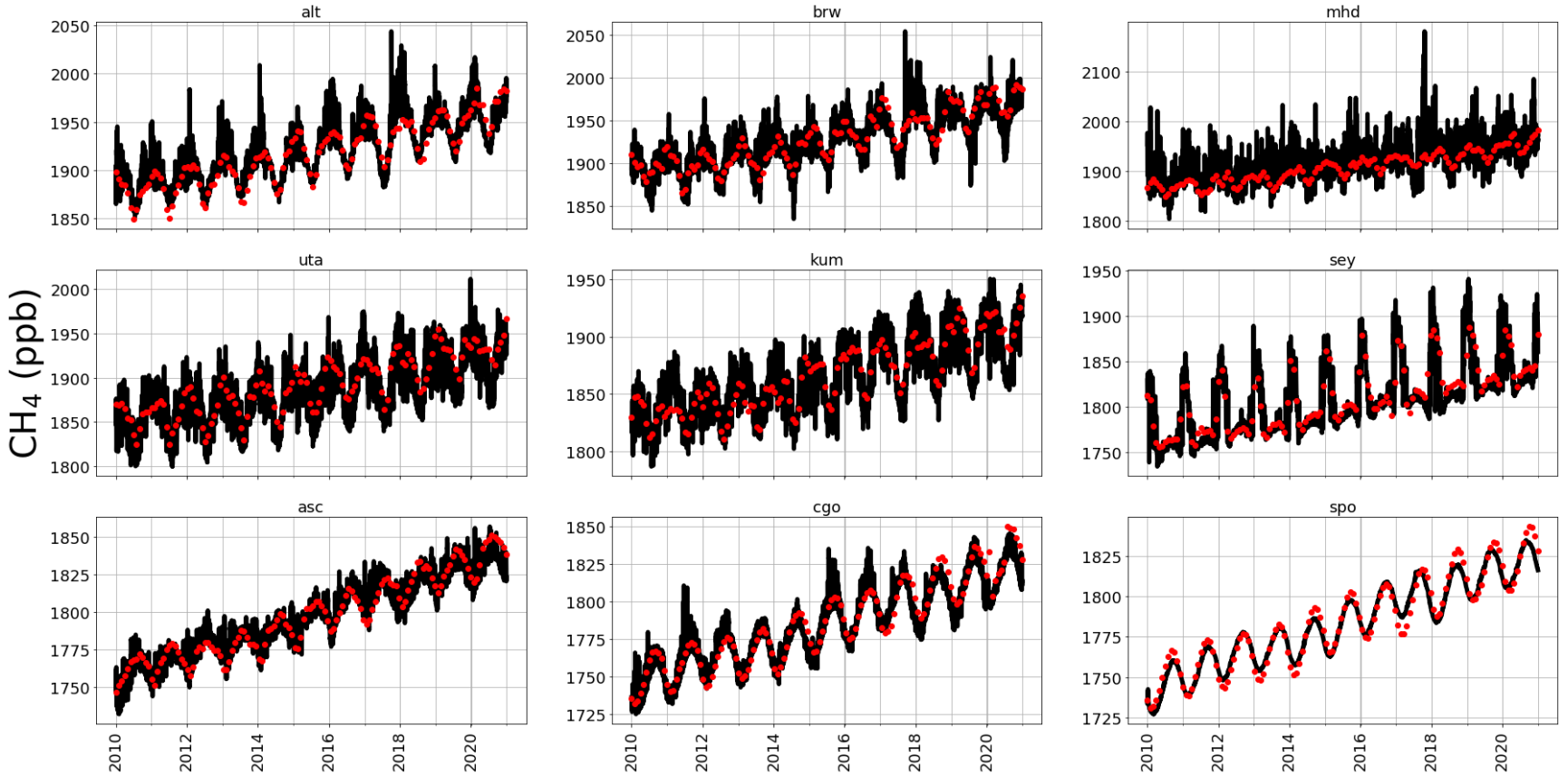

Figure 2.7: 3-hourly GOSAT surface *a posteriori* CH_4 values (ppb, black) at the location of a number of NOAA sites (sites are detailed in Table A1), over the period 2010-2020. NOAA monthly mean values from the same sites indicated for comparison (ppb, red dots).

Smaller residuals are found between *a posteriori* emissions and the measurements (mean residual 9.01 ppb; root-mean-square error (RMSE) 11.94 ppb) than between the *a priori* values and the measurements (mean residual 13.06 ppb; RMSE 17.13 ppb) (Figures 2.5, 2.6 and 2.7). This compares well with McNorton et al. (2018), with *a posteriori* root-mean-square error of 12.3 ppb. Likewise, there is good agreement of amount fraction estimates using GOSAT data (Figure 2.7; mean residual 41.72 ppb, RMSE 51.57 ppb). This indicates that both inversion approaches are doing a good job in solving for regional CH_4 fluxes, as the residuals are improved versus the prior.

Figure 2.8 shows regional *a priori* emission estimates and *a posteriori* emission estimates inferred from the NOAA/NIES ground-based data and GOSAT data. The *a priori* emissions are constructed from the sources and meteorology as detailed in Section 2.2 (geographical distribution of sources is indicated by Figure 2.2). From this plot, one can observe strong emissions increases over the time series (2004-2020), especially for tropical regions (North Africa +19.9 Tg/yr, China +21.6 Tg/yr, and Tropical South America +14.2 Tg/yr, 2004-2020).

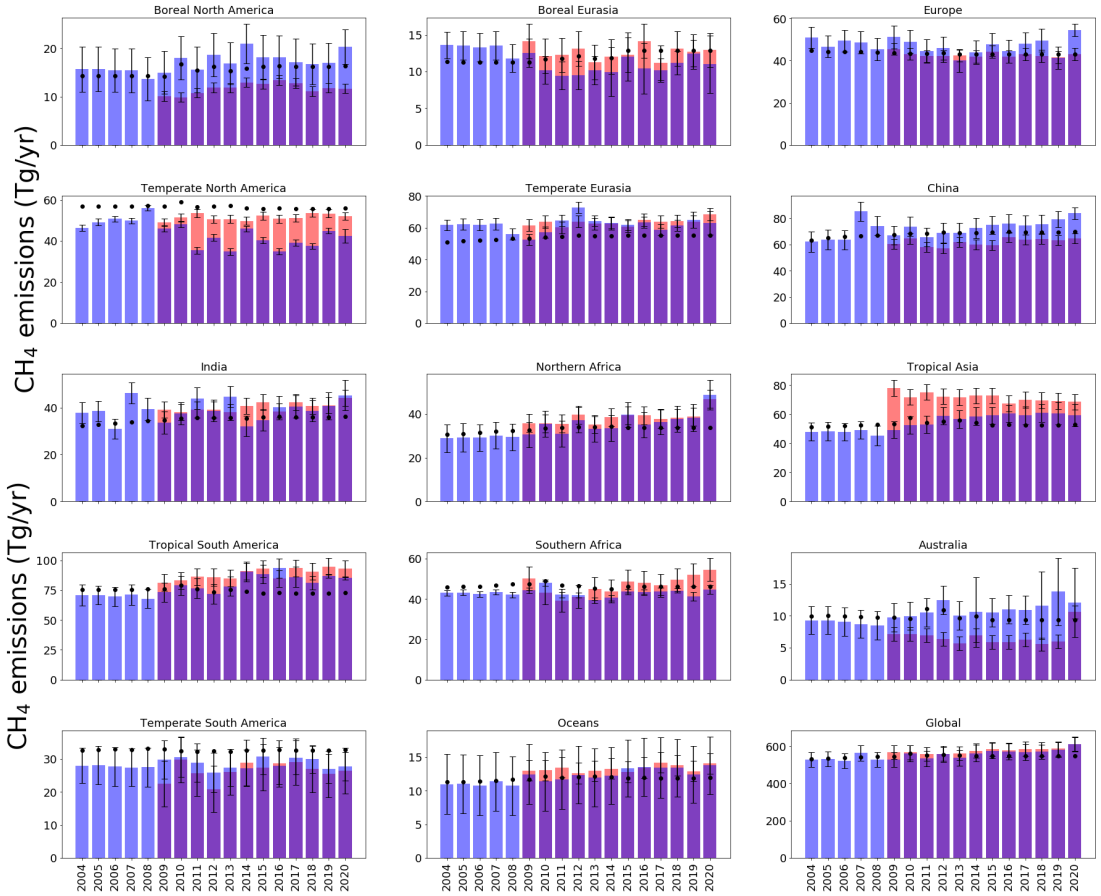

Figure 2.8: *A posteriori* emissions estimates (Tg/yr) produced from an inversion using ground-based data (blue), and GOSAT data-based *a posteriori* emissions estimates (red, with record starting in 2010), for the regions indicated by Figure 2.1. *A-priori* emissions estimates are indicated by black dots. *A posteriori* uncertainties are whisker bars.

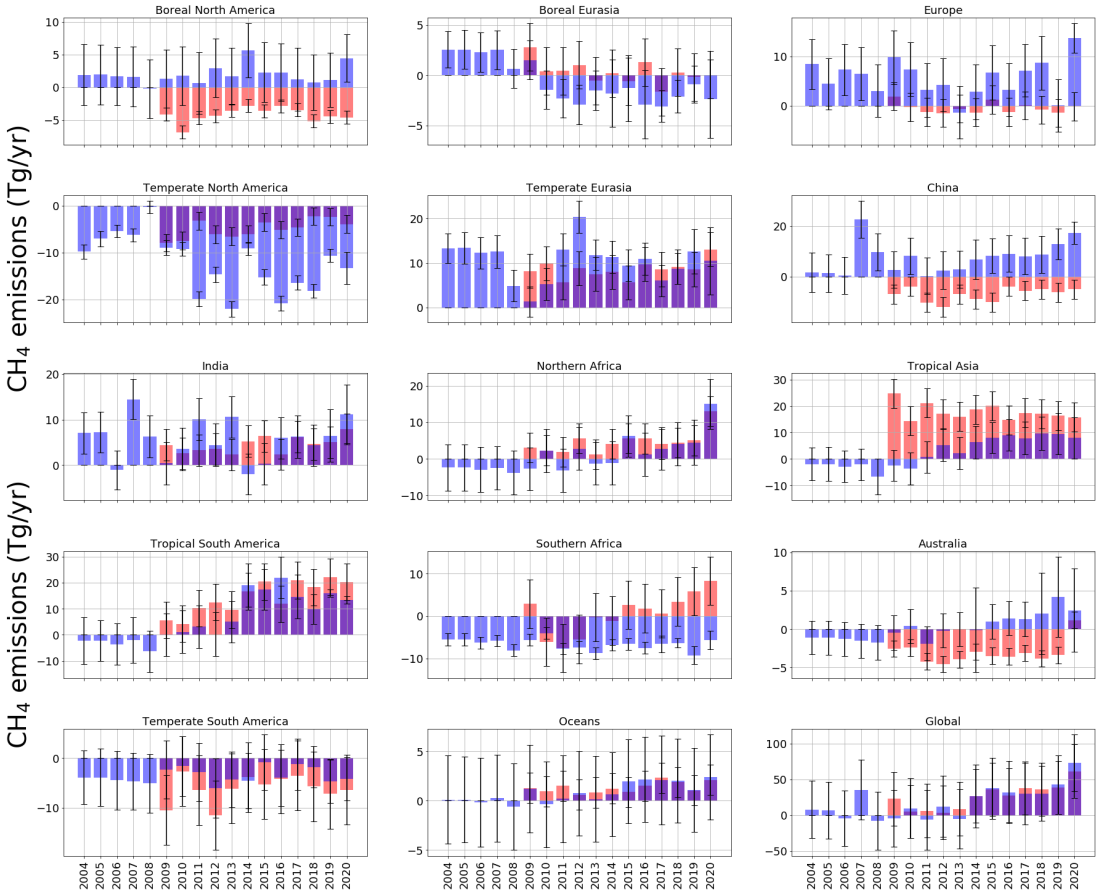

Figure 2.9: Yearly CH_4 emissions (Tg/yr) from each of the inversion regions in latitudinal order (geographic coverage indicated by Figure 2.1), for both ground-based and GOSAT inversion results. The emissions are a residual value, relative to the *a priori* yearly emission for each region. Uncertainties in yearly emissions are indicated, as calculated from inversion calculations, with a *a priori* uncertainty of 50% for the ground-based *in situ* results and 60% for the GOSAT results. The ground-based *a posteriori* is in blue; the GOSAT *a posteriori* are in red.

Figure 2.9 shows the regional differences between *a priori* and *a posteriori* emission estimates, with absolute plotted in Figure 2.8. Here the yearly average difference between the *a posteriori* and the *a priori* emissions are shown, for both ground-based and GOSAT inversion results. This both indicates the changes from the *a priori* emissions and allows comparison of the two independent approaches. The *a priori* emissions are constructed as detailed in Section 2.2. Absolute emissions values (Figure 2.8) demonstrate the increases in CH_4 emissions over the time series, especially for tropical regions (North Africa +19.9 Tg/yr, China +21.6 Tg/yr, and Tropical South America +14.2 Tg/yr, 2004-2020). At a global scale, higher emissions relative to *a priori* emissions of 72 $\pm$ 35.51 Tg/yr in 2020 for the ground-based *in situ* inversion and 61.5 $\pm$ 37.3 Tg/yr higher emissions for the GOSAT inversion. The ground-based *in situ* inversion results indicate that this difference originates from tropical regions such as Tropical South America (+13.5 $\pm$ 1.9 Tg/yr in 2020), North Africa (+15.1 $\pm$ 6.8 Tg/yr, 2020) and China (+17.3 $\pm$ 4.4 Tg/yr, 2020). There are decreases relative to *a priori* emissions in 2020 in Temperate North America (-13.3 $\pm$ 3.4 Tg/yr), Southern Africa (-5.6 $\pm$ 2.1 Tg/yr), Temperate South America (-4.1 $\pm$ 4.0 Tg/yr) and Boreal Eurasia (-2.3 $\pm$ 3.9 Tg/yr). Therefore, the estimates from bottom up inventories underestimate CH_4 emissions, especially in tropical regions. According to this analysis of ground-based *in situ* data, there is a shift, with mid-latitudinal emissions being overestimated and tropical emissions underestimated.

Likewise, the GOSAT-based inversion results indicate *a posteriori* emissions increases from the *a priori* emissions are centred around tropical regions. In 2020, there are emissions increases from the *a priori* estimates in Tropical South America (+20.3 $\pm$ 1.9 Tg/yr) and North Africa (+13.1 $\pm$ 6.8 Tg/yr). Temperate regions also decrease, specifically Temperate North America (-3.9 $\pm$ 1.8 Tg/yr) and Temperate South America (-6.4 $\pm$ 7.1 Tg/yr)

There are some differences between the two inversion results. Specifically, emissions from Boreal North America and China are lower than the *a priori* emissions for the GOSAT-based inversion (-4.6 $\pm$ 1.1 and -5.1 $\pm$ 3.8 Tg/yr in 2020 respectively), but increase for the ground-based *in situ* inversion (+4.4 $\pm$ 3.62 and +17.3 $\pm$ 4.4 Tg/yr in 2020 respectively). Despite differences in the absolute annual emissions estimates, both the GOSAT-based inversion and the ground-based *in situ* based inversion indicate a gradual emissions increase in China from 2012. Sheng et al. (2021) find anthropogenic CH_4 emissions from China increasing by 0.36 Tg/yr/yr from 2012 to 2017 onwards using GOSAT data. Comparing the same time period, an increase of Chinese emissions is observed, by 0.72 Tg/yr/yr for ground-based *in situ*; 1.34 Tg/yr/yr for GOSAT.

Emissions increases are observed across the timeseries (by comparing the yearly regional emissions in 2020 to those in 2004) from tropical regions such as North Africa (+17 Tg/yr), Tropical Asia (+10 Tg/yr) and Tropical South America (+8 Tg/yr). The increase in tropical emissions has been suggested by previous studies, whether using GOSAT data or ground-based *in situ* data as constraints in a 3D CTM inversion (Fujita et al., 2020; McNorton et al.,

2016, examining (2003-2015) and (1995-2013) respectively). The increase in North Africa is especially noteworthy in 2020, where emissions have been attributes to increased wetland emissions by previous studies (Lunt et al., 2019, 2021; Pandey et al., 2021). Conversely, both approaches indicate decreases over the entire timeseries in temperate regions, such as Temperate North (-2 Tg/yr) and South America (-0.5 Tg/yr).

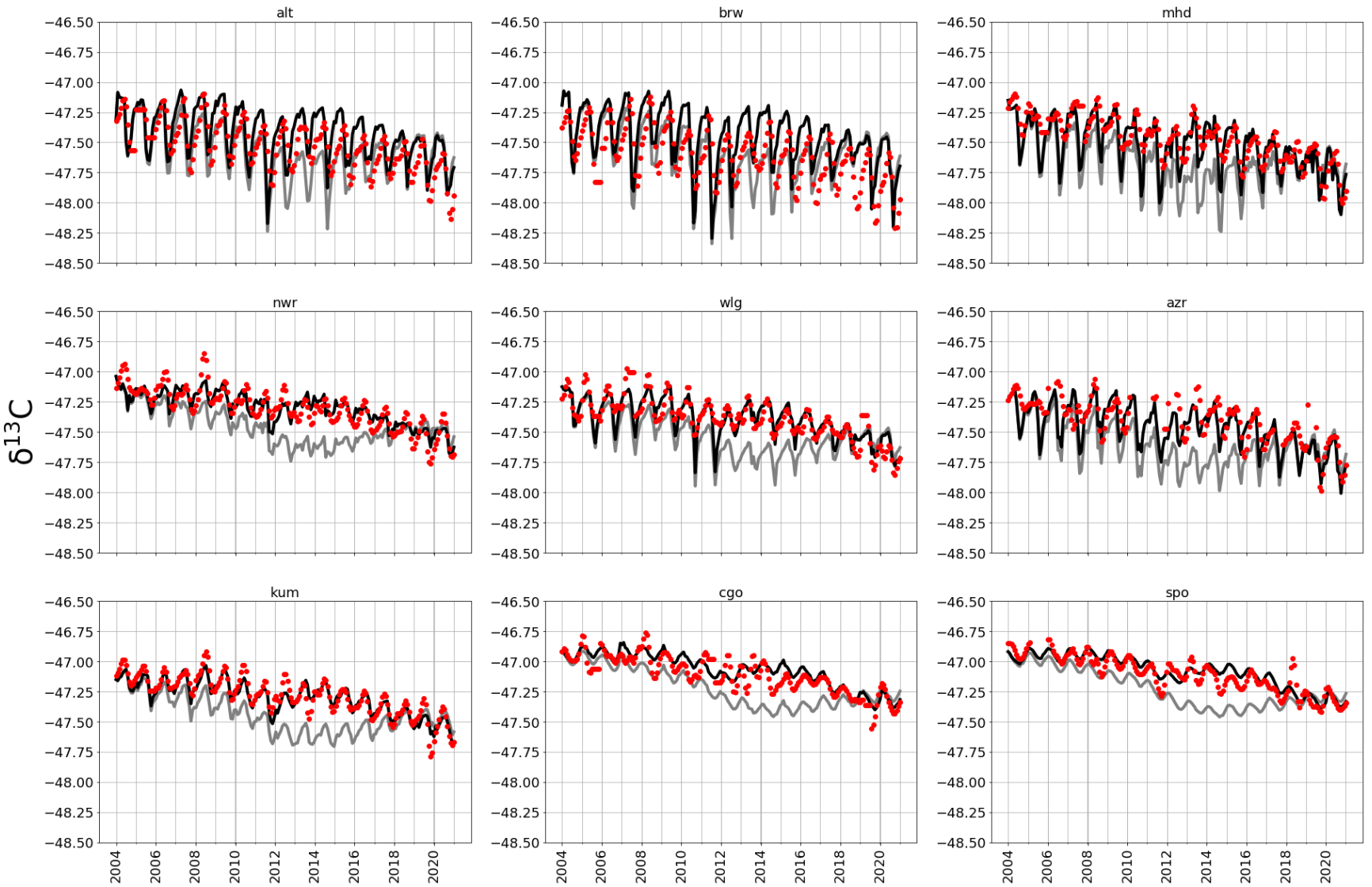

Figure 2.10: *A priori* (grey) and *a posteriori* (black) monthly estimates of atmospheric δ^{13}C (‰), simulated at multiple NOAA sites across latitudes (site indicated by subplot titles, with site details in Table A1). Red dots indicate monthly average δ^{13}C data from CU-INSTAAR for the respective sites.

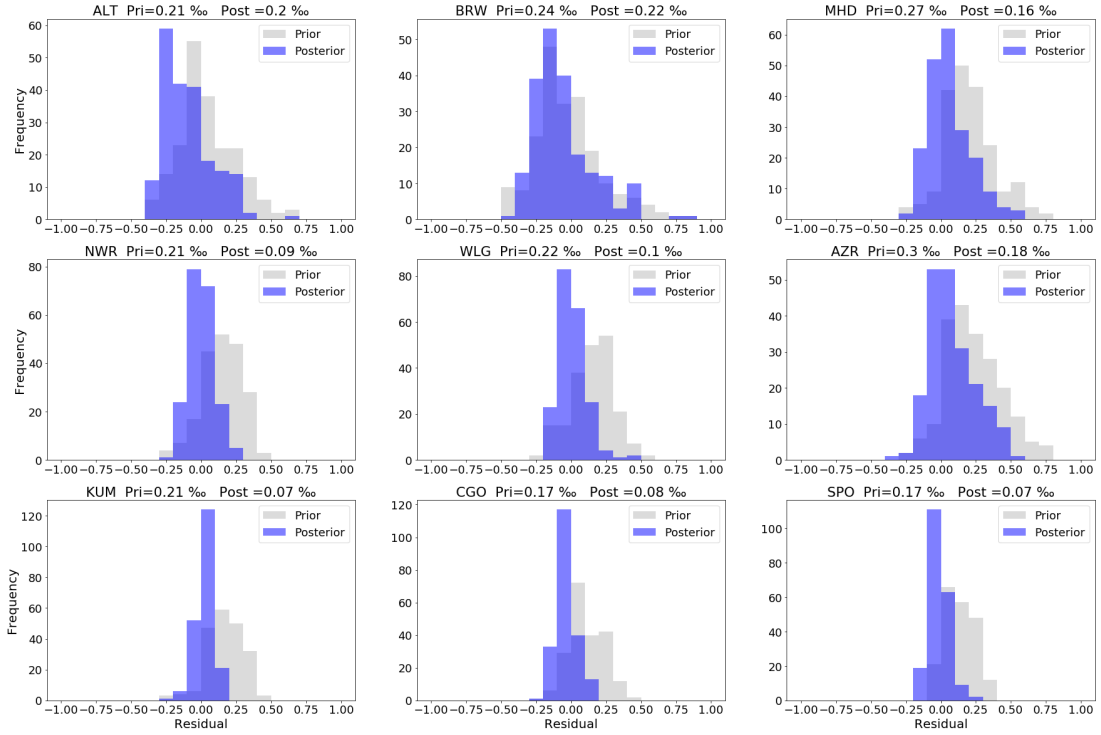

Figure 2.11: *A priori* (grey) and *a posteriori* (blue) histograms representing residuals between modelled values of δ^{13}C and those measured at sites (model -measurement, ‰). Model values are sampled at the grid square which corresponds with each site location. *A priori* and *a posteriori* root-mean-square error is indicated for each site.

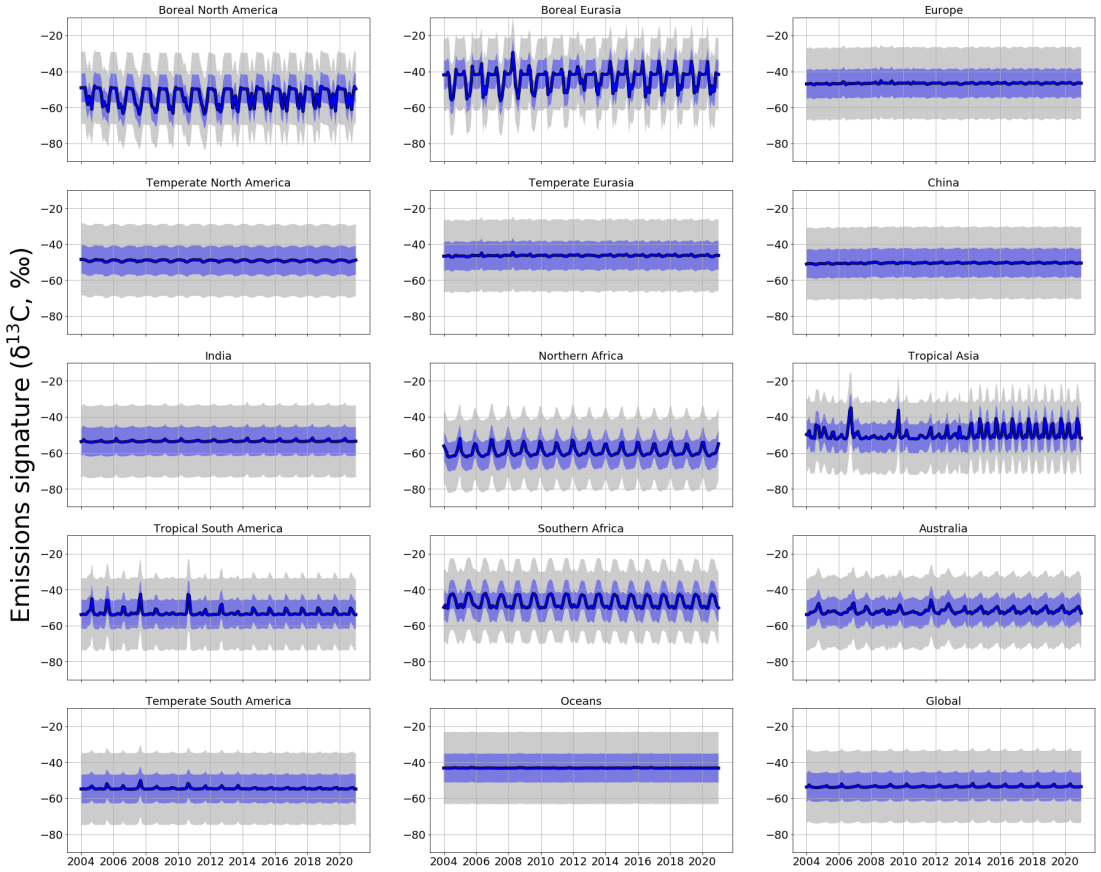

Figure 2.12: Monthly *a priori* (grey) and *a posteriori* (blue) regional δ^{13}C source signatures (‰). Values are produced using ground-based *in situ* δ^{13}C data. Uncertainties in signatures are indicated as surrounding bars, with *a priori* uncertainties of 15‰. Post-2014, regional emissions are repeated yearly, due to this being the final year included in the emissions inventories.

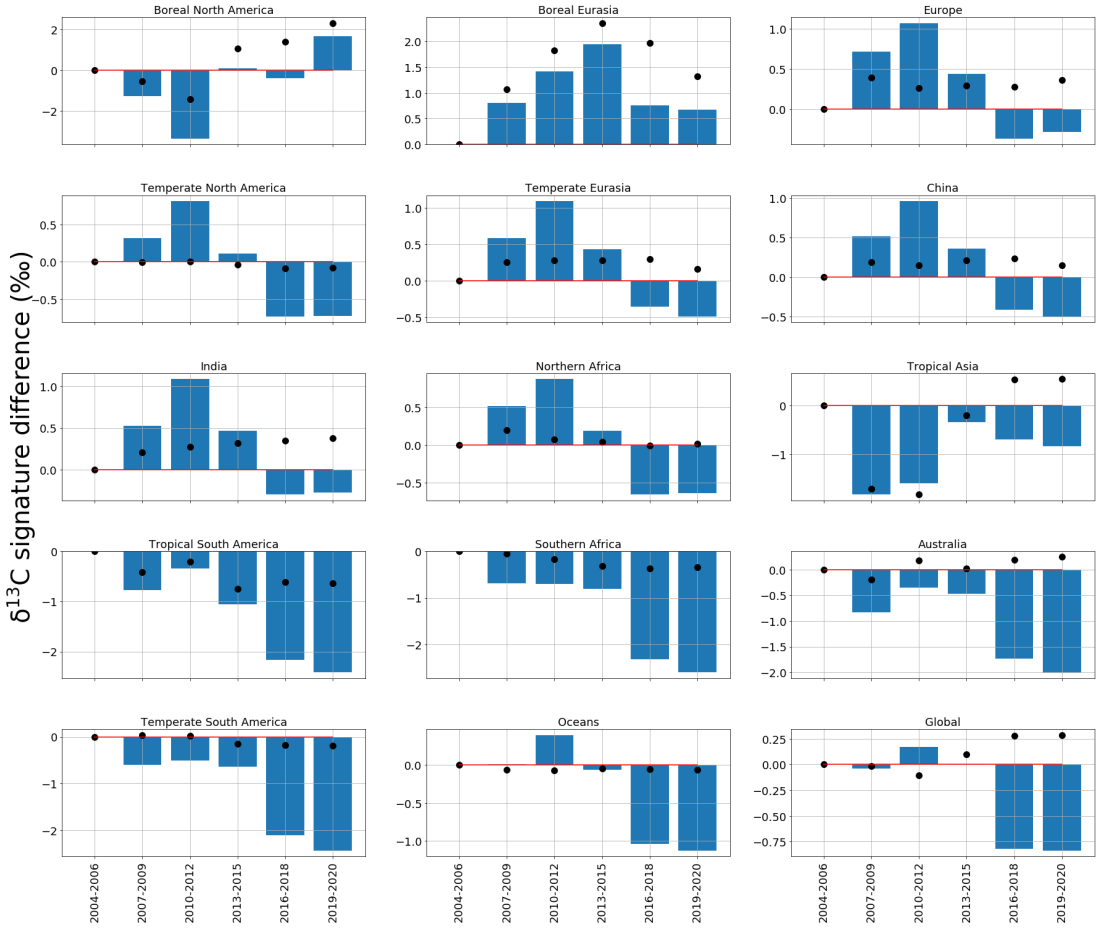

Figure 2.13: Regional and global *a posteriori* δ^{13}C emissions signatures (‰), in three-yearly groups (2004-2006, 2007-2009, 2010-2012, 2013-2015, 2016-2018, 2019-2020) as a residual from the 2004-2006 *a posteriori* regional emissions signature value. The equivalent *a priori* values are black dots. The regions are those solved for in the CH_4 and δ^{13}C inversions and are indicated by Figure 2.1.

The corresponding *a posteriori* regional δ^{13}C emissions signatures produce atmospheric δ^{13}C values that are in better agreement with measurements than *a priori* values (Figures 2.10 and 2.11), particularly during 2008-2018 when *a priori* emissions signatures lead to atmospheric δ^{13}C values that are lighter than the measurements. Figure 2.10 shows δ^{13}C *a priori* and *a posteriori* values at site locations. The *a posteriori* signatures result in smaller residuals between the *a posteriori* simulation and measurement (mean residual 0.11‰, RMSE 0.15‰), than from the prior (mean residual 0.19‰, RMSE 0.23‰). These compare well to McNorton et al. (2018) (*a posteriori* RMSE 0.1‰) and Fujita et al. (2020) (*a posteriori* RMSE 0.08 -0.25‰).

Figure 2.12 shows the monthly regional source signature values for *a priori* and *a posteriori* simulations. General observations from this figure are that lighter signatures are observed (-62‰) from Northern Boreal regions (Boreal North America and Eurasia), which indicates the dominance of biogenic emissions here. Conversely, heavy signatures (-40‰, indicative of a greater proportion of thermogenic emissions) are recorded from regions such as Temperate Eurasia, Australia and Southern Africa. Some regional δ^{13}C signatures have a much stronger seasonal cycle than others (strongest in Boreal North America and Boreal Eurasia but also in Northern and Southern Africa), with lighter values during summer months, driven by higher proportion of biogenic emissions. Sites in these regions are therefore influenced by a stronger seasonal biogenic source, assuming that thermogenic emissions have a smaller seasonal cycle (peaking in winter). Less significant seasonality is therefore indicative of anthropogenic emissions making up a significant part of the emissions mix (observed for example in China and Temperate Eurasia). Tropical Asia shows a yearly cycle with dual peaks, which is due to a combination of wetland and rice emissions. This assessment assumes that sources are playing the most significant role in controlling seasonal cycle in δ^{13}C signature, whereas changing magnitude of sinks could also play a role here.

Figure 2.13 shows *a posteriori* regional δ^{13}C source signatures, grouped into three-yearly bands, as a residual from the 2004-2006 value. There is a general trend towards lighter regional source signatures of δ^{13}C across the time series. This trend has been ongoing since 2012 and is observed in all regions worldwide, however is strongest as compared with *a priori* estimates in Tropical and Southern Hemispheric regions such as Tropical South America and Southern Africa (1.8‰ and 2.1‰ lighter than *a priori* source signatures for 2019-2020, respectively). There is also evidence of a period around 2012 where signatures shift heavier (by 1.0‰ compared with *a priori* signatures), especially in the Northern Hemisphere, before trending lighter again. The heavy trend being dominated by the Northern Hemisphere indicates a greater proportion of anthropogenic emissions in this region at this time. This heavy shift around 2008 and light shift in 2012 are noted by Nisbet et al. (2016), who use a

box model and examine data from sites measured by NOAA and Royal Holloway, University of London (RHUL). They found that changes in removal rates would not explain these anomalies; the events are therefore attributed to changing emissions. Emissions growth post-2012 aligns with atmospheric growth rates plotted in Figures 2.4, 2.8.

In Figure 2.14, all information is combined into a zonal plot, reported every 30° in latitude, for total CH_4 emissions and the corresponding changes in regional source signatures of δ^{13}C. Consistency is found between the magnitude of the changes in CH_4 changes inferred from ground-based NOAA/NIES data and GOSAT data, particularly in the low latitudes. The plot also shows there has been a progressive increase in emissions from tropical latitudes (20 Tg/yr) and a significant decrease at northern and southern mid-latitudes (-5 Tg/yr). A move towards lighter regional source signatures of δ^{13}C is seen across all latitudinal bands. The largest shift by the end of the time series (of 3.0‰) occurs in Southern Hemisphere tropical regions (corresponding with Tropical Asia or Tropical South America, for example). Comparing Figures 2.13 and 2.14, similar trends are observed across latitudinal bands and the regions within them, for example trends in European and Chinese signatures align with the 30 -60° N latitudinal band. The comparison is not exact due to some regions spanning across latitudinal bands (such as Oceans). Results compare well with Nisbet et al. (2019), who use a box model to fit emissions scenarios to *in situ* measurements, examining 2000-2018. They show strongest emissions increases from the tropics (+20 Tg/yr, Figure 5). They likewise show a trend of atmospheric δ^{13}C becoming increasingly light across the time series, by 0.03‰/yr.

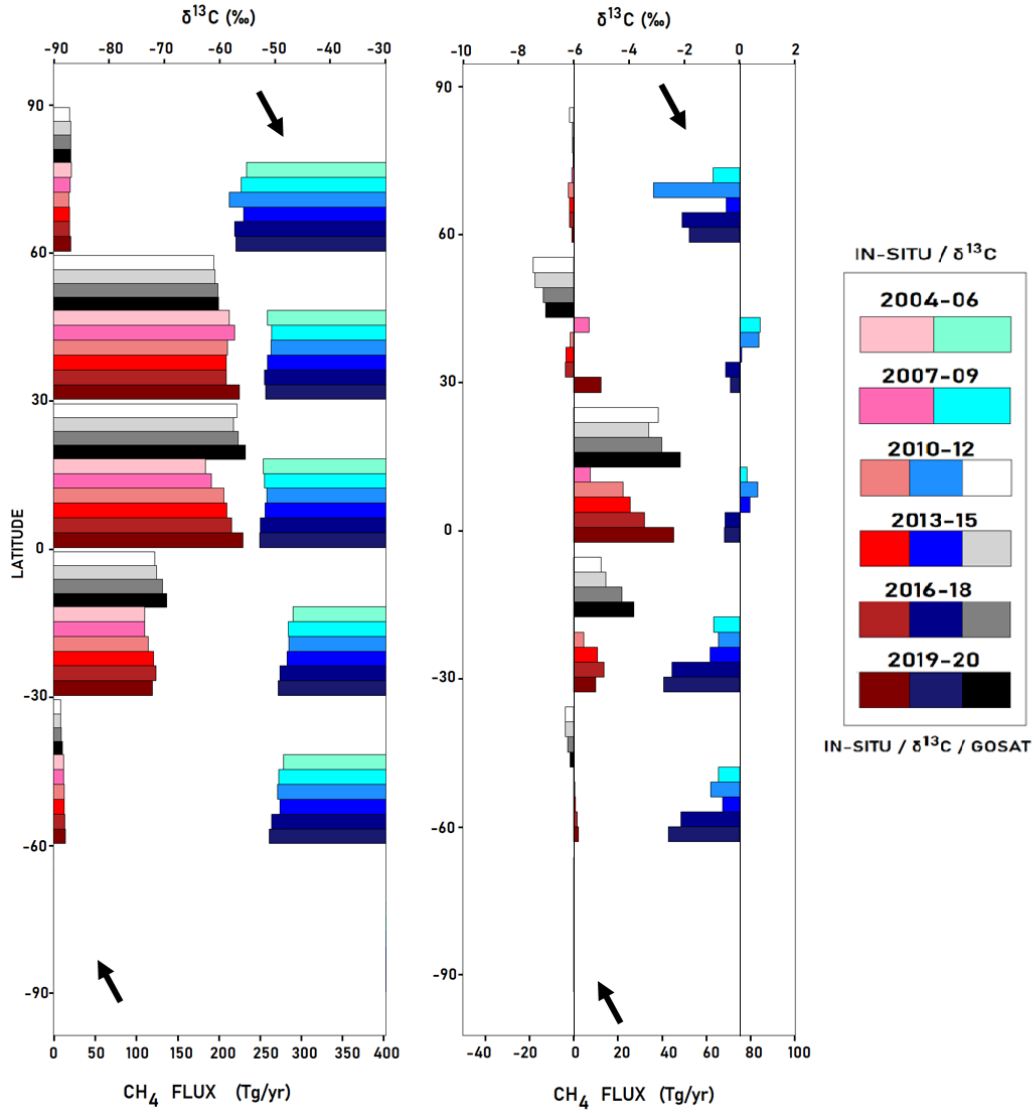

Figure 2.14: Left: Variation of mean emissions (Tg/yr) with latitude in 30° bands, averaged into groups based upon year (2004-2006, 2007-2009, 2010-2012, 2013-2015, 2016-2018, 2019-2020) in reds, as well as GOSAT emissions averages by latitude in greys (GOSAT inversion results begin in 2010). Variations in δ^{13}C emissions signature (‰) for the same latitudinal bands in the same year groups are in blue. Key indicates year groups. Right: Same year groups as left, but indicating the difference in emissions or δ^{13}C emissions signature (‰), between each year group and 2004-2006 value.

To examine the sensitivity of the results to changes in OH, a single sensitivity run is constructed, made up of two parts. First, a 0.5%/yr uniform decrease is imposed upon the 3-D OH field from 2004 to 2019, following similar trends suggested by Turner et al. (2017) and second, OH is uniformly decreased by 5% in 2020 to describe estimated changes due to a global-scale reduction in emissions of nitrogen oxides (NO_x) associated with the first COVID-19 lockdown (Laughner et al., 2021; Miyazaki et al., 2021). It has also been suggested that OH amount fractions may have actually increased 2000-2016 due to increasing water vapour and NO_x in the tropics (Zhao et al., 2019), however considering the scenario under COVID-19 lockdowns in 2020, a decreasing trend over the previous years is only considered here. A similar approach to this was followed and evaluated by Feng et al. (2022). *A posteriori* emissions are then re-calculated, inferred from the ground-based *in situ* data. Figure 2.15 shows that the 0.5% per year negative trend in OH does not make a significant difference to *a posteriori* estimates, reflecting the large *a posteriori* uncertainties. However, the sudden 5% decrease in OH during 2020 results in a marked reduction (9%, 50 Tg/yr) in the increased emissions necessary to explain the increase in atmospheric CH_4. This reduction in emissions particularly affects high-emitting regions such as China and Tropical Asia. Despite this, the results are within the *a posteriori* uncertainties of the control calculation, that does not include a year-to-year change in OH. On balance, given the large-scale, unprecedented changes in atmospheric chemistry during 2020, OH did play a role in global growth rate of CH_4 but changes in emissions overwhelm the impact from reduced OH. The model fits similarly well to the data with or without considering the OH trend (Figure 2.16).

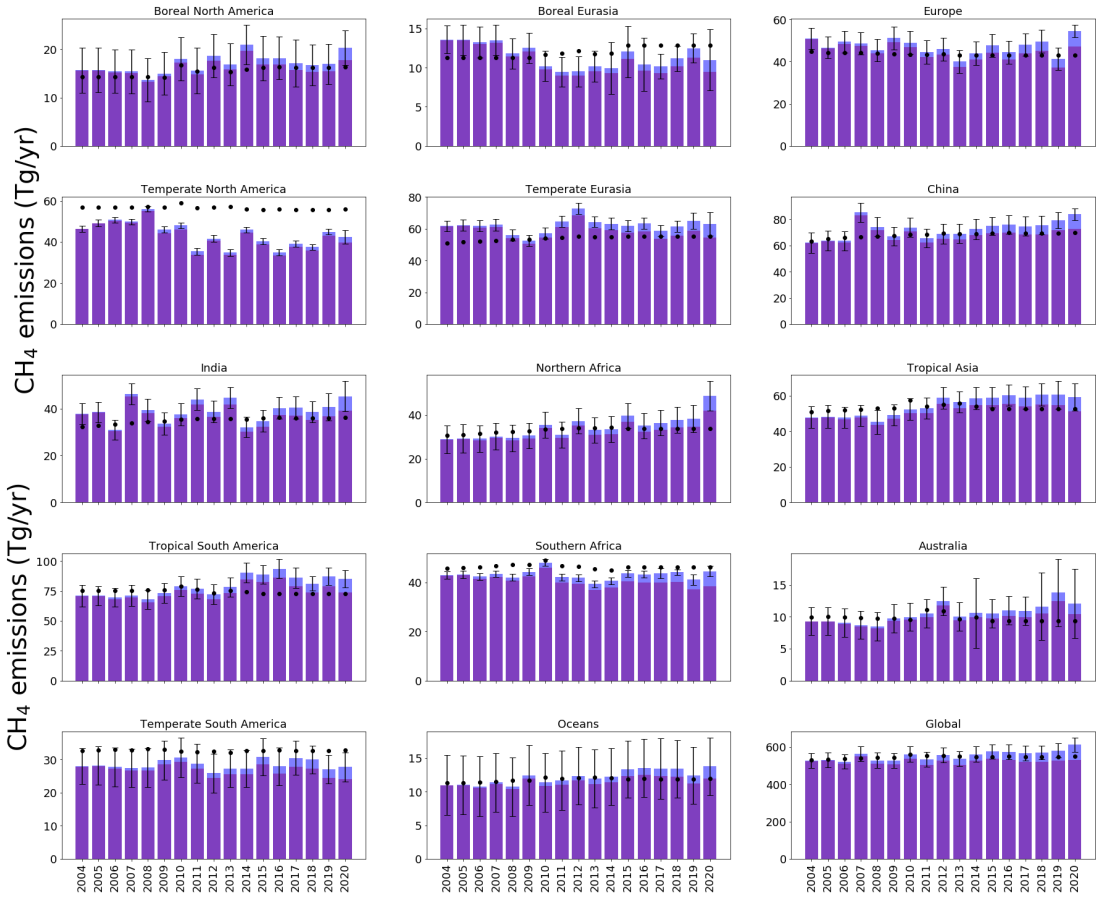

Figure 2.15: Comparing yearly emissions (Tg/yr) for each region of the inversion (indicated by Figure 2.1), for the *a posteriori* CH_4 simulation (using ground-based data; blue) and the regional emissions of the OH tests (as described in-text; red). OH tests always result in lower emissions than *a posteriori* emissions. Regional uncertainties for the *a posteriori* emissions are indicated.

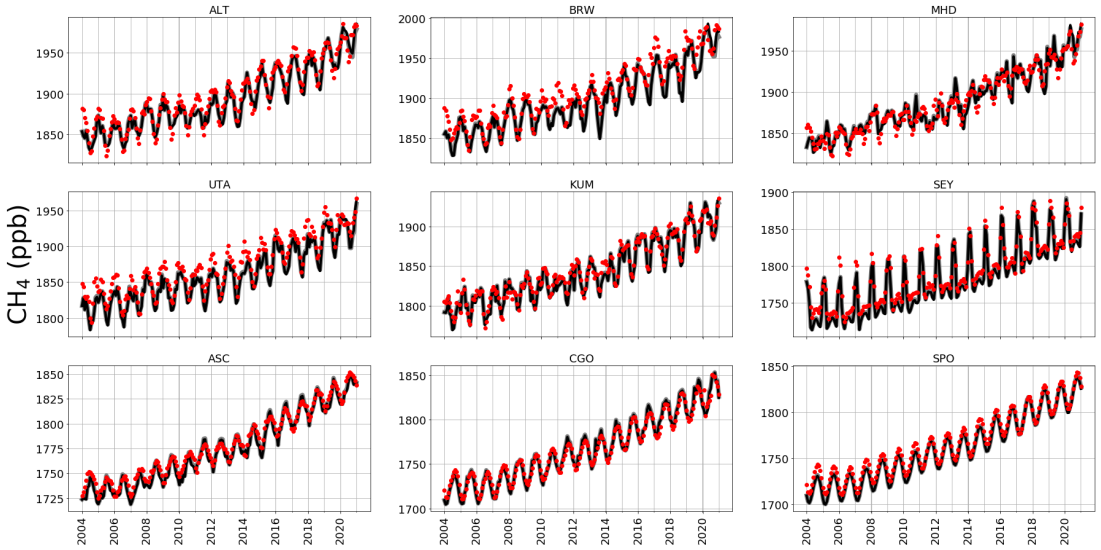

Figure 2.16: Amount fraction CH_4 (ppb) at the location of multiple NOAA network sites, with subplot title indicating site. Demonstrating the effect of OH tests (a 0.5% yearly reduction 2004-2019 followed by 5% reduction in 2020 in response to the COVID-19 pandemic), on amount fraction values at each site location. Grey line is the OH test amount fraction, black line are the amount fractions under *a posteriori* emissions and red dots are monthly-averaged CH_4 amount fractions from each site.

2.3.1 Region Correlations

Figures 2.17 and 2.18 indicate the correlation between regions solved for in the CH_4 and $\delta^{13}C$ inversion, respectively, determined by the *a posteriori* error covariance matrix, $\mathbf{A}$. Values are calculated by normalising the diagonals of the error covariance matrix (Eq. (2.6)). Examining Figure 2.17, there are no significant correlations between the regions for the CH_4 flux inversion. The error covariance matrix is normalised following, where $\mathbf{Q}$ is the normalised matrix:

$$\mathbf{Q} = \frac{\mathbf{A}_{ij}}{\sqrt{\mathbf{A}_{ii}\mathbf{A}_{jj}}}. \tag{2.7}$$

Some significant *a posteriori* correlations are found between neighbouring regions for the *a posteriori* $\delta^{13}C$ source signatures (Figure 2.18), determined by the *a posteriori* error covariance matrix, $\mathbf{A}$, which indicates that the inversion cannot differentiate between the source signatures of neighbouring regions (such as Southern Africa and Temperate South America). This is a result of not having enough geographically-spaced data to separate contributions from different regions, and means there is limited capacity to separate the changing $\delta^{13}C$ signatures of the regions in this inversion. This aligns with Basu et al. (2022), who used both CH_4 amount fraction and $\delta^{13}C$ measurements to determine that tropical biogenic sources are driving CH_4 growth, however measurement coverage limits possible conclusions based upon isotope ratio measurements. Nevertheless, the trend of stronger emissions of lighter CH_4 is clear, due to an increased role in biogenic or wetland emissions in the global source makeup. Lan et al. (2021) corroborate this using a 3D chemical transport model to simulate different possible emissions scenarios, and find that biogenic emissions (wetlands, agriculture and waste) are responsible for the strong trend in $\delta^{13}C$, examining 1984-2016.

Figures 2.19 and 2.20 show the *a posteriori* matrix of contribution functions for the CH_4 and $\delta^{13}C$ inversions, respectively. This indicates the extent to which sites used in the inversion influence particular regions. Values are calculated by:

$$MOCF = \mathbf{A}\mathbf{H}^{\mathrm{T}}\mathbf{B}^{-1}, \tag{2.8}$$

where $\mathbf{A}$, $\mathbf{H}$ and $\mathbf{B}$ are as described in Eq. (2.5).

Based on Figures 2.19 and 2.20, it can be seen that certain regions are not being constrained by site data. For both CH_4 and $\delta^{13}C$, regions such as Tropical South America, Australia and Southern Africa are poorly constrained by the data, as a result of the poor geographic coverage of site locations, especially in the Southern Hemisphere (Figure 2.1). Deploying more instrumentation would increase geographic coverage of data and therefore improve constraints on CH_4 amount fractions and $\delta^{13}C$ signatures.

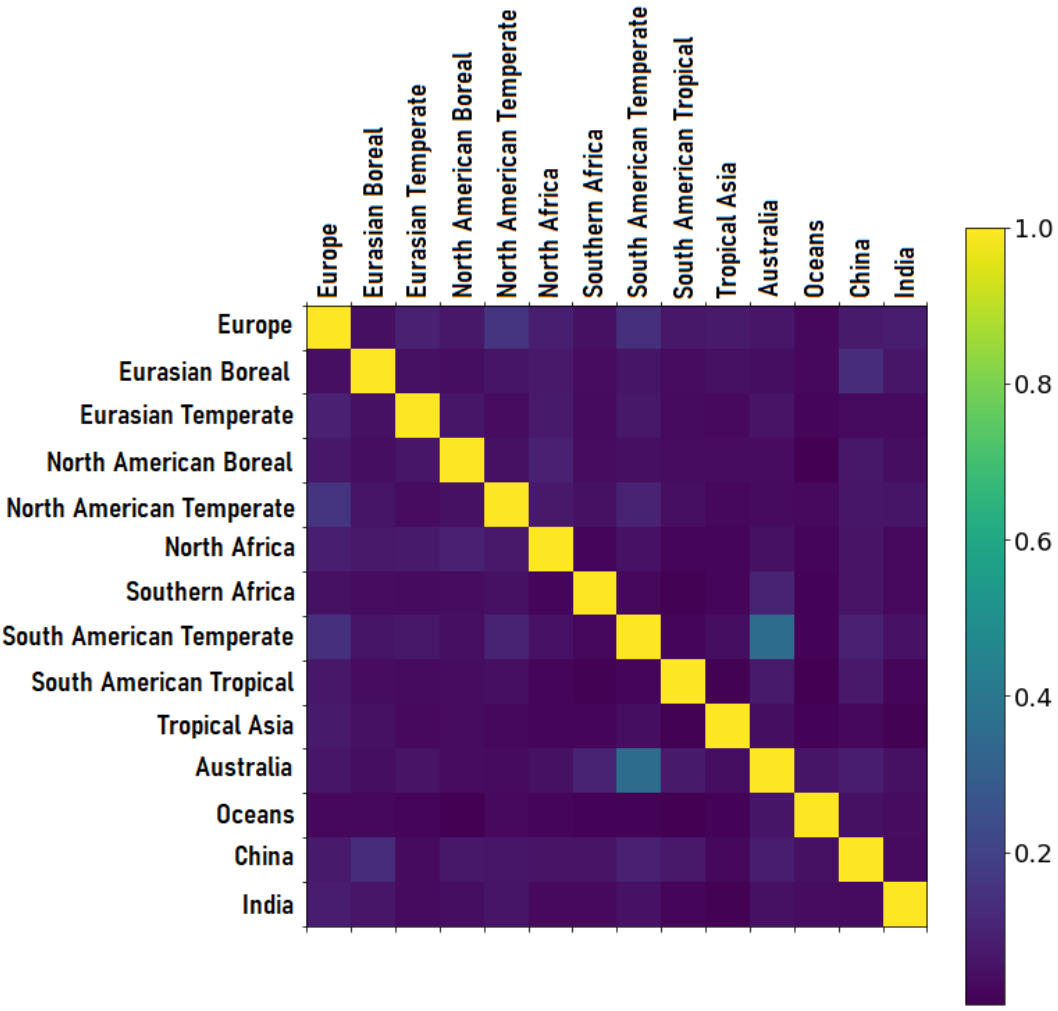

Figure 2.17: Correlation between regions inverted for in the CH_4 emissions inversion using ground-based data. The correlations are produced by normalising the diagonals of the error covariance matrix (Eq. (2.6)). Correlation indicated by colourbar.

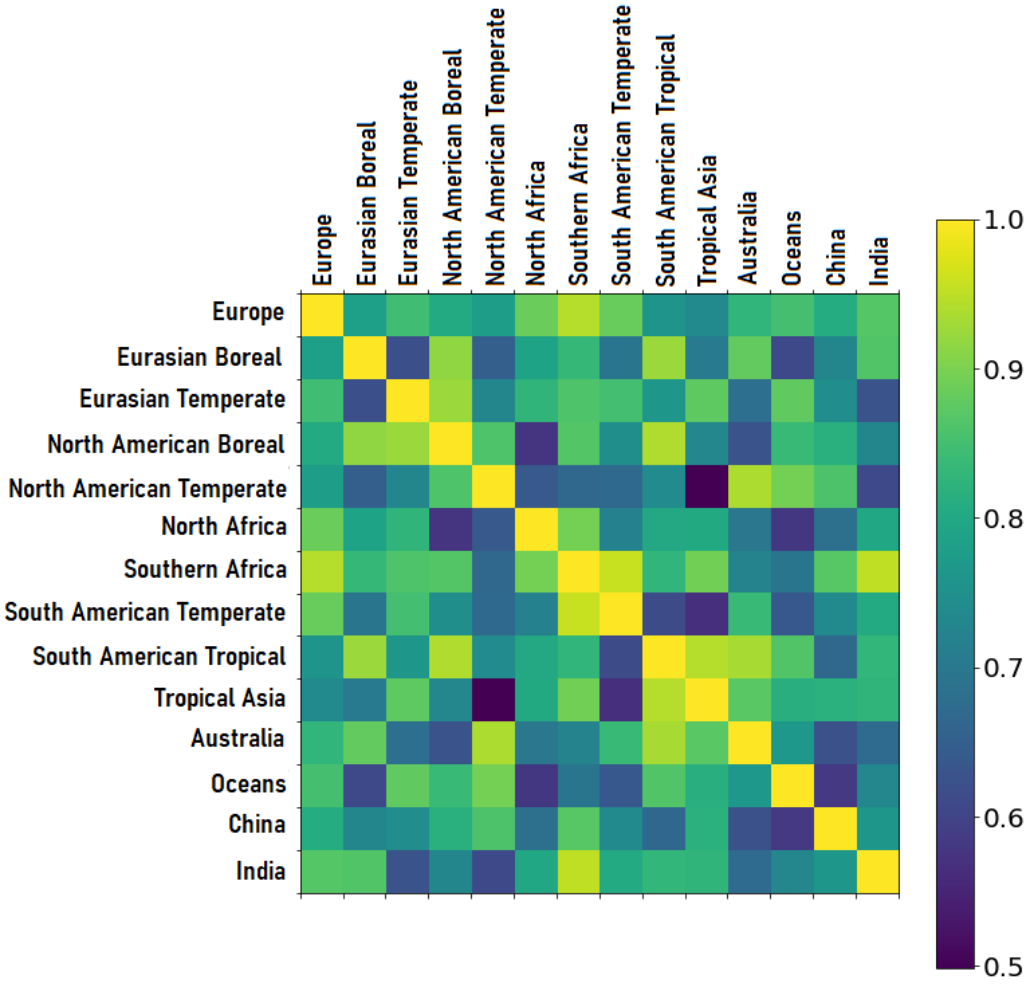

Figure 2.18: Correlation between regions solved for in the δ^{13}C inversions, using ground-based δ^{13}C data as a constraint. Values are calculated from the normalisation of the error covariance matrix (Equation 2.6), as in Figure 2.17.

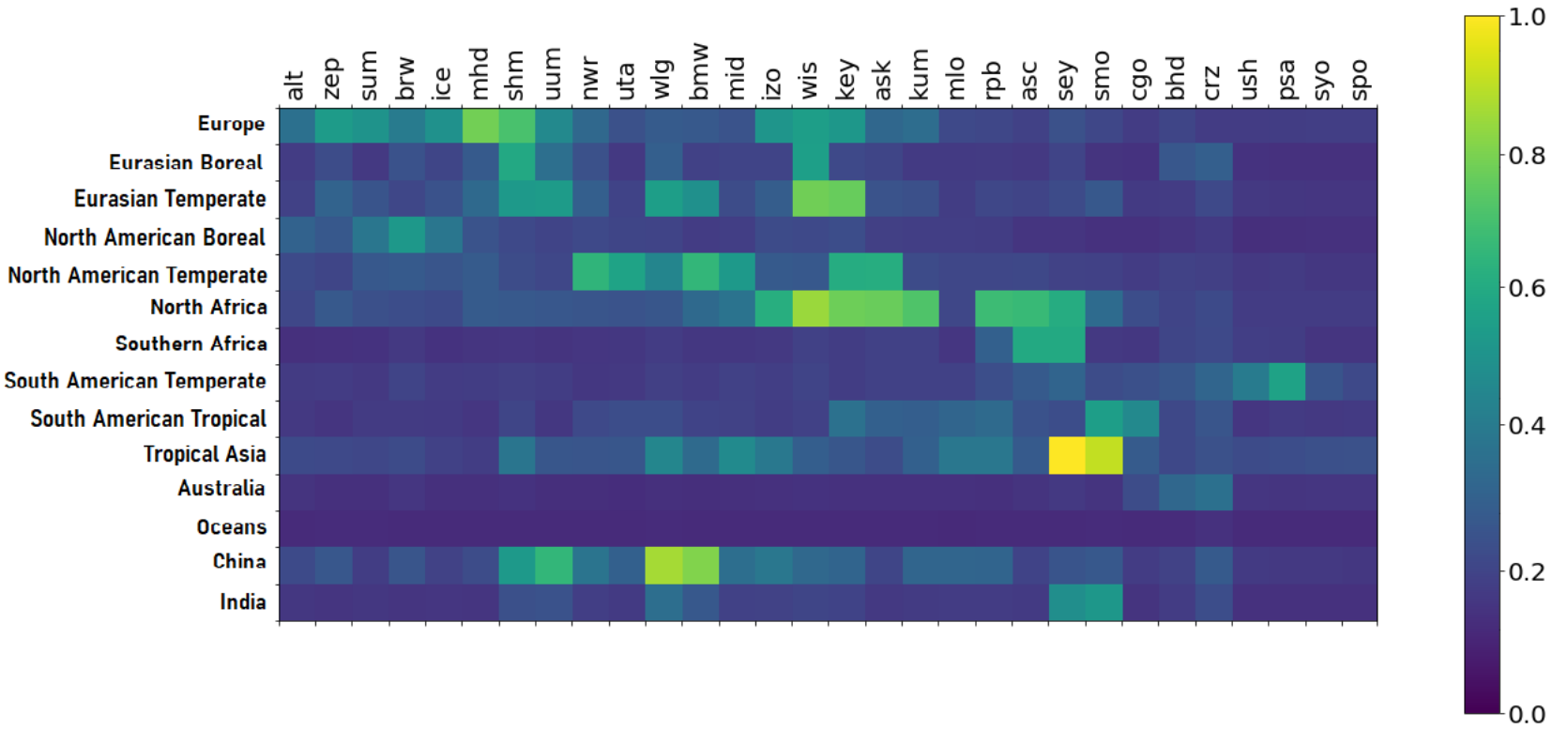

Figure 2.19: Matrix of contribution functions for the CH_4 inversion, indicating the extent to which different sites constrain different regions in the CH_4 inversion.

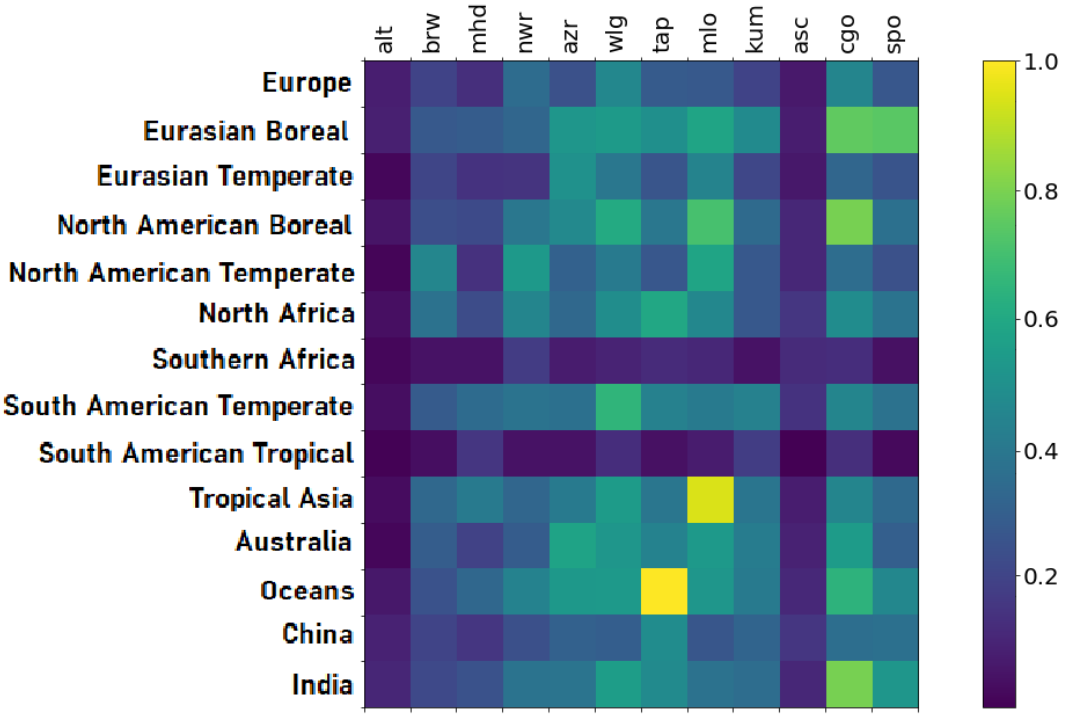

Figure 2.20: As in Figure 2.19, for the δ^{13}C inversion.

2.4 Conclusions

Regional CH_4 emission estimates and $\delta^{13}C$ signatures have been estimated for the period 2004-2020, inclusively, by fitting the GEOS-Chem 3-D atmospheric chemistry transport model to ground-based *in situ* amount fraction data and GOSAT atmospheric column data using inverse methods. Collectively, these results indicate that the post-2007 increase in CH_4 emissions are best explained by a progressive latitudinal shift in emissions from the northern mid-latitudes to tropics latitudes. This shift is less obvious over shorter periods. *A posteriori* CH_4 emission estimates inferred from both the ground-based and GOSAT data show larger tropical emissions, particularly over North Africa, Tropical Asia, and Tropical South America, at the same time as the mid-latitudinal emission proportion decreases. Source signature estimates inferred from the $\delta^{13}C$ measurements over the same time period shows that the latitudinal shift in CH_4 emissions is due to larger proportion of biogenic sources. The results are broadly consistent with previous studies that focus on other periods (Fujita et al., 2020; Lan et al., 2021; McNorton et al., 2018; Nisbet et al., 2019; Yin et al., 2021).

Control calculations are used monthly 3-D distributions of OH without any year-to-year variation. To explore how changes in OH might affect these results, a sensitivity experiment was run, for which the monthly 3-D OH fields were decreased 0.5%/yr from 2004 to 2019, inclusively, based on values proposed by previous studies (Turner et al., 2017). For this sensitivity experiment, the OH results are within a few percent of the control calculations and steadily decreasing OH concentrations are not responsible for observed changes in the distribution of CH_4. Also considered is how a proposed larger 5% change in 2020 (Laughner et al., 2021; Miyazaki et al., 2021), due to widespread COVID-19 related emission reductions in nitrogen oxides, affected results. This results in smaller CH_4 emissions increases during 2020, as expected, but they are still within control *a posteriori* emissions estimates for 2020.

Poor geographic coverage of ground-based data results in larger uncertainties for regional emission estimates that are poorly covered, i.e., high and low latitudes. For total CH_4, this deficiency can be partly addressed using the satellite data, but isotopes are not currently retrieved reliably from satellite remote sensing instruments. In this study, there are only three long-term measurement sites for $\delta^{13}C$ employed in the Southern Hemisphere. A consequence of this data sparseness is strong correlations between source signatures from neighbouring regions (Figure 2.18). The study was further limited by picking measurements sites for which data are available over the study period (Figure 2.1). Source sector signatures $\delta^{13}C$ are taken as mean values from Sherwood et al. (2017), representing current best knowledge of sectoral signatures. Different sectors produce a range of possible $\delta^{13}C$ values, and there are significant overlaps between recorded source signatures (Douglas et al., 2017). These data have greater value when they are used in a broader context with other data, as described in this study. Satellite observations are also used to identify that large-scale emission changes over regions that coincide with wetlands. The collective evidence demonstrates that increasing

natural, tropical emissions play a significant role in the observed atmospheric growth of CH_4. Greater confidence in source attribution of changes in atmospheric CH_4 may come from collecting and interpreting δD and multiply-substituted 'clumped' isotopes (Douglas et al., 2017), alongside δ^{13}C. This needs to be accompanied by laboratory and field measurements of these isotopes to improve delineation between different sectors. Increased sampled frequency of field measurements could be performed using continuous isotope ratio monitoring instruments (as described in Chapters 3 and 4).

This work is also consistent with recent studies that have reported anomalous large CH_4 emissions over eastern Africa (east Africa and the Horn of Africa) due to elevated rainfall over upstream catchment areas (Lunt et al., 2019, 2021; Pandey et al., 2021). These large-scale precipitation changes have been linked with the positive phase of the Indian Ocean Dipole (Feng et al., 2022), which describes a sea-surface gradient over the Indian Ocean. Similarly, increase CH_4 emissions over the Amazon basin (Wilson et al., 2021) are linked with large-scale changes in climate (Feng et al., 2022).

These substantial increases in natural CH_4 emissions will have major implications for achieving the goals of the Paris Agreement (Nisbet et al., 2019). It is more difficult to reduce natural emissions than to reduce anthropogenic emissions, and so the increased natural emissions found here could throw off emissions reductions efforts. There will therefore be additional pressure to reduce anthropogenic emissions (including individual's carbon footprints), in order to offset these increasing emissions from natural sources.

Overall, this chapter has achieved the aim of the first overarching research question for the thesis -to understand how CH_4 amount fractions and isotope ratios have varied over the period 2004-2020, and to understand what regions and sources are responsible. Inversion results indicate that biogenic tropical emissions are responsible for the observed variations in both CH_4 and δ^{13}C from ground-based *in situ* monitoring stations. This feeds into the overall thesis aim of considering ground-based *in situ* capability, as the work has shown that ground-based *in situ* isotope ratio measurements are currently insufficient to separate source signature contributions from individual regions.

2.4.1 Future Work

Future work arising from this chapter should concern more regular measurements of rare isotopologues of CH_4, which should be the aim of future measurement campaigns. Greater confidence in source attribution of changes in atmospheric CH_4 will come from collecting and interpreting a wider range of CH_4 isotope ratios, including δD and multiply-substituted 'clumped' isotopes (Douglas et al., 2017). This needs to be accompanied by laboratory and field measurements of these isotopes to improve delineation between different sectors. Furthermore, trends in OH and other sinks could be examined in more detail in the future, for

example how the examined OH trends affect atmospheric δ^{13}C. Zhao et al. (2019) found that OH may actually have been following an increasing trend from 2000-2016, which could be assessed. The impact of increasing OH trends upon CH_4 and δ^{13}C could be examined in the future.

Chapter 3

Data Processing for Analysis of δ^{13}C and δD Methane Using a Laser Spectrometer Based System

Aspects of this work are covered in the published work 'Boreas: A Sample Preparation-Coupled Laser Spectrometer System for Simultaneous High-Precision In Situ Analysis of δ^{13}C and δ^{2}H from Ambient Air Methane', Rennick et al. (2021).

3.1 Introduction

The overall aim of the thesis is to examine atmospheric ground-based monitoring capability, to understand changes in atmospheric methane (CH_4) budget. This chapter advances the thesis by addressing the second research question as outlined in Chapter 1: How should data from a newly developed laser-based measurement system be processed to produce high precision data for analysis? This chapter addresses the question by first detailing a new CH_4 isotopologue measurement instrument, designing a data processing method for this instrument, and finally by demonstrating the data processing method on selected sample data. The analysis will examine the instrument's capability to monitor changing CH_4 sources.

Atmospheric measurements of CH_4 amount fractions and isotope ratio, are used to estimate the magnitude of CH_4 emissions sources. Observations of CH_4 isotope ratios indicate the process or sector that produces emissions, which would significantly enhance our ability to improve reported emissions inventories, leading to a better understanding of how greenhouse gas emissions are changing over time.

A result of Chapter 2 was that there is a lack of atmospheric monitoring stations which have a reliable, high precision, long-term time series of isotope ratio values. This limits capability to differentiate between emissions drivers both on global and regional scales. Current methods to measure CH_4 isotope ratios are not at the point of routine development as they have

significant requirements in terms of space and maintenance. Even in a laboratory environment, the limitations of cost and time in building instruments to make such measurements are significant, and relatively few laboratories have such measurement capability; fewer than 20 laboratories around the world are performing ongoing measurements (Umezawa et al., 2018).

The previous chapter focused solely on δ^{13}C isotope ratio data, due to a paucity of δD measurements, both temporally and geographically. δD is not as frequently measured as δ^{13}C because the isotopologue CH_3D appears in lower amount fractions than $^{13}CH_4$ (Table 1.2), and is therefore more challenging to measure. As a result of being less frequently measured, δD source signatures are less clearly defined than those of δ^{13}C (Figure 1.2), however δD signatures have the potential to delineate between fossil fuel and biogenic sources. Emission inventories do allow for a sectoral breakdown of CH_4 emissions, however methods of verifying these emissions are limited. Measurements are used to feed into models which compare measurements to the inventory emissions; this allows us to understand drivers behind emission sources and increases. Therefore, superior measurement techniques are required in order to adequately quantify and verify emissions estimates. This would inform policy makers, ultimately allowing emission reductions targets set out by national and international government bodies to be met.

3.1.1 Isotope Ratio Measurements of CH_4 Using Laser Based Methods

The increased availability of laser spectroscopy-based techniques for CH_4 isotope ratio measurement, which operate independently at increased frequency and reduced maintenance cost, has made *in situ* analysis more accessible. This allows for more frequent and widespread measurements, while increasing data quality. However, high signal-to-noise ratio and high-quality instrument stability are key for making these measurements.

High precision isotope ratio measurements of CH_4 using optical techniques is still in its infancy. Currently, δ^{13}C and δD measurements are typically made using Isotope Ratio Mass Spectrometry (IRMS) (Bock et al., 2014, 2010; Brass & Röckmann, 2010; Fisher et al., 2006; Sapart et al., 2011; Schmitt et al., 2014). IRMS consists of ionising a gaseous sample, then accelerating it on a track where it is deflected by a magnet, and measured by a series of Faraday cups. Lighter ions bend on a tighter radius, leading to ions being separated based upon their mass/charge ratio. The result is isotope ratio values (e.g. $^{13}C/^{12}C$). IRMS instrumentation is commercially available and provides a high sample analysis turnover of several minutes per sample. For CH_4 carbon isotope ratio analysis, the sample is generally oxidised into CO_2 (following removal of CO_2 and other gases in the air sample, using a preconcentration system) before being passed into the spectrometer. For hydrogen isotope ratio analysis, the CH_4 is pyrolised into H_2 (Brass & Röckmann, 2010). IRMS is able to produce high levels of precision, approximately 0.05‰ for $^{13}C/^{12}C$, and 1.0‰ for D/H. This approach is unable to process condensable gases, or molecules such as water, meaning samples are required to undergo

preparation prior to analysis. Furthermore, IRMS is expensive, large, and requires skilled operators. In most large-scale networks, flasks are taken in the field before being transported back to a laboratory setting to be analysed. This limits the temporal and spatial resolution of measurements.

Laser Absorption Spectrometry is a non-destructive optical technique which allows direct and precise measurements of CH_4 isotopologues. In this technique, a laser light source is fired on a sample and is tuned through different wavelengths. The light absorption of the laser is measured by a detector, as a function of the wavelength being swept over. The amount of absorption at a given frequency is related to the concentration of individual isotopologues in the sample. These instruments are generally less bulky and more portable than IRMS instruments and potentially require less maintenance, hence allowing for more spatially diverse deployments locations over longer time periods. However, a significant issue with optical measurements is that they are not able to make sufficiently high precision measurements of δ^{13}C and δD due to the low abundance of CH_4 present in ambient air, this then results in poor signal-to-noise ratio. One method to improve the signal-to-noise ratio is to preconcentrate the analyte in question (here, CH_4) out of the air sample and analyse via an optically based instrument. This technique is known as 'preconcentration', and is described in the next section, along with improvements on current methods.

3.1.2 Preconcentration

Preconcentration is performed by using a cold trap containing an adsorbent trapping material, to which analytes can bind to and diffuse through, depending on the temperature. The trap is first cooled so that the adsorbing capacity for the target substance (here CH_4) is sufficiently large, while the majority of the remaining bulk gases (such as N_2, O_2, Ar) pass through. During desorption, the trap temperature is gradually increased in a step-wise manner so that any contaminating analytes (which were co-adsorbed with the CH_4) are eluted separately.

Other measurements of CH_4 isotopologues using optical instruments without preconcentration, specifically of $^{13}CH_4$ and $^{12}CH_3D$, were performed by Bergamaschi et al. (1994). They reported precision of 0.44‰ and 5.1‰ on measurements for δ^{13}C and δD respectively. Rella et al. (2015) and Miles et al. (2018) performed field-based measurements of δ^{13}C using optical measurement, with precision of 0.1‰ and 0.2‰ respectively. The recorded precision on these studies considerably worse than IRMS (0.05‰ on δ^{13}C and 1.0 on δD), which demonstrates the need for additional steps (preconcentration) to improve precision.

The approach of using combined preconcentration and laser spectroscopy techniques to measure CH_4 isotope ratios, has been examined in previous studies. Eyer et al. (2016) developed a system for preconcentrating CH_4 before measurement by a laser spectrometer. They were successful in making measurements of both δ^{13}C and δD, however the recorded precision was worse than traditional IRMS (they achieved precision of 0.19‰ for δ^{13}C and

1.9‰ for δD). This study also highlighted significant problems for analysis, that included the potential for breakthrough on traps (due to the large sample volume needed) and the issue of variable oxygen content of the trapped sample, that creates a matrix effect in analysis by laser spectroscopy. It is therefore an aim in the isotope ratio metrology field to construct an optical instrument with improved precision, capable of making regular measurements of CH_4 isotope ratios.

3.1.3 Data Processing

A key difference between IRMS and current optical techniques is IRMS measures isotope ratio values of samples ($^{13}C/^{12}C$, D/H), whereas optical techniques can measure the amount fractions of individual isotopologues ($^{12}CH_4$, $^{13}CH_4$ and $^{12}CH_3D$). These values must be calibrated and processed in order to produce useful and useable δ values that are useful for future modelling studies to understand variations in CH_4 emissions sources. Data processing approaches have been geared towards IRMS measurement (i.e. processing based upon isotope ratio values) but with the emergence of optical techniques, new approaches for data processing must to be established. This chapter therefore develops a data processing approach for an optical continuous monitoring instrument.

Data analysis approaches for optical instruments have been examined by several studies (e.g. Bowling et al., 2003; Braden-Behrens et al., 2017; Esler et al., 2000; Flores et al., 2017; Griffis et al., 2005; Griffith, 2018; Griffith et al., 2012; Miles et al., 2018; Pang et al., 2016; Rella et al., 2015; Steur et al., 2021; Tans et al., 2017; Tuzson et al., 2011; Vardag et al., 2015; Wehr et al., 2013; Wen et al., 2013). Griffith (2018) assess and outline approaches for calibrating on $\delta^{13}C$ from CO_2, assimilating data from earlier studies (Flores et al., 2017; Griffith et al., 2012; Tans et al., 2017). They calibrate the data using two approaches: an 'isotopologue' and a 'ratio' approach, which involves calibrating on either directly measured isotopologue amount fractions or on calculated isotope ratio values (which is a similar approach to that followed for calibrating on IRMS values). They find that the ratio approach results in corrections having to be made for amount fraction dependency, wherein ratio values varying depending upon CH_4 amount fraction as a result of not calibrating the isotopologue values. The isotopologue approach is therefore recommended. Similarly, Steur et al. (2021) examine data processing for an optical instrument which measures $\delta^{13}C$, $\delta^{18}O$ and $\delta^{17}O$ of CO_2 simultaneously. They perform both calibration approaches on sample data from the optical instrument and find that both calibration approaches result in similar precision for $\delta^{13}C$. They recommend the isotopologue method so as to avoid the amount fraction dependency. This chapter expands upon these works by applying the calibration approaches to measurements of CH_4 isotopologues from an optical instrument, and considering further steps (such as a drift correction and offset adjustment to align data with external laboratories) to obtain data with best possible precision.

The chapter focuses specifically on the 'Boreas' instrument, a new CH_4 preconcentrator capable of coupling to a laser spectrometer. Here, the Boreas system is described and an approach for data analysis examined, and some sample data analysis demonstrated. Rennick et al. (2021) describe the 'Boreas' preconcentration system in terms of the hardware, the measurement procedures and calibration approach. This chapter expands upon that work by including a rigorous and transparent assessment of the options for drift in instrument response and offset correction during calibration, in order to maximise the quality of the new measurement data set in terms of frequency, precision and accuracy of measurement (for isotope ratios and the reported CH_4 amount fractions).

3.2 *In Situ* System Setup

'Boreas' is new a CH_4 preconcentration instrument coupled to a laser spectrometer, which is able to make high precision, continuous measurements of CH_4 isotopologues. This instrument was constructed at the UK's National Physical Laboratory (NPL) in 2019. It is composed of multiple parts: a preconcentrator system attached to a sampling interface, attached in turn to an Aerodyne mid-infrared dual-laser spectrometer (Aerodyne Research, Inc, TILDAS-FD-L2), which measures individual isotopologues $^{12}CH_4$, $^{13}CH_4$ and CH_3D. The spectrometer is calibrated using high amount fraction primary reference materials (AF PRMs) of CH_4 in nitrogen, and the preconcentrator is calibrated separately using a compressed whole air reference standard. The isotope ratio values of the AF PRMs were assigned from measurements made by RHUL ($\delta^{13}C$) and from average values of measurements made at Mace Head Observatory in western Ireland (δD). The whole air reference is sampled at regular intervals by the instrument, in an identical way to the ambient air sample. The system is set up to allow remote operation (it is fully automated) and the only consumables are the N_2 carrier gas and the PRM gases. The instrument is described in full by Rennick et al. (2021).

Essential to setting up this new instrument is establishing the correct data processing approach for processing from isotopologue amount fractions to δ values.

3.2.1 Heathfield Atmospheric Monitoring Site

The initial runs of the instrument took place at NPL, sampling from a roof inlet at 17 m height (51.42° N, 0.34° W). This location is nearby local pollution sources considering its positioning in Greater London (for example, gas pipes, small fires and waste facilities). Since May 2021 the instrument has been based at the Heathfield atmospheric monitoring site, West Sussex (50.98° N 0.23° E), where operation and further improvements have continued. The monitoring site is located away from strong sources of pollution near a small market town (the predominant southwesterlies here pass through little land from the Atlantic Ocean). The aim of measurement in this location is therefore to monitor the isotopic signature of

regional emissions. Measurements from this site are used to calculate emission maps of trace gas species in the UK. The Monitoring Site is part of the UK Deriving Emissions linked to Climate Change (UK DECC) network, as well as a World Meteorological Organisation Global Atmosphere Watch (WMO-GAW) regional site. The site has been active since 2014, installed by the University of Bristol, and has been operated by NPL since 2017.

Alongside CH_4 measurements, there are instruments in place to measure the amount fraction of other major GHGs including carbon dioxide (CO_2), nitrous oxide (N_2O), SF_6 and other trace gas species such as carbon monoxide (CO), ozone (O_3), nitrogen dioxide (NO_2) and radon (Rn). The air is sampled from a 100 m and 50 m height. The large inlet height gives the tower a large sampling footprint covering south-east England and northern Europe. These measurements are used to validate the UK greenhouse gas emissions for the UK government's Department for Business, Energy and Industrial Strategy, reported in the annual submission to the UNFCCC (Manning et al., 2022).

3.2.2 Preconcentration Unit

The preconcentration unit for Boreas was built at NPL. The trap consists of a 2 mm tube containing HayeSep-D ®, which is wrapped around a cylindrical standoff attached to the cold end of a cryocooler (CryoTel GT Sunpower Inc., USA). This cryocooler reaches temperatures of 40 K, and is kept in a vacuum. The temperature of the trap is monitored using a pair of thermocouples attached to the inside of the the standoff and trap tubing.

3.2.3 Measurement Protocol

One measurement cycle consists of four steps (outlined in Figure 3.1). First, the air sample is brought to the head of the trap, and dried using a Nafion drier. The trap is opened for 540 seconds after being purged. After entering the trap, the air sample diffuses along and CH_4 is separated from bulk gases such as O_2 and N_2 based on the temperature ramp. The trap temperature is not controlled by active heating during trapping. After approximately 540s, the trap has reached 103 K and trapping is complete, with trace gases from 5 L of sampled air contained on the trap. The trap is then slowly heated to 373 K and flushed with N_2, separating CH_4 from other trace gases. The next step is elution, wherein the CH_4 is directed into the spectrometer sampling cell. The exact temperature and pressure for this step have to be optimised, in order to transfer maximum CH_4 into the spectrometer. Finally the trap is reconditioned, where the trap is purged and allowed to cool passively, before the cycle can start again.

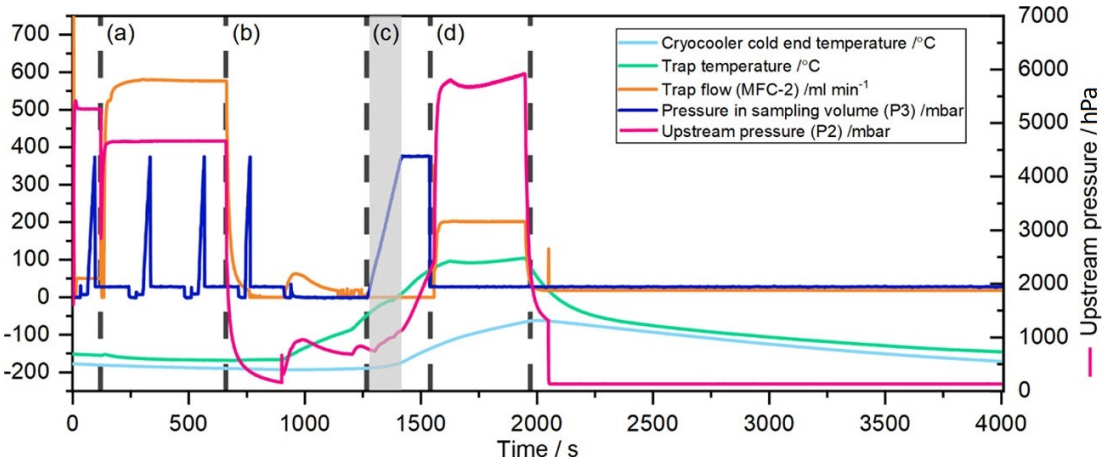

Figure 3.1: Stripchart of various instrument parameters during a measurement run. Left axis: cryocooler cold-end temperature; trap temperature (thermocouple attached midway on the outside of the trap tubing); trap flow (recorded using the mass flow controller downstream of the trap); and sampling volume pressure. The sampling volume pressure's four peaks between 0 and 750 s are loading of the standards, independent of the preconcentrator operation. Right axis: upstream pressure. Vertical dashed lines mark the boundaries of each phase (a) trapping, (b) separation, (c) elution, and (d) reconditioning.

3.2.4 Spectrometer

The laser spectrometer instrument is a commercial high-resolution dual-laser direct absorption instrument (Aerodyne Research, Inc, TILDAS-FD-L2).

Once the ambient air sample has been preconcentrated, it is loaded into the spectrometer cell to a target pressure and held during the measurement. After a stabilisation period of 30 seconds, a pair of quantum cascade lasers are swept over two frequency ranges (1293.702-1293.816 cm^{-1} for $^{12}CH_4$ and $^{13}CH_4$ and 1306.883-1307.077 cm^{-1} for $^{12}CH_4$ and $^{12}CH_3D$), at a rate of 1.7 kHz. The light transmission is captured and the spectrum is fitted once a second by the spectrometer software (TDLWintel, Aerodyne Research Inc.) and the average response taken over the final 100 seconds; the measurement precision is the standard error of this average.

The spectrum is fitted for each absorption line and a polynomial fit to the baseline. The sample pressure and temperature are measured in the absorption cell, and the position, strength and line broadening parameters (due to the nitrogen background gas) used in calculating the spectral fit are taken from the HIgh-resolution TRansmission molecular AbsorptioN (HITRAN) database (Rothman et al., 2005). The entire recorded absorption spectrum is matched to the strong $^{12}CH_4$ absorption line, meaning all absorption lines are fitted simultaneously, reducing interference.

3.2.5 Reference Materials

Two, bracketing, high-AF PRMs prepared from CH_4 in N_2 were used as calibration standards for the spectrometer, by directly filling into the spectrometer cell (described as 'low' and 'high' standards). These PRMs were all originally filled under background air from Mace Head Observatory, western Ireland. Two further high-AF PRM are used to validate the spectrometer calibration; a calibration target 'CT' using CH_4 from the same source, and a spectrometer target 'ST' containing CH_4 from a different source, filled under thermogenic air in Greater London. Whole-air gas standards are also used, which have also been filled at Mace Head Observatory in Ireland, under background conditions from the north Atlantic. The compressed whole-air gas standards are treated in the same manner as air samples to test the performance of Boreas. The whole air standard is named 'Boreas Target', denoted here as 'BT'. The synthetic AF PRMs enabled the calibration and performance of the spectrometer to be known separately, and BT is used to assess the performance of the full Boreas system. One BT tank is expected to be ran for six months, at which point another tank of air from Mace Head is sampled, and used to replace the former.

A full measurement run consists of measurements of the high and low standards by the spectrometer, followed by the 'sample' measurement, which would either be the air sample or BT. Both the sample and BT are preconcentrated before being measured for isotopologues by the spectrometer.

The δ^{13}C values for BT and the AF PRMs were assigned, from values externally measured at Royal Holloway, University of London (RHUL), using a modified Gas Chromatography IRMS system (Trace Gas and 362 Isoprime mass spectrometer, Isoprime Ltd.; as described by Fisher et al. (2006)). Each cylinder was analysed 12 times in October 2020. These externally-measured values were obtained for quality control on Boreas measurements and to provide a link to other international laboratories (Umezawa et al., 2018). The RHUL measured δ^{13}C values for BT and ST are listed in Table 3.1, along with recorded precision.

RHUL did not measure δD on the AF PRMs or BT due to instrumental issues. Therefore, the 'known' δD values have to be assigned based on another metric. The value chosen for BT is the mean value of monthly-averaged δD from the Mace Head Observatory in western Ireland, which is a part of both the UK Deriving Emissions linked to Climate Change (DECC) network and the NOAA-INSTAAR network. Mace Head is a background measurement site (i.e. not strongly influenced by pollution events). It is both the site within the NOAA-INSTAAR network closest to the Heathfield atmospheric monitoring site, and where BT was filled. The values are averaged over the period 2004-2009, the time period for which the site was measuring δD. The resulting values are -92.63‰ for δD for BT and -192.70‰ for the AF PRMs (these were sampled under thermogenic air). Each BT tank has been estimated to last for six months under measuring after every air measurement. Each new BT tank is assigned a δD value based upon the Mace Head average, regardless of the time of year it was sampled. The new

tank is measured to determine how it differs from the previous tank, and a δ value therefore assigned to the new tank. This may lead to inaccurate estimation of the δD signature of BT and the PRMs. Because of uncertainty in the assigned value, it is important to test the impact of this assigned value on the AF PRMs upon BT measurements, and upon the precision of the measurements as a whole. Figure 3.2 shows that the calibrated value on BT varies depending upon the assigned value on the AF PRMs. However, the chosen value did not have an impact upon the precision on Boreas data.

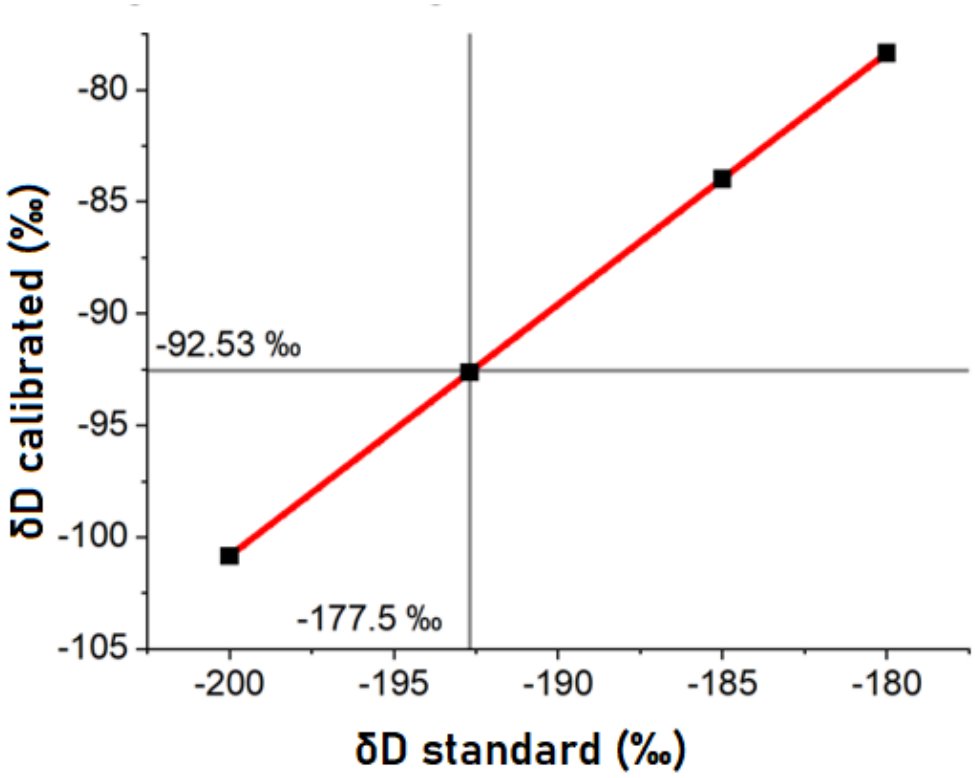

Figure 3.2: Testing how assigning different δD values to the AF PRMs (δD standard, ‰) affects the measured value for δD on BT (δD calibrated, ‰).

Table 3.1: Table of RHUL-measured values for BT and ST for δ^{13}C (and assigned uncertainties). Estimated values for δD for BT are based upon average values from NOAA-INSTAAR measurement sites, and for ST are typical values for thermogenic air. There are therefore no values for δD uncertainty.

Tank	Mean δ^{13}C (‰)	δ^{13}C Uncertainty (‰)	Mean δD (‰)	δD Uncertainty (‰)
BT	-47.41	0.04	-92.63	-
ST	-41.27	0.06	-192.7	-

3.3 Calibration

Two possible approaches for calibrating Boreas isotope ratio values are examined; the 'isotopologue' and 'ratio' method. Both of these approaches effectively calibrate isotope ratio data (Griffith, 2018; Steur et al., 2021), and so both are examined to determine which is the best approach for Boreas data processing.

3.3.1 Isotopologue Method

In order to calibrate isotopologue values as measured by Boreas, the first method examined is the 'isotopologue' method of calibration (following Griffith, 2018, Rennick et al., 2021, Steur et al., 2021). In this calibration approach, individual isotopologues ($^{12}CH_4$, $^{13}CH_4$ and $^{12}CH_3D$) are calibrated by examining the relationship between measured and known isotopologue amount fractions (as measured by RHUL) on the AF PRMs. The amount fractions for each isotopologue on the AF PRMs are not measured by RHUL, just the δ values and total amount fraction, so the amount fractions of individual isotopologues need to be calculated. The isotope ratio values are calculated by rearranging the δ equation from Chapter 1:

$$^{13}r = {}^{13}r_{ref} \times (1 + \delta^{13}C), \tag{3.1}$$

$$^{2}r = {}^{2}r_{ref} \times (1 + \delta D), \tag{3.2}$$

where ^{13}r is $^{13}C/^{12}C$ and ^{2}r is D/H. $^{13}r_{ref}$ and $^{2}r_{ref}$ are the reference standards from isotope ratio calculations (VPDB and VSMOW respectively). The amount fractions for each isotopologue are:

$$X_{211} = \frac{1}{R_{sum}}, \tag{3.3}$$

$$X_{311} = \frac{^{13}r}{R_{sum}}, \tag{3.4}$$

$$X_{212} = \frac{4 \times {}^{2}r}{R_{sum}}, \tag{3.5}$$

where 211 refers to $^{12}CH_4$, 311 is $^{13}CH_4$ and 212 is CH_3D, and R_{sum} is the sum of products of all isotope ratios, calculated by:

$$R_{sum} = (1 + {}^{13}r)(1 + {}^{2}r)^4. \tag{3.6}$$

The relative amount fractions of each isotopologue are then multiplied by the total CH_4 amount fraction for the AF PRMs as measured by RHUL (Y_{CH_4}), to give each isotopologue's amount fraction:

$$Y_{211} = X_{211} \times Y_{CH_4} = \frac{Y_{CH_4}}{R_{sum}}, \tag{3.7}$$

$$Y_{311} = X_{311} \times Y_{CH_4} = Y_{CH_4} \times \frac{^{13}r}{R_{sum}}, \tag{3.8}$$

$$Y_{212} = X_{212} \times Y_{CH_4} = Y_{CH_4} \times \frac{4 \times ^2 r}{R_{sum}}. \tag{3.9}$$

The Boreas measured and externally-measured amount fractions for each isotopologue are then linearly related:

$$I = aY + b, \tag{3.10}$$

where I is the instrument response (Boreas measured amount fraction) and Y is the externally-measured amount fraction for each isotopologue on the AF PRMs.

The gradient (a) and y-intercept (b) for a run using the known isotopologue amount fractions of the high and low AF PRMs are calculated using a regression line. The next step is to apply a and b to calculate the calibrated values of the isotopologues for the air or BT sample, using Equation 3.10; where I is the measured values and Y is the calibrated value of isotopologue amount fraction. As the standards are measured every run, a and b will vary between each measurement run.

Precision (for which 4-point rolling standard deviation of BT is recorded) and the mean RHUL offset following calibration are recorded in Table 3.2.

It is important to verify that the spectrometer used here produces a response directly proportional to known value of isotopologue amount fraction. Ideally, this assumption of linearity is valid, and this procedure will report an amount fraction directly proportional to the amount fraction. At high CH_4 amount fractions, however, the line shapes produced within the spectrometer can be distorted, resulting in a deviation from a proportional response that can be quantified using an intercept and gradient.

This linearity is tested using a set of four samples produced separately from the AF PRMs. The same parent CH_4 is used to prepare the four samples (which is diluted in nitrogen). Neglecting fractionation during dilution, the isotopologue-specific instrument response will be proportional to the sample CH_4 amount fraction.

Figure 3.3 plots the residuals from the linear regression of instrument response to amount fraction for the four samples for each isotopologue, and gives the Pearson correlation coefficient for each. Residuals are shown because of the different amount fractions tested. All show high correlation (> 0.9), meaning that the instrument response is linear to the amount fraction of the AF PRM being recorded. This justifies using a regression fit for instrument calibration through the isotopologue method.

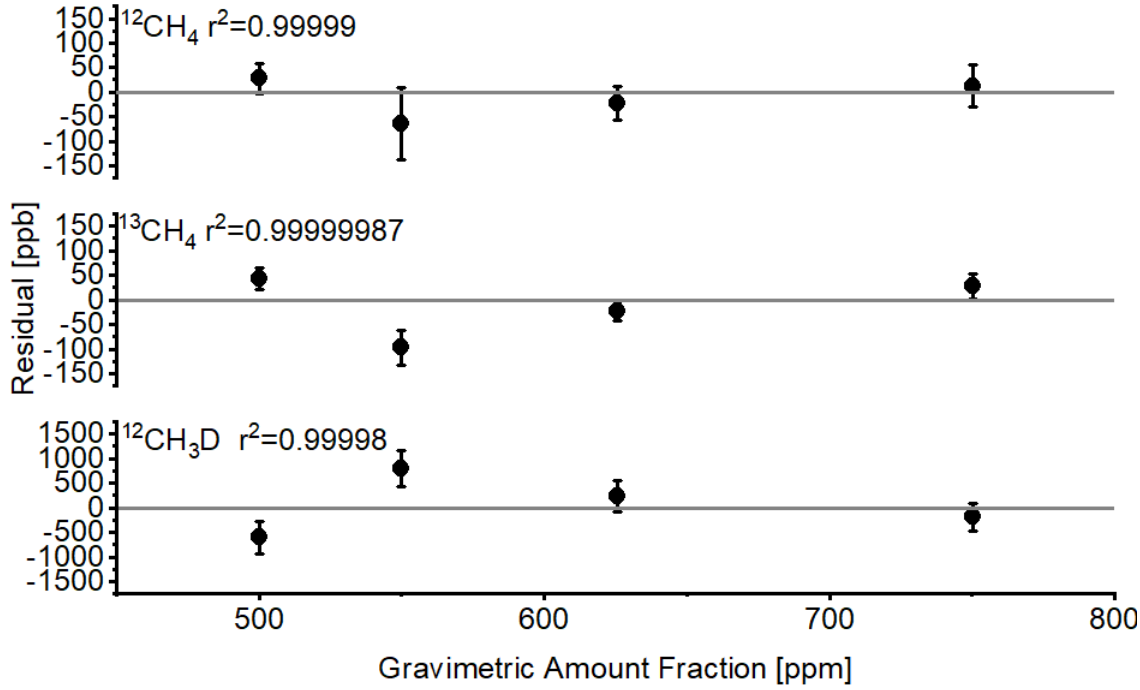

Figure 3.3: Residuals (ppb) from the linear regression of a sample of amount fraction data reported by the Aerodyne spectrometer software (TDLWintel) part of Boreas, with the 'known' values of the CH_4 amount fractions on the sample from RHUL. The label for each plot gives the species and the Pearson correlation coefficient, to test whether the assumption of linearity between measured and known values is valid for calibration calculations. Gravimetric amount fraction is used in this case, instead of the amount fraction (ppb; nmol/mol) used in the rest of the thesis, because RHUL measure gravimetric amount fraction on the tanks, which is then converted to amount fraction for Boreas data processing.

3.3.2 Ratio Method

An alternative approach to the 'isotopologue' approach of calibration is to calibrate based upon isotope ratio values (Griffith, 2018; Steur et al., 2021). In this approach, the reference standard (VPDB for δ^{13}C and VSMOW for δD) is calculated from each measurement run using externally- and Boreas-measured isotope ratio values, on one of the AF PRMs:

$$r_{VPBD,std} = \frac{r_{std}}{\delta^{13}C_{known} + 1}, \tag{3.11}$$

where r_{std} is the ratio of the measured values of $^{12}CH_4$ and $^{13}CH_4$ for the AF PRMs. The *known* subscript refers externally-measured δ value. The isotope ratio of the sample is then:

$$\delta^{13}C_{sample} = \frac{r_{sample}}{r_{VPDB,std}} + 1. \tag{3.12}$$

In following this approach for optical instruments, there arises an 'amount fraction dependency', wherein inaccuracies occur due to the instrument response for isotope ratio values varying between recorded isotopologue amount fractions, as a result of calculating isotope ratio values before calibration (Braden-Behrens et al., 2017; Flores et al., 2017; Griffith, 2018; Griffith et al., 2012; Pang et al., 2016; Rella et al., 2015; Steur et al., 2021; Wen et al., 2013). This dependency can be accounted for by considering the relationship between AF PRMs with different amount fractions (one 'high' and one 'low'), following:

$$m = \frac{\delta^{13}C_{high}}{I_{high} - I_{low}}, \tag{3.13}$$

where I is instrument response for $high$ or low amount fraction PRM, and δ^{13}C is the calibrated measured δ^{13}C value on the high amount fraction PRM. This is then applied to δ^{13}C of BT or air:

$$\delta^{13}C_{sample,corrected} = \delta^{13}C_{sample} - m(I_{sample} - I_{high}), \tag{3.14}$$

where I is the instrument response (measured value) for the given isotopologue.

The results of applying each calibration technique are detailed in Table 3.2. The difference in precision for each technique is within the uncertainty of the instrument data. The 'isotopologue' method results in better precision and lower offset compared with externally-measured values. Furthermore, it avoids having to characterise and account for the amount fraction dependence. This is therefore the calibration method which is pursued.

Table 3.2: Table of calibrated precision on δ^{13}C and δD for the Boreas Target (BT) tank, over the time series June 18-30th 2021. Both the ratio and isotopologue methods are explored. 'Mean RSD' is the average four-point rolling standard deviation to represent precision. 'Offset' is the difference between the average value and the externally-measured value for the tank (Table 3.1).

Method	δ	Mean value (‰)	Mean RSD (‰)	Offset (‰)
Isotopologue	δ^{13}C	-47.0956	0.0755	0.3144
Ratio	δ^{13}C	-47.0245	0.1024	0.3855
Isotopologue	δD	-92.3256	1.0134	0.3044
Ratio	δD	-92.2591	1.3870	0.3709

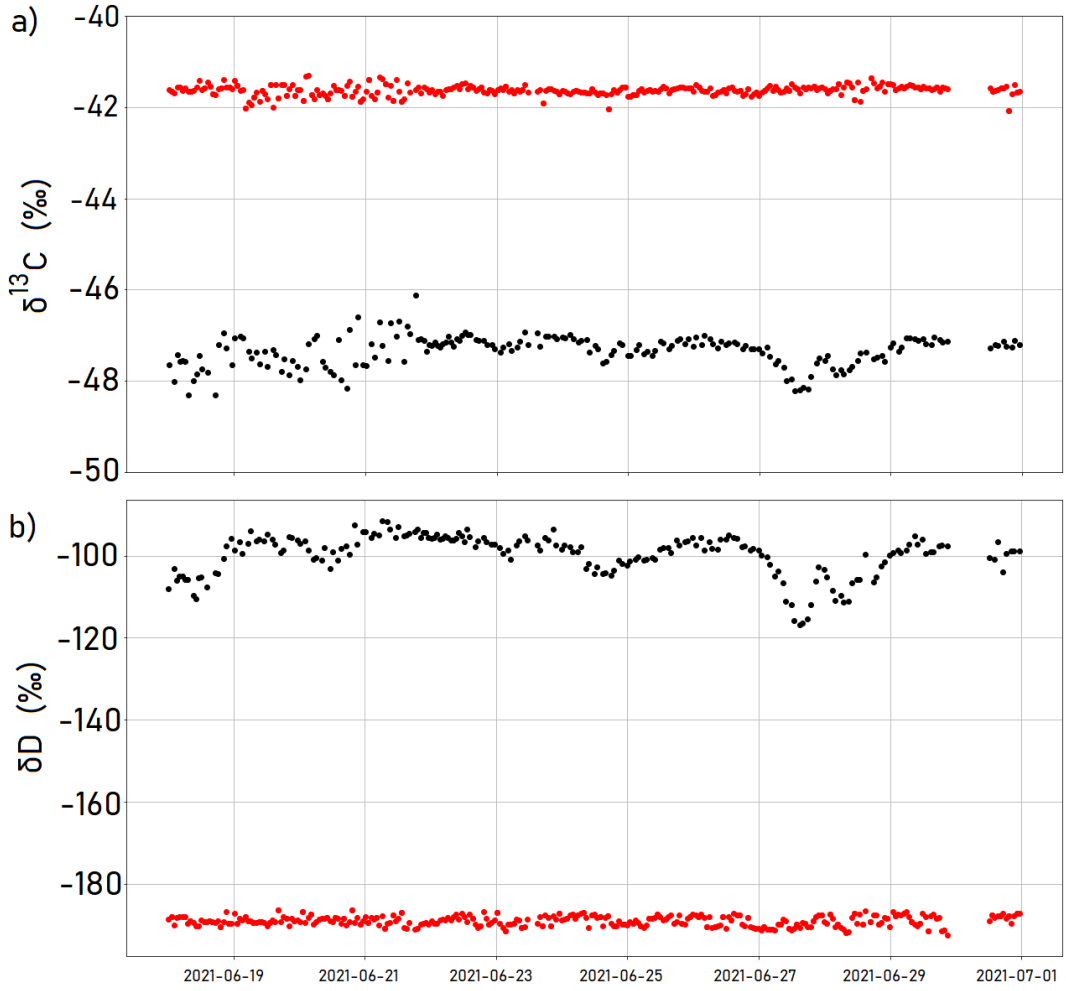

Figure 3.4: Time series of sample data as recorded by Boreas over the period June 18-30th 2021. a) δ^{13}C data and b) δD data, having been calibrated and drift corrected (‰). Red dots are ST data and black dots are air data.

3.4 Drift Correction

To further reduce the signal-to-noise ratio within Boreas, it is possible to account for drift within the instrument. Drift is a form of low-frequency noise, changing slowly in the instrument, which results in poor signal-to-noise ratio for the measurement of a reference value. The Boreas hardware is composed of many components, the accumulated drift of which over time results in a drifting of the measured isotopologues. Once measurements commence, measured values of isotopologues on the AF PRMs vary between measurements. The accumulated drift inevitably leads to uncertainty in our calibration procedure; therefore, drift must accounted for to ensure our system remains accurate and precise.

The timestamp originally assigned to each isotopologue measurement from Boreas is the beginning of each run cycle, rather than the exact time of the air sample measurement (Section 3.2). As such, a linear interpolation on a and b is performed each measurement cycle, between the timestamp and the exact time at which the air measurement is taken:

$$a_1, dc = \text{int}(a_1, a_2), \tag{3.15}$$

$$b_1, dc = \text{int}(b_1, b_2), \tag{3.16}$$

where a_1 and a_2 are the gradient to be drift corrected and the gradient of the following run respectively, and dc implies drift corrected. The same approach is applied for b, with b_1 and b_2 being the y-intercept to be drift corrected and of the following run, respectively. Calibrated isotopologue values are subsequently calculated. Table 3.3 and Figure 3.4 shows data from 18-30$^{\text{th}}$ June 2021, when Boreas was located at Heathfield atmospheric monitoring site, with drift correction performed. This time period was chosen for tests as it represents a period after deployment when the instrument was recording consistent precision.

Table 3.3 indicates that performing a drift correction on a and b decreases the four point rolling standard deviation of the data, compared with Table 3.2, by approximately 0.01‰ for δ^{13}C and 0.1‰ for δD. Therefore, for routine data processing, a drift correction on the calibration values is performed (gradient and y-intercept), calculated for each measurement run, using the isotopologue method of calibration.

Table 3.3: Drift corrected 4-pt rolling standard deviations for δ^{13}C and δD on the Boreas Target (BT) and Spectrometer Target (ST) tanks, covering the period June 18-30th 2021. The drift correction follows the isotopologue method. Number of measurements were 139 and 278 for BT and ST respectively.

Tank	Mean δ^{13}C (‰)	δ^{13}C Mean RSD (‰)	Mean δD (‰)	δD Mean RSD (‰)
BT	-47.1010	0.06780	-92.3843	0.9135
ST	-41.4785	0.04500	-190.4288	0.2313

3.5 Internal Offset Adjustment

The term 'internal offset adjustment' is used to refer to the procedure for accounting for differences between measurements made by Boreas and those of a lab which is tied to an international isotope ratio measurement scale. This enables comparisons of measurements between laboratories worldwide, and means the measurements can be used together in modelling studies. Boreas measurements are tied to RHUL measurements, through RHUL performing the external measurement of NPL reference gases. RHUL measurements in turn have been assessed relative to other international laboratories (Umezawa et al., 2018). This facilitates the use of Boreas data in global and regional-scale CH_4 modelling studies.

There are two possible approaches to perform this adjustment. In these approaches, the extent of correction applied to a given air or BT datum is based upon the average correction of the four BT data points which bracket the given datum in time.

The first approach is to adjust the drift-corrected delta values by an offset value (Griffith, 2018, Steur et al., 2021) in a convenient subtraction of delta values (Eqs. (3.17), (3.18)). Here, δ_{dc} is the drift corrected δ value, and δ_{RHUL} is the RHUL-measured value:

$$offset(2) = \text{mean}(\delta_{dc}(0,1,3,4) - \delta_{RHUL}), \tag{3.17}$$

$$\delta_{final} = \delta_{dc} - offset. \tag{3.18}$$

The second approach uses a scale factor to the drift-corrected isotope ratio values (Griffith, 2018, Steur et al., 2021; Eqs. (3.19), (3.20)), before calculating delta (Eq. (3.21)).

$$SF(2) = \text{mean}(\frac{R_{dc}(0,1,3,4)}{R_{RHUL}}), \tag{3.19}$$

$$R_{final} = R_{dc} \times SF, \tag{3.20}$$

$$\delta_{final} = (\frac{R_{final}}{R_{VPDB}} - 1), \tag{3.21}$$

where R is the isotope ratio (dc is drift corrected; $final$ is the Boreas measured value; $VPDB$ is Vienna Pee Dee Belemnite, the hypothetical material representing a δ^{13}C value of zero (Coplen et al., 2006)) and SF is the scale factor applied. Numbers refer to the number of the data point within a time series (i.e., the scale factor of the second data point in a series depends on the ratio values for the first, third, fourth and fifth).

Figure 3.5 indicates the absolute difference between the two approaches at each timestamp for the air data collected between 18-30th June 2021. The difference between the two approaches does not exceed the uncertainty on δ^{13}C or δD (0.07‰ 0.91‰, Table 3.3). Marginally improved offsets from RHUL-measured BT are attained using the scale factor method (an improvement in offset of 0.00023‰ for δ^{13}C and 0.00020‰ for δD; Table 3.4); however these changes are significantly smaller than typical precision on BT (0.07‰ for δ^{13}C, 0.91‰ for δD Table 3.3). The difference between the two approaches is therefore too small to be recognised by Boreas for this sample data. The scale factor approach is continued due to the lower offset from RHUL.

Table 3.4: Mean rolling standard deviation and mean final offset from RHUL-measured values on BT, for both δ^{13}C and δD data, for the period June 18-30th 2021. Two offset adjustment techniques are examined: the 'subtraction' and 'scale factor' approach.

Measure	Technique	Mean δ (‰)	Mean RSD (BT, ‰)	Mean Offset (BT, ‰)
δ^{13}C	Subtraction	-47.2383	0.0678	0.1717
δ^{13}C	Scale Factor	-47.2385	0.0678	0.1715
δD	Subtraction	-92.4982	0.9135	0.1318
δD	Scale factor	-92.4984	0.9135	0.1316

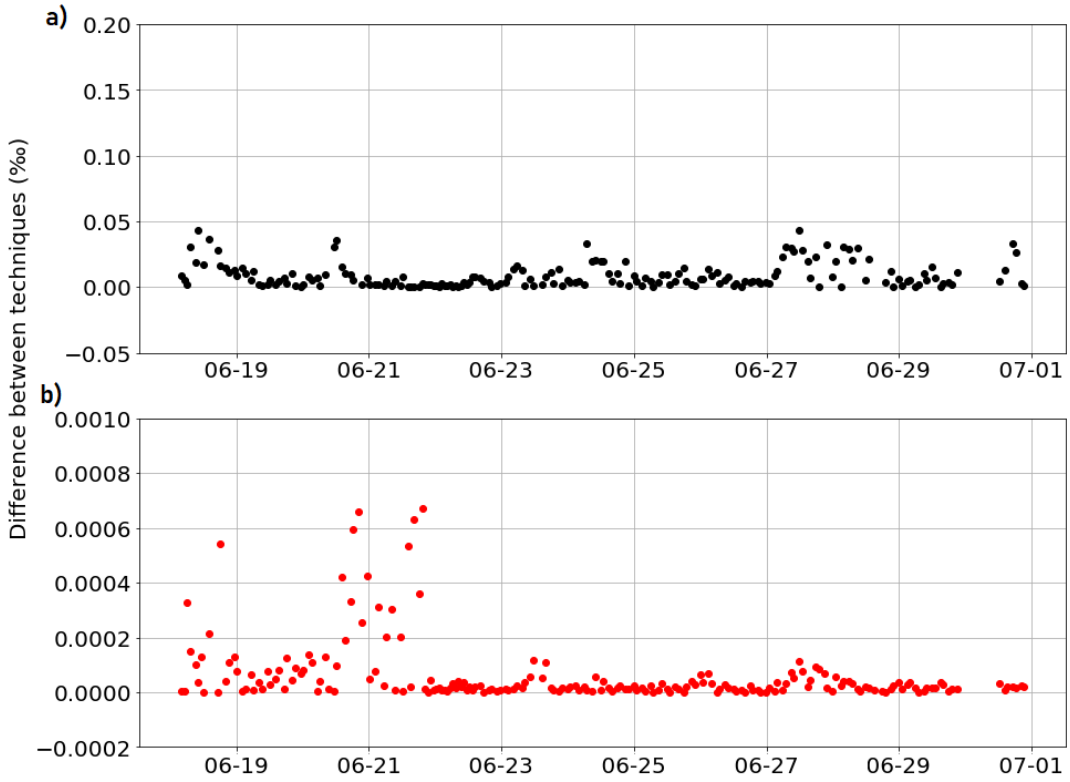

Figure 3.5: Time series of sample data as recorded by Boreas over the period June 18-30th 2021 (‰). Values indicate the absolute difference between performing different offset adjustment approaches; the subtraction and scale factor methods. Both analysis approaches were performed for a) δ^{13}C and b) δD BT values, and differences plotted.

3.5.1 Extent of Offset Correction

The preceding tests were performed using a time series of δ data from 18-30th June, as measured by Boreas. However, in reality, measured air data may vary by more than what was measured in this particular time series (for example, under extreme pollution events). Therefore, it is important to check whether the difference between performing the subtraction and scale factor approaches would be greater (and exceed Boreas uncertainties) under different air values and BT offsets. Therefore, a test is performed to examine how the difference between approaches varies with different measured air values and under different BT offsets.

The range (difference between the air data point and BT) of examined δ values was between 0 to 20‰ for δ^{13}C and 0 to 50‰ for δD. The greater range for δD was chosen because δD has a broader range of published values than δ^{13}C (Figures 1.2, 3.12). Different offsets were applied: of 0.2, 0.5 and 1.0‰ for δ^{13}C and 1.0, 2.0, 3.0‰ for δD. Both correction approaches (subtraction and scale factor) were applied to each data point, and the resulting δ values compared.

Figure 3.6 indicates the difference between the two approaches, for various δ ranges and offsets. Under the offset Boreas is performing at (0.1‰ for δ^{13}C and 1.0‰ for δD, Table 3.4), measured δ^{13}C air values more than 15‰ away from BT (-62.2 to -32.2‰), would result in a significant difference between offset approaches. For δD, the difference between approaches does not become significant under typical Boreas offset, up to a range of 50‰.

Were the offset on BT measured values to become greater, then the difference between approaches becomes significant at smaller range of air values. For δ^{13}C, the range to make adjustment approach significant decreases to 6‰ for an offset of 0.5‰ and 3‰ for an offset of 1.0‰. For δD, the significant range is 42‰ for an offset of 2.0‰ and 28‰ for an offset of 3.0‰.

Under extreme pollution events, measured air values may be more than 15‰ (δ^{13}C) distinct from BT (-62.2 to -32.2‰). Therefore, it is important to perform the offset adjustment approach which results in lowest offset from externally measured δ values (the scale factor approach).

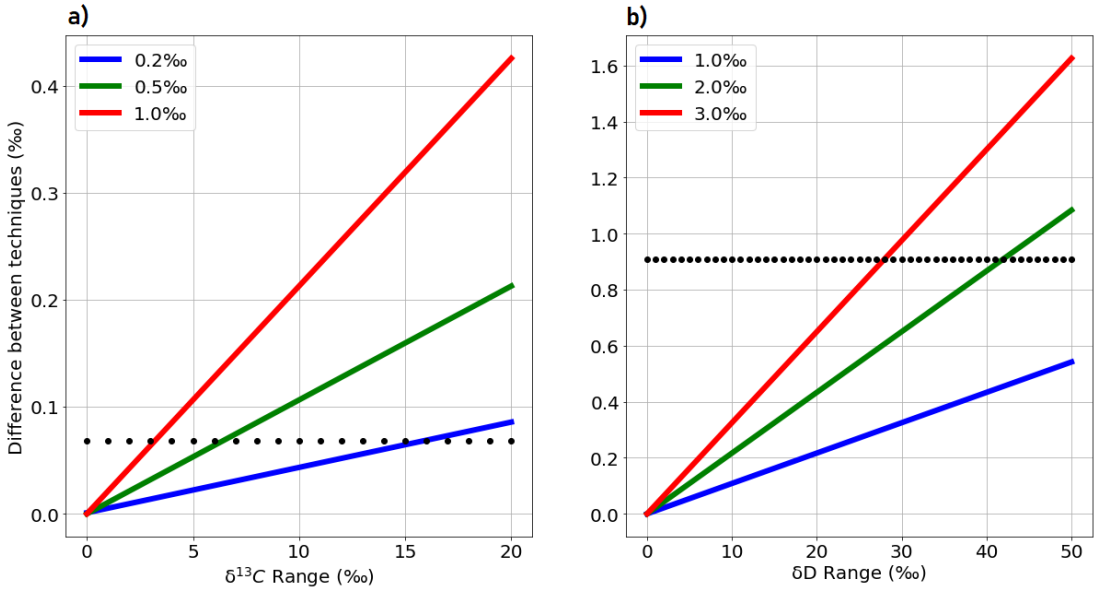

Figure 3.6: Examining the absolute difference in final δ value between the two offset techniques (subtraction and scale factor approaches), across a range of a) δ^{13}C and b) δD values (‰). 'Range' indicates the difference between the data point and the known value on BT. Line colour indicates the offset examined. The black spotted line is Boreas precision (0.07‰ for δ^{13}C and 0.91‰ for δD)

3.6 Amount Fraction Calculation

3.6.1 Comparison with Picarro amount fraction data

At the Heathfield atmospheric monitoring site there is situated a Picarro G2401 instrument which has been recording CH_4 amount fractions at one-minute intervals since 2018 (Picarro Inc., 2021). This instrument measures amount fractions of total CH_4 using cavity ring-down spectroscopy, giving precise and simultaneous amount fraction measurements of carbon monoxide (CO), CO_2 and CH_4 at parts-per-billion (ppb) sensitivity, and water (H_2O) vapor at parts-per-million (ppm) sensitivity. The instrument is able to provide measurements with negligible drift and meets WMO and ICOS performance requirements for atmospheric CO, CO_2, and CH_4 measurements (Picarro Inc., 2021). Precision at 5 seconds, 5 minutes, and 60 minutes is 1, 0.5, and 0.3 ppb for CH_4 respectively (Picarro Inc., 2021). The instrument reports both wet and dry mole fractions; an internal theoretical calculations is therefore applied in order to report the dry mole fraction of each gas analysed. The Picarro measures CH_4 at the Heathfield atmospheric monitoring site, at both a 100 m and 50 m inlet height.

These Picarro data are therefore used as a quality control test on the performance of Boreas *in situ*. Furthermore, the Heathfield data will be released for use in atmospheric modelling work; in these data sets, the Picarro amount fraction data will be published alongside δ values from Boreas, so it is important to ensure the data correspond well (also to identify issues with Boreas). The Picarro samples alternately from a 100 m and 50 m inlet on the Heathfield tower, whereas Boreas samples solely from 100 m height, and so only Picarro data from this height are utilised in comparison.

These data are used as an additional assessment of the performance of Boreas *in situ*, because they are exactly co-located and measure similar objectives.

3.6.2 Calculation Approach

The individual CH_4 isotopologue data as measured by Boreas needed to be combined and calibrated into CH_4 amount fractions in order to facilitate comparison with the Picarro data. The recorded measurements of each major isotopologue ($^{12}CH_4$, $^{13}CH_4$, CH_3D) from Boreas are summed to obtain CH_4 amount fractions. Two potential approaches for calculating a calibrated amount fraction value are examined herein.

The first is referred to as the 'response' technique. In this approach, the CH_4 amount fraction is determined by referencing to BT. Despite the fact that BT is sampled through Boreas under identical conditions as the air sample, differences in regulator pressures and/or sample humidity can cause variations in the trap flow rate and volume of the sample. Therefore, calculation and normalisation is performed on the instrument response (IR) for BT and air (the ratio between the measured $^{12}CH_4$ amount fraction and the Boreas trap volume (v_{trap}); Eq. (3.22)). The BT value is interpolated onto the air measurement time. The ratio between the air and interpolated BT instrument response (Equation 3.23) is then multiplied by the 'known' amount fraction value of the BT (measured by an external laboratory) to give the CH_4 amount fraction in an air sample (Eq. (3.24)):

$$IR = \frac{^{12}CH_4, meas}{v_{trap}}, \tag{3.22}$$

$$IRratio = \frac{IR_{air}}{IR_{BT}(interp)}, \tag{3.23}$$

$$CH_4(air, calc) = IRratio \times CH_4(known, BT). \tag{3.24}$$

The second technique employs a Pre-Concentration Factor (PCF), which is calculated as the relative volume of the Boreas trap (v_{trap}) to the Aerodyne cell volume (v_{aero}), indicating the extent of the preconcentration of CH_4 through Boreas (Eqs. (3.25), (3.26)). The measured preconcentrated CH_4 amount fraction in air by Boreas is then scaled by the PCF to give the ambient CH_4 amount fraction (Eq. (3.27)).

The Aerodyne cell volume is not recorded for each run, so must be calculated using the CH_4 amount fractions on BT to calculate the PCF (using Eq. 3.25), and therefore the Aerodyne cell volume (rearranged Eq. (3.26), as v_{trap} is recorded each run). The Aerodyne cell volume of the BT measurement nearest in time to each air measurement is the one that is used in each case.

$$PCF(BT) = \frac{CH_4(meas)}{CH_4(known)}, \tag{3.25}$$

$$PCF(air) = \frac{v_{trap}}{v_{aero}(BT)}, \tag{3.26}$$

$$CH_4(air) = \frac{CH_4(meas)}{PCF(air)}. \tag{3.27}$$

Therefore, total CH_4 amount fraction data for a time series of June 2021 data can be compared with Picarro data. The CH_4 amount fraction from the Picarro is recorded every minute, whereas Boreas samples ambient air for an 8-minute period every hour. To facilitate comparison, the Picarro data was averaged for the equivalent 8-minute period that Boreas was sampling (Figure 3.7).

Table 3.5: Pearson correlation coefficients for the response and PCF techniques for calculating total CH_4 amount fraction data from Boreas. The correlation of each method with the Picarro G2401 CH_4 data are indicated. The data covers the period of June 18-30th 2021 (Figure 3.7).

	Response	**PCF**	**Picarro**
Response	-	0.99852	0.94950
PCF	0.99852	-	0.95970
Picarro	0.94950	0.95970	-

The ‘response’ and ‘PCF’ techniques show good agreement; there is a correlation of 0.9985. The PCF method has a greater correlation with Picarro data (Table 3.5, Figure 3.7b), and so this is the technique which is pursued for amount fraction calculation from Boreas.

The data used in Figure 3.7 are where the timestamps match exactly. The Picarro and Boreas systems are well correlated, with an Pearson correlation coefficient of 0.9597, under the PCF technique.

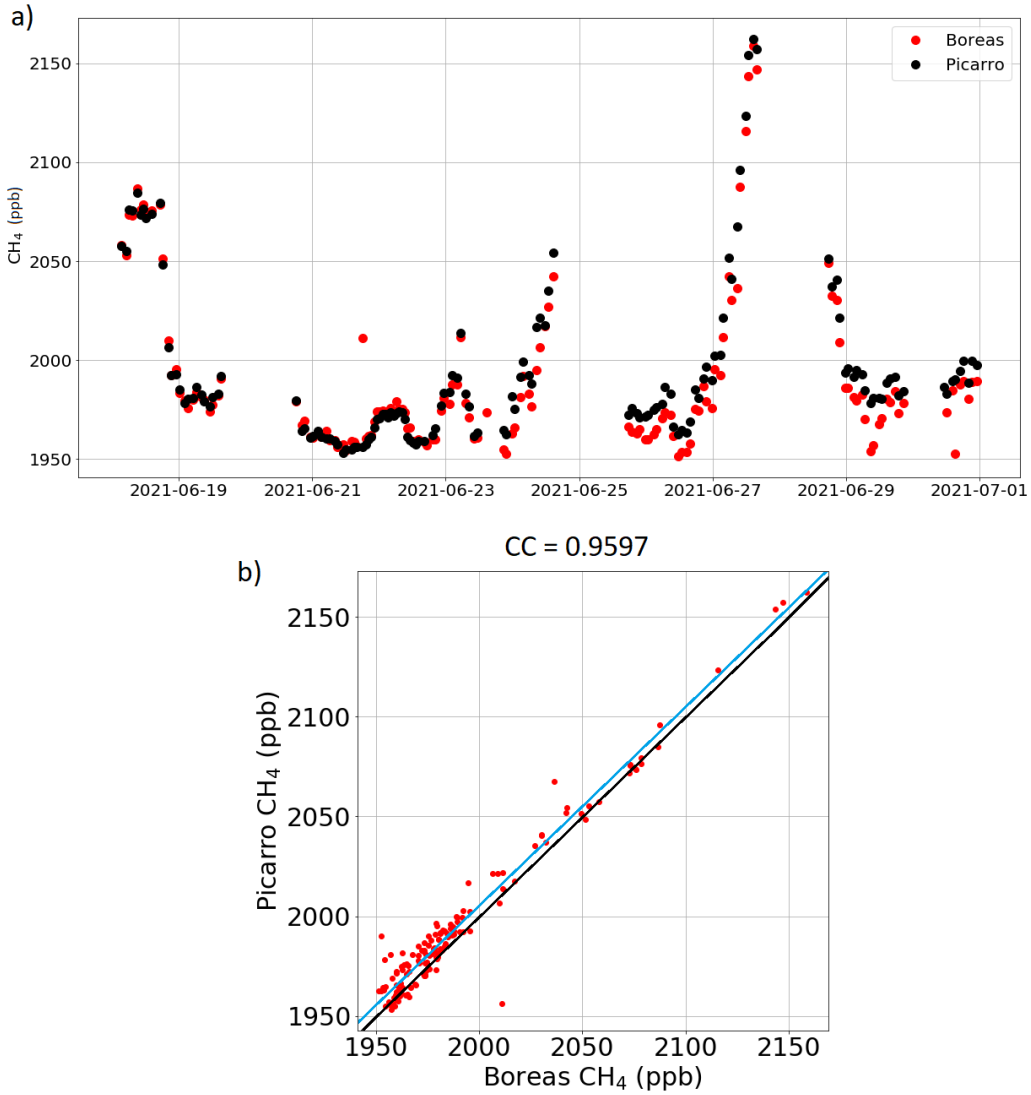

Figure 3.7: a) Time series (June 2021) of CH_4 amount fraction data (ppb), as calculated using the PCF method for the Boreas data and measured directly by the Picarro G2401 instrument at the Heathfield atmospheric monitoring site. The red dots are the Boreas amount fraction data and the black are the Picarro amount fraction data.
b) Correlation between CH_4 amount fractions as measured by Boreas and the Picarro. Data are directly measured for the Picarro G2401 instrument and has to be calculated using the PCF technique for the Boreas data. Both are located at the Heathfield atmospheric monitoring site. Blue line is the line of best fit for the data, with gradient 1.004. Black line is the 1:1 equivalent line. Correlation coefficient (CC) is indicated.

3.7 Frequency of measurement

As mentioned, the preconcentrator is calibrated using a compressed whole air standard (BT) from the Mace Head atmospheric monitoring station in Ireland. This whole air standard is calibrated for δ^{13}C externally by RHUL using IRMS. While Boreas was undergoing optimisation at NPL, BT was measured after every ambient air sample run. This allowed for the performance of the preconcentrator (based on precision of the two BT runs either side of the air measurement) to be monitored and also allowed the offset to RHUL IRMS measurements to be regularly recorded.

To maximise the number of long term air measurements while ensuring that the internal offset adjustment is calculated with the required frequency, BT should be run as infrequently as possible without loss of instrument precision. Therefore, once Boreas was in place and running at the Heathfield atmospheric monitoring site, it is necessary to examine whether the frequency of BT measurements can be reduced. To do this, a time series of data are obtained from 17th December 2020 - 3th January 2021, 15th - 17th January 2021 and 1st - 15th February 2021 (Figure 3.9). This time series was chosen as BT is measured after every air measurement, before deployment to Heathfield. To assess measurement frequency of BT, every other measurement of BT was removed from the data set. What difference this makes to recorded RHUL offset across the month's time series is examined:

$$offset_{all} : \text{mean}(offset(1), offset(2), offset(3), offset(4)...), \tag{3.28}$$

$$offset_{2} : \text{mean}(offset(1), offset(3), offset(5), offset(7)...). \tag{3.29}$$

This is expanded by removing every second and third in a set of three, and continuing up to every seventh measurement (i.e. removing six continuous measurements in every seven). Mean offsets from these tests are indicated in Figure 3.8a and c; there are multiple data points for each test due to different possible combinations in the tests (for example, removing every first or second data point in a set of two).

Figure 3.8b) and d) shows the same tests; however, these indicate the absolute difference between the given test and measuring Boreas Target with the original regularity ('1' in subplot a); i.e. measuring after every air measurement run). This is calculated by the absolute difference in RSD at concurrent timestamps.

The uncertainty on BT for Boreas for δ^{13}C is 0.07‰; therefore it would appear that measuring BT every sixth air measurement is appropriate, as beyond this where the difference in offset from measuring BT after each air measurement exceeds 0.07‰ (Figure 3.8). For δD, the frequency could be even lower, as the difference from BT being measured after every air measurement does not reach the Boreas δD precision up to the range examined (every seventh measurement). The tests stopped at seven because of the precision limit for δ^{13}C being reached.

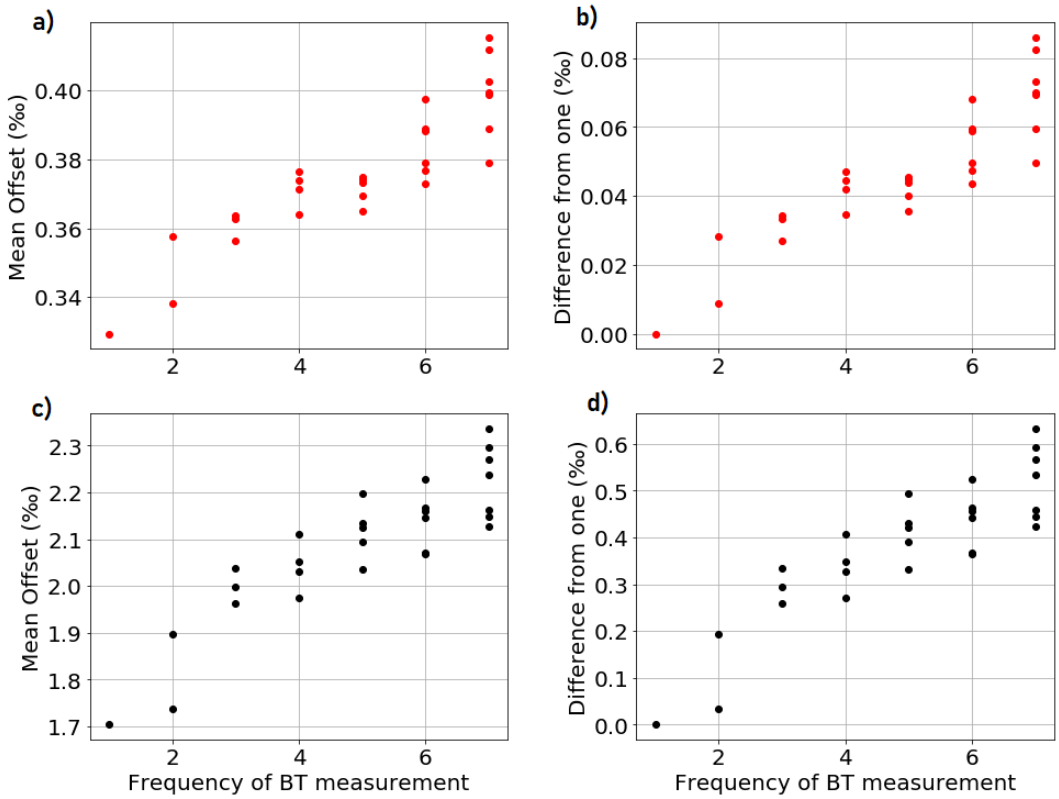

Figure 3.8: Frequency of Boreas Target measurements test, to examine whether the Boreas Target could be measured less frequently without compromising on data uncertainty. Data are a time series of 18-30th June 2021. 'Frequency' represents what data are included in the test — for example '2' is every other measurement included, '3' is every third. There are multiple data points for each frequency, because there are multiple options for which data points are removed (i.e. for the test wherein every other data point is removed, the first or second in each set of two data points could be removed). Subplots a) and c) indicate mean offset from RHUL-measured BT values across the time series for each test (for δ^{13}C and δD, respectively). b) and d) indicate the absolute difference between the mean δ value of each frequency, and the mean δ value measuring BT at the maximum frequency (i.e. '1' in subplot a, for δ^{13}C and δD respectively.

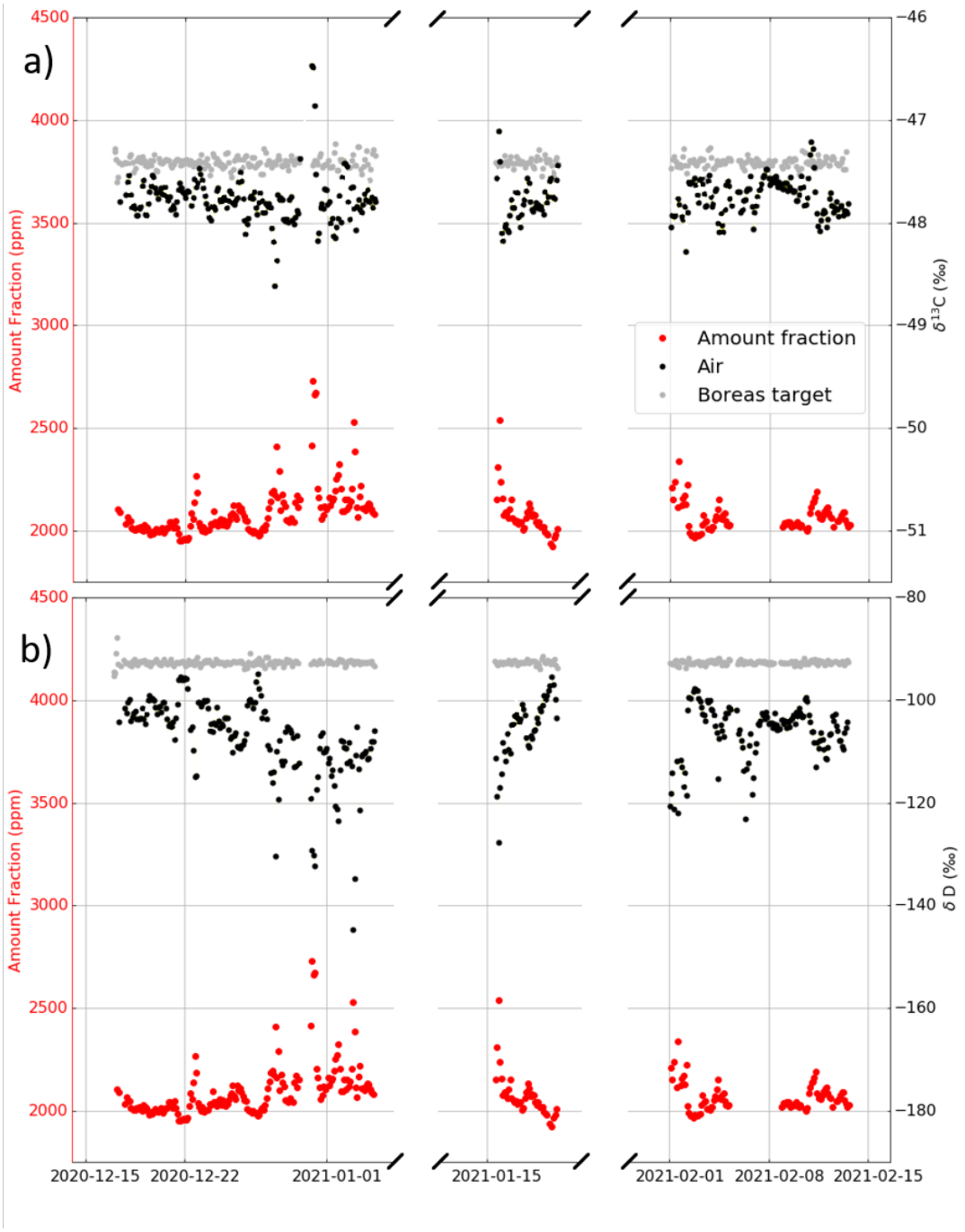

Figure 3.9: Time series of a) δ^{13}C and b) δD measurements (‰) made at NPL from a roof sampling inlet, over December 2020 - February 2021, along with amount fraction data. The isotope ratio data has been offset adjusted, in order to be in line with data as measured by RHUL and therefore data measured by international laboratories. Red dots are amount fraction calculated from Boreas using the PCF method; black dots are air δ values; grey dots are BT δ values.

3.8 Data Analysis

Here, some example data analysis on typical data produced by Boreas is demonstrated. NPL-based data are presented as there are a greater mix of sources (especially pollution sources) in this location, which provides a better opportunity to demonstrate the ability of Boreas to differentiate between emissions sources.

Polar Plots

The time series of London air from the NPL roof inlet, representing 17th December 2020 - 3th January 2021, 15th - 17th January 2021 and 1st - 15th February 2021 (Figure 3.9) is examined to assess Boreas performance.

The calibrated and drift-correct isotopic data from this time series are used to construct polar plots that are representative of SW London air. These data are useful in determining CH_4 sources and sinks in this location. The meteorological data are obtained from the Met Office Bushy Park weather station, which is located 300 m ESE from the roof inlet at NPL.

Polar plots of the measurements are a tool to represent the data, produced using the OpenAir software in R (Carslaw & Ropkins, 2012). They are structured with the location of the NPL roof inlet as the origin, wind speed as the radius, wind direction as angle, and a colour map representing the δ signature measured. δ^{13}C and δD data are shown here (Figure 3.10).

The δ^{13}C polar plot (Figure 3.10) indicates a prevalence of light CH_4 (-47.85‰) to the SE. The air here is a combination of multiple sources, however potential sources can be determined by thinking about locations that are relatively lighter or heavier than others. The wind speed, direction and relative δ signature combined lead to the possible source of each data point. For the light signature (-47.85‰) to the SE, considering wind speed (up to seven knots) and direction, this light CH_4 is indicative of the location of a water treatment facility in Beddington (51.38° N, 0.13° W). The similar light signature observed to the SW originates from another water treatment facility in Walton-upon-Thames (51.40° N, 0.40° W). The heavier CH_4 signature in the north and southwest (-47.5‰, wind speed 5 knots) are suggestive of a pyrogenic origin, which considering NPL's location would point towards gas and household combustion emissions from what is a heavily populated area. There may also be influence, considering location and wind speed, from the nearby Heathrow airport (for example from aeroplane refuelling). This demonstrates that data as measured by Boreas is capable of separating different emissions sources on a local pollution scale. These values are isotopically approximately 0.5‰ lighter than mean values for London recorded by Saboya et al. (2022) in Kensington, and more than 2‰ lighter than mean signatures for the Greater London area as measured by Zazzeri et al. (2017). This is indicative of the less urbanised nature of Teddington compared with Central London.

The δD polar plot (Figure 3.10b) shows similar trends to the δ^{13}C polar plot. Heavy signatures (-95‰ at a wind speed of 8 knots) to the SW and N dominate the plot, which suggests the origin is household emissions (e.g. small fires and gas pipes). There is a significant light signature to the NW, which was also present in the δ^{13}C plot, however stands out more significantly here. Considering the low wind speed (less than 4 knots), this may originate from wetlands in Staines (51.45° N, 0.49°W).

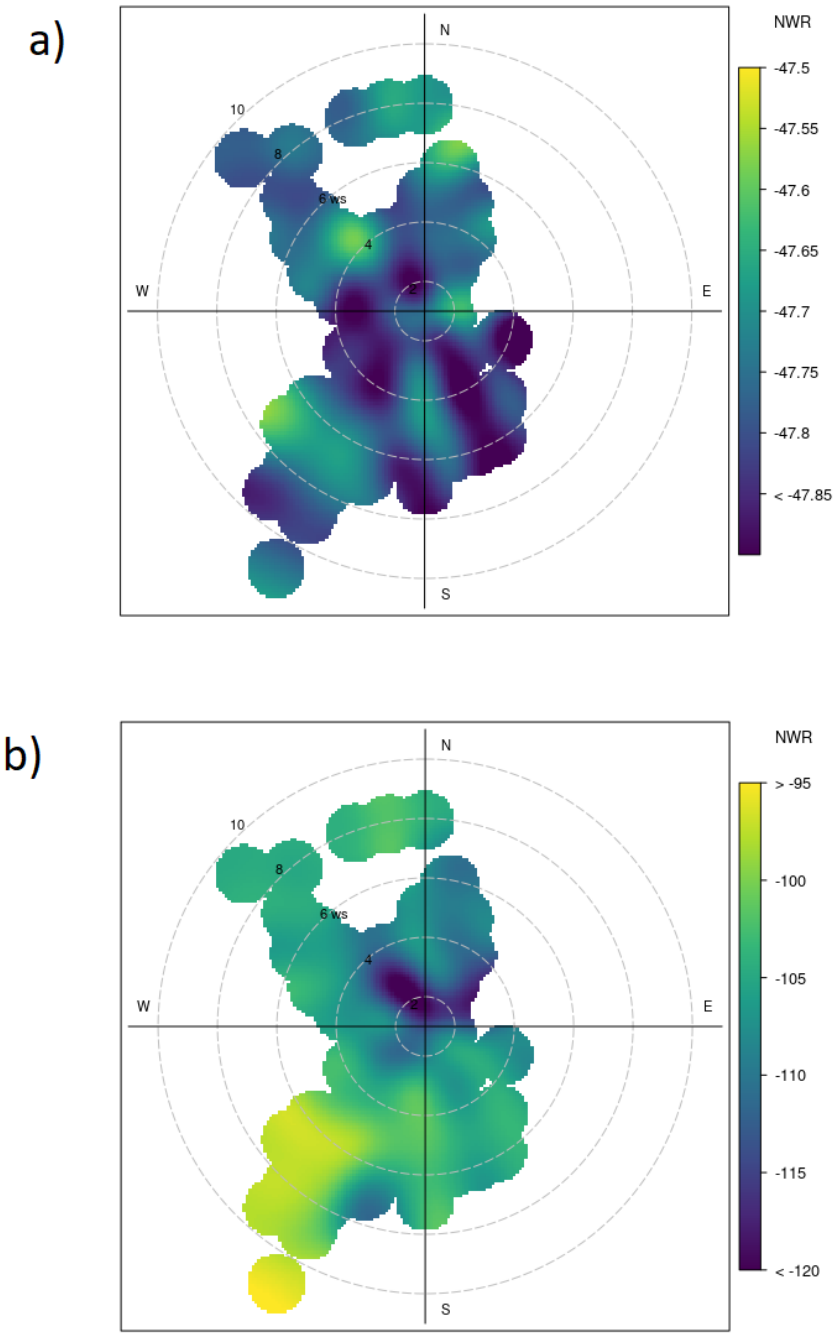

Figure 3.10: a) δ^{13}C and b) δD data as recorded by Boreas, while located at NPL. Radius from the origin indicates wind speed and the angle represents direction, with compass points indicated. The origin is the location of the roof inlet at NPL. Data are a combination of 17th December 2020 - 3th January 2021, 15th - 17th January 2021 and 1st - 15th February 2021. 'NWR' refers to 'Non-parametric Wind Regression', which calculates and smoothes the relationship between δ value and wind direction (Henry et al., 2002).

Keeling and Miller-Tans Analyses

In order further examine the provenance of the measured CH_4 from the time series of December 2020 - February 2021, Keeling and Miller-Tans analyses are performed on observed pollution events in the air record from NPL. A pollution event is determined by a series of at least 5 data points which deviate from the background in a spike shape (thereby discounting solitary points so as to reduce anomalies being included).

A Keeling plot (Keeling, 1961) is a common way to constrain a single-source system from a background, in this case to separate a CH_4 pollution event and the background air. This approach originates from the principle of conservation of mass, following:

$$\delta_{obs} \times C_{obs} = \delta_S \times C_S + \delta_B \times C_B, \tag{3.30}$$

$$C_{obs} = C_S + C_B, \tag{3.31}$$

where C indicates amount fraction. The suffixes obs, S and B represent observation, source, and background, respectively. The Keeling plot approach is derived from Equations 3.30 and 3.31 in the form

$$y = mx + c : \tag{3.32}$$

$$\delta_{obs} = C_B(\delta_B - \delta_S) \times (\frac{1}{C_{obs}}) + \delta_S. \tag{3.33}$$

In this approach, the δ^{13}C signature is plotted on the y axis and 1/amount fraction is on the x axis. A straight line drawn between plotted data points, and the y-intercept is the signature of the source of the event being examined (Keeling, 1958, 1961). The Keeling approach is appropriate in setting with a stable background, which may not be appropriate for this data, in which the air could be mixed from multiple sources, considering the proximity of NPL to a major city and therefore various emissions sources. An example is shown in Figure 3.11.

The Miller-Tans approach (Miller & Tans, 2003) is an alternative approach to Keeling plot approach, for analysing the source of pollution events. In this case, the background signature is directly specified in each calculation. This is useful in an area with a fluctuating background signature, such as one with fluctuating wind direction bringing in amount fractions from different sources. It is therefore a more flexible approach than the Keeling plot method, which assumes a constant background value for every data point in the calculation. In this case, the

background value for a pollution event was based upon the mean isotope ratio value of the six points which bracket the pollution event in time (i.e. three points either side), provided these points are not themselves defined as a separate pollution event. Both approaches are included here because Keeling is the more established approach, and Miller-Tans is an improvement upon this technique. Performing both tests is to double check the resulting signatures.

This approach is mathematically equivalent to Keeling analysis (Equation 3.33; Miller & Tans, 2003), however in this case the y axis is the difference between observed and background product of δ and amount fraction and the x axis the difference between the observed and background amount fraction. The gradient is therefore the δ value. This is calculated from the Keeling approach, as:

$$\delta_{obs} \times C_{obs} = \delta_B \times C_B - C_B + \delta_S \times (C_{obs} - C_B), \tag{3.34}$$

$$\delta_{obs} \times C_{obs} = \delta_S \times C_{obs} - C_B(\delta_B - \delta_S), \tag{3.35}$$

$$(\delta_{obs} \times C_{obs}) - (\delta_B \times C_B) = \delta_S \times (C_{obs} - C_B), \tag{3.36}$$

in the form

$$y = mx. \tag{3.37}$$

C is amount fraction and δ is recorded δ value. Suffixes obs, S and B represent observation, source, and background, respectively.

Considering the specific pollution event indicated by Figure 3.11, we find that this event has a δ^{13}C source signature of -49.5 $\pm$ 0.7‰ from Keeling analysis and -47.9 $\pm$ 3.9‰ from Miller-Tans analysis. The event has a δD signature of -226.1 $\pm$ 34‰ from Keeling analysis and -229.7 $\pm$ 30‰ from Miller-Tans analysis. There is good agreement with the two approaches when considering Miller-Tans uncertainties. Considering the typical source signatures as measured for different sectors (Figure 3.12), the origin of this pollution event is thermogenic in origin. Considering wind speeds for this time series (Figure 3.10), this pollution event arose from housing areas surrounding NPL.

In total over the examined time series, ten separate pollution peaks were identified (Figure 3.9, Table 3.6). The results of Keeling and Miller-Tans analyses on the ten identified pollution peaks are indicated in Figure 3.12 and Appendix A2. The accepted 'delta' value is the mean of the result from Keeling and Miller-Tans analyses (Table 3.7). The average difference between each approaches is 1.07‰ for δ^{13}C and 12.03‰ for δD. Average uncertainty was 1.99‰ for Keeling δ^{13}C, 2.27 for Miller-Tans δ^{13}C, 28.7‰ for Keeling δD and 27.1 for Miller-Tans δD.

This analysis overall indicates a prevalence of thermogenic CH_4 pollution at this location (50% of the pollution events fall within the thermogenic section of Figure 3.12), which, considering the setting in suburban SW London, suggests household emissions origin, such as gas fires and localised combustion. This supports the polar plots from this location (Figure 3.10), which showed that heavier δ^{13}C signatures, indicative of pyrogenic origin, CH_4 originates from NW.

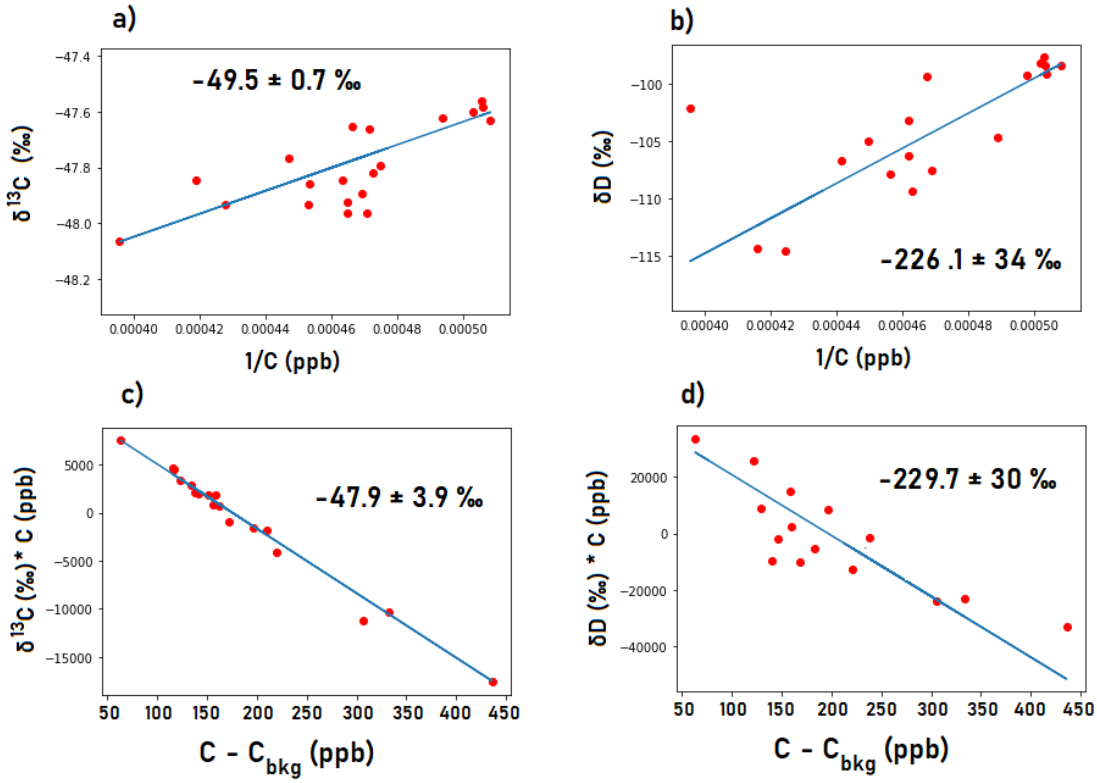

Figure 3.11: Keeling (subplots a and b) and Miller Tans (subplots c and d) analyses of a single pollution event (1st February 2021), for (a,c) δ^{13}C and (b,d) δD. 'δ' is the delta value as recorded by Boreas, and 'C' is the amount fraction. The better the fit (blue line) to the data points (red points), the pollution event is suggested to be of a single origin. The suggested source signature (y-intercept for Keeling and gradient for Miller-Tans) is listed, along with the error on fit (root mean square error, RMSE).

Table 3.6: Keeling (‘**K**’) **and Miller-Tans (‘M-T’) analyses of ten pollution events as identified from the time series 15th December 2020 to 15th February 2021 (Figure 3.9. Uncertainty (RMSD) on the fit of each approach is indicated (‘Unc’).**

Date	δ^{13}C K (‰)	Uncertainty (‰)	δ^{13}C M-T (‰)	Unc (‰)	δD K (‰)	Unc (‰)	δD M-T (‰)	Unc (‰)
22/12/2020	-46.6	0.8	-46.7	0.7	-203.9	30	-201.6	39
27/12/2020	-50.3	0.9	-50.3	0.9	-189.5	15	-181.9	14
28/12/2020	-48.0	1.5	-48.0	1.4	-152	34	-148	14
30/12/2020	-39.9	1.5	-40.1	1.4	-160.5	14	-130.4	19
01/01/2021	-62.2	2.3	-64.2	2.5	-321.4	32	-347.6	23
15/01/2021	-52.2	4.3	-52.0	4.0	-117.3	35	-151.2	40
16/01/2021	-49.6	2.9	-47.9	3.9	-117.7	40	-121.3	46
01/02/2021	-49.5	0.7	-47.9	3.9	-246.1	34	-249.7	30
06/02/2021	-52.5	1.1	-48.9	0.7	-231.6	28	-228.3	29
10/02/2021	-52.8	2.9	-51.3	3.3	-200.6	25	-206.4	17

Table 3.7: Mean values of Keeling and Miller-Tans analyses for ten pollution events as identified from the time series 15th December 2020 to 15th February 2021 (Figure 3.9. 'Diff' indicates the absolute difference between the source signature calculated by Keeling and Miller-Tans analyses on each pollution event.

Date	δ^{13}C Mean (‰)	Diff (‰)	δD Mean (‰)	Diff (‰)
22/12/2020	-46.65	0.1	-202.75	2.3
27/12/2020	-50.30	0.0	-185.70	7.6
28/12/2020	-48.00	0.0	-150.00	4.0
30/12/2020	-40.00	0.2	-145.45	30.1
01/01/2021	-63.20	2.0	-334.50	26.2
15/01/2021	-52.10	0.2	-134.25	33.9
16/01/2021	-48.75	1.7	-119.50	3.6
01/02/2021	-48.70	1.6	-247.90	3.6
06/02/2021	-50.70	3.6	-229.95	3.3
10/02/2021	-52.05	1.5	-203.50	5.8

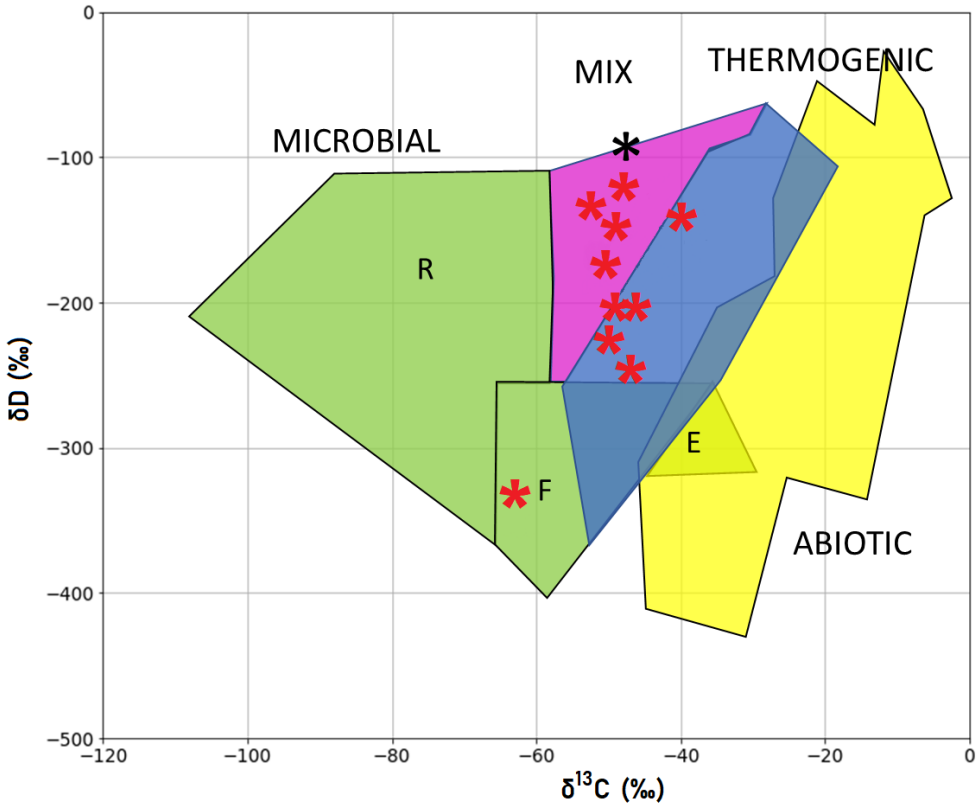

Figure 3.12: Result of Keeling and Miller-Tans analyses for δ^{13}C and δD, for ten pollution events across the time series of Figure 3.9 (15th December to 15th February). The red stars are different pollution events and the black star represents background atmosphere. Fields are based upon Sherwood et al. (2017) and Douglas et al. (2017). 'R' refers to biogenic CO_2 reduction, 'F' refers to biogenic fermentation, 'E' refers to biogenic evaporate setting.

3.9 Conclusions

This chapter concerns the approach used in the processing of data from NPL's 'Boreas' CH_4 preconcentrator. Each step in the data processing approach is examined, including calibrations on the measured isotopologues, a drift correction to account for drift within the instrument, and an offset adjustment to ensure the measurements are valid for adjusting onto an international scale. A calibration on isotopologue values and offset adjustment using a scale factor approach are recommended. It was found that regular measurements of whole-air standards are important for calibration, and should be done at least after every sixth air measurement in order to increase the frequency of air measurements while maintaining good precision. Amount fraction data based on the recorded isotopologue values are calculated, using a 'Preconcentration Factor' method, which takes into account the extent of preconcentration occurring during the measurement. The resulting amount fraction data compares well with independently measured co-located *in situ* amount fraction data (using a Picarro G2401 instrument).

The data as recorded by the Boreas instrument is measured with the intention of being of value to the atmospheric science community. The published data, recorded at approximately an hourly scale, will include amount fraction data (as calculated using the PCF technique). δ^{13}C and δD of sampled air and BT runs are also included, which have been fully calibrated and drift corrected (using the scale factor approach). The precision on δ values (the four-point rolling standard deviation of the bracketing compressed whole standard) as well as offset to RHUL values will be recorded.

Also presented are an example of some data recorded at the NPL site, December 2020 - February 2021. The data covers multiple weeks of continuous δ^{13}C and δD measurements, and the data presented is shown to be able to delineate between and identify nearby sources of CH_4. Specifically, during this time period Boreas was able to differentiate between pyrogenic and biogenic pollution events which can be traced directly to sources in the local area. These analyses demonstrate that Boreas is able to distinguish between different sources of CH_4 emissions, which is useful for categorising and understanding drivers of emissions increases.

Overall, this chapter has contributed to the overall aim of the thesis (understanding ground-based *in situ* monitoring capability) by developing data analysis protocol for a new optical measurement instrument, capable of producing a new, continuous, high precision data set. By performing sample analysis on some data, the work demonstrates the instruments capability to differentiate between emissions source types and therefore contribute to understanding how the CH_4 budget is varying over time.

3.9.1 Future Work

Future work regarding the Boreas instrument will concern the ongoing data processing of measured data at the Heathfield atmospheric monitoring site. It will be necessary to maintain the data set and ensure it is of sufficient quality to be useful in inversions and other modelling studies, to understand how sources and sinks of CH_4 are changing over time. The aim of future work will include performing analysis on the Heathfield-based measured δ signatures, to analyse any pollution sources that may arise. The sources in this location would be biogenic in origin, due to significant agricultural presence in the area.

In the future, improvements in optical instruments will enable measurements of rarer isotopologues of CH_4. This has already been performed by Ono et al. (2014), made measurements of pure methane $^{13}CH_3D$ using a laser instrument, with a precision of 0.7‰. Preconcentration has also been used to measured clumped (multiply-substituted) isotopes. Prokhorov and Mohn (2022) present a preconcentration system which (when coupled to a laser spectrometer) is able to measure δ^{13}C, δD and $\Delta^{13}CH_3D$, by preconcentrating large (18 L) volumes of air.

Boreas is planned to remain in place at Heathfield for the foreseeable future. There are however plans to construct more Boreas instruments in the future. These are expected to be deployed at locations which are of interest to CH_4 emissions studies, such as in the Arctic, or African wetlands. The next question which therefore arises, is where optical continuous instruments should best be located in order to best capture variations in isotope ratio values, for background CH_4 isotope ratio monitoring. This is addressed in Chapter 4.

Chapter 4

Potential Improved Monitoring of δ^{13}C and δD Methane Through Deployment of Continuous Monitoring Systems

4.1 Introduction

The aim of this project is to examine ground-based *in situ* monitoring capability, to understand the changing atmospheric methane (CH_4) budget. This chapter assesses the third research question as outlined in Chapter 1: Where should new ground-based *in situ* monitoring instruments be located in order to measure CH_4 and isotope ratios most effectively? This achieves the aim of assessing ground-based monitoring capability as it examines the potential benefit of deploying ground-based *in situ* instruments to multiple locations.

The deployment of continuous ground-based measurement sites would improve geographic coverage and sampling frequency of CH_4 isotope ratio data. This results in better understanding of how sources and sinks of CH_4 are changing over time. As such, this chapter considers where it would be most useful to the atmospheric science community to deploy new continuous monitoring instruments around the world, in order to capture variations in CH_4 isotope ratios. Specifically, the instrument 'Boreas' (as described in Chapter 3; Rennick et al., 2021) is used as the basis for analysis, as this represents some of the latest advances in CH_4 isotope ratio continuous monitoring instrumentation.

Chapter 2 consisted of inversions for both CH_4 fluxes and δ^{13}C signatures of large-scale regions, over the period 2004-2020. The inversion for regional CH_4 fluxes found that an emissions shift has taken place, with tropical regions producing an increasing proportion of CH_4 emissions, in place of northern mid-latitudes. In solving for δ^{13}C, the results showed that the emissions have increasingly light signatures (indicative of a biogenic origin) centred around the tropics. A limitation on this result was the lack of geographical coverage of ground-based sites, especially for δ^{13}C, which lead to strong correlations between regions (Figure 2.18), meaning that the individual contributions from regions cannot be separated. The paucity of ground-based data was therefore a limiting factor in effectively performing an inversion upon

large-scale regional source signature variations. There are a limited number of ongoing CH_4 isotope ratio measuring sites, for which there are fewer than 20 research groups operational worldwide, which includes those measuring isotope ratios from ice cores and in-lab, rather than regular measurements from sites (Umezawa et al., 2018). The most common approach for measuring isotope ratios is Isotope Ratio Mass Spectroscopy (IRMS), with air collected through flask sampling. Measurement frequency is therefore low, as samples are sent to a central lab for analysis, and they require a level of manual work to operate.

The primary reason for the lack of isotope ratio measurement sites is the expense and complexity involved in constructing a machine capable of measuring CH_4 isotope ratios to a sufficient precision. Regular measurements of δD are especially limited. This may be because the isotopologue CH_3D is present in lower amount fraction than $^{13}CH_4$ (Table 1.2), and is therefore more challenging to measure. Furthermore, typical sectoral δD source signatures overlap more than δ^{13}C signatures (Douglas et al., 2017; Sherwood et al., 2017), and so have been perceived as not being a priority for measurement deployment. However, this data could provide an additional constraint (alongside δ^{13}C data) upon inversion studies. Additional constraints would reduce uncertainties in inversion results, strengthening conclusions of how sources and sinks of CH_4 are changing over time.

Currently, the most widespread network of isotope ratio measurements is the National Oceanic and Atmospheric Administration Earth System Research Laboratories (NOAA-ESRL) network, with established sites around the world that measure δ^{13}C, using discrete flask sampling. Other networks that measure δ^{13}C through flask sampling include RHUL, National Institute for Water and Atmospheric Research (NIWA, New Zealand), Tohuku University and Institute for Marine and Atmospheric research Utrecht (IMAU; Nisbet et al., 2019). The location of a subset of current NOAA network sites that will be used in this chapter are indicated by Figure 4.1. The names and exact locations of sites are indicated by Table A1. The isotope ratio 'δ' values for flask samples are measured at the University of Colorado Institute of Arctic and Alpine Research Stable Isotope Laboratory (CU-INSTAAR), using IRMS (Dlugokencky et al., 2005). The samples are measured discretely on a weekly scale, and are also combined as monthly averages.

Chapter 3 presented the data analysis procedure from a new laser-based measurement instrument 'Boreas', capable of continuous *in situ* monitoring. The chapter details how the instrument is constructed, the data analysis protocol on the instrument, and presents some example data. From the Boreas instrument, independent measurements of CH_4 isotopologues, using a preconcentration system attached to a Tunable Infrared Laser Direct Absorption Spectroscopy instrument, can achieve precision comparable with those typically achieved using IRMS. The instrument is currently in place at the Heathfield atmospheric monitoring site, however, here the potential for deployment of continuous monitoring instruments (using Boreas as a basis) is examined.

With the introduction of continuous instruments to the network, there is the potential for a significant increase in the frequency of isotope ratio measurements. These instruments record data at a near-hourly resolution, as opposed to weekly discrete sampling for flask networks. With the deployment of continuous monitoring instruments, variations in isotope ratios would be more finely monitored. The instruments record data more frequently (by factor of 168 $\times$, as continuous instruments measure every hour as opposed to every week under a flask sampling system) and will pick up shorter-term events (such as pollution pulses) that are missed on the weekly scale. Likewise, flask sampling data could be skewed by recording a short-lived pollution event, which then affects the result for the whole week. Therefore, continuous instruments bring additional data and improved monitoring for measuring both monthly-scale trends (such as for a large-scale inversion; Fujita et al., 2020; Lan et al., 2021; McNorton et al., 2018) and short-lived pollution events (such as those identified and examined in Chapter 3), by increasing sampling frequency.

In theory, flask sampling could be scaled up with more regular measurement, which would increase sampling frequency; however, this would be significantly more expensive and labour-intensive. However, continuous *in situ* monitoring can operate remotely and independently.

This chapter therefore examines the potential deployment of a new continuous isotope ratio measurement instrument (with precision that matches that of Boreas). This is considered both at the location of current network sites, and where to hypothetically position an entirely new monitoring site, to capture variations in CH_4 isotope ratios. To achieve this, an assessment factor 'detectability' is used to indicate how well an instrument at any given location would capture variations in an isotope ratio 'δ' signal, on a daily or monthly scale.

The prospect of adding new continuous isotope ratio measurements at the location of current network sites was examined by Rigby et al. (2012). They assess how adding these continuous isotope measurements would reduce uncertainty in a global inversion, by simulating continuous pseudo data of δ^{13}C and δD. They examine the impact of continuous isotope data on both flask samples at the locations of NOAA-ESRL network sites, and daily samples at the locations of AGAGE network sites, for the year 2000. Their approach considers adding this continuous isotope data to all of the current measurement system and setup. They perform an inversion using the pseudo data and examine how *a posteriori* results and uncertainties are affected. They find that uncertainties on national-scale fluxes are reduced by up to 10% by the inclusion of continuous isotope ratio data, indicating that this data would improve resolution of emissions for a large-scale CH_4 inversion. This study looked at the locations of current measurement sites in a single year, whereas this chapter examines both current network locations and potential new sites, over multiple years. Furthermore, this chapter utilises forward modelling for considering instrument deployment rather than inversion approach.

Thonat et al. (2019) use a detectability metric to assess potential instrument performance. They calculate a detectability value for potential δ^{13}C instruments at the location of multiple Arctic sites. They simulate δ^{13}C using a chemical transport model, produce rolling standard deviations on this data, and compare multiple instrument uncertainties to these standard deviations. They then examine what sources dominate at the site locations, using emissions inventories, to understand necessary uncertainties for certain sectors. They find that in order to detect anthropogenic sources, one would require an instrument with lower uncertainties (0.05‰) than the uncertainties necessary to detect wetland signatures (0.2‰), meaning an instrument of optimum performance is required for natural emissions detection. This differs from the approach as followed in this chapter, in that they focus on only δ^{13}C signals, and only Arctic-based site locations are examined. This chapter therefore expands this approach by using the detectability metric, but examining the entire world and considering new site locations, for both δ^{13}C and δD. This chapter examines a single uncertainty based upon current available instrumentation rather than multiple theoretical uncertainties.

A few factors must be considered when considering where to position an instrument; the potential detection of signals and the accessibility of the location. Positioning will also be dependant on what the overarching aim of the measurement campaign is — whether to focus on daily or monthly-scale variations in CH_4 isotope ratios, or to capture aspects of both. The focus of a measurement campaign may also be to examine variation in emissions source signatures and sinks — all of these possibilities are examined.

This chapter therefore focuses on the detectability of signals of δ^{13}C and δD, at multiple locations around the world. In representing a range of latitudes with the network sites chosen (Figure 4.1), a range of dominant source types is also represented, such as wetlands at Alert and Barrow stations (ALT and BRW), thermogenic sources (Tae-Ahn Peninsula, TAP) and even sites with no strong emissions influence (Figure 2.2). The aim is to give an indication as to where a new continuous monitoring instrument should be positioned (within the current measurement network) in order for it to capture the highest amount of monthly-scale and daily-scale variations in these atmospheric δ signals. This is expanded to consider deploying instruments to new locations, producing a recommendation for the locations that should be targeted in the future for CH_4 isotope ratio measurement campaigns. The chapter also considers the sensitivity of each location to changes in emissions and sinks.

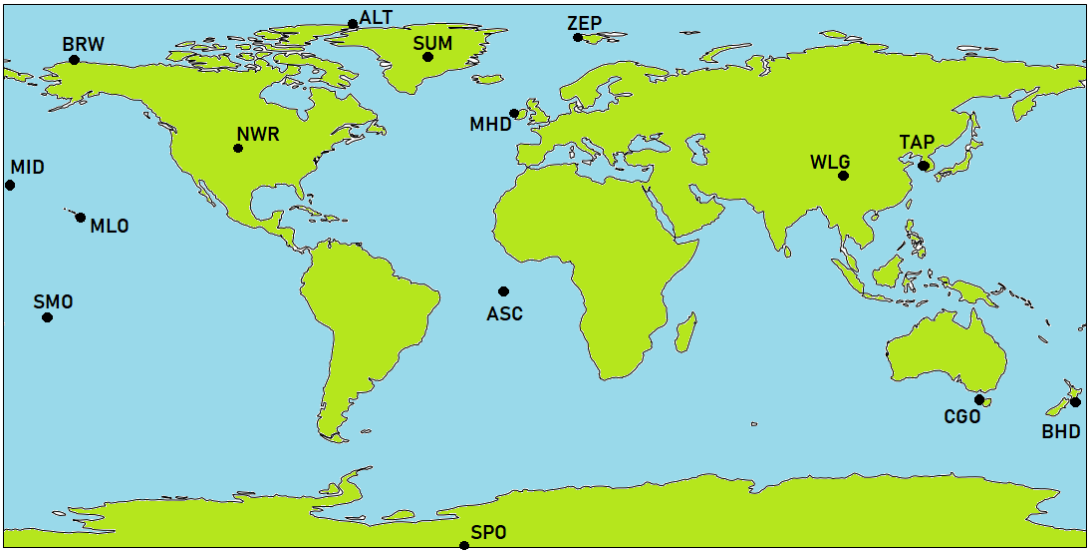

Figure 4.1: Indicating the location of NOAA-ESRL network sites which are used to consider potential deployment of a new continuous monitoring instrument. The sites were chosen to represent a range of latitudes. They are a subset of those employed in Chapter 2 as a constraint in the CH_4 and $\delta^{13}C$ inversions. Site details are listed in Table A1.

4.2 Model

In order to examine what amount of variation a continuous monitoring instrument would capture in multiple locations, analysis is performed upon daily and monthly-scale simulations of $\delta^{13}C$ and δD, from 2016-2020. The output from the model is at a daily resolution, and to produce monthly outputs the daily scale values within a given month are averaged.

These are simulated using v12-01 of the GEOS-Chem 3D chemical transport model, ran at a $4^\circ \times 5^\circ$ resolution with 47 vertical levels up to 80 km above the surface (Bey et al., 2001). The setup of the model follows the same approach as was established in Chapter 2. The meteorology used is MERRA-2 meteorology reanalysis data (Gelaro et al., 2017), with native resolution degraded to match the model. The emissions inventories employed are listed in Table 2.1, and all are handled by the Harvard-NASA Emissions Component (HEMCO) software of GEOS-Chem. Sinks represented are OH, Cl (using values from from Sherwen et al. (2016)) and soil (gridded by Fung et al., 1991). These are given as monthly values but with no intra-annual variability, as discussed in Chapter 2.

In order to simulate isotope ratios, the approach as detailed in Chapter 2 is followed: that is, simulating isotopologues separately (e.g. for $\delta^{13}C$; $^{12}CH_4$ and $^{13}CH_4$) and combining simulated isotopologue amount fractions into δ values after the simulations are complete. Sectoral emissions in the HEMCO-emissions file are scaled according to typical source signatures as recorded by Sherwood et al. (2017), in which is compiled recorded source signatures from literature (Table 1.1). Calculating isotopologue emissions from sectoral δ values involves

calculating the relative abundance of each isotope, back calculated from the source signature in δ space of any given source (as described in detail in Chapter 2, section 2.2.3). For the δ^{13}C simulations, Chapter 2 *a posteriori* regional emissions and δ^{13}C emissions source signatures are used. Sink behaviours are described by Kinetic Isotope Effect (KIE) values, which represent the extent to which sinks are fractionated for individual isotopologues. They are handled in the same manner as they are in Chapter 2. The sinks of OH and Cl (Table 1.3) are calculated at each time step (described in detail in Chapter 2). Soil is treated as a negative emission in GEOS-Chem, and is therefore treated differently from the other sinks in the simulations. The KIE in this case is accounted for by applying a scale factor to the HEMCO-emissions file.

The model is 'spun up' over 60 years by repeating a given year's meteorology, with emissions and sinks similarly repeated each year. The emissions are scaled according to typical source signatures and KIE values (described in Chapter 2), until isotope ratio values are balanced. 60 years is six times the atmospheric lifetime of CH_4 has been proven to be sufficient to allow amount fractions to stabilise (this was examined for Chapter 2; Figure 2.3). Simulated atmospheric δ^{13}C values for 2016-2020 are indicated by Figure 4.2.

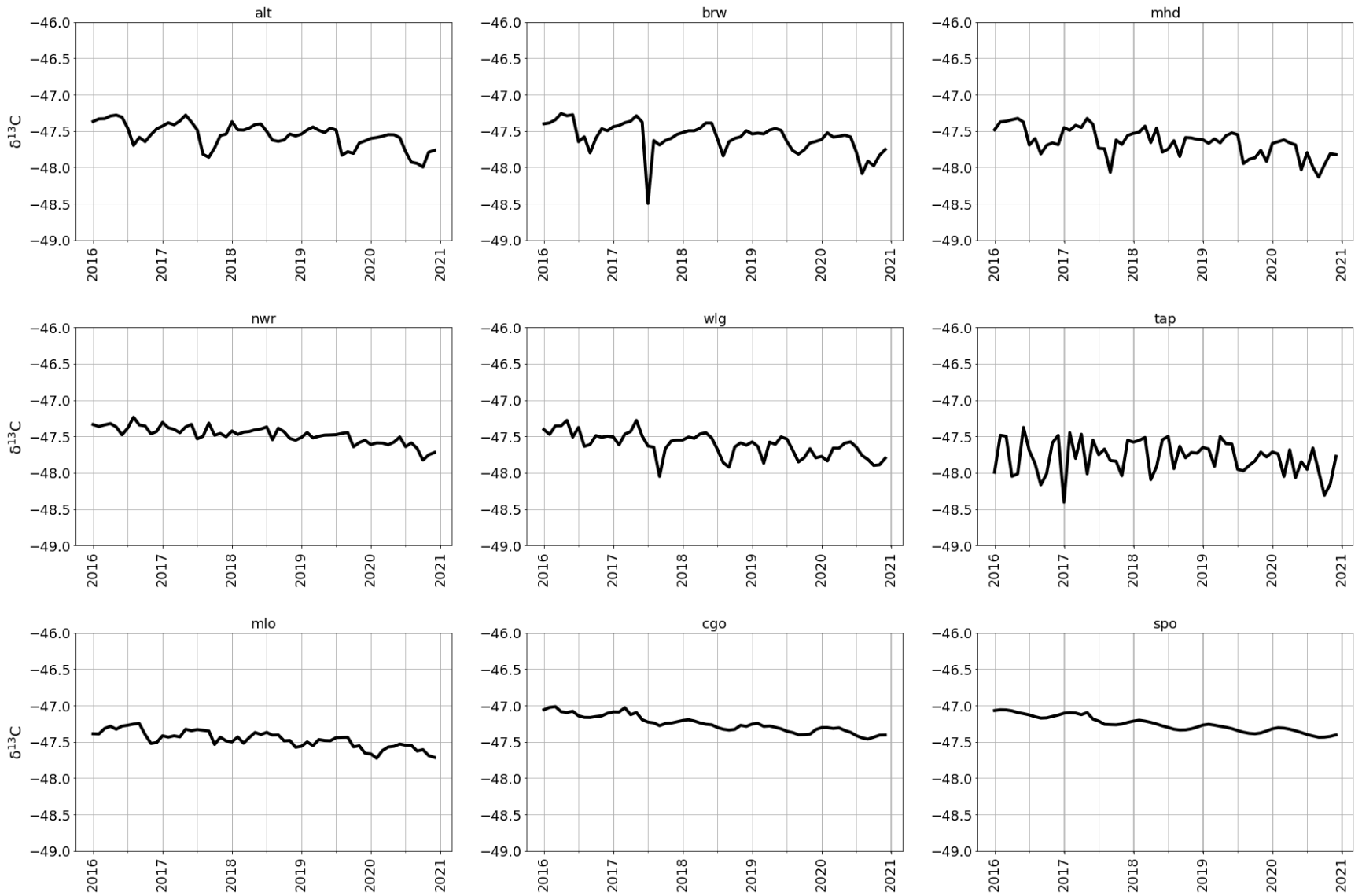

Figure 4.2: Simulated atmospheric δ^{13}C values (‰) over the period 2016-2020, at a series of site locations in latitudinal order. Site indicated by subplot titles, with site details in Table A1.

4.2.1 δD Simulation

The simulations and subsequent inversions of Chapter 2 were made possible due to monthly-scale monthly reported data sets of ground-based *in situ* δ^{13}C being available. However, in the case of δD the amount of data available to provide constraints upon modelling is very limited. There were a series of 15 measurement sites for δD comprising part of the NOAA network, located at sites which also measure δ^{13}C and CH_4. These sites operated from 2004-2009, however were to be discontinued due to issues with instrumentation (White et al., 2016). As of now there are not enough δD measurement sites with data publicly available to justify a global inversion; for example there is one Northern and one Southern Hemisphere site managed by Tohoku University that produces δD data (Umezawa et al., 2009). The majority of measurements of δD come from ice cores and lab-based samples (Umezawa et al., 2018). This is why an inversion for regional δD signatures was not included in Chapter 2. To simulate δD for the purposes of this chapter, a synthetic simulation was constructed, based upon typical recorded sectoral δD source signatures (Sherwood et al., 2017).

The δD simulation is constructed following the same approach as was followed in Chapter 2 for simulating δ^{13}C — that is, using the *a posteriori* regional emissions from the CH_4 inversion as a basis. Typical δD source signatures from Sherwood et al. (2017) were applied to emissions sectors, and kinetic isotope effects applied to the sinks (Table 1.3). The model is spun up for 60 years to allow amount fractions to reflect the modern atmosphere (Figure 4.3). Instead of performing an inversion using ground-based δD data as a constraint, the simulations of δD were ran forwards. The forward simulations were compared with typical background atmosphere values from the aforementioned Tohoku University sites (Umezawa et al., 2009), to make sure the values are representative of what is expected in the model (i.e. do not deviate rapidly from expected values across the time series). The simulated δD values at a series of site location is indicated by Figure 4.4.

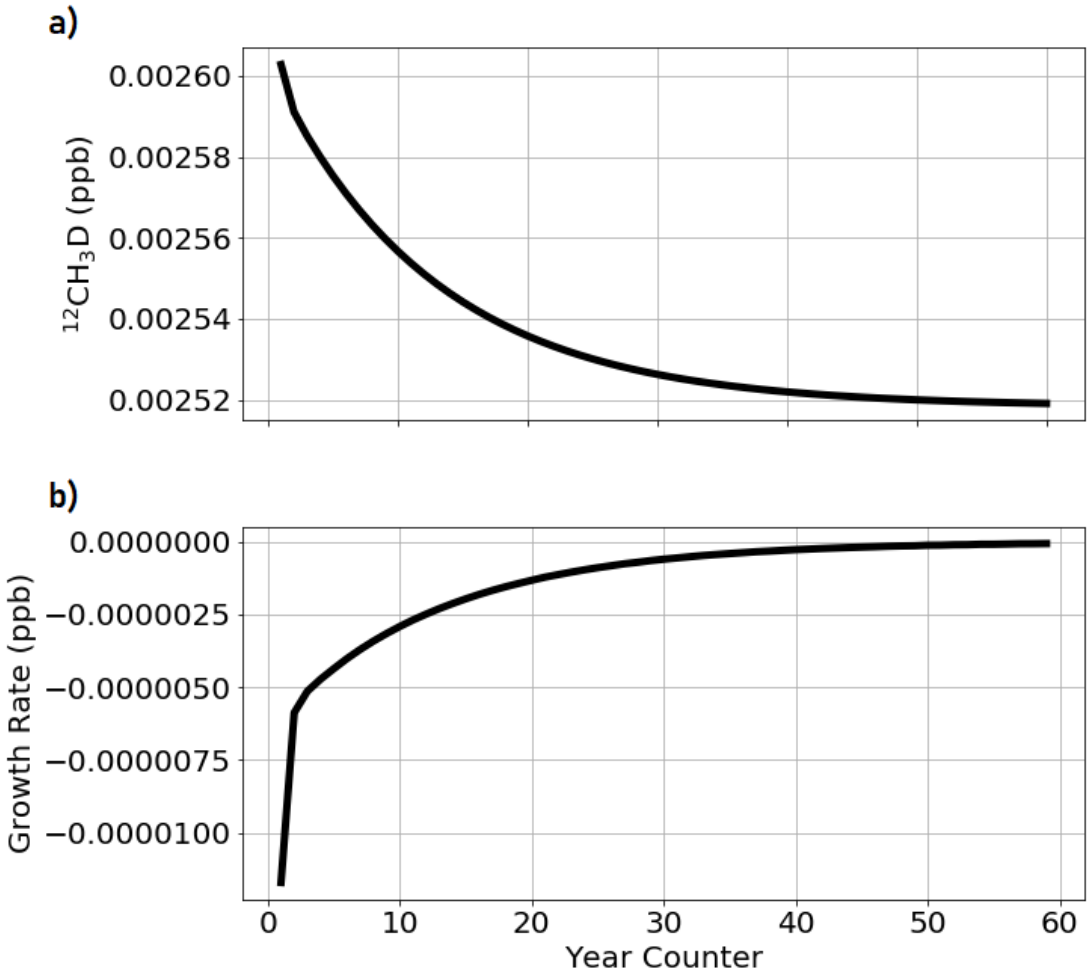

Figure 4.3: Spin up of CH_3D over 60 years of repeating the emissions and meteorology of a single year. a) amount fraction of CH_3D (ppb) corresponding to January of each year, at the grid square which represents Alert station, Canada, for each year of spin up over 60 years. b) Growth rate of spin up (subtracting CH_3D amount fraction (ppb) for one year from the previous year).

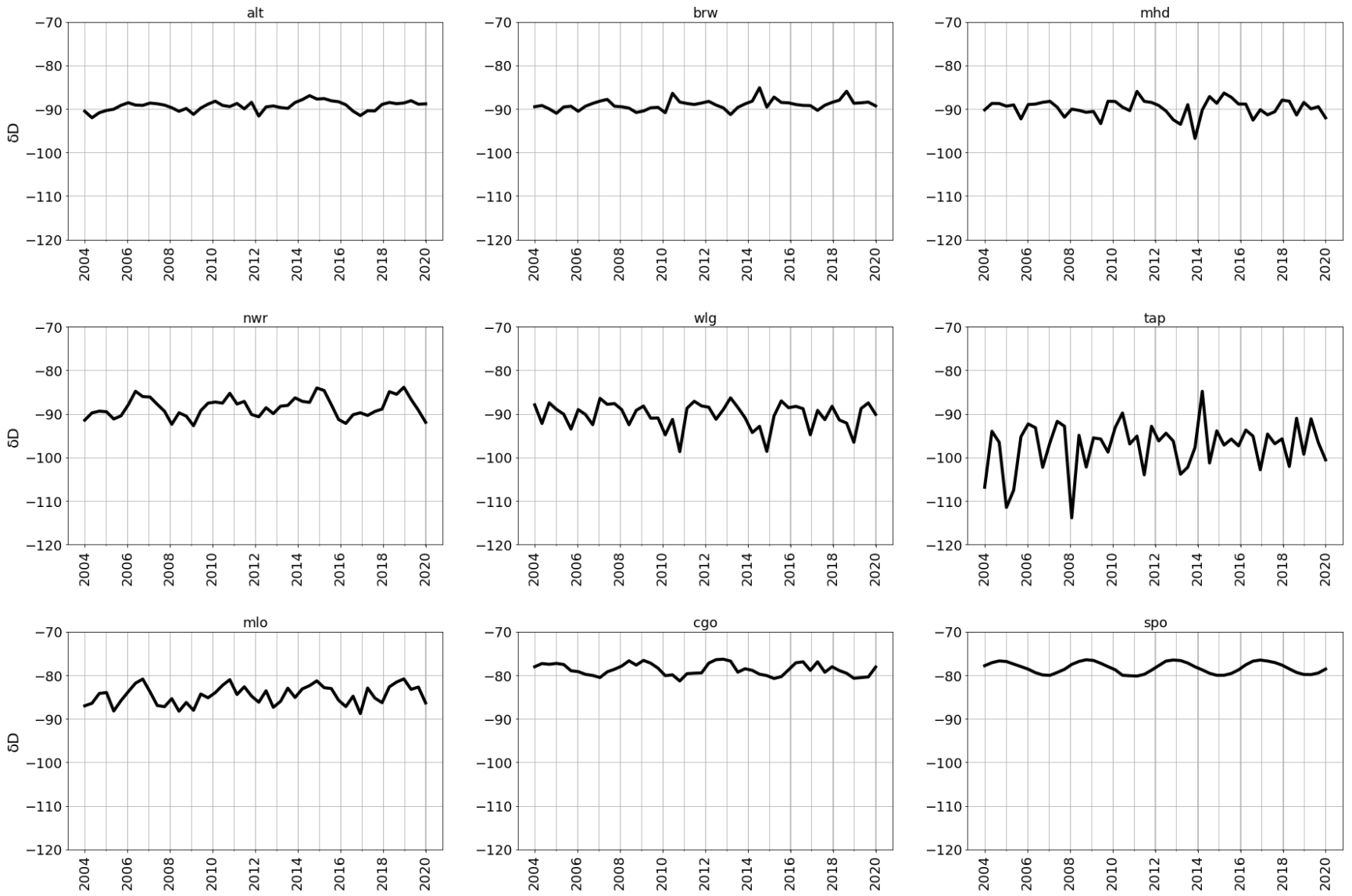

Figure 4.4: Simulated atmospheric δD values (‰), 2016-2020, at a series of site locations in latitudinal order. Site indicated by subplot titles, with site details in Table A1.

4.3 Analysis Approach

Three-point rolling standard deviations are calculated on the δ values simulated at each grid square in the model. The rolling standard deviation is calculated as the standard deviation of a set of three δ values. The set of three values used is then shifted in time by one position and recalculated. This approach is repeated until the end of the time series being examined (in this case the values are calculated on monthly and daily δ values, 2016-2020).

The rolling standard deviation therefore describes how much the signal is varying by on a three-monthly (or three-daily) scale. These rolling standard deviations are compared with continuous instrument precision (as reported in Chapter 3 for the Boreas instrument, and by Rennick et al., 2021). If the rolling standard deviation value is greater than the precision, the instrument would be able to detect this variation; if less than, the instrument will not detect it. This is the same approach as Thonat et al. (2019). As such, a time series of whether variations are detected or not is produced. An example of the approach followed is shown in Figure 4.5, on monthly δ^{13}C data 2016-2020. The result of this analysis is the number of detectable events over time series, as a percentage of all possible events. This value is referred to as 'detectability', calculated as:

$$events = |\text{where} : (RSDev > precision)|, \tag{4.1}$$

$$detectability\ (\%) = \frac{events}{N} \times 100, \tag{4.2}$$

where $events$ is the number of events where $RSDev$ is greater than precision and N is the number of possible events being within the time period; monthly this would be 58 and for daily this would be 1823.

The years 2016-2020 were simulated and examined, in order to be able to assess detectability for both δ^{13}C and δD over multiple years, both to examine seasonality and to limit the chance of a particular year (with extreme meteorology) skewing results. Monthly detectability was chosen as the primary assessment criteria because the focus of this thesis overall is to examine the contribution of ground-based *in situ* data to understanding large scale changes in CH_4 over an extended time period. Therefore, considering monthly-scale changes is more appropriate than focusing on daily-scale changes, such as those caused by short-lived pollution events.

The detectability approach is applied to each $4^\circ \times 5^\circ$ grid box within the model: producing rolling standard deviation values across the entire 2016-2020 time series for daily and monthly scale variations (primarily focusing on monthly-scale variations), and thereby assessing detectability for that particular location. These values are represented as a world map, visually demonstrating how detectability varies with location.

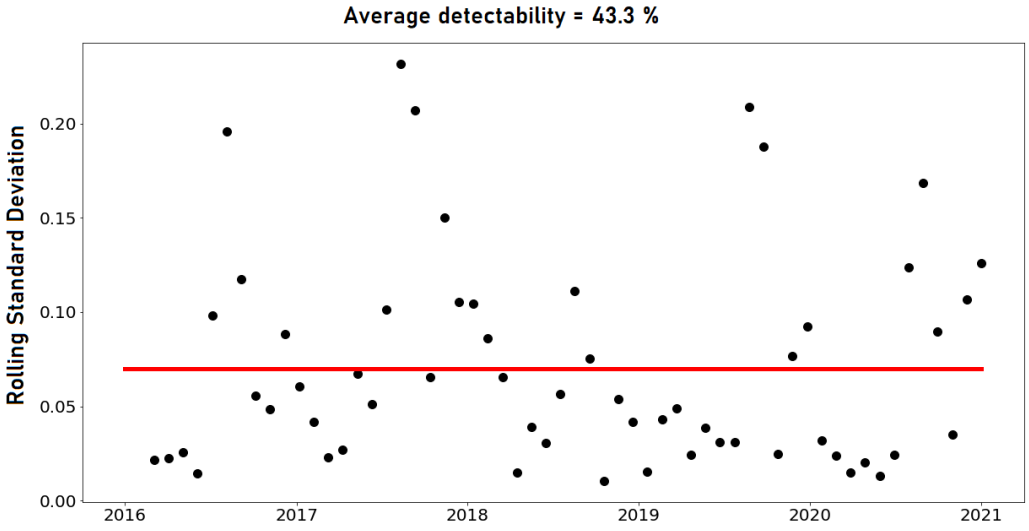

Figure 4.5: Example of how detectability is calculated; in this case, for δ^{13}C on a monthly scale, at the grid square in the model which corresponds with Alert station (82.28° N 62.30° W), over the period 2016-2020. The three-point rolling standard deviation of monthly scale δ^{13}C values are plotted, and compared with typical precision on continuous instrumentation, which for δ^{13}C is 0.07‰. The percentage of rolling standard deviation values which exceed the known precision is deemed the detectability.

4.3.1 New Site Location

With the deployment of new continuous monitoring instrumentation, entirely new locations outwith the current measurement network are considered. To assess new site locations, one must consider the aim of the deployment (whether the aim is to capture daily or monthly-scale variations), along with the accessibility of the location. Aims of deployment may be to:

— Monitor monthly-scale isotope ratio trends.
—Monitor daily-scale events.
—Monitor a combination of daily events and monthly-scale trends.

In all of these cases, a continuous monitoring instrument would bring new data in terms of more frequent sampling than is possible under the current flask sampling network, due to increased sampling frequency better defining both daily and monthly-scale variations. The ability to monitor on both scales is therefore a boon of continuous monitoring systems.

To examine locations for these scenarios, deployment aims have to be considered. For example, if the interest is to monitor monthly-scale trends, the location should have high detectability on a monthly scale and lower detectability on a daily scale (that is, daily-scale has less of an influence than monthly-scale variations). For monitoring daily-scale variations, such as for categorising pollution sources, the location should have highest daily-scale detectability vs monthly-scale (i.e. a dominance of daily-scale events in the time series). The possibilities are therefore:

$$monthlyscale = detectability_{monthly} > detectability_{daily}, \tag{4.3}$$

$$dailyscale = detectability_{daily} > detectability_{monthly}. \tag{4.4}$$

With correct positioning of a continuous isotope ratio site, it may be possible to measure both daily and monthly scale variations from a single site. To examine the optimum site for this, the aim is to find a location where daily-scale events are captured, but do not dominate the record and therefore overshadow monthly-scale variations in a time series. Therefore, for a site that examines both scales, the ideal site is a location with approximately 50% of daily-scale events captured and maximum (90%) monthly-scale events captured.

4.3.2 Source Signature and Sink Tests

This chapter also examines the sensitivity of site locations to a shift in the global atmospheric isotope ratio signature. In two separate tests, the sensitivity of locations to changes in emissions source signatures and the OH sink are examined. The global δ^{13}C signature has an increasingly light trend in recent years (Chapter 2; Lan et al., 2021), and so a shift in emissions signatures is a possibility that may be targeted in future instrument deployment. Variations in CH_4 sinks have been proposed to play an important role in the changing CH_4 budget (Lan et al., 2021; Rigby et al., 2017; Turner et al., 2017; Zhao et al., 2019); the aim of instrument deployment may therefore be to monitor changes in sinks. Placing continuous monitoring instruments in sites that are sensitive to changes in sinks and source signature would lead to better quantification of how amount fractions and δ values are changing over time. In turn, this better understanding is fed into modelling efforts for CH_4 and its isotope ratios, to improve both emissions and sink estimation.

To explore what effect emissions source signatures have upon detectability, all sectoral source signatures were adjusted globally to be 5‰ heavier for δ^{13}C tests. For δD tests, source signatures were adjusted heavier by 20‰. This difference in test approach is because the range of measured δD source signatures (considering signatures from published studies) is greater than δ^{13}C, by approximately four times (δ^{13}C recorded values range from 0-110‰

whereas δD source signatures vary from 0-450‰; (Douglas et al., 2017; Sherwood et al., 2017)). The new, heavier δ values therefore need to be stable, so that the observed changes are genuinely as a result of the heavier source signatures, rather than the time series rapidly changing due to scaling of emissions. Global emissions of $^{13}CH_4$ or CH_3D are scaled heavier for all sources, so as to produce mean δ^{13}C and δD values that are 5 or 20‰ (respectively) heavier than the mean 'delta' values of the original simulation. Resulting values are ensured to be stable by spinning up the model for twenty years (twice than the lifetime of CH_4), and checking the values are stable at the new mean background, 5 or 20‰ heavier than the original simulation. The new values should have different seasonal cycle to the control simulation, meaning changes in detectability. Detectabilities from the source signature tests and the control simulation are then compared, over the period 2016-2020.

Separately to the source signature tests, sensitivity of locations to the OH sink is examined. For the sink tests, the magnitude of global OH is decreased by 5% worldwide, by scaling the 3D OH field by 0.95 x in GEOS-Chem. The extent of scaling was applied to both the isotopologue simulations for both δ^{13}C and δD, as the difference in fractionation between the two has already been accounted for by the different KIEs applied to the sinks in the model. The isotopologue simulations are spun up for twenty years to ensure resulting isotope ratios are stable. The resulting values are compared with the control simulation detectability, to examine the impact of changing sink magnitude.

4.4 Results

4.4.1 Deployment at δ^{13}C Sites

Detectability was examined on a daily and monthly scale on atmospheric δ^{13}C signatures, 2016-2020. Best precision on continuous isotope ratio monitoring instruments is assumed to be 0.07‰ for δ^{13}C measurement (as described in Chapter 3 for using a new laser spectrometer based system).

The results of detectability analysis are indicated by Figure 4.6 on a global scale, and Figures 4.9a and 4.10a, for the specific locations within the model that correspond with the location of NOAA network ground-based measurement sites. In Figure 4.6, the colour bar shows detectability for each $4^\circ \times 5^\circ$ grid square in the model.

Daily-scale analysis of detectability is dependent upon there being daily-scale variations in the signal. Therefore, detectability on a daily scale is tied to locations of active emissions sources, producing daily-scale variability. This is demonstrated by Figure 4.6a, where highest daily-scale detectability for δ^{13}C is recorded at locations with active CH_4 emissions (and possible pollution sources), such as China, Europe and India, where detectability exceeds 80% (meaning 80% of daily-scale variations would be captured) at specific model grid squares. Specifically, these locations align with wetland emissions in northern Russia and Canada, and anthropogenic rice and coal emissions in China (Figure 2.2). Detectability decreases to 0% of variations reliably captured in remote oceanic locations (Figure 4.6a), or uninhabited land areas with low numbers of methane emission sources, such as Antarctica.

Figure 4.6b shows that monthly-scale variation would be captured if the instrument were to be positioned in the Northern Hemisphere, especially over land masses. Detectability is highest over Eurasia, especially Russia, China and India, where detectability exceeds 90% for certain grid square locations. These are large scale regions, representing a range of sources, including wetlands (Siberia), rice fields (SE Asia), agriculture (India) and oil and gas emissions (Russia) (Figure 2.2). There is also high detectability (exceeding 90%) in central Africa and South America - these regions are dominated by wetland emissions (Lunt et al., 2021; Wilson et al., 2021), which were shown to be an increasingly important source of emissions in Chapter 2. Detectability decreases to as low as 0% of monthly-scale emission variations being detected in the Southern Ocean and Antarctica.

The site location with highest monthly and daily detectability (Figures 4.9a, 4.10a), for an instrument with the precision of a continuous monitoring instrument, is Tae-Ahn Peninsula (TAP), located in the Republic of Korea. At this site, monthly-scale detectability over the whole time series is 65% for daily-scale and 80% for monthly variations. Emissions sources at this site location is primarily dominated by emissions from rice fields, and from wetlands in

northern Russia (Dlugokencky et al., 1993), which demonstrates that a continuous monitoring instrument is capable of detecting monthly-scale changes in δ^{13}C at sites which measure CH_4 originating from biogenic, pyrogenic or thermogenic sources. The strong variability in the δ^{13}C signal at this site is indicated by Figure 4.2.

Lowest detectability (at site locations) for δ^{13}C is located at the South Pole (SPO) site, with none (0%) of daily and monthly scale variations over 2016-2020 being captured. This is a 'background' site (i.e. not strongly influenced by active sources in the vicinity), indicating the importance of strong active sources in detectability, under the precision at which this instrument would be operating. The lack of strong variability at this site is indicated by Figure 4.2. Therefore, nothing would be gained by operating a continuous instrument at this site.

There is latitudinal dependency upon detectability at site locations, with the highest around the tropics (Figures 4.9a and 4.10a, where sites listed are in latitudinal order north to south). Detectability of signals is greater in the Northern Hemisphere: an average of 15% and 42% in the Northern Hemisphere, versus 3% and 8% in Southern Hemisphere, for daily and monthly-scale events respectively. This emphasises the importance of active CH_4 sources in producing detectable variations (which are more significant in the Northern Hemisphere and tropics than in the Southern Hemisphere).

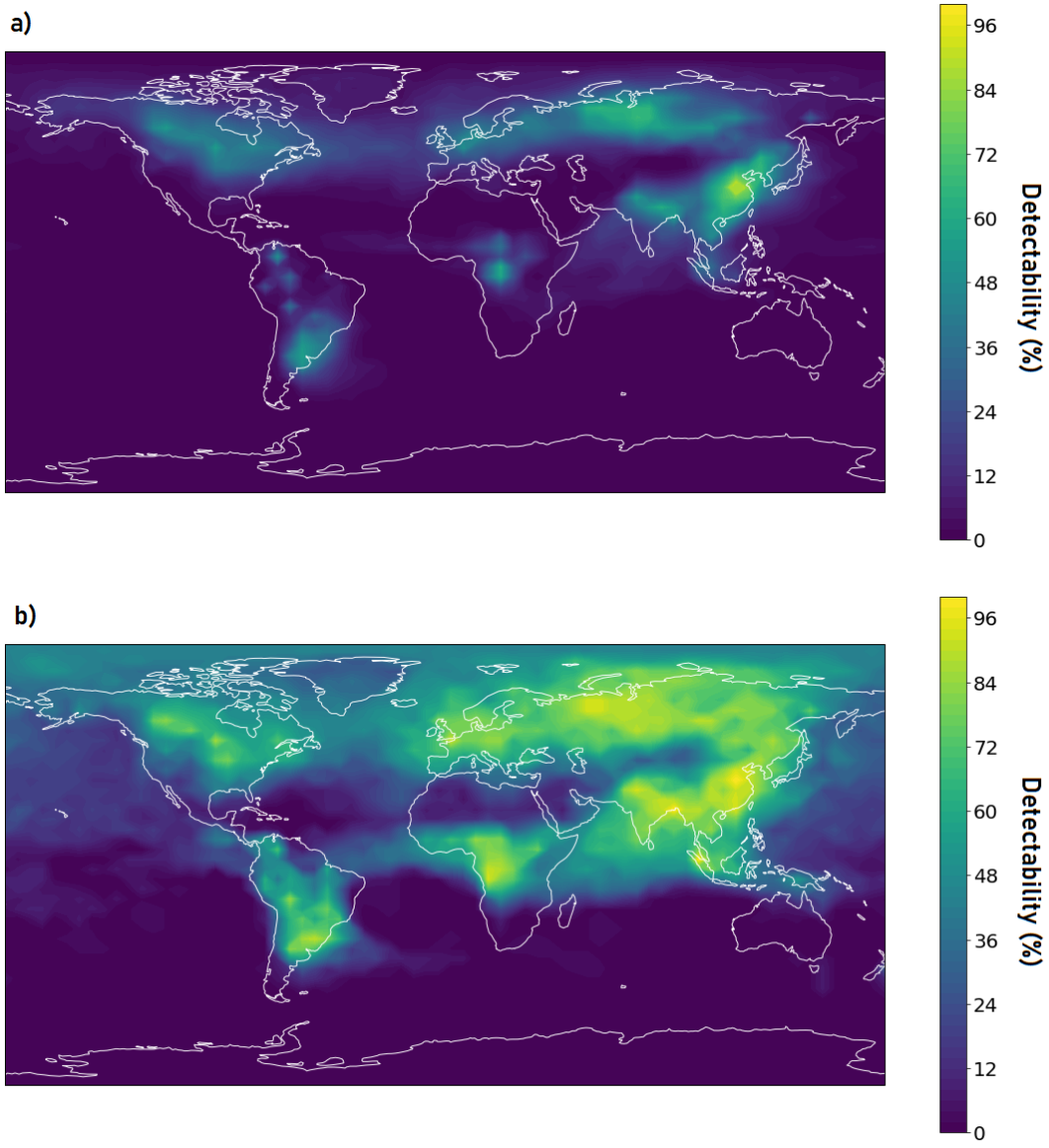

Figure 4.6: Detectability on an a) daily and b) monthly scale all around the world (on a $4^\circ \times 5^\circ$ grid) for δ^{13}C, 2016-2020. Detectability is recorded as a percentage of event variability that would be captured under the precision of a continuous monitoring instrument, on both time scales.

4.4.2 Added Value of δD

One of the potential advantages of laser spectroscopy is the ability to efficiently measure multiple isotope systems simultaneously, not requiring separate preparation systems that are the requirements of measurement by IRMS. Additional new data could therefore be brought to the global measurement network in the form of δD measurements alongside δ^{13}C. Currently, δD measurements are limited, with the majority taking place offline on unique individual samples (or ice cores), rather than in a prolonged measurement campaign, and are not currently ongoing at NOAA network site locations. Typical precision on δD measurements for a continuous monitoring instrument is assumed to be 0.91‰ (the precision of Boreas, Chapter 3), which is used to assess detectability at each model grid square and site location within the model.

On a global scale (Figure 4.7), higher detectability is obtained for δD than for δ^{13}C, because the attainable precision is higher relative to the atmospheric δ signals modelled (driven by large source signatures distinct from background). The global detectability for δD is greater than that of δ^{13}C by an average of 12% on a daily scale and 21% on a monthly scale. For daily scale analysis (Figure 4.7a), highest detectability is recorded in similar regions to δ^{13}C, such as specific grid cells located in China and Europe, where detectability in specific grid cells exceeds 90%. Lowest daily detectability (as low as 0% of variations reliably captured) is recorded in the Southern Hemisphere, around Antarctica. This again demonstrates the importance of highly variable active sources in producing (and therefore recording) sufficiently high daily-scale variations in isotope ratios for detection.

Detectability on a monthly scale is indicated by Figure 4.7b. The highest detectability values on a monthly scale occur primarily over land masses (for example Russia and China, where detectabilities exceed 90%). Similar detectabilities are observed over central Africa and South America. This demonstrates that a continuous instrument would be effective at capturing monthly-scale variability at locations with different dominant source types, including thermogenic (China) and biogenic (Africa) emissions sources (Figure 2.2). Lowest detectability on this scale reduces to 10%, around the Southern Ocean and Antarctica. Here, the variations on a monthly scale are not large enough to be reliably detected, so nothing would be gained by deploying a continuous monitoring instrument.

Considering the performance at the location of current NOAA network sites (Figures 4.9a; 4.10a), the site location with highest detectability is again TAP (the Korean Peninsula site). Here, 80% of daily-scale variations and 95% of monthly-scale variations would be detected. The lowest detectability is at Alert station (ALT), Summit station (SUM) and South Pole station (SPO), where detectability is less than 1% for daily-scale and 18% for monthly-scale. Strong variability at TAP and weaker variability at polar sites is demonstrated by Figure 4.4. Similar to δ^{13}C, there is a latitudinal dependency of detectability at site locations, with detectability reducing at more extreme latitudes and highest around the tropics. Average Northern Hemisphere

detectability is 16% on a daily scale and 41% on a monthly scale; Southern Hemisphere average is 1% and 7% on a daily and monthly scale respectively. At most site locations, there is higher detectability obtained for the instrument on δD versus δ^{13}C. At some site locations (Mauna Loa, MLO), detectability differs between δ^{13}C and δD by as much as 70% on a monthly scale. MLO is located far away from active sources of pollution, as indicated by the lack of variability in signals (Figures 4.2 and 4.4) resulting in low daily detectability (Figure 4.9). Therefore this change not due to different emissions, rather due to higher attainable precision on δD relative to modelled values.

As such, the deployment of a continuous monitoring instrument for measuring monthly-scale changes in δD would be effective, at a variety of locations and under a variety of emissions scenarios. The deployment of such an instrument would add new information to the global network, by adding in δD data at a high frequency, demonstrating how δD emissions signatures are changing over time at a fine temporal scale. Northern Hemisphere site locations capture isotope ratio variations effectively. δD source signatures overlap more than δ^{13}C (Sherwood et al., 2017, 2021), however this may be due to it not being as frequently measured. Menoud et al. (2022) made new mobile measurements of both δ^{13}C and δD around Europe. They found that δD was able to delineate between fossil fuel and biogenic sources. This data would therefore provide an additional constraint upon emissions fluxes in inversion studies, reducing uncertainty in results.

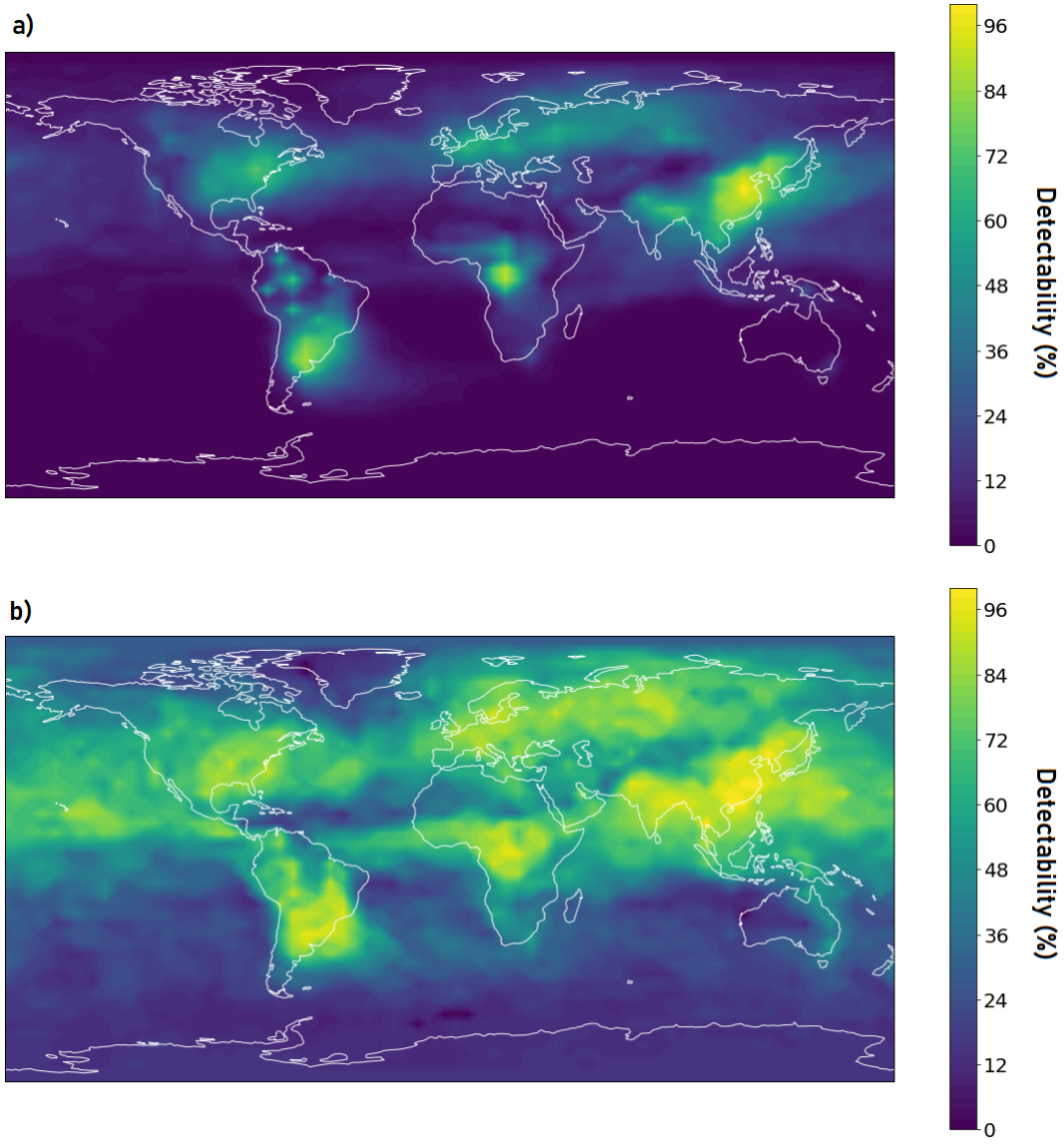

Figure 4.7: Detectability on a a) daily and b) monthly scale for δD that would be recorded by a continuous monitoring instrument at each grid square within the model (representing the entire world on a $4^\circ \times 5^\circ$ grid), 2016-2020.

4.4.3 Potential New Site Locations

Monitoring Monthly-Scale Variations

The results of tests for a new site location are indicated by Figure 4.8. On this plot, the colour bar indicates the difference in detectability between daily and monthly assessment, with greater difference indicating greater influence of monthly-scale events and less influence of daily-scale events.

Examining δ^{13}C (Figure 4.8a), the locations which would meet this criteria are Northern Russia and the central Indian Ocean for δ^{13}C. Here, detectability differs by over 70% for monthly as opposed to daily detectability, indicating that these regions are not affected by daily-scale variability, but monthly-scale variations would be captured by a continuous monitoring instrument. The northern regions are influenced by natural emissions from both wetlands and thawing permafrost, and due to the remote nature of these regions from human infrastructure, are not influenced by daily-scale events such as pollution pulses. Indian Ocean regions are affected by biogenic emissions, for example from wetlands located in Africa. Wetland signatures have a seasonal cycle (Figure 2.2) and therefore have an influence on monthly-scale detectability more significantly than daily.

For δD (Figure 4.8b), the greatest difference in detectability comparing monthly with daily detectability is in the tropics (Atlantic, Indian and Pacific Oceans), where an instrument would capture 70% more variations on a monthly scale than it would on a daily scale. These tropical locations are influenced by biogenic sources, for example African and Tropical South American wetlands (Figure 2.2). Chapter 2 demonstrated the increasing influence of tropical wetland emissions in the CH_4 budget, and so this region would be of particular interest for modelling. The remote nature of central oceanic locations means that the isotope ratio values are less influenced by short-lived anthropogenic pollution, which controls daily-scale detectability results. These site locations would therefore be useful for deployment of a continuous monitoring instrument to finely measure monthly-scale changes in CH_4 isotope ratios.

Monitoring Daily-Scale Variations

Continuous instruments report data on an approximately hourly scale, which allows for measurement of short-term variations in isotope ratios, such as on daily-scale. This would correspond with locations that show high daily detectability on Figures 4.6a and 4.7a. For both metrics, eastern Asia (>80% for δ^{13}C and >90% δD) meet these conditions. Central Africa and South America (Uruguay) also exceed 80% detectability for δD at particular grid squares. An instrument positioned here would effectively capture daily-scale variability, from a range of sources (rice in China, wetlands in central Africa and wetlands/livestock in Uruguay). However, it is difficult to disentangle daily and monthly-scale variations in these locations, as detectability for both is high.

For focus solely on daily-scale variations, the locations which have high detectability on daily-scale versus monthly-scale events (daily detectability exceeds monthly) are examined. In this case, lowest values in Figure 4.8 meet these conditions.

The regions with greater daily than monthly scale detectability for both δ^{13}C and δD are locations such as eastern China (changing by 4% for δ^{13}C and 3% for δD), and oceanic locations such as the Southern Hemispheric Oceans (changing by 5%; δ^{13}C) and Greenland (2%; δD). The Southern Hemisphere Oceans and Greenland show low detectability for both daily and monthly scale detectability (Figures 4.6, 4.7), which results in the little change between the two metrics. The lack of daily-scale detection here therefore does not make these locations suitable for deployment. Eastern China is more promising as this shows high daily-scale detectability, indicative of strong anthropogenic influence in this region (Figures 4.6, 4.7; Dlugokencky et al., 1993). At this location a continuous monitoring instrument would be effective at measuring and categorising short-lived pollution sources, for example.

Monitoring A Combination of Both Monthly and Daily-Scale Variations

With the added sampling frequency brought by using continuous instruments, both daily-scale (driven by short-lived pollution pulses) and monthly-scale variations of isotope ratios are captured from a single site. For this aim, daily-scale variations are captured, but without dominating the time series.

For δ^{13}C, specific grid-square locations that meet the aims for both monthly and daily-scale monitoring are situated within Siberia (60% daily and 90% monthly detection), central Africa (50% daily detection and 90% monthly detection) and eastern Canada (50% daily and 80% monthly); demonstrated by Figure 4.6. These locations are dominated by wetland emissions, which have more of an influence on a seasonal scale. The daily-scale variations may originate from co-located anthropogenic sources such as agriculture (Africa, Canada) or oil and gas leaks (Russia, Canada). Central African wetlands have been proven to be an important driver behind increasing CH_4 emissions (Chapter 2) and therefore would be a location of particular interest for instrument deployment.

For δD, eastern Europe (50% daily and 90% monthly) and eastern Canada (60% daily and 85% monthly) would meet these conditions (Figure 4.7). These regions cover a variety of sources, with monthly-scale variations being controlled by wetlands, and daily-scale variations originating from oil and gas emissions or agriculture. Chapter 2 indicated that these mid-latitude locations are playing a decreasing role in the CH_4 budget; continued monitoring using a continuous instrument would quantify these changes at high frequency, to understand how they are changing and therefore the overall CH_4 budget is changing.

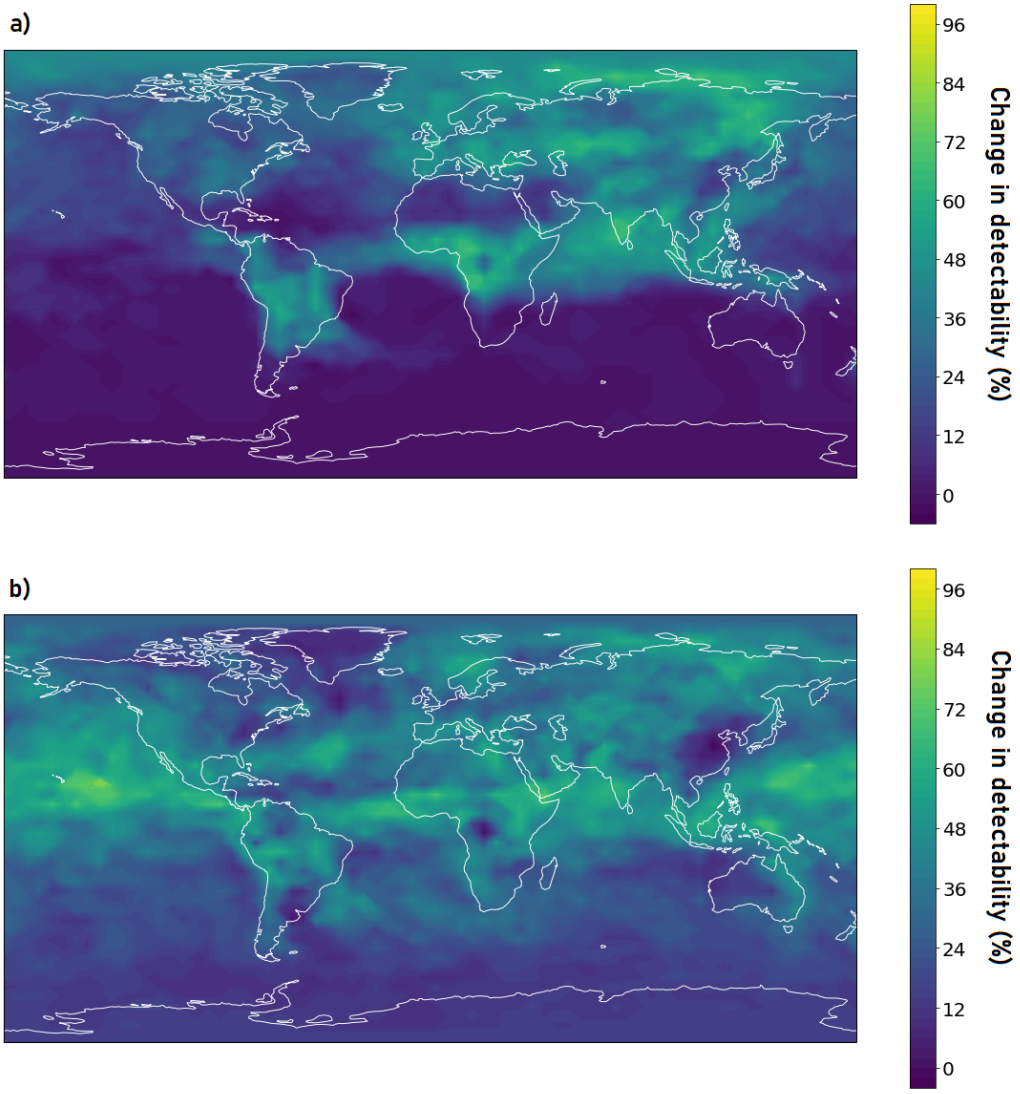

Figure 4.8: Examining the difference between daily and monthly detectability for a) δ^{13}C and b) δD. The aim is to find somewhere with minimum daily detectability vs maximum monthly detectability (therefore the greatest difference between the two metrics), in order to locate an instrument to examine monthly-scale trends without daily-scale influence. For capturing daily-scale variations, the opposite is true (considering locations where maximum daily-scale vs monthly-scale variations are captured).

4.4.4 Source Signature Sensitivity

The impact of the emissions sensitivity tests at sampled site locations in the model are demonstrated by Figures 4.9b and 4.10b.

On a daily scale for δ^{13}C and δD, the pattern of detectability changes shows a latitudinal dependency, with greatest sensitivity to the heavier signature in tropical regions. Sites with greatest changes due to 5‰ or 20‰ heavier emissions are Mt Waliguan (WLG; 26% for δ^{13}C and 24% for δD) and Niwot Ridge (NWR; 21% for δ^{13}C and 17% for δD). These sites are susceptible to anthropogenic emissions (from rice fields in China and cities/agriculture in the USA; Figure 2.2), and therefore have highly variable sources present nearby. This is further indicated by the variability at this sites across the time series (Figures 4.2, 4.4). These sites have some of the highest daily detectability of the site locations examined (Figure 4.9), indicating the tie between these highly variable sources and variations in source signatures.

On a monthly scale for δ^{13}C, American Samoa (SMO) site location shows strong difference between the control simulation and emissions tests; a change of 5% detectability for both metrics. For δD, Mace Head (MHD) and South Pole (SPO) show changes of 4% and 7% respectively. These sites have higher detectability on a monthly scale than on a daily scale (Figures 4.10a and 4.9a), and that the atmospheric signal varies smoothly (Figures 4.2 and 4.4), indicating that these locations are susceptible to these monthly scale variations in δ values. A continuous monitoring instrument positioned at these locations would categorise monthly-scale variations in δ at a high frequency.

4.4.5 Sink Sensitivity

The effect of the sink tests on specific site locations is explored (Figures 4.9c and 4.10c). This is performed separately from the source signature test. On a daily scale, Barrow station (BRW) has the greatest sensitivity for δ^{13}C, with the 5% reduction in OH resulting in just 1% change in detectability. Niwot Ridge (NWR) and Midway Island (MID) have the greatest sensitivity to changes in OH for δD, with changes of 3% each from the 5% decrease in OH. In all cases, the daily-scale change in detectability is less than 5% for the OH tests and is smaller relative to the monthly-scale changes, demonstrating that OH is does not strongly influence signals on a daily scale.

On a monthly scale, for δ^{13}C, greatest sensitivity to OH is in the Southern Hemisphere oceans; the most sensitive site locations are at American Samoa (SMO), with a difference between detectability between simulations of 4%. For δD, Alert station (ALT) is the most sensitive to to a 5% reduction in OH, with a 8% change in detectability at this location. Extreme latitudes are sensitive to changes in OH for both δ^{13}C and δD; for example, Zeppelin station (ZEP, with detectability change of 5% for δ^{13}C and 2% for δD) and South Pole station (5% δ^{13}C), having the greatest detectability change.

OH has a seasonal cycle with amount fractions peaking in winter (Canty & Minschwaner, 2002). In reducing the magnitude of the OH field in simulations, the magnitude of seasonal cycle is reduced, which in turn impacts the seasonal cycle of the isotope ratio values. The isotopologue CH_3D has a larger KIE for the reaction with OH (Table 1.3), and therefore δD will be more affected by changes of the seasonal cycle of OH than δ^{13}C, demonstrated by Figure 4.10c.

At ALT, monthly-scale wetland emissions control variability on a monthly scale (ALT is insensitive to daily-scale variations; Figure 4.9a), and so varies smoothly across the time series (Figures 4.2 and 4.4). This is also the case at ZEP and SUM sites, which are similarly located in high northern latitudes. The greater impact of OH in the high latitude Northern Hemisphere is due to air being more mixed. There is stronger poleward flow in the Northern Hemisphere due to more landmass creating a rougher surface, which causes westerlies to lose momentum and track northwards. The impact of the 5% reduction in OH is therefore highest at high northern latitudes for δD (Figure 4.10c).

At tropical sites (TAP, WLG, MID), the seasonal cycle of OH has less of an influence (the 5% change in detectability results in less than 2% change in detectability). The sites have high detectability on a daily and monthly scale (4.9, 4.10), as a result of strong variability across the time series (Figures 4.2, 4.4). This suggests that detectability in the tropical sites is controlled by the influence of nearby active emissions sources, which leads to high variability in the time series on both scales, effectively masking the influence of sink variability. Positioning a continuous monitoring instrument in northern polar locations would therefore be most useful for capturing OH variability.

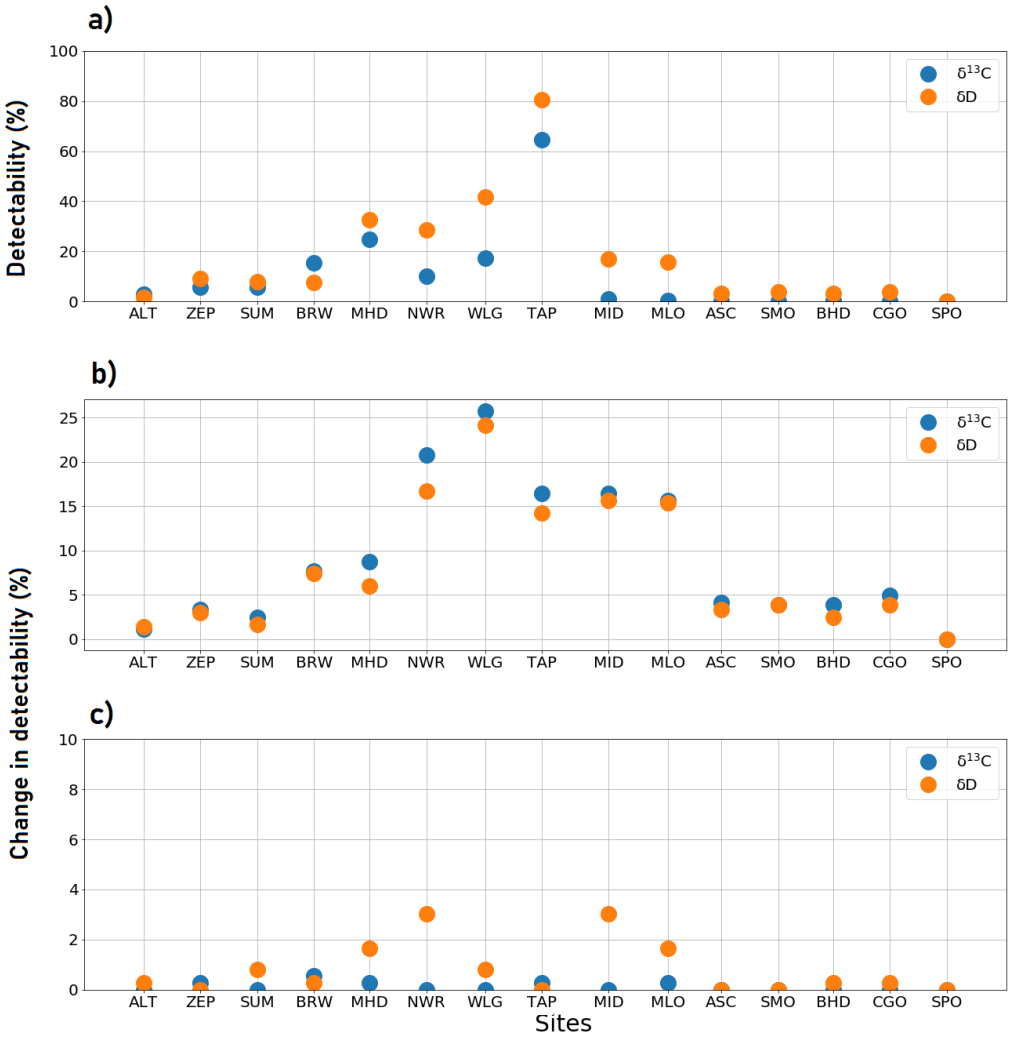

Figure 4.9: a) daily-scale detectability of both δ^{13}C and δD at the grid squares in the model which correspond with the listed NOAA network sites (which are in latitudinal order), over the period 2016-2020. b) The effect of source signature tests (all source signatures shifted heavier by 5‰ for δ^{13}C and 20‰ for δD), upon daily detectability at the listed NOAA network site locations within the model. c) Effect of OH tests (depressing worldwide OH by 5%) upon daily detectability at the location of sites as listed, 2016-2020. b) and c) represent two individual tests, calculated by the absolute difference at the grid square for the location of each site (2016-2020), between a control simulation and one with perturbed source signatures or sink around the world.

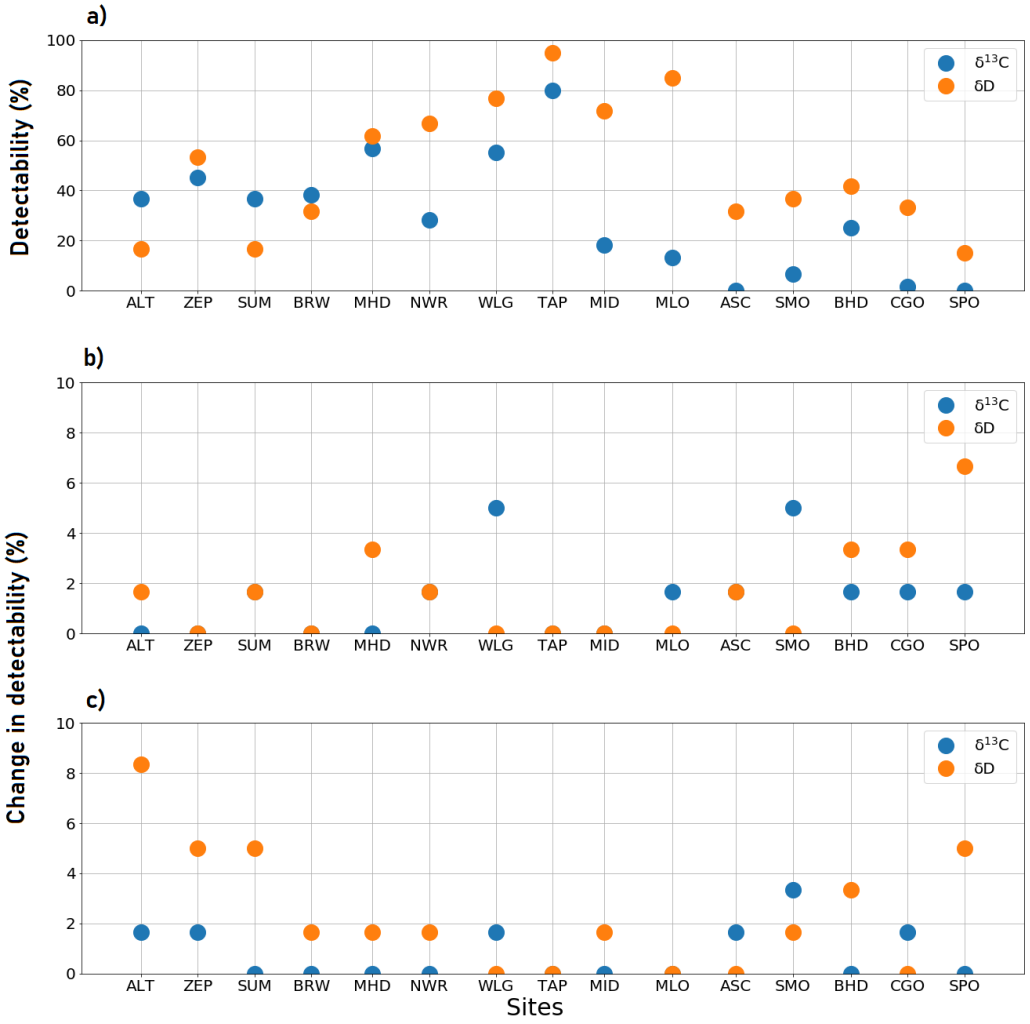

Figure 4.10: a) monthly-scale detectability of both δ^{13}C and δD at the grid squares in the model which correspond with the listed NOAA network sites (in latitudinal order), for the 'control' simulation over the period 2016-2020. b) The effect of source signature tests (heavier by 5% for δ^{13}C and 20% for δD), upon monthly detectability at the listed NOAA network site locations within the model. c) Effect of OH tests (depressing worldwide OH by 5%) upon monthly detectability at the location of sites as listed, 2016-2020. b) and c) represent separate tests, calculated by the absolute difference at the grid square for the location of each site (2016-2020), between a control simulation and one with perturbed source signatures or sink around the world.

4.5 Accessibility

For establishing a new site location, accessibility is an important consideration. An advantage of continuous monitoring instruments is that they are automated and therefore do not require people to make flask samples. However, should problems arise with the instrument, this has to be a consideration in deployment.

For monitoring monthly-scale changes, Arctic or central oceanic site locations present challenges in terms of accessibility, as they are all ocean or permafrost based. This would make it difficult to set up and access the instrument, in the case of unexpected breakdown. For operating in high latitudes, cold temperature may also be an issue, and so the instrument would need cold-weather protection (such as protective housing). For example, at the NOAA South Pole monitoring site there is a specially-built facility to maintain temperature (with six-inch thick insulation and sealed windows), which is manned year-round by at least two members of staff. The station is in a designated 'Clean Air Sector' to negate any pollution influence, and is heated electronically (US Department of Commerce, 2022).

Tropical site locations present a deployment challenge in terms of humidity and high temperature. The island-based site locations would also require protective housing in order to avoid damage from wind exposure. In capturing daily-scale variations, eastern Asia showed highest relative daily-scale detectability for both δ^{13}C and δD. These potential sites are located around cities and populated areas, so access for equipment and specialists should be possible. Again, high temperature and humidity may be an issue in this region and so the instrument may need weather defence.

A location to capture both daily and monthly-scale variations would be eastern Europe and eastern Canada. These are at similar latitudes to where the Boreas instrument has been located (the Heathfield atmospheric monitoring station, where it is housed at 21°C) and so weather or extreme temperatures should not be as much of a consideration. They also should be readily accessible for scientists to check on the instrument should the need arise.

4.6 Conclusions

In conclusion, the deployment of a new, continuous monitoring instrument would be effective at capturing monthly-scale variations in CH_4 isotope ratios if deployed to the locations of current NOAA measurement sites.

For δ^{13}C, monthly and daily-scale variations would be captured in the Northern Hemisphere, especially in eastern Asia and central Africa, where more than 80% of monthly-scale and 90% of daily-scale variations would be captured (Figure 4.6). This performance is due to the influence of active sources leading to high variability. Detectability all around the world is higher by 21% on average for δD measurements as opposed to δ^{13}C, however the locations of grid squares with highest detectability (in this case, in excess of 90% on both a daily and monthly scale, Figure 4.7) are consistent (eastern Asia, central Africa, South America). This is indicative of better relative performance of the instrument for δD than for δ^{13}C (Chapter 3).

At specific site locations, highest detection for both daily and monthly scale shows a latitudinal dependency, with higher detection at Northern Hemisphere sites. Highest detection is at Tae-Ahn Peninsula site (more than 60% on a daily scale and more than 80% on a daily scale; Figures 4.9a and 4.10a). This location has strong variability across the time series, shown by Figures 4.2 and 4.4. Considering specific site locations, this instrument would capture variations in δD more effectively then δ^{13}C, by up to 20% on a daily scale and up to 70% on a monthly scale (Figures 4.9a and 4.10a).

Establishing a new site location depends upon the aim of the instrument deployment. For monthly-scale monitoring, locations such as Arctic and tropical oceanic regions would be influenced by monthly-scale variations from wetland emissions without the influence of daily-scale events (difference of 60% detectability, Figure 4.8). For capturing daily-scale events, eastern Asia and central Africa represent locations with higher relative detectability of 3-5% for daily-scale compared with monthly-scale variations. A positive of continuous monitoring instruments is the potential to measure both daily and monthly-scale variations; in this case, northern mid-latitudes (such as Canada and eastern Europe) have a good balance of 50% of daily-scale variations and 90% of monthly-scale variations captured. In all of these cases, continuous monitoring would improve temporal resolution on these events, in order to better understand and categorise both monthly-scale variations and daily-scale events.

Variations in emissions source signatures have an impact upon continental site locations on a daily scale and remote oceanic site locations on a monthly scale. This indicates the importance of active sources in the daily-scale variability, such as those produced by pollution events. OH sink variations have greatest impact at remote polar locations, where emissions sources do not dominate the time series. The sink influence is greater on a monthly scale than daily, and is especially impactful for δD due to the higher KIE, in the Northern Hemisphere due to stronger poleward transport.

Continuous measurements of CH_4 isotope ratios would be useful for inversion studies, as constraints to understand the driving forces behind increasing amount fractions of CH_4 observed worldwide. If new sites were established in addition to current network sites then additional constraints would result in uncertainties on fluxes would be reduced. With reduced uncertainties, CH_4 fluxes are clearly defined, increasing understanding and confidence of how emissions are varying. This in turn discerns what sectors to focus upon for working towards emissions reduction aims, such as those outlined by the Paris Agreement, limiting the impact of ongoing climate change. For a large-scale global inversion which covers multiple years (such as that performed in Chapter 2), the aim of deployment would be to capture monthly-scale variations in CH_4 isotope ratios. The recommended locations for establishing a new site in this context would therefore be to tropical oceanic locations, such as the central Atlantic and Indian Oceans. This also aligns with the findings of Chapter 2, that tropical locations are driving increases in the CH_4 budget.

Within this analysis, a limiting factor upon location recommendations is that the model is at a coarse resolution ($4^\circ \times 5^\circ$ resolution). These results therefore represent broad-scale recommendations, with large-scale regions as the recommendations. When considering exact locations for deployment, the area within each cell would have to be examined in detail. For example, if the measurement aim were to examine monthly-scale trends, the exact location for deployment would have to be positioned at a distance from point sources, to avoid the influence of pollution on a monthly-scale scale.

Overall, this chapter has progressed the thesis by examining the capabilities of a new ground-based *in situ* instrument around the world. The work has assessed where an instrument should be located to effectively capture variations in CH_4 isotope ratios. A continuous monitoring instrument would be effective at capturing δ^{13}C and δD, with more than 80% of variations captured, if deployed at tropical site locations. For an entirely new deployment, northern mid-latitudinal locations (such as eastern Canada) have a good balance of monitoring daily and monthly-scale variations.

4.6.1 Future Work

This chapter examines the potential future usage of a continuous monitoring instrument, and additional information that the instrument could bring to the current network. The analysis is based upon the Boreas instrument, currently located at the Heathfield atmospheric monitoring site in the UK. In the future this instrument will be reproduced and future Boreas instruments deployed to new locations. For deployment of a new site, the aim of the deployment is important to bear in mind, be it monthly-scale monitoring (tropical oceanic regions); daily-scale variations (eastern Asia); or a combination of both (eastern Europe, eastern Canada).

This analysis was based upon up-to-date precision for continuous monitoring instrumentation (represented by the Boreas instrument). In the future, instrument precision may be improved, which would require the analysis to be performed again and re-assessed for the improved precision of a future instrument.

Chapter 5

Conclusions and Future Work

5.1 Conclusions

The overall aim of this thesis was to advance the understanding of the changing atmospheric CH_4 budget, by examining ground-based *in situ* monitoring capabilities. This was achieved by using a combination of both modelling and metrology techniques. The novel features of this work include:

1) A 3D chemical transport model (CTM) being used to simulate regional CH_4 and $\delta^{13}C$, performing inversions to determine how large-scale regional emissions and $\delta^{13}C$ source signatures have varied over 17 years.

2) Establishment of a data analysis procedure for measurements of CH_4 isotope ratios made by a continuous CH_4 preconcentration system. The instrument 'Boreas' was developed at the UK's National Measurement Institute, the National Physical Laboratory (NPL). Also shown is analysis of a sample data set produced by the instrument, demonstrating how the instrument performs for emissions identification.

3) Examination of a hypothetical deployment of a continuous monitoring instrument around the world. The analysis considers deployment at current NOAA measurement network site locations and at potential new site locations (where there are currently no measurement networks in existence). The aforementioned 3D CTM was used to simulate δ values, and instrument specifications considered, to assess the detection limit of signals.

These novel approaches (over three research chapters) assessed the following research questions, as outlined in Chapter 1:

1) How have CH_4 amount fractions and isotope ratios varied over a recent 17 year period, and what regions/sources are responsible?

2) How should data from a newly developed laser-based measurement system be processed to produce high precision data for analysis?

3) Where should ground-based *in situ* continuous monitoring instruments be located, in order to measure CH_4 isotope ratios most effectively?

The impact of answering these questions leads to advancements in both CH_4 modelling and metrology. Understanding what regions and sources are driving observed increases in CH_4 amount fractions through modelling indicates what specific sectors are driving emissions increases (Fujita et al., 2020; Lan et al., 2021; McNorton et al., 2018), and therefore what sources should be targeted for emissions reductions scenarios. Developing and deploying an instrument capable of continuous monitoring of CH_4 isotope ratios means that changes in CH_4 emissions are monitored independently at high precision and high frequency, improving both sampling frequency and geographic coverage of measurements. These measurements can feed back into future modelling work by providing additional constraints on inversion studies, which should give more accurate results in terms of driving forces behind amount fraction and isotope ratio variations. Currently, inversions based upon ground-based *in situ* data are limited by station coverage, especially for isotope ratios (Chapter 2), and so more high-frequency measurements can meet this need. These multiple studies all lead to better understanding of how the atmosphere is changing in response to climate change.

5.1.1 Large-Scale Regional Inversions for CH_4 Emissions and δ^{13}C Signature, 2004-2020

Chapter 2 addressed the first research question — how have CH_4 amount fractions and isotope ratios varied over recent a 17 year period, and what regions/sources are responsible? This chapter examined ground-based monitoring capability by understanding the utility of the current ground-based *in situ* network for large-scale inversion studies.

CH_4 and δ^{13}C were simulated for the entire world on a $2^\circ \times 2.5^\circ$ resolution from 2004-2020 using the GEOS-Chem 3D chemical transport model (Bey et al., 2001). An inversion over this period was performed using a Maximum *A Posteriori* (MAP) approach, solving for regional CH_4 fluxes and δ^{13}C source signatures. Monthly CH_4 and δ^{13}C data were used as a constraint, from NOAA-ESRL and CU-INSTAAR, respectively. The results were compared (for part of the time series) with a similar inversion which solved for the CH_4 fluxes of regions using data from the Greenhouse gas Observing SATellite (GOSAT) as a constraint, over the period 2010-2020.

This time period (2004-2020) was specifically examined to understand the driving forces behind the uptick of CH_4 amount fractions which occurred post-2007, following the amount fractions being approximately constant in the period 1999-2007 (Figure 1.1, Lan et al., 2021). This increase in amount fractions occurred at the same time as the global atmospheric δ^{13}C signature began to shift lighter (Figure 1.1), and so the forces behind this increasingly light trend were also examined through a δ^{13}C emissions source signature inversion.

Considering *a posteriori* emissions using ground-based *in situ* CH_4 data, the balance of CH_4 sources post-2007 was found to have shifted from the northern mid-latitudes to tropical regions. The results of the $\delta^{13}C$ inversion indicate that tropical emissions have light $\delta^{13}C$ source signatures. Combining this result with finer-scale studies using satellite data (e.g Feng et al., 2022; Lunt et al., 2021; Wilson et al., 2021), we attribute these increases to tropical wetland emissions. The increase of natural emissions presents an issue for future emissions mitigation, as natural emissions are more challenging to reduce than anthropogenic emissions (Comyn-Platt et al., 2018). Meeting emissions reduction goals (such as those outlined by the Paris Agreement) will therefore be more challenging, and require more strict reductions from anthropogenic sources.

The results of the satellite data inversion show good agreement with the ground-based *in situ* measurement inversion results, both on a global scale and in terms of the regions responsible for changes in CH_4 fluxes (namely North Africa, India and Tropical South America). However, there are certain regions where the approaches disagree, such as over China, where GOSAT finds a decrease relative to *a priori* emissions, but the ground-based *in situ* inversion finds increases. These discrepancies arise from areas being poorly covered by ground-based *in situ* data, and limits on satellite data detection (such as due to cloud cover in tropical regions).

As well as emissions driving amount fraction changes, changes in atmospheric sinks have been proposed as a driving force behind global CH_4 amount fraction growth (Rigby et al., 2017; Turner et al., 2017). To examine the role of OH in CH_4 emissions increases, sensitivity tests examining a 0.5%/yr decrease in global OH (following Turner et al., 2017), following by a 5% decrease in 2020 in response to COVID-19 lockdown changing NO_2 patterns (Laughner et al., 2021; Miyazaki et al., 2021), while still using CH_4 amount fraction and $\delta^{13}C$ data as a constraint. These variations in OH result in emissions that are lower by as much as 50 Tg/yr (in 2020) compared with *a posteriori* emissions. However, the resulting emissions are within the uncertainty of the *a posteriori* CH_4 emissions values. Changes in OH therefore may have played a role in CH_4 amount fraction increases, but would not be solely responsible for CH_4 emissions changes over the period 2004-2020.

An issue which is highlighted from the performed inversions (especially for $\delta^{13}C$) is the lack of spatial coverage of ground-based *in situ* isotope ratio monitoring sites. This leads to *a posteriori* $\delta^{13}C$ emissions signatures from some regions being strongly correlated, meaning that the emissions signatures from these regions cannot be individually determined. The work performed in Chapters 3 and 4 addresses the lack of ground based *in situ* isotope ratio monitoring sites by introducing a new instrument capable of continuously measuring isotope ratios at high precision, and assessing where would be best to position such an instrument for optimal and efficient use of the data.

5.1.2 Data Processing for Analysis of δ^{13}C and δD Methane Using a Laser Spectrometer Based System

Chapter 3 addressed the second research question — how should data from a newly developed laser-based measurement system be processed to produce high frequency data for analysis? This chapter examined ground-based monitoring capabilities by introducing a newly developed instrument. 'Boreas' was developed at NPL in 2019 and is capable of making continuous high precision, high frequency measurements of CH_4 isotopologues ($^{12}CH_4$, $^{13}CH_4$ and $^{12}CH_3D$). In establishing a new instrument it is important to outline the necessary steps to produce calibrated δ values.

The data processing procedure consists of calibrating recorded isotopologue amount fractions using an 'isotopologue' method (Griffith, 2018; Rennick et al., 2021; Steur et al., 2021). This approach uses primary reference materials (PRMs), independently measured by RHUL for quality control and for linking data to international laboratories. The relationship between Boreas-measured and independently-measured isotopologue amount fractions on these PRMs are used to calibrate the isotopologue measurements made by Boreas. A drift correction was also performed as a part of the calibration, to account for drift within Boreas over the run cycle.

For Boreas-measured values to be of use in modelling studies, they should be on the same scale as RHUL measurements, so that they can be associated with other international laboratories. Therefore, an offset adjustment is performed on Boreas isotope ratio values, using a scale factor to relate Boreas-measured PRM isotope ratio values to RHUL-measured PRM isotope ratio values.

Another consideration for Boreas measurements is that, to make the instrument most efficient, the system should maximise the number of air measurements recorded. In the initial setup, the Boreas Target tank (BT) is measured in turn after every air measurement. BT is a compressed clean-air standard filled at Mace Head in Ireland (one of the UK-DECC network sites) and is used to confirm the repeatability of the preconcentrator. To maximise the number of air measurements, measuring the gas standard following every sixth air measurement was found to be appropriate to ensure a balance between maximising air measurements and ensuring that the internal offset adjustment is calculated with the required frequency.

Although Boreas is primarily designed for measuring $^{12}CH_4$, $^{13}CH_4$ and $^{12}CH_3D$, calibrated CH_4 amount fraction data can also be calculated from the individual isotopologue measurements. The isotopologue data are calibrated by considering the extent of preconcentration (the ratio between the volume of the Boreas trap and the spectrometer sample volume), for each measurement cycle. To quality control isotopologue amount fractions from Boreas, the

data are compared with amount fraction values measured by a Picarro G2401, co-located with Boreas at the Heathfield atmospheric monitoring site. The Boreas amount fraction corresponded well with amount fraction values measured by the Picarro instrument, indicating that this approach is effective.

In addition to data from the Heathfield site, a time series of data from when Boreas was operating at NPL was presented. This time series demonstrates the capability of Boreas to isolate specific sources in different environments (i.e. in a city setting where NPL is located). Using both Keeling and Miller-Tans analysis, the source of individual CH_4 pollution events was identified, which demonstrated instrument capability to delineate between source types using isotope ratio data.

As a result of the data presented in this chapter, questions arise regarding what additional information could be added to the global measurement network if the Boreas instrument was placed at monitoring stations around the globe. This question is addressed in Chapter 4.

5.1.3 Potential Improved Monitoring of δ^{13}C and δD Through Deployment of Continuous Monitoring Systems

Chapter 4 addressed the third research question — where should ground-based *in situ* continuous monitoring instruments be located in order to measure CH_4 isotope ratios most effectively? This chapter examined ground-based monitoring capability by establishing where would be most beneficial for future modelling work to position continuous optical instruments.

In the deployment of continuous optical instruments, sampling frequency is increased (hourly rather than approximately weekly for flask sampling, Dlugokencky et al. (2020)), due to improved portability and the low maintenance required. As a result of the increased frequency of sampling, short-lived pollution events can be finely monitored and understood. For monitoring trends over a longer time series, the chance of an anomalous event skewing results is reduced, improving reporting of isotope ratio trends.

δ^{13}C and δD were simulated using GEOS-Chem, over the period 2016-2020. δ^{13}C was simulated using *a posteriori* fluxes and source signatures for δ^{13}C, from the inversions performed in Chapter 2. Simulations for δD were created synthetically, based upon published source signatures for different sectors, rather than from an inversion, due to the lack of available data.

Global values of 'detectability' were calculated based upon simulated δ^{13}C and δD values. Detectability indicates how effectively a continuous monitoring instrument would capture variations in δ^{13}C and δD, on both daily and monthly scales, by comparing rolling standard deviations to typical continuous monitoring instrument precision, based upon the Boreas precision from Chapter 3. These results were presented both on a global scale and at the specific locations in the model which correspond with the locations of NOAA sites.

The chapter results indicate that a continuous monitoring instrument would be effective at capturing monthly-scale changes in δ^{13}C and δD, if positioned at the same location as NOAA network sites in the Northern Hemisphere, such as east Asia based sites. Detectability for specific grid cells located in east Asia exceed 90% of daily-scale and 80% of monthly-scale events for both δ^{13}C and δD. Generally, detectability for δD is greater than for δ^{13}C (by an average of 12% on a daily scale and 21% on a monthly scale), demonstrating that this instrument performs relatively better for δD than for δ^{13}C. Detectability reduces to as low as 0% for δ^{13}C and less than 10% for δD at the South Pole, meaning that variations would not be captured here. Therefore active emissions sources (rather than a background site) create the variations necessary to be picked up by the continuous monitoring instrument.

At specific site locations, highest daily and monthly detectability is in tropical regions in east Asia. Specifically, Tae-Ahn Peninsula site has highest detectability; 65% and 77% on a daily and monthly scale respectively for δ^{13}C, 90% on both daily and monthly scale for δD. This site has strong variability resulting from sources from rice and coal mines in China (Dlugokencky et al., 1993), leading to high detectability. The metric decreases to less than 5% detectability for δ^{13}C and δD at polar site locations, with low variability.

In terms of new site locations, the analysis considered three scenarios: to capture monthly-scale changes, daily-scale changes, or a combination of both. Using continuous monitoring instruments allow both daily and monthly-scale monitoring. For monthly-scale monitoring, the tests showed that Siberia and central ocean regions (central Atlantic, Pacific and Indian Oceans) were the most promising in this regard, showing good monthly detectability (more than 70% of variations captured) with minimal influence of pollution events. For daily-scale pollution event monitoring, east Asia is a location where daily-scale events dominate over monthly-scale, due to strong variability from nearby anthropogenic sources (such as rice and coal). For a balance of capturing monthly and daily-scale events, locations with daily detectability captured for part of the year, without overwhelming the signal (approximately 50% variations captured), would be eastern Europe and eastern Canada, where wetland emissions dominate the seasonal cycle and daily-scale variations arise from anthropogenic sources such as agriculture.

A series of sensitivity tests were performed to examine what effect varying source signatures and sinks has on detectability, for both δ^{13}C and δD measurements. To achieve this, the global source signature was scaled heavier by 5‰ for δ^{13}C and 20‰ for δD. For the sink tests, the magnitude of OH in the model was decreased globally by 5%. Following spin-up, the detectability tests were performed on the new values to examine what locations were sensitive to emissions signature and sinks. Most sensitive to changes in global source signature were tropical locations such as in east Asia on a daily scale, due to strong variability of signals

being driven by anthropogenic emissions. The OH sink tests had the greatest effect at sites in the polar regions on a monthly scale. δD northern polar locations were most strongly affected by the reduced OH amount fractions; this is due to OH having a greater effect upon CH_3D than $^{13}CH_4$ and poleward flow in the Northern Hemisphere.

To be useful for a large-scale inversion (such as that performed in Chapter 2), locations for continuous deployment would be tropical islands in the Atlantic and Indian Oceans, where monthly variations are captured without daily-scale event influence. These are large-scale regions, so would have to be explored in finer detail to avoid interference. For example, if the aim is to explore monthly-scale variations, avoid the influence of nearby point sources.

5.2 Future Work

5.2.1 Regular δD measurement

In Chapter 2, the inversions were performed to solve for regional CH_4 emissions and δ^{13}C emission source signatures, omitting the second-most common stable isotope ratio, δD. δD represents the proportion of deuterium (the most common isotopologue of which is CH_3D) relative to hydrogen in atmospheric CH_4, and δD signatures vary depending upon emissions type (Douglas et al., 2017).

An inversion for δD was not performed in this case due to the paucity of δD data available, resulting from the few ongoing regular monitoring stations around the world. The NOAA network set up regular measurements of δD in 2005 at 15 sites, however these sites were decommissioned in 2009 as a result of instrumentation issues (White et al., 2016). The lack of regular measurements is a result of the expense and complexity involved in constructing a measurement system for isotope ratios (this is also the case for measurements of δ^{13}C, but CH_3D is approximately 100 $\times$ more rare than $^{13}CH_4$, so is more difficult to measure; Table 1.2). As a result of it being less frequently measured, δD signatures appear to be less sensitive to different emissions types (Figure 1.2). However, Menoud et al. (2022) took mobile measurements of both δ^{13}C and δD around Europe using IRMS, and found that δD was especially effective at differentiating between fossil fuel and microbial source types. Therefore, additional measurements of δD would be of great use to the atmospheric modelling community to delineate between sources. Furthermore, if used as constraints in atmospheric inversion studies, δD would reduce uncertainties in results.

Warwick et al. (2016) previously simulated δD in a 3D CTM. They use a composite of NOAA data from 2005-09 to compare to their simulation to *in situ* data, simulating the Arctic over one year. Similarly Rigby et al. (2012) use pseudo-data to simulate global δD values over one year, unconstrained by *in situ* data. Chapter 4 has advanced from these studies in simulating δD

globally over multiple years, 2016-2020. These are all forward simulations, meaning that the emissions are not constrained by *in situ* data. If measurements of δD were more widespread, there would be enough data to perform an inversion using ground-based *in situ* data, for regional δD signatures, like in Chapter 2.

Overall, more regular and widespread measurements of δD data would be useful for atmospheric modelling. These data could provide additional constraints on inversions, reducing uncertainty upon the drivers of CH_4 amount fraction changes. As such, restarting regular measurements of δD at multiple locations around the world should be focus for the future.

5.2.2 Clumped Isotopes

Multiply-substituted ('clumped') isotopes may provide an additional constraint on changing proportions of sources and sinks. Clumped isotopes refer to molecules with multiple isotopic replacements in the same molecule, for example, $^{13}CH_3D$ and $^{12}CH_2D_2$ are the two most common clumped isotopologue species for CH_4 (Eiler, 2007). Studies surrounding clumped isotopes (e.g. Douglas et al., 2017; Stolper et al., 2014) have shown that clumped isotope signatures (Δ values) can be used as an atmospheric tracer. Clumped isotope signatures vary depending upon CH_4 formation conditions, with heavier isotopologues requiring more energy (corresponding with a higher temperature of CH_4 formation setting) to break apart chemical bonds.

The quantity of clumped isotopes in a sample is presented in Δ notation, calculated as:

$$\Delta = \left(\frac{R_{meas}}{R_{stochastic}} - 1\right), \tag{5.1}$$

where R_{meas} is the ratio of rare isotopologue to the most common isotopologue $^{12}CH_4$. $Stochastic$ refers to a state in which isotopes are randomly distributed across all of the isotopologues in a sample (i.e what the ratio would be if ^{13}C and D were randomly distributed across the isotopologues).

These clumped isotopes exist in very low abundances in the atmosphere (the most common clumped isotope is $^{13}CH_3D$, making up 0.000692% of all CH_4; Stolper et al. (2014)). Therefore, there is a significant challenge associated with their measurement. However, advances in preconcentration technology (as demonstrated by Boreas, Chapter 3) are making continuous measurements of these isotopes more realistic.

Previous measurements of clumped isotopes have mostly been lab-based, on individual air samples rather than continuously. Measurements have been made using both mass spectrometry (Stolper et al., 2014) and laser spectroscopy techniques (Ono et al., 2014; Prokhorov & Mohn, 2022). Considering the improvements in field-based measurements (Eyer et al.,

2016; Prokhorov & Mohn, 2022; Rennick et al., 2021), remote field measurements of clumped isotopes of CH_4 will become more readily available in the future. Efforts have begun to simulate clumped isotopes of CH_4 in modelling; Chung and Arnold (2021) simulate $\Delta^{13}CH_3D$ and $\Delta^{12}CH_2D_2$ using a 12-box global model, over three decades.

In the future, more regular and widespread measurements of clumped isotopes would provide additional evidence to CH_4 inversion studies by improving source delineation, both on a regional or global scale. These potential data would provide additional constraints upon modelling and inversion studies, indicating how the balance of CH_4 sources have shifted over time and therefore what sectors should be targeted for future emissions reductions strategies.

5.2.3 Further Sink Tests

It is important to examine both sources and sinks as possible drivers behind observed CH_4 amount fraction increases and changing $\delta^{13}C$ signatures. For example, a decrease in atmospheric OH (the most abundant sink of CH_4) would result in increased atmospheric CH_4 amount fractions. The subject of changing sinks being responsible for the observed changes in CH_4 amount fractions has been proposed by multiple studies (Nisbet et al., 2016; Rigby et al., 2017; Turner et al., 2019, 2017).

Chapter 2 considers only a decreasing OH trend over an extended time series (2004-2019), based upon suggested trends from Turner et al. (2017), with a more extreme depression of OH levels in 2020 (of 5%, as proposed by Laughner et al. (2021); Miyazaki et al. (2021)). 2020 is an extreme case, with unprecedented changes in human behaviour due to lockdowns as a result of the the COVID-19 pandemic. The proposed mechanism is that reduced NO_x emissions from reduced transport emissions had in turn suppressed OH production. However, measurements of OH are challenging, due to the very low atmospheric lifetime of OH (0.01 - 1 s, Stone et al. (2012)). This therefore makes it difficult to understand atmospheric OH trends and implement these changes into models.

By only considering a decreasing trend in OH, the work in Chapter 2 ignores that OH may be instead following an increasing trend, as suggested by Zhao et al. (2019). Increased global OH would mean faster decomposition of CH_4, which, without emissions changing, would result in decreasing amount fractions.Therefore, in order for this scenario (of increased OH trends) to match with observed emissions of CH_4 from ground-based data (i.e increasing trends), there would have to be increased regional emissions relative to the *a posteriori* emissions estimates.

Furthermore, only the impact of OH changes on CH_4 amount fractions are examined in this thesis. It would also be prudent to examine the impact of OH on CH_4 isotope ratios. For example, Lan et al. (2021) examined the impact of changes in OH on $\delta^{13}C$ data using a 3D chemical transport model, and found that decreasing OH on the scale that Turner et al. (2017)

suggested (a decrease of 7% globally, 2003-2016), cannot reconcile with measured $\delta^{13}C$ data. Changes in other sinks of CH_4 (such as Cl and the soil sinks) are also not examined in Chapter 2 as a driver of amount fraction increase. However, these sinks are on a much smaller scale than the OH sink (as detailed in Chapter 1), and so would have less of an impact on isotope ratio values.

Therefore, in light of the results from Chapter 2 and from previous studies, future work should include examining the impact of different trends in OH and other sinks, along with their impact on isotope ratio data. This would clarify changes in the CH_4 budget over 2004-2020 and provide additional information to allow scientists to achieve a more rounded understanding of the global methane budget with the hope this would allow more efficient mitigation strategies on greenhouse gases.

5.2.4 Boreas Deployment

Boreas is at present in place at the UK-DECC network's Heathfield atmospheric monitoring site. The data measured there requires ongoing processing, analysis and preparation. The data from Boreas will used in regional-scale inversions, for example to understand how the UK's mix of sources is varying over time.

Currently, there is only one Boreas instrument in operation. The future plan is to build more instruments and deploy these to various global atmospheric monitoring sites. Boreas represents new progress in optical measurements, by achieving similar precision to those from conventional isotope ratio mass spectrometry methods, while allowing continuous, high precision, remote measurements. The construction of 'Boreas II' at NPL is currently underway. (Chapter 3; Rennick et al. (2021)). The aim is to create a more reproducible construction protocol, to enable the build of unlimited CH_4 preconcentrators in the future.

Analysis in Chapter 3 demonstrated that continuous isotope ratio data from Boreas is capable of delineating between biogenic, thermogenic and pyrogenic source types. The increased sampling frequency (without the need of regular maintenance) means that variations in isotope ratios (for both monthly-scale and daily-scale pollution events) are more clearly defined. This is true both from an already established site and an entirely new site location.

Considering the results from Chapter 4, a measurement campaign for a continuous monitoring instrument to central oceanic regions (such as the central Pacific, Atlantic and Indian Oceans) would be best to measure monthly-scale changes in CH_4 isotope ratios, without the influence of pollution events. One of the major benefits of continuous measurement is that both monthly-scale and daily-scale variations in isotope ratios are measured. These site locations present challenges in terms of accessibility because of weather exposure and distance from infrastructure. East Asian locations have higher detectability on a daily scale than a monthly scale due to the influence of highly variable anthropogenic emissions nearby. A deployment location

to capture both monthly and daily-scale events would be in parts of eastern Canada. Another consideration (which will require future work) will therefore be to develop infrastructure to protect the instrument from elemental damage, such as from weathering an exposure at isolated site locations.

With the deployment of future Boreas instruments, understanding of variations in CH_4 isotope ratios would be improved. This would contribute to understanding the driving forces behind changing CH_4 emissions. Understanding emissions variations highlights important sectors to focus on for future emissions mitigation, in order to achieve emissions reductions goals as set out in the Paris Agreement (Ganesan et al., 2019).

5.3 Summary

The work in this thesis has examined the capabilities of ground-based *in situ* CH_4 isotope ratio data in determining the drivers behind rising contemporary CH_4 emissions, both in terms of source magnitude and sectoral delineation. It has also demonstrated the utility of ground-based *in situ* measurements of CH_4 isotope ratios δ^{13}C and δD, in order to to understand the changing sources and sinks of CH_4. It has shown how large-scale regional CH_4 fluxes and δ^{13}C signatures have varied over 2004-2020; determined how data analysis should be performed on a new, high-frequency high-precision instrument, and established globally where this instrument should be positioned to best capture variations in the primary stable isotope ratios δ^{13}C and δD.

Inversions for regional CH_4 emissions and δ^{13}C signatures were performed, over an extended period, using ground-based *in situ* data (solving for 2004-2020). This established the capability of the network in its current state. Tropical wetland emissions were found to have increased in the post-2007 uptick of CH_4, indicated by increased CH_4 emissions from North Africa, Tropical Asia, and Tropical South America. δ^{13}C source signatures are trending lighter, especially over the tropics, indicating that the emissions here are microbial in origin. Therefore, the ground-based *in situ* data was capable of determining geographical and sectoral drivers of emission trends. A limitation in using ground-based *in situ* data is the lack of data coverage, especially for isotope ratio data, which leads to difficulty in separating regional contributions to the CH_4 budget.

Following this, the setup of a new high-precision continuous CH_4 isotopologue measurement instrument was examined, which could bring new ground-based *in situ* data. The data processing protocol for this instrument was established, in order to produce calibrated δ values of optimum precision. Separate steps of calibrating on isotopologue measurements, drift correcting calibration factors, and making an adjustment on isotope ratio values, was

found to be necessary in order to optimise the instrument. Data analysis was performed on a sample time series, which demonstrated that the instrument is capable of delineating between specific source types, such as identifying waste water treatment facilities when positioned at NPL Headquarters in south-west London.

Finally, the thesis examined the potential capability of continuous monitoring instruments at multiple locations. This chapter explores locations to position a new atmospheric monitoring site, in order to capture background changes in CH_4 and source signatures. Boreas was found to effectively detect changes in CH_4 isotope ratios at the location of current NOAA measurement sites, especially for δD. In terms of the position of an entirely new site, central tropical oceans were found to effectively obtain measurements of both δ^{13}C and δD on a monthly scale, without the influence of pollution events. Locations in east Asia would capture daily-scale variations effectively due to the influence of highly variable anthropogenic emissions, and positioning an instrument at an eastern Canadian site would capture a balance of both monthly and daily-scale variations. The deployment of new continuous monitoring instrumentation would therefore lead to expansion of the network, new data, and improved attribution of source signatures.

This thesis has determined that ground-based *in situ* data are capable of delineating between different source types of CH_4 emissions. This data can determine how the CH_4 emissions budget is changing over time and therefore what sectors should be targeted for emissions reductions. Overall, reducing carbon emissions such as CH_4 on both a national and individual scale will be a necessary focus for the future in order to protect the planet's ecosystems and limit the impacts of climate change.

Appendix A

Appendix

A.1 Site Identifiers

Table A.1: Sites that are included in the *in-situ* inversion. All sites are part of the NOAA network, other than KRS, which is part of the JR-STATION network, monitored by NIES Japan.

Code	Full Name	Latitude (°)	Longitude (°)
ALT	Alert Station	82.28	-62.30
ZEP	Ny-Alesund, Svalbard	78.90	11.89
SUM	Summit, Greenland	72.60	-38.42
BRW	Barrow Station	71.32	156.61
ICE	Storhofdi,Iceland	63.40	-20.29
KRS	Karasevoe, Siberia	58.14	82.25
MHD	Mace Head, Ireland	53.33	-9.90
SHM	Shemya Island, Alaska	52.71	174.12
UUM	Ulaan Uul, Mongolia	44.45	111.09
NWR	Niwot Ridge, Colorado	40.05	-105.59
UTA	Wendover, Utah	39.90	-113.72
WLG	Mt. Waliguan, China	36.29	100.90
BMW	Bermuda	32.26	-64.88
WIS	Ketura, Israel	29.96	35.06
IZO	Izana, Tenerife	28.31	-16.50
MID	Midway Islands	28.22	-177.37
KEY	Key Biscane, Florida	25.67	-80.16
ASK	Assekrem, Algeria	23.26	5.63
KUM	Cape Kumukahi, Hawaii	19.56	-154.89
MLO	Mauna Loa, Hawaii	19.54	-155.58
RPB	Ragged Point, Barbados	13.17	-59.43
SEY	Mahe Island, Seychelles	-4.68	55.53
ASC	Ascension Island	-7.97	-14.40
SMO	American Samoa	-14.25	-170.56
CGO	Cape Grim	-40.68	144.69
BHD	Baring Head	-41.40	174.87
CRZ	Crozet Island	-46.43	51.85
USH	Ushuaia, Argentina	-54.84	-68.31
PSA	Palmer Station, Antarctica	-64.77	-64.05
SYO	Syowa Station, Antarctica	-69.01	39.59
SPO	South Pole, Antarctica	-89.98	-24.8

A.2 Pollution Analysis

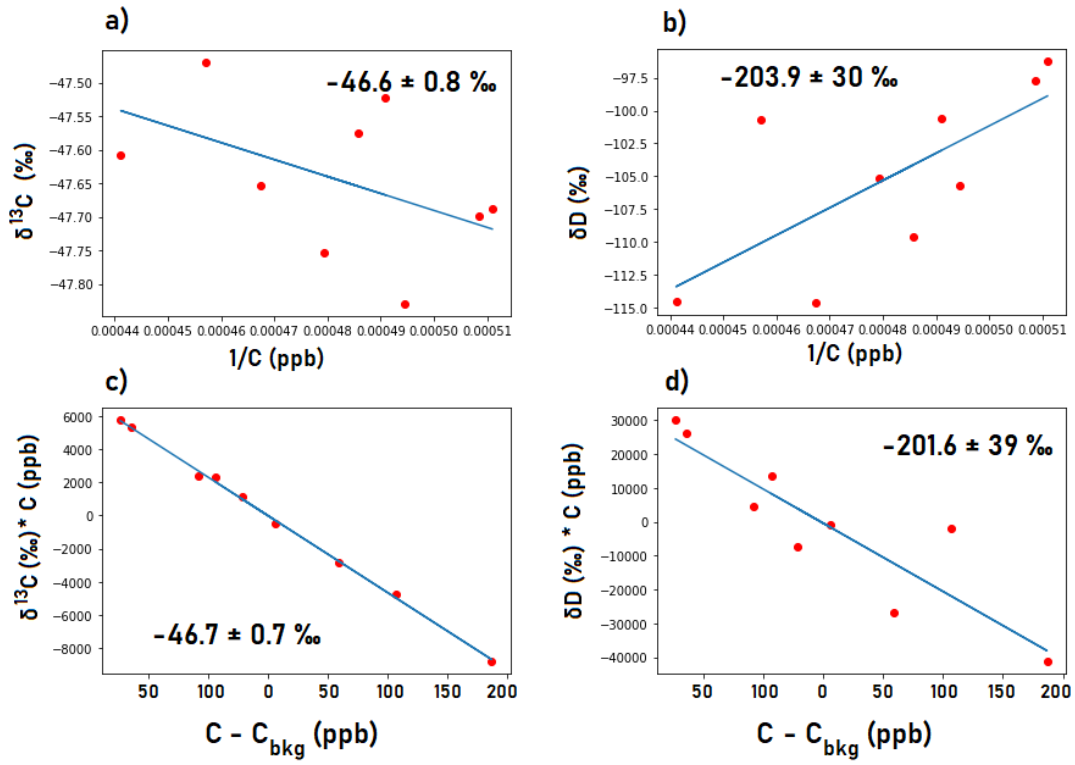

Figure A.1: Keeling (subplots a and b) and Miller Tans (subplots c and d) analysis of a single pollution event (12pm-9pm 22nd December 2020), for (a,c) δ^{13}C and (b,d) δD. 'δ' is the delta value as recorded by Boreas, and 'C' is the amount fraction concentration. The better the fit (blue line) to the data points (red points), the more likely it is that the pollution event is of a single origin. The suggested source signature (y-intercept for Keeling and gradient for Miller-Tans) is listed, along with the error on fit (root mean square error, RMSE).

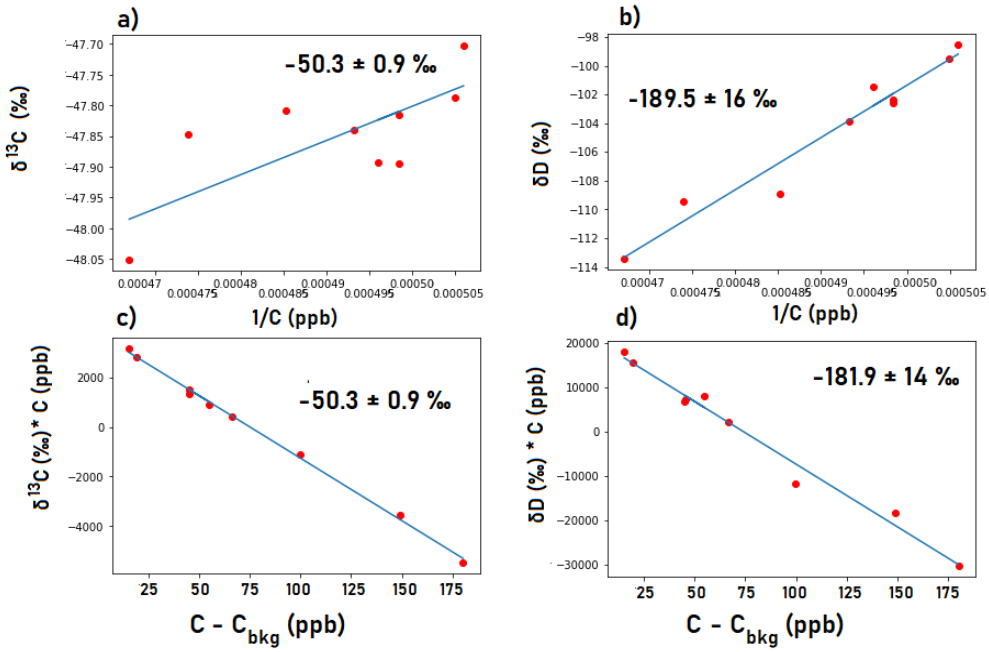

Figure A.2: Keeling (subplots a and b) and Miller Tans (subplots c and d) analysis of a single pollution event (2pm-11pm 27th December 2020), for (a,c) δ^{13}C and (b,d) δD.

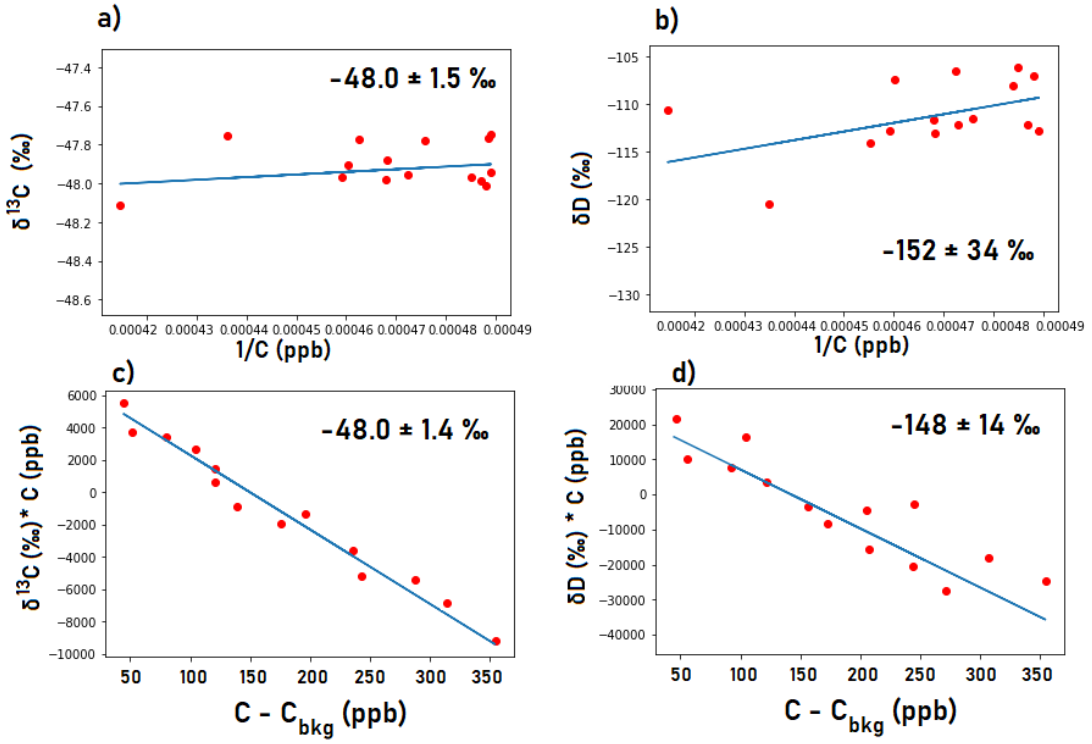

Figure A.3: Keeling (subplots a and b) and Miller Tans (subplots c and d) analysis of a single pollution event (6am-8pm 28th December 2020), for (a,c) δ^{13}C and (b,d) δD.

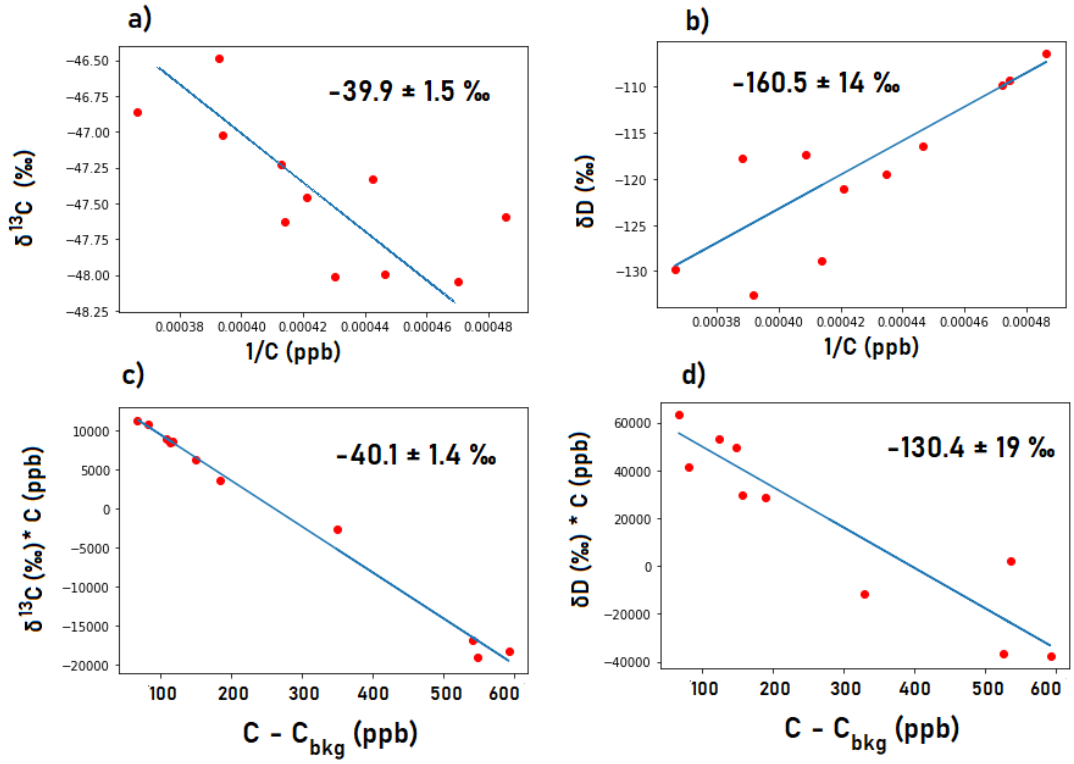

Figure A.4: Keeling (subplots a and b) and Miller Tans (subplots c and d) analysis of a single pollution event (3pm 30th - 2am 31st December 2020), for (a,c) δ^{13}C and (b,d) δD.

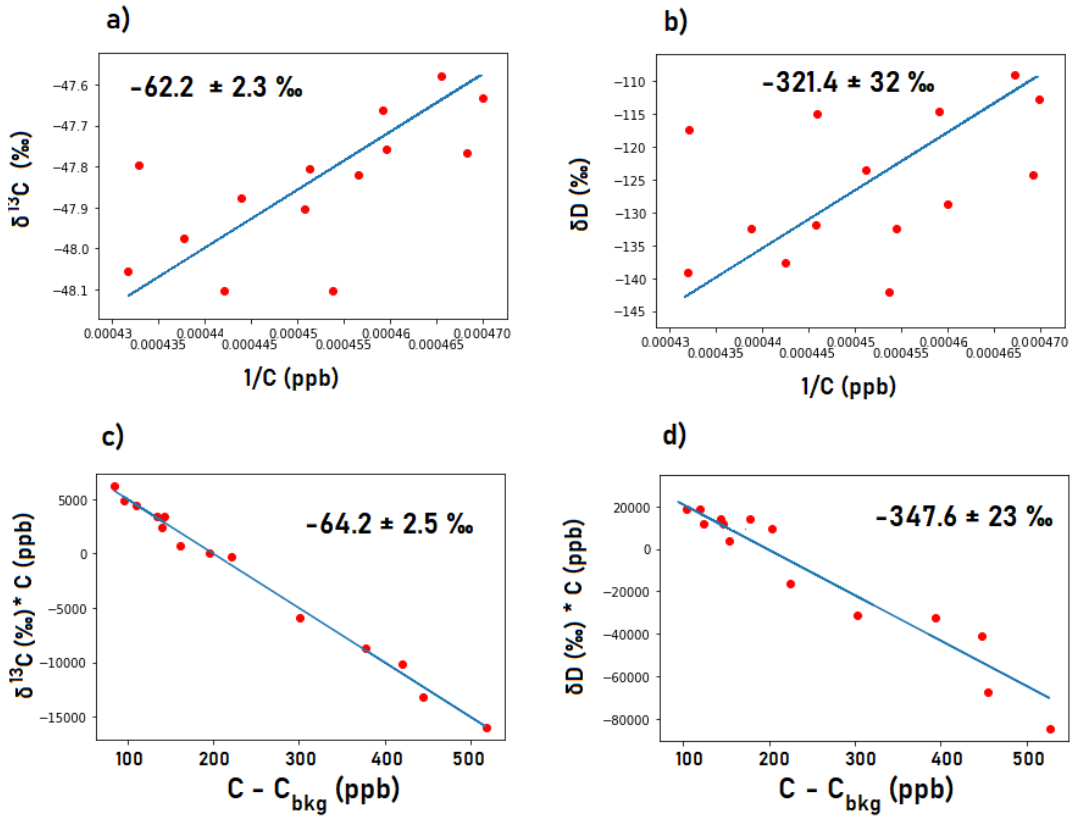

Figure A.5: Keeling (subplots a and b) and Miller Tans (subplots c and d) analysis of a single pollution event (6pm 1st 8am 2nd January 2021), for (a,c) δ^{13}C and (b,d) δD.

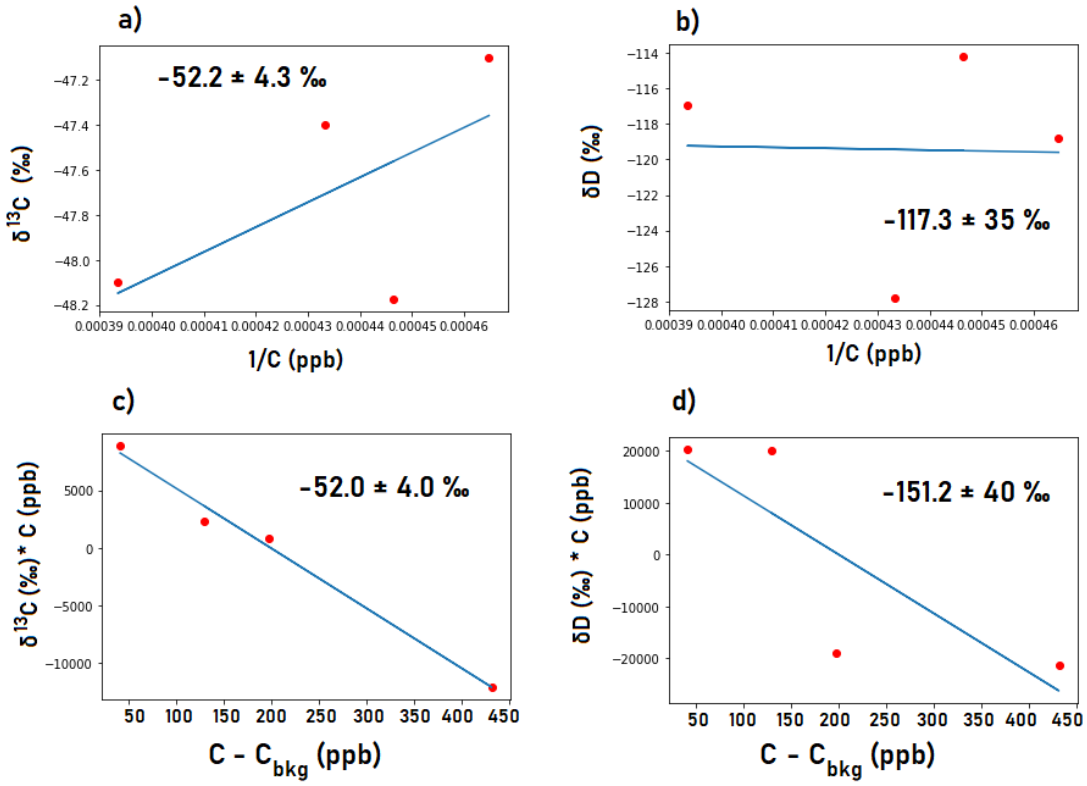

Figure A.6: Keeling (subplots a and b) and Miller Tans (subplots c and d) analysis of a single pollution event (3pm - 7pm 15th January 2021), for (a,c) δ^{13}C and (b,d) δD.

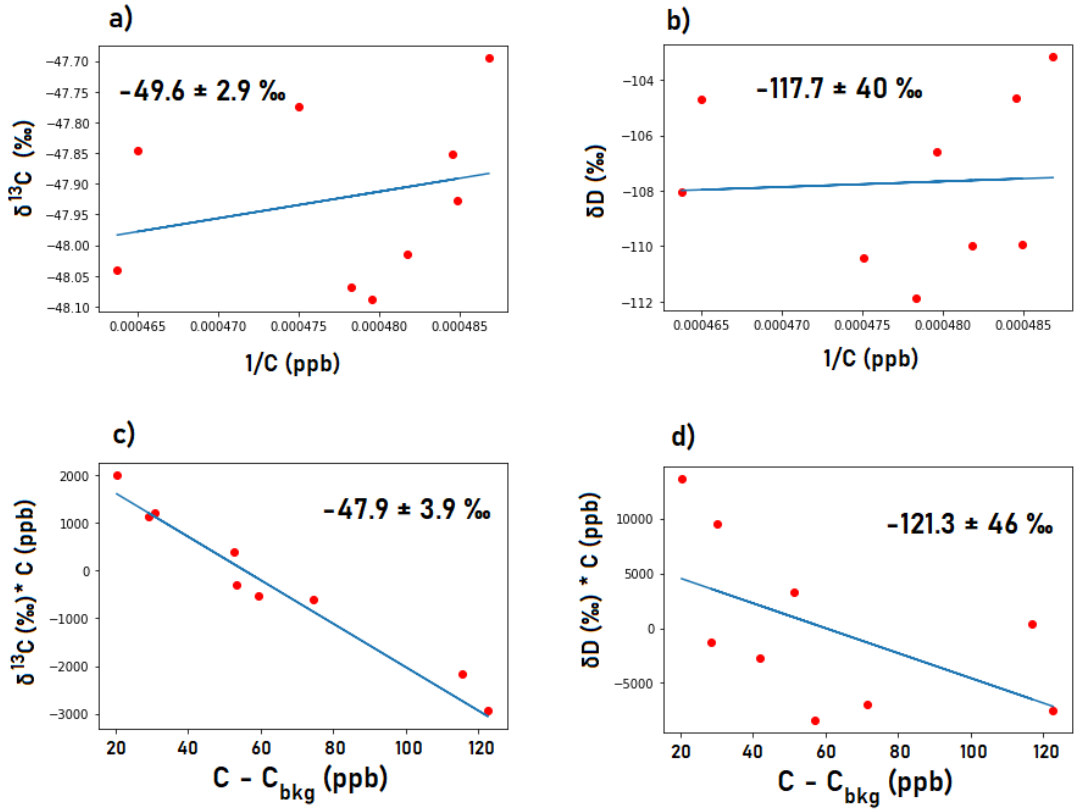

Figure A.7: Keeling (subplots a and b) and Miller Tans (subplots c and d) analysis of a single pollution event (12pm - 9pm 16th January 2021), for (a,c) δ^{13}C and (b,d) δD.

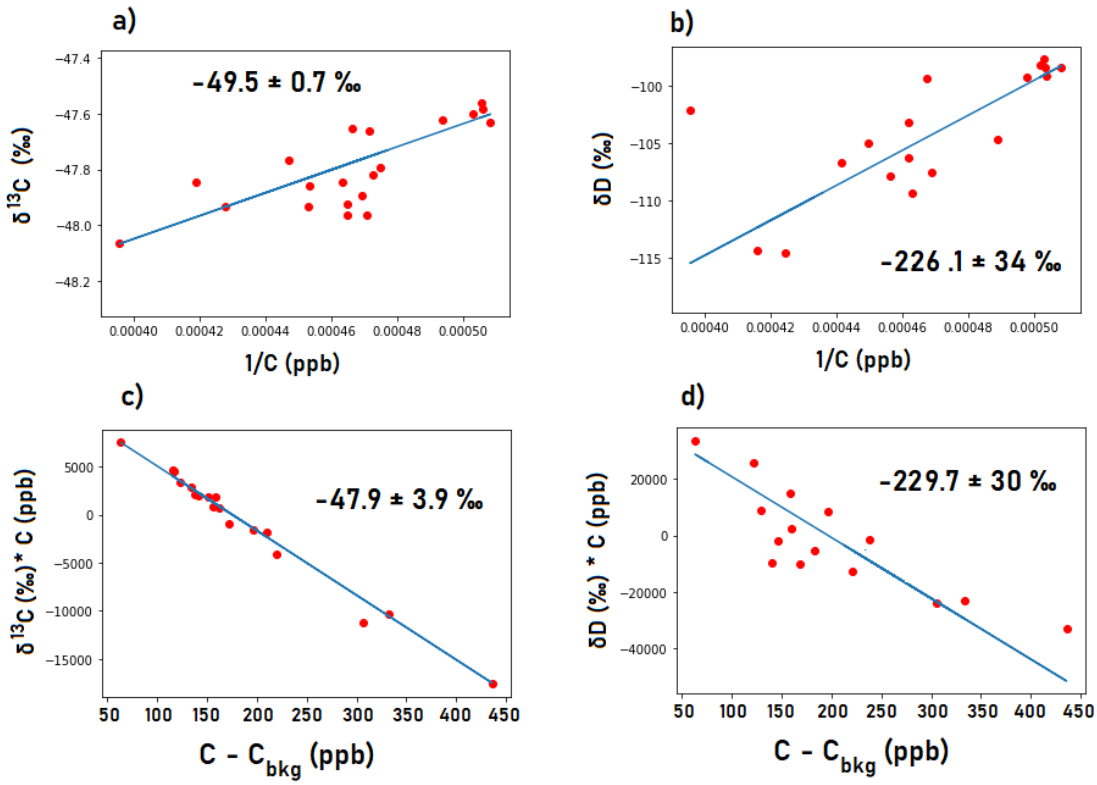

Figure A.8: Keeling (subplots a and b) and Miller Tans (subplots c and d) analysis of a single pollution event (9am 1st - 5am 2nd February 2021), for (a,c) δ^{13}C and (b,d) δD.

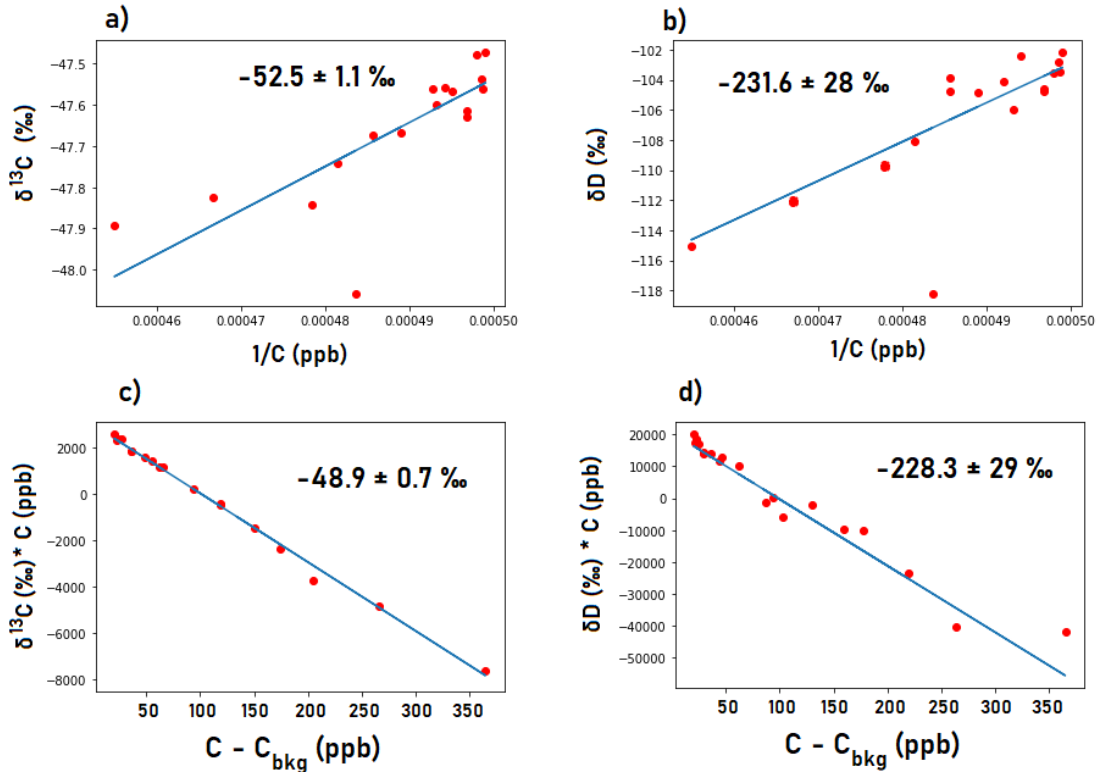

Figure A.9: Keeling (subplots a and b) and Miller Tans (subplots c and d) analysis of a single pollution event (2am - 7pm 6th February 2021), for (a,c) δ^{13}C and (b,d) δD.

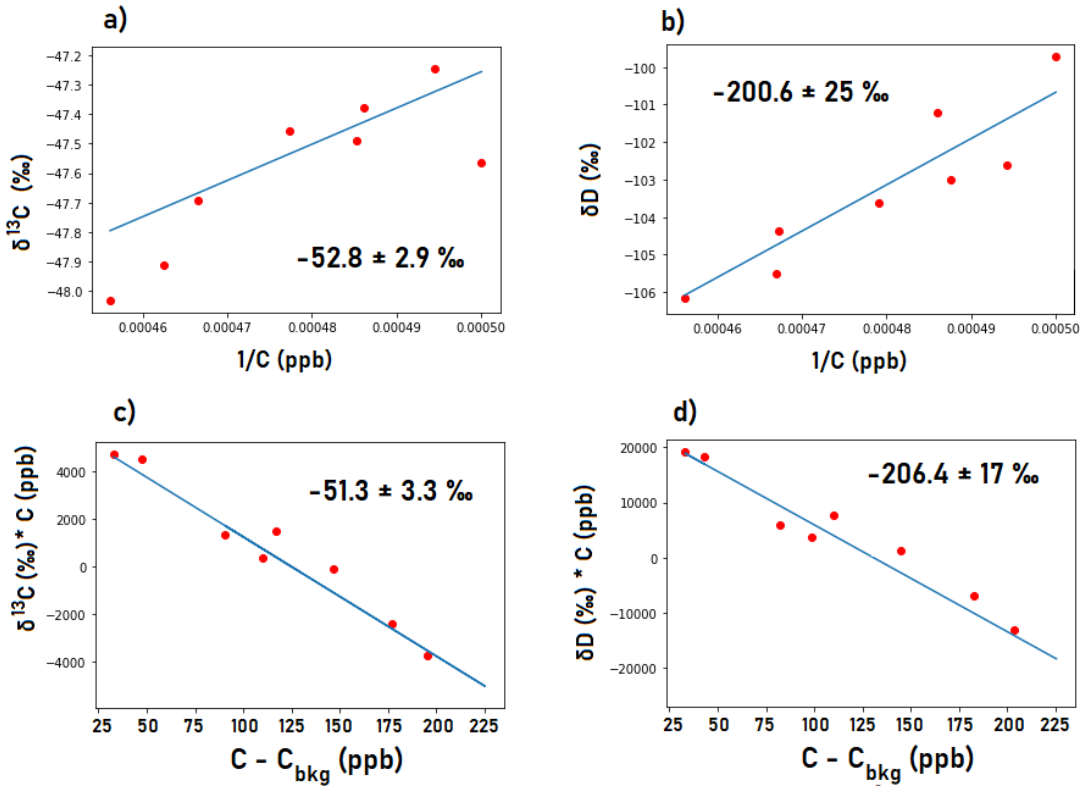

Figure A.10: Keeling (subplots a and b) and Miller Tans (subplots c and d) analysis of a single pollution event (12pm - 8pm 10th February 2021), for (a,c) δ^{13}C and (b,d) δD.

Bibliography

Archimède, H., Eugène, M., Marie Magdeleine, C., Boval, M., Martin, C., Morgavi, D., ... Doreau, M. (2011). Comparison of methane production between C3 and C4 grasses and legumes. *Animal Feed Science and Technology*, *166-167*, 59-64. (Special Issue: Greenhouse Gases in Animal Agriculture - Finding a Balance between Food and Emissions) doi: 10.1016/j.anifeedsci.2011.04.003

Arrhenius, S. (1896). On the influence of carbonic acid in the air upon the temperature of the ground. *The London, Edinburgh, and Dublin Philosophical Magazine and Journal of Science*, *41*(251), 237-276.

Badr, O., Probert, S., & O'Callaghan, P. (1992). Sinks for atmospheric methane. *Applied Energy*, *41*(2), 137-147. doi: 10.1016/0306-2619(92)90041-9

Basu, S., Lan, X., Dlugokencky, E., Michel, S., Schwietzke, S., Miller, J. B., ... Manca, G. (2022). Estimating Emissions of Methane Consistent with Atmospheric Measurements of Methane and δ^{13}C of Methane. *Atmospheric Chemistry and Physics Discussions*, *2022*, 1–38. doi: 10.5194/acp-2022-317

Bergamaschi, P., Schupp, M., & Harris, G. W. (1994). High-precision direct measurements of $^{13}CH_4/CH^{12}_4$ and $^{12}CH_3D/^{12}CH_4$ ratios in atmospheric methane sources by means of a long-path tunable diode laser absorption spectrometer. *Appl. Opt.*, *33*(33), 7704–7716. doi: 10.1364/AO.33.007704

Bey, I., Jacob, D. J., Yantosca, R. M., Logan, J. A., Field, B. D., Fiore, A. M., ... Schultz, M. G. (2001). Global modelling of tropospheric chemistry with assimilated meteorology: Model description and evaluation. *Journal of Geophysical Research Atmospheres*, *106*(D19), 23073–23095. doi: 10.1029/2001JD000807

Bloom, A. A., Bowman, K. W., Lee, M., Turner, A. J., Schroeder, R., Worden, J. R., ... Jacob, D. J. (2017). A global wetland methane emissions and uncertainty dataset for atmospheric chemical transport models (WetCHARTs version 1.0). *Geosci. Model Dev*, *10*, 2141–2156. doi: 10.5194/gmd-10-2141-2017

Bock, M., Schmitt, J., Beck, J., Schneider, R., & Fischer, H. (2014). Improving accuracy and precision of ice core δD(CH_4) analyses using methane pre-pyrolysis and hydrogen post-pyrolysis trapping and subsequent chromatographic separation. *Atmospheric Measurement Techniques*, *7*(7), 1999–2012. doi: 10.5194/amt-7-1999-2014

Bock, M., Schmitt, J., Behrens, M., Möller, L., Schneider, R., Sapart, C., & Fischer, H. (2010). A gas chromatography/pyrolysis/isotope ratio mass spectrometry system for high-precision δD measurements of atmospheric methane extracted from ice cores. *Rapid Communications in Mass Spectrometry*, *24*(5), 621-633. doi: 10.1002/rcm.4429

Bowling, D. R., Sargent, S. D., Tanner, B. D., & Ehleringer, J. R. (2003). Tunable diode laser absorption spectroscopy for stable isotope studies of ecosystem–atmosphere CO_2 exchange. *Agricultural and Forest Meteorology*, *118*(1), 1-19. doi: 10.1016/S0168-1923(03)00074-1

Braden-Behrens, J., Yan, Y., & Knohl, A. (2017). A new instrument for stable isotope measurements of ^{13}C and ^{18}O in CO_2 – instrument performance and ecological application of the Delta Ray IRIS analyzer. *Atmospheric Measurement Techniques*, *10*(11), 4537–4560. doi: 10.5194/amt-10-4537-2017

Brass, M., & Röckmann, T. (2010). Continuous-flow isotope ratio mass spectrometry method for carbon and hydrogen isotope measurements on atmospheric methane. *Atmospheric Measurement Techniques Discussions*, *3*. doi: 10.5194/amtd-3-2433-2010

Bréas, O., Guillou, C., Reniero, F., & Wada, E. (2001). The global methane cycle: isotopes and mixing ratios, sources and sinks. *Isotopes Environ Health Stud.*. doi: 10.1080/10256010108033302

Burkholder, J. B., Sander, S. P., Abbatt, J., Barker, J. R., Cappa, C., Crounse, J. D., ... Wine, P. H. (2020). *Chemical kinetics and photochemical data for use in atmospheric studies, evaluation no. 19* (Tech. Rep.). Jet Propulsion Laboratory, Pasadena: JPL Publication 19-5. Retrieved 2020-06-01, from `https://jpldataeval.jpl.nasa.gov/pdf/NASA-JPL-20Evaluation-2019-5.pdf`

Canty, T., & Minschwaner, K. (2002). Seasonal and solar cycle variability of OH in the middle atmosphere. *Journal of Geophysical Research: Atmospheres*, *107*(D24), ACH 1-1-ACH 1-6. doi: 10.1029/2002JD002278

Carslaw, D. C., & Ropkins, K. (2012). openair — An R package for air quality data analysis. *Environmental Modelling And Software*, *27–28*(0), 52–61. doi: 10.1016/j.envsoft.2011.09.008

Chung, E., & Arnold, T. (2021). Potential of Clumped Isotopes in Constraining the Global Atmospheric Methane Budget. *Global Biogeochemical Cycles*, *35*(10), e2020GB006883. (e2020GB006883 2020GB006883) doi: 10.1029/2020GB006883

Comyn-Platt, E., Hayman, G., Huntingford, C., Chadburn, S. E., Burke, E. J., Harper, W. J., Anna B.and Collins, ... Sitch, S. (2018). Carbon budgets for 1.5 and 2 °C targets lowered by natural wetland and permafrost feedbacks. *Nature Geoscience*, *11*, 568–573. doi: 10.1038/s41561-018-0174-9

Coplen, T. B., Brand, W. A., Gehre, M., Groning, M., Meijer, H. A. J., Toman, B., & Verkouteren, R. M. (2006). New Guidelines for δ^{13}C Measurements. *Analytical chemistry (Washington)*, *78*(7), 2439-2441.

Crutzen, P. J., & Andreae, M. O. (1990). Biomass Burning in the Tropics: Impact on Atmospheric Chemistry and Biogeochemical Cycles. *Science*, *250*(4988), 1669-1678. doi: 10.1126/science.250.4988.1669

Crutzen, P. J., Aselmann, I., & Seiler, W. (1986). Methane production by domestic animals, wild ruminants, other herbivorous fauna, and humans. *Tellus B*, *38B*(3-4), 271-284. doi: 10.1111/j.1600-0889.1986.tb00193.x

Crutzen, P. J., Heidt, L. E., Krasnec, J. P., Pollock, W. H., & Seiler, W. (1979). Biomass burning as a source of atmospheric gases CO, H_2, N_2O, NO, CH_3Cl and COS. *Nature*, *282*(5736), 253-256. doi: 10.1038/282253a0

Dlugokencky, E., Crotwell, A., Mund, J., & Thoning, K. (2020). *Atmospheric Methane Dry Air Mole Fractions from the NOAA GML Carbon Cycle Cooperative Global Air Sampling Network, 1983-2019, Version: 2020-07.* doi: 10.15138/VNCZ-M766

Dlugokencky, E., Harris, J., Chung, Y., Tans, P., & Fung, I. (1993). The relationship between the methane seasonal cycle and regional sources and sinks at Tae-ahn Peninsula, Korea. *Atmospheric Environment. Part A. General Topics*, *27*(14), 2115-2120. doi: 10.1016/0960-1686(93)90041-V

Dlugokencky, E., Myers, R. C., Lang, P. M., Masarie, K. A., Crotwell, A. M., Thoning, K. W., ... Steele, L. P. (2005). Conversion of NOAA atmospheric dry air CH_4 mole fractions to a gravimetrically prepared standard scale. *Journal of Geophysical Research: Atmospheres*, *110*(D18). doi: 10.1029/2005JD006035

Dlugokencky, E., Steele, L., Lang, P., & Masarie, K. (1994). The growth rate and distribution of atmospheric methane. *Journal of Geophysical Research: Atmospheres*, *99*(D8), 17021-17043. doi: 10.1029/94JD01245

Douglas, P. M., Stolper, D. A., Eiler, J. M., Sessions, A. L., Lawson, M., Shuai, Y., ... Kitchen, N. (2017). Methane clumped isotopes: Progress and potential for a new isotopic tracer. *Organic Geochemistry*, *113*, 262–282. doi: 10.1016/j.orggeochem.2017.07.016

Duncan, B. N., Strahan, S. E., Yoshida, Y., Steenrod, S. D., & Livesey, N. (2007). Model study of the cross-tropopause transport of biomass burning pollution. *Atmospheric Chemistry and Physics*, *7*(14), 3713–3736. doi: 10.5194/acp-7-3713-2007

Eiler, J. M. (2007). "Clumped-isotope" geochemistry-The study of naturally-occurring, multiply-substituted isotopologues. *Earth and Planetary Science Letters*, *262*(3-4), 309–327. doi: 10.1016/j.epsl.2007.08.020

Esler, M. B., Griffith, D. W. T., Wilson, S. R., & Steele, L. P. (2000). Precision Trace Gas Analysis by FT-IR Spectroscopy. 2. The $^{13}C/^{12}C$ Isotope Ratio of CO_2. *Analytical Chemistry*, *72*(1), 216-221. doi: 10.1021/ac990563x

Etiope, G., Ciotoli, G., Schwietzke, S., & Schoell, M. (2019). Gridded maps of geological methane emissions and their isotopic signature. *Earth System Science Data*, *11*(1), 1–22. doi: 10.5194/essd-11-1-2019

Evensen, G. (1994). Sequential data assimilation with a nonlinear quasi-geostrophic model using Monte Carlo methods to forecast error statistics. *Journal of Geophysical Research: Oceans*, *99*(C5), 10143-10162. doi: 10.1029/94JC00572

Evensen, G. (2003). The Ensemble Kalman Filter: theoretical formulation and practical implementation. *Ocean Dynamics*, *53*(4). doi: 10.1007/s10236-003-0036-9

Eyer, S., Tuzson, B., Popa, M. E., van der Veen, C., Röckmann, T., Rothe, M., ... Mohn, J. (2016). Real-time analysis of $\delta^{13}C$- and δD-CH_4 in ambient air with laser spectroscopy: method development and first intercomparison results. *Atmospheric Measurement Techniques*, *9*(1), 263–280. doi: 10.5194/amt-9-263-2016

Feinberg, A. I., Coulon, A., Stenke, A., Schwietzke, S., & Peter, T. (2018). Isotopic source signatures: Impact of regional variability on the $\delta^{13}CH_4$ trend and spatial distribution. *Atmospheric Environment*, *174*, 99–111. doi: 10.1016/J.ATMOSENV.2017.11.037

Feng, L., Palmer, P. I., Bösch, H., & Dance, S. (2009). Estimating surface CO_2 fluxes from space-borne CO_2 dry air mole fraction observations using an ensemble Kalman Filter. *Atmospheric Chemistry and Physics*, *9*(8), 2619–2633. doi: 10.5194/acp-9-2619-2009

Feng, L., Palmer, P. I., Bösch, H., Parker, R. J., Webb, A. J., Correia, C. S. C., ... Zahn, A. (2017). Consistent regional fluxes of CH_4 and CO_2 inferred from GOSAT proxy $XCH_4 : XCO_2$ retrievals, 2010–2014. *Atmospheric Chemistry and Physics*, *17*(7), 4781–4797. doi: 10.5194/acp-17-4781-2017

Feng, L., Palmer, P. I., Zhu, S., Parker, R. J., & Liu, Y. (2022, 16). Tropical methane emissions explain large fraction of recent changes in global atmospheric methane growth rate. *Nature Communications*, *13*(1), 1378. doi: 10.1038/s41467-022-28989-z

Fisher, R., Lowry, D., Wilkin, O., Sriskantharajah, S., & Nisbet, E. (2006). High-precision, automated stable isotope analysis of atmospheric methane and carbon dioxide usingcontinuous-flow isotope-ratio mass spectrometry. *Rapid Communications in Mass Spectrometry*, *20*(200-208).

Flores, E., Viallon, J., Moussay, P., Griffith, D. W. T., & Wielgosz, R. I. (2017). Calibration Strategies for FT-IR and Other Isotope Ratio Infrared Spectrometer Instruments for Accurate $\delta^{13}C$ and $\delta^{18}O$ Measurements of CO_2 in Air. *Analytical Chemistry*, *89*(6), 3648-3655. doi: 10.1021/acs.analchem.6b05063

Foote, E. (1856). Circumstances affecting the heat of the sun's rays. *American Journal of Scientific Arts*, *22*(382-383).

Fraser, A., Palmer, P. I., Feng, L., Bösch, H., Parker, R., Dlugokencky, E. J., ... Langenfelds, R. L. (2014). Estimating regional fluxes of CO_2 and CH_4 using space-borne observations of XCH_4: XCO_2. *Atmospheric Chemistry and Physics*, *14*(23), 12883–12895. doi: 10.5194/acp-14-12883-2014

Fujita, R., Morimoto, S., Maksyutov, S., Kim, H.-S., Arshinov, M., Brailsford, G., ... Nakazawa, T. (2020). Global and Regional CH_4 Emissions for 1995–2013 Derived From Atmospheric CH_4, δ^{13}C-CH_4, and δD-CH_4 Observations and a Chemical Transport Model. *Journal of Geophysical Research: Atmospheres*, *125*(14), e2020JD032903. (e2020JD032903 2020JD032903) doi: 10.1029/2020JD032903

Fung, I., John, J., Lerner, J., Matfhews, E., Prather, M., Steele, L. P., & Fraser, P. J. (1991). Three-dimensional model synthesis of the global methane cycle. *Journal Of Geophysical Research*, *96*(D7), 33–46.

Ganesan, A. L., Schwietzke, S., Poulter, B., Arnold, T., Lan, X., Rigby, M., ... Manning, M. R. (2019). Advancing Scientific Understanding of the Global Methane Budget in Support of the Paris Agreement. *Global Biogeochemical Cycles*, *33*(12), 1475-1512. doi: 10.1029/2018GB006065

Ganesan, A. L., Stell, A. C., Gedney, N., Comyn-Platt, E., Hayman, G., Rigby, M., ... Hornibrook, E. R. C. (2018). Spatially Resolved Isotopic Source Signatures of Wetland Methane Emissions. *Geophysical Research Letters*, *45*(8), 3737–3745. doi: 10.1002/2018GL077536

Gelaro, R., McCarty, W., Suárez, M. J., Todling, R., Molod, A., Takacs, L., ... Zhao, B. (2017). The modern-era retrospective analysis for research and applications, version 2 (MERRA-2). *Journal of Climate*, *30*(14), 5419–5454. doi: 10.1175/JCLI-D-16-0758.1

Gierczak, T., Talukdar, R. K., Herndon, S. C., Vaghjiani, G. L., & Ravishankara, A. R. (1997). Rate Coefficients for the Reactions of Hydroxyl Radicals with Methane and Deuterated Methanes. *The Journal of Physical Chemistry A*, *101*. doi: doi:10.1021/jp963892r

Griffis, T., Lee, X., Baker, J., Sargent, S., & King, J. (2005). Feasibility of quantifying ecosystem–atmosphere C18O16O exchange using laser spectroscopy and the flux-gradient method. *Agricultural and Forest Meteorology*, *135*(1), 44-60. doi: 10.1016/j.agrformet.2005.10.002

Griffith, D. W. T. (2018). Calibration of isotopologue-specific optical trace gas analysers : A practical guide. *Atmospheric Measurement Techniques*, *11*, 6189–6201.

Griffith, D. W. T., Deutscher, N. M., Caldow, C., Kettlewell, G., Riggenbach, M., & Hammer, S. (2012). A Fourier transform infrared trace gas and isotope analyser for atmospheric applications. *Atmospheric Measurement Techniques*, *5*(10), 2481–2498. doi: 10.5194/amt-5-2481-2012

Gurney, K. R., Law, R. M., Denning, A. S., Rayner, P. J., Baker, D., Bousquet, P., ... Yuen, C.-W. (2002). Towards robust regional estimates of CO_2 sources and sinks using atmospheric transport models. *Nature*, *415*(6872), 626–630. doi: 10.1038/415626a

Henry, R. C., Chang, Y.-S., & Spiegelman, C. H. (2002). Locating nearby sources of air pollution by nonparametric regression of atmospheric concentrations on wind direction. *Atmospheric Environment*, *36*(13), 2237-2244. doi: 10.1016/S1352-2310(02)00164-4

Janssens-Maenhout, G., Crippa, M., Guizzardi, D., Muntean, M., Schaaf, E., Dentener, F., ... Oreggioni, G. D. (2019). EDGAR v4.3.2 Global Atlas of the three major greenhouse gas emissions for the period 1970–2012. *Earth System Science Data*, *11*(3), 959–1002. doi: 10.5194/essd-11-959-2019

Keeling, C. D. (1958). The concentration and isotopic abundances of atmospheric carbon dioxide in rural areas. *Geochimica et Cosmochimica Acta*, *13*(4), 322-334. doi: 10.1016/0016-7037(58)90033-4

Keeling, C. D. (1960). The Concentration and Isotopic Abundances of Carbon Dioxide in the Atmosphere. *Tellus*, *12*(2), 200-203. doi: 10.3402/tellusa.v12i2.9366

Keeling, C. D. (1961). The concentration and isotopic abundances of carbon dioxide in rural and marine air. *Geochimica et Cosmochimica Acta*, *24*(3), 277-298. doi: 10.1016/0016-7037(61)90023-0

Keller, M., Goreau, T. J., Wofsy, S. C., Kaplan, W. A., & McElroy, M. B. (1983). Production of nitrous oxide and consumption of methane by forest soils. *Geophysical Research Letters*, *10*(12), 1156-1159. doi: 10.1029/GL010i012p01156

Khalil, M., & Rasmussen, R. A. (1984). The atmospheric lifetime of methylchloroform (CH_3CCl_3). *Tellus B: Chemical and Physical Meteorology*, *36*(5), 317-332. doi: 10.3402/tellusb.v36i5.14914

Kirschke, S., Bousquet, P., Ciais, P., Saunois, M., Canadell, J. G., Dlugokencky, E. J., ... Zeng, G. (2013). *Three decades of global methane sources and sinks* (Vol. 6) (No. 10). Nature Publishing Group. doi: 10.1038/ngeo1955

Laidler, K. J. (1987). *Chemical Kinetics, Third Edition*. Pearson Education.

Lan, X., Basu, S., Schwietzke, S., Bruhwiler, L. M. P., Dlugokencky, E. J., Michel, S. E., ... Crippa, M. (2021). Improved Constraints on Global Methane Emissions and Sinks Using δ^{13}C-CH_4. *Global Biogeochemical Cycles*, *35*(6), e2021GB007000. (e2021GB007000 2021GB007000) doi: 10.1029/2021GB007000

Laughner, J. L., Neu, J. L., Schimel, D., Wennberg, P. O., Barsanti, K., Bowman, K. W., ... Zeng, Z.-C. (2021). Societal shifts due to COVID-19 reveal large-scale complexities and feedbacks between atmospheric chemistry and climate change. *Proceedings of the National Academy of Sciences*, *118*(46). doi: 10.1073/pnas.2109481118

Lunt, M. F., Palmer, P. I., Feng, L., Taylor, C. M., Boesch, H., & Parker, R. J. (2019). An increase in methane emissions from tropical Africa between 2010 and 2016 inferred from satellite data. *Atmospheric Chemistry and Physics*, *19*(23), 14721–14740. doi: 10.5194/acp-19-14721-2019

Lunt, M. F., Palmer, P. I., Lorente, A., Borsdorff, T., Landgraf, J., Parker, R. J., & Boesch, H. (2021). Rain-fed pulses of methane from East Africa during 2018–2019 contributed to atmospheric growth rate. *Environmental Research Letters*, *16*(2), 024021. doi: 10.1088/1748-9326/abd8fa

Manning, A., O'Doherty, S., Young, D., Redington, A., Say, D., Pitt, J., ... Simmonds, P. (2022). *Long-term atmospheric measurement and interpretation of radiatively active trace gases* (Tech. Rep.). Exeter, UK: Met Office and University of Bristol and National Physical Laboratory. Retrieved 2020-05-01, from `https://assets.publishing.service.gov.uk/government/uploads/system/uploads/attachment_data/file/1092410/verification-uk-greenhouse-gas-emissions-using-atmospheric-observations-annual-report-2021.pdf`

Masson-Delmotte, V., Zhai, P., A. Pirani, S. C., C. Péan, S. B., Caud, N., Chen, Y., ... Zhou, B. (2021). *Climate Change 2021: The Physical Science Basis. Contribution of Working Group I to the Sixth Assessment Report of the Intergovernmental Panel on Climate Changes* (Tech. Rep.). WMO Geneva: IPCC.

McKinney, C. R., McCrea, J. M., Epstein, S., Allen, H. A., & Urey, H. C. (1950). Improvements in Mass Spectrometers for the Measurement of Small Differences in Isotope Abundance Ratios. *Review of Scientific Instruments*, *21*(8), 724-730. doi: 10.1063/1.1745698

McNorton, J., Chipperfield, M. P., Gloor, M., Wilson, C., Feng, W., Hayman, G. D., ... Montzka, S. A. (2016). Role of OH variability in the stalling of the global atmospheric CH_4 growth rate from 1999 to 2006. *Atmospheric Chemistry and Physics*, *16*(12), 7943–7956. doi: 10.5194/acp-16-7943-2016

McNorton, J., Wilson, C., Gloor, M., Parker, R., Boesch, H., Feng, W., & Chipperfield, M. (2018). Attribution of recent increases in atmospheric methane through 3-D inverse modelling. *Atmos. Chem. Phys*, *18*(June), 1–34. doi: 10.5194/acp-2018-474

Menoud, M., van der Veen, C., Lowry, D., Fernandez, J. M., Bakkaloglu, S., France, J. L., ... Röckmann, T. (2022). Global inventory of the stable isotopic composition of methane surface emissions, augmented by new measurements in Europe. *Earth System Science Data Discussions*, 1–31. doi: 10.5194/essd-2022-30

Michel, S., Clark, J., & Vaughn, B. (2021). *Stable Isotopic Composition of Atmospheric Methane (13C) from the NOAA GML Carbon Cycle Cooperative Global Air Sampling Network, 1998-2020.* doi: 10.15138/9p89-1x02

Miles, N. L., Martins, D. K., Richardson, S. J., Rella, C. W., Arata, C., Lauvaux, T., ... Sweeney, C. (2018). Calibration and field testing of cavity ring-down laser spectrometers measuring CH_4, CO_2, and $\delta^{13}CH_4$ deployed on towers in the Marcellus Shale region. *Atmospheric Measurement Techniques*, *11*(3), 1273–1295. doi: 10.5194/amt-11-1273-2018

Miller, J. B. (2002). Development of analytical methods and measurements of $^{13}C/^{12}$ C in atmospheric CH_4 from the NOAA Climate Monitoring and Diagnostics Laboratory Global Air Sampling Network. *Journal of Geophysical Research*, *107*(D13), 4178. doi: 10.1029/2001JD000630

Miller, J. B., & Tans, P. P. (2003). Calculating isotopic fractionation from atmospheric measurements at various scales. *Tellus B*, *55*(2), 207-214. doi: 10.1034/j.1600-0889.2003.00020.x

Miyazaki, K., Bowman, K., Sekiya, T., Takigawa, M., Neu, J. L., Sudo, K., ... Eskes, H. (2021). Global tropospheric ozone responses to reduced NO_x emissions linked to the COVID-19 worldwide lockdowns. *Science Advances*, *7*(24), eabf7460. doi: 10.1126/sciadv.abf7460

Morgenstern, O., Hegglin, M. I., Rozanov, E., O'Connor, F. M., Abraham, N. L., Akiyoshi, H., ... Zeng, G. (2017). Review of the global models used within phase 1 of the Chemistry–Climate Model Initiative (CCMI). *Geoscientific Model Development*, *10*(2), 639–671. doi: 10.5194/gmd-10-639-2017

Moss, A. R., Jouany, J.-P., & Newbold, J. (2000). Methane production by ruminants: its contribution to global warming. *Ann. Zootech.*, *49*(3), 231-253. doi: 10.1051/animres:2000119

Naus, S., Montzka, S. A., Pandey, S., Basu, S., Dlugokencky, E. J., & Krol, M. (2018). Constraints and biases in a tropospheric two-box model of OH. *Atmos. Chem. Phys. Discuss.*, *2018*, 1–29. doi: 10.5194/acp-2018-798

Nisbet, E. G., Dlugokencky, E. J., Manning, M. R., Lowry, D., Fisher, R. E., France, J. L., ... Ganesan, A. L. (2016). Rising atmospheric methane: 2007–2014 growth and isotopic shift. *Global Biogeochemical Cycles*, *30*(9), 1356–1370. doi: 10.1002/2016GB005406

Nisbet, E. G., Manning, M. R., Dlugokencky, E. J., Fisher, R. E., Lowry, D., Michel, S. E., ... White, J. W. C. (2019). Very Strong Atmospheric Methane Growth in the 4 Years 2014–2017: Implications for the Paris Agreement. *Global Biogeochemical Cycles*, *33*(3), 318-342. doi: 10.1029/2018GB006009

Ono, S., Wang, D. T., Gruen, D. S., Sherwood Lollar, B., Zahniser, M. S., McManus, B. J., & Nelson, D. D. (2014). Measurement of a doubly substituted methane isotopologue, $^{13}CH_3D$, by tunable infrared laser direct absorption spectroscopy. *Analytical Chemistry*, *86*(13), 6487–6494. doi: 10.1021/ac5010579

Palmer, P. I., Feng, L., Lunt, M. F., Parker, R. J., Bösch, H., Lan, X., ... Borsdorff, T. (2021). The added value of satellite observations of methane forunderstanding the contemporary methane budget. *Philosophical Transactions of the Royal Society A: Mathematical, Physical and Engineering Sciences*, *379*(2210), 20210106. doi: 10.1098/rsta.2021.0106

Pandey, S., Houweling, S., Lorente, A., Borsdorff, T., Tsivlidou, M., Bloom, A. A., ... Aben, I. (2021). Using satellite data to identify the methane emission controls of South Sudan's wetlands. *Biogeosciences*, *18*(2), 557–572. doi: 10.5194/bg-18-557-2021

Pang, J., Wen, X., Sun, X., & Huang, K. (2016). Intercomparison of two cavity ring-down spectroscopy analyzers for atmospheric $^{13}CO_2$ / $^{12}CO_2$ measurement. *Atmospheric Measurement Techniques*, *9*(8), 3879–3891. doi: 10.5194/amt-9-3879-2016

Parker, R., Boesch, H., Byckling, K., Webb, A. J., Palmer, P. I., Feng, L., ... Velazco, V. (2015). Assessing 5 years of GOSAT Proxy XCH_4 data and associated uncertainties. *Atmospheric Measurement Techniques*, *8*(11), 4785–4801. doi: 10.5194/amt-8-4785-2015

Parker, R., Boesch, H., Cogan, A., Fraser, A., Feng, L., Palmer, P. I., ... Wunch, D. (2011). Methane observations from the Greenhouse Gases Observing SATellite: Comparison to ground-based TCCON data and model calculations. *Geophysical Research Letters*, *38*(15).

Parker, R., Webb, A., Boesch, H., Somkuti, P., Barrio Guillo, R., Di Noia, A., ... Wunch, D. (2020). A decade of GOSAT Proxy satellite CH_4 observations. *Earth System Science Data*, *12*(4), 3383–3412. doi: 10.5194/essd-12-3383-2020

Picarro Inc. (2021). *G2401 Gas Concentration Analyzer.* Retrieved 2022-05-16, from `https://www.picarro.com/g2401_gas_concentration_analyzer`

Prinn, R., Weiss, R., Arduini, J., Arnold, T., DeWitt, H., Fraser, P., ... L., Z. (2018). History of chemically and radiatively important atmospheric gases from the Advanced Global Atmospheric Gases Experiment (AGAGE). *Earth Syst. Sci. Data*, *10*(985-1018).

Prokhorov, I., & Mohn, J. (2022). CleanEx: A Versatile Automated Methane Preconcentration Device for High-Precision Analysis of $^{13}CH_4$, $^{12}CH_3D$, and $^{13}CH_3D$. *Analytical Chemistry*, *94*(28), 9981-9986. (PMID: 35776914) doi: 10.1021/acs.analchem.2c01949

Randerson, J., Van Der Werf, G., Giglio, L., Collatz, G., & Kasibhatla, P. (2017). *Global Fire Emissions Database, Version 4.1 (GFEDv4).* ORNL Distributed Active Archive Center. doi: 10.3334/ORNLDAAC/1293

Rella, C. W., Hoffnagle, J., He, Y., & Tajima, S. (2015). Local- and regional-scale measurements of CH_4, $\delta^{13}CH_4$, and C_2H_6 in the Uintah Basin using a mobile stable isotope analyzer. *Atmospheric Measurement Techniques*, *8*(10), 4539–4559. doi: 10.5194/amt-8-4539-2015

Rennick, C., Arnold, T., Safi, E., Drinkwater, A., Dylag, C., Webber, E. M., ... Lowry, D. (2021). Boreas: A Sample Preparation-Coupled Laser Spectrometer System for Simultaneous High-Precision In Situ Analysis of $\delta^{13}C$ and $\delta 2H$ from Ambient Air Methane. *Analytical Chemistry*, *93*(29), 10141–10151. (PMID: 34260200) doi: 10.1021/acs.analchem.1c01103

Rice, A. L., Butenhoff, C. L., Teama, D. G., Röger, F. H., Khalil, M. A. K., & Rasmussen, R. A. (2016). Atmospheric methane isotopic record favors fossil sources flat in 1980s and 1990s with recent increase. *Proceedings of the National Academy of Sciences*, *113*(39), 10791–10796. doi: 10.1073/pnas.1522923113

Rigby, M., Manning, A. J., & Prinn, R. G. (2012). The value of high-frequency, high-precision methane isotopologue measurements for source and sink estimation. *Journal of Geophysical Research: Atmospheres*, *117*(D12). doi: 10.1029/2011JD017384

Rigby, M., Montzka, S. A., Prinn, R. G., White, J. W. C., Young, D., O'Doherty, S., ... Park, S. (2017). Role of atmospheric oxidation in recent methane growth. *Proceedings of the National Academy of Sciences*, *114*(21), 5373–5377. doi: 10.1073/pnas.1616426114

Rodgers, C. D. (2000). *Inverse Methods for Atmospheric Sounding : Theory and Practice*. World Scientific.

Rothman, L., Jacquemart, D., Barbe, A., Benner, D. C., Birk, M., Brown, L., ... To, R. (2005). The HITRAN 2004 molecular spectroscopic database. *Journal of Quantitative Spectroscopy & Radiative Transfer*, *96*(2), 139–204. doi: 10.1016/j.jqsrt.2004.10.008

Saboya, E., Zazzeri, G., Graven, H., Manning, A. J., & Englund Michel, S. (2022). Continuous CH_4 and $\delta^{13}CH_4$ measurements in London demonstrate under-reported natural gas leakage. *Atmospheric Chemistry and Physics*, *22*(5), 3595–3613. doi: 10.5194/acp-22-3595-2022

Santoni, G. W., Lee, B. H., Goodrich, J. P., Varner, R. K., Crill, P. M., McManus, J. B., ... Wofsy, S. C. (2012). Mass fluxes and isofluxes of methane (CH_4) at a New Hampshire fen measured by a continuous wave quantum cascade laser spectrometer. *Journal of Geophysical Research: Atmospheres*, *117*(D10). doi: 10.1029/2011JD016960

Sapart, C. J., van der Veen, C., Vigano, I., Brass, M., van de Wal, R. S. W., Bock, M., ... Röckmann, T. (2011). Simultaneous stable isotope analysis of methane and nitrous oxide on ice core samples. *Atmospheric Measurement Techniques*, *4*(12), 2607–2618. doi: 10.5194/amt-4-2607-2011

Sasakawa, M., Shimoyama, K., Machida, T., Tsuda, N., Suto, H., Arshinov, M., ... Maksyutov, S. (2010). Continuous measurements of methane from a tower network over Siberia. *Tellus B*, *62*(5), 403-416. doi: 10.1111/j.1600-0889.2010.00494.x

Saunois, M., Bousquet, P., Poulter, B., Peregon, A., Ciais, P., Canadell, J. G., ... Zhu, Q. (2016). The global methane budget 2000-2012. *Earth Syst. Sci. Data*, *8*, 697–751. doi: 10.5194/essd-8-697-2016

Saunois, M., Stavert, A. R., Poulter, B., Bousquet, P., Canadell, J. G., Jackson, R. B., ... Zhuang, Q. (2020). The Global Methane Budget 2000–2017. *Earth System Science Data*, *12*(3), 1561–1623. doi: 10.5194/essd-12-1561-2020

Schaefer, H., Schaefer, H., Fletcher, S. E. M., Veidt, C., Lassey, K. R., Brailsford, G. W., ... White, J. W. C. (2016). A 21st century shift from fossil-fuel to biogenic methane emissions indicated by $13CH_4$. *Science*, *352*(6281), 1–10.

Schmitt, J., Seth, B., Bock, M., & Fischer, H. (2014). Online technique for isotope and mixing ratios of CH_4, N_2O, Xe and mixing ratios of organic trace gases on a single ice core sample. *Atmospheric Measurement Techniques*, *7*(8), 2645–2665. doi: 10.5194/amt-7-2645-2014

Schuldt, K. N., Aalto, T., Andrews, A., Aoki, S., Arduini, J., Baier, B., ... di Sarra, A. G. (2021). *Multi-laboratory compilation of atmospheric methane data for the period 1983-2020; obspack_CH_4_1_GLOBALVIEWplus_v4.0_2021-10-14.* doi: 10.25925/20211001

Schwietzke, S., Sherwood, O. A., Bruhwiler, L. M., Miller, J. B., Etiope, G., Dlugokencky, E. J., ... Tans, P. P. (2016). Upward revision of global fossil fuel methane emissions based on isotope database. *Nature*, *538*(7623), 88–91. doi: 10.1038/nature19797

Seiler, W., & Crutzen, P. J. (1980). Estimates of gross and net fluxes of carbon between the biosphere and the atmosphere from biomass burning. *Climatic Change*, *2*(3), 207-247. doi: 10.1007/BF00137988

Sheng, J., Tunnicliffe, R., Ganesan, A. L., Maasakkers, J. D., Shen, L., Prinn, R. G., ... Lu, X. (2021). Sustained methane emissions from China after 2012 despite declining coal production and rice-cultivated area. *Environmental Research Letters*, *16*(10), 104018. doi: 10.1088/1748-9326/ac24d1

Sherwen, T., Schmidt, J. A., Evans, M. J., Carpenter, L. J., Großmann, K., Eastham, S. D., ... Ordóñez, C. (2016). Global impacts of tropospheric halogens (Cl, Br, I) on oxidants and composition in GEOS-Chem. *Atmospheric Chemistry and Physics*, *16*(18), 12239–12271. doi: 10.5194/acp-16-12239-2016

Sherwood, O., Schwietzke, S., Arling, V. A., & Etiope, G. (2017). Global inventory of gas geochemistry data from fossil fuel, microbial and burning sources, version 2017. *Earth System Science Data*, *9*(2), 639–656. doi: 10.5194/essd-9-639-2017

Sherwood, O., Schwietzke, S., & Lan, X. (2021). Global Inventory of Fossil and Non-fossil δ^{13}C-CH_4 Source Signature Measurements for Improved Atmospheric Modeling. *Earth Syst. Sci. Data*. doi: 10.15138/qn55-e011

Snover, A. K., & Quay, P. D. (2000). Hydrogen and carbon kinetic isotope effects during soil uptake of atmospheric methane. *Global Biogeochemical Cycles*, *14*(1), 25–39. doi: 10.1029/1999GB900089

Steele, L. P., Fraser, P. J., Rasmussen, R. A., Khalil, M. A. K., Conway, T. J., Crawford, A. J., ... Thoning, K. W. (1987). The Global Distribution of Methane in the Troposphere. *Journal of Atmospheric Chemistry*, *5*. doi: 10.1007/BF00048857

Steur, P. M., Scheeren, H. A., Nelson, D. D., McManus, J. B., & Meijer, H. A. J. (2021). Simultaneous measurement of δ^{13}C, δ^{18}O and δ^{17}O of atmospheric CO_2 – performance assessment of a dual-laser absorption spectrometer. *Atmospheric Measurement Techniques*, *14*(6), 4279–4304. doi: 10.5194/amt-14-4279-2021

Stolper, D. A., Sessions, A. L., Ferreira, A. A., Santos Neto, E. V., Schimmelmann, A., Shusta, S. S., ... Eiler, J. M. (2014). Combined ^{13}C-D and D-D clumping in methane: Methods and preliminary results. *Geochimica et Cosmochimica Acta*, *126*, 169–191. doi: 10 .1016/j.gca.2013.10.045

Stone, D., Whalley, L. K., & Heard, D. E. (2012). Tropospheric OH and HO2 radicals: field measurements and model comparisons. *Chemical Society Reviews*, *41*. doi: 10.1039/ C2CS35140D

Tans, P. P., Crotwell, A. M., & Thoning, K. W. (2017). Abundances of isotopologues and calibration of CO_2 greenhouse gas measurements. *Atmospheric Measurement Techniques*, *10*(7), 2669–2685. doi: 10.5194/amt-10-2669-2017

Thonat, T., Saunois, M., Pison, I., Berchet, A., Hocking, T., Thornton, B. F., ... Bousquet, P. (2019). Assessment of the theoretical limit in instrumental detectability of northern high-latitude methane sources using δ^{13}C atmospheric signals. *Atmospheric Chemistry and Physics*, *19*(19), 12141–12161. doi: 10.5194/acp-19-12141-2019

Turner, A. J., Frankenberg, C., & Kort, E. A. (2019). Interpreting contemporary trends in atmospheric methane. *Proceedings of the National Academy of Sciences*, *116*(8), 201814297. doi: 10.1073/pnas.1814297116

Turner, A. J., Frankenberg, C., Wennberg, P. O., & Jacob, D. J. (2017). Ambiguity in the causes for decadal trends in atmospheric methane and hydroxyl. *Proceedings of the National Academy of Sciences*, *114*(21), 5367–5372. doi: 10.1073/pnas.1616020114

Tuzson, B., Henne, S., Brunner, D., Steinbacher, M., Mohn, J., Buchmann, B., & Emmenegger, L. (2011). Continuous isotopic composition measurements of tropospheric CO_2 at Jungfraujoch (3580 m a.s.l.), Switzerland: real-time observation of regional pollution events. *Atmospheric Chemistry and Physics*, *11*(4), 1685–1696. doi: 10.5194/acp-11-1685-2011

Tyndall, J. (1861). The Bakerian Lecture: On the absorption and radiation of heat by gases and vapours, and on the physical connexion of radiation, absorption, and conduction. *Philosophical Transactions of the Royal Society of London*, *151*(1-36), 28-29.

Umezawa, T., Aoki, S., Nakazawa, T., & Morimoto, S. (2009). A High-precision Measurement System for Carbon and Hydrogen Isotopic Ratios of Atmospheric Methane and Its Application to Air Samples Collected in the Western Pacific Region. *Journal of the Meteorological Society of Japan. Ser. II*, *87*(3), 365-379. doi: 10.2151/jmsj.87.365

Umezawa, T., Brenninkmeijer, C. A. M., Röckmann, T., van der Veen, C., Tyler, S. C., Fujita, R., ... Levin, I. (2018). Interlaboratory comparison of δ^{13}C and δD measurements of atmospheric CH_4 for combined use of data sets from different laboratories. *Atmospheric Measurement Techniques*, *11*(2), 1207–1231. doi: 10.5194/amt-11-1207-2018

UNFCCC. (2015). *The Paris Agreement.* Retrieved 2022-06-01, from `https://treaties.un.org/pages/ViewDetails.aspx?src=TREATY&mtdsg_no=XXVII-7-d&chapter=27&clang=_en` (UNTC XXVII 7.d)

United Nations Environment Programme and Climate and Clean Air Coalition. (2021). *Global Methane Assessment: Benefits and Costs of Mitigating Methane Emissions*. Nairobi: United Nations Environment Programme.

Urey, H. C. (1948). Oxygen Isotopes in Nature and in the Laboratory. *Science*, *108*(2810), 489-496. doi: 10.1126/science.108.2810.489

US Department of Commerce, N. (2022). *Global Monitoring Laboratory - South Pole Observatory.* Retrieved 2022-06-01, from `https://gml.noaa.gov/obop/spo/observatory.html`

Vardag, S. N., Hammer, S., Sabasch, M., Griffith, D. W. T., & Levin, I. (2015). First continuous measurements of δ^{18}O-CO_2 in air with a Fourier transform infrared spectrometer. *Atmospheric Measurement Techniques*, *8*(2), 579–592. doi: 10.5194/amt-8-579-2015

Vaughn, B., Miller, J., Ferretti, D., & White, J. (2004). Stable isotope measurements of atmospheric co_2 and ch_4. In *Handbook of stable isotope analytical techniques, vol 1* (chap. 14). Elsevier.

Voulgarakis, A., Naik, V., Lamarque, J.-F., Shindell, D. T., Young, P. J., Prather, M. J., ... Zeng, G. (2013). Analysis of present day and future OH and methane lifetime in the ACCMIP simulations. *Atmos. Chem. Phys.*, *13*, 2563–2587. doi: 10.5194/acp-13-2563-2013

Warwick, N., Cain, M., Fisher, R., J.L., F., Lowry, D., Michel, S., ... Pyle, J. (2016). Using δ^{13}C-CH_4 and δD-CH_4 to constrain Arctic methane emissions. *Atmospheric Chemistry and Physics*, *16*, 14891–14908. doi: doi:10.5194/acp-16-14891-2016

Wehr, R., Munger, J., Nelson, D., McManus, J., Zahniser, M., Wofsy, S., & Saleska, S. (2013). Long-term eddy covariance measurements of the isotopic composition of the ecosystem–atmosphere exchange of CO_2 in a temperate forest. *Agricultural and Forest Meteorology*, *181*, 69-84. doi: 10.1016/j.agrformet.2013.07.002

Wen, X.-F., Meng, Y., Zhang, X.-Y., Sun, X.-M., & Lee, X. (2013). Evaluating calibration strategies for isotope ratio infrared spectroscopy for atmospheric $^{13}CO_2$ / $^{12}CO_2$ measurement. *Atmospheric Measurement Techniques*, *6*(6), 1491–1501. doi: 10.5194/amt-6-1491-2013

White, J., Vaughn, B., & Michel, S. (2016). *Stable Isotopic Composition of Atmospheric Methane (2H) from the NOAA ESRL Carbon Cycle Cooperative Global Air Sampling Network, 2005-2009, Version: 2016-04-26,.* Retrieved 2022-06-01, from `ftp://aftp.cmdl.noaa.gov/data/trace_gases/ch4h2/flask/`

Whitehill, A., Joelsson, M., Schmidt, J., Wang, D., Johnson, M., & Ono, S. (2017). Clumped isotope effects during OH and Cl oxidation of methane. *Geochimica et Cosmochimica Acta*, *196*, 307–325. doi: 10.1016/j.gca.2016.09.012

Wilson, C., Chipperfield, M. P., Gloor, M., Parker, R. J., Boesch, H., McNorton, J., ... Monks, S. A. (2021). Large and increasing methane emissions from eastern Amazonia derived from satellite data, 2010–2018. *Atmospheric Chemistry and Physics*, *21*(13), 10643–10669. doi: 10.5194/acp-21-10643-2021

Worden, J., Bloom, A., Pandey, S., Jiang, Z., Worden, H., Walker, T., ... Röckmann, T. (2017). Reduced biomass burning emissions reconcile conflicting estimates of the post-2006 atmospheric methane budget. *Nature Communications*, *8*. doi: 10.1038/s41467-017-02246-0

Yin, Y., Chevallier, F., Ciais, P., Bousquet, P., Saunois, M., Zheng, B., ... Frankenberg, C. (2021). Accelerating methane growth rate from 2010 to 2017: leading contributions from the tropics and East Asia. *Atmospheric Chemistry and Physics*, *21*(16), 12631–12647. doi: 10.5194/acp-21-12631-2021

Zazzeri, G., Lowry, D., Fisher, R. E., France, J. L., Lanoisellé, M., Grimmond, C. S. B., & Nisbet, E. G. (2017, July). Evaluating methane inventories by isotopic analysis in the London region. *Scientific Reports*, *7*. doi: 10.1038/s41598-017-04802-6

Zazzeri, G., Lowry, D., Fisher, R. E., France, J. L., Lanoisellé, M., Kelly, B. F. J., ... Nisbet, E. G. (2016). Carbon isotopic signature of coal-derived methane emissions to the atmosphere: from coalification to alteration. *Atmospheric Chemistry and Physics*, *16*(21), 13669–13680. doi: 10.5194/acp-16-13669-2016

Zhao, Y., Saunois, M., Bousquet, P., Lin, X., Berchet, A., Hegglin, M. I., ... Zheng, B. (2019). Inter-model comparison of global hydroxyl radical (OH) distributions and their impact on atmospheric methane over the 2000–2016 period. *Atmospheric Chemistry and Physics*, *19*(21), 13701–13723. doi: 10.5194/acp-19-13701-2019

Zhou, L., Kitzis, D., & Tans, P. (2009). *Report of the Fourth WMO Round-Robin Reference Gas Intercomparison, 2002-2007* (Tech. Rep.). Geneva, Switzerland: World Meteorological Organisation.